Subspace Identification of Biomedical Systems: Application to Dynamic Joint Stiffness

Seyed Kian Jalaleddini

Doctor of Philosophy

Biomedical Engineering Department

McGill University

Montreal,Quebec

July 9, 2015

A thesis submitted to McGill University in partial fulfillment of the requirements of the degree of Doctor of Philosophy

To my parents:

for their love and support

ABSTRACT

This thesis presents some new analytical tools and methods for the identification of Hammerstein and parallel-cascade systems which are of particular relevance to the study of dynamic joint stiffness. Joint stiffness plays a critical role in the control of posture and movement and it has been extensively used to describe the biomechanics of joints. Consequently, its accurate measurement is important to many research fields. Dynamic joint stiffness can be modelled as a block oriented nonlinear system having two parallel pathways: intrinsic stiffness which is due to the mechanical properties of the joint, muscles and tissues; and reflex stiffness which is due to stretch reflex mechanisms.

This thesis presents objective methods that advance the ability to quantify stiffness in three main ways. Firstly, it describes an analytical framework for the accurate and efficient decomposition of total joint torque into its intrinsic and reflex components. This is important since these are generated and change together and cannot be measured individually. Previous analytical tools used an iterative approach to decompose the torque which failed to converge in important experimental conditions. Secondly, it develops a new state-space model of stiffness with a minimal number of parameters, each directly related to the individual element of stiffness. This facilitates the physiological interpretation of identification results. The parameters of previous state-space models were not explicitly related to the underlying elements. Thus, while they predicted the torque accurately, they did not model individual components of stiffness.

Thirdly, it provides a solution for measuring stiffness from multiple, short, quasi-stationary data segments. In functionally important tasks, both pathways become time-varying or show switching behaviour and so input-output data are non-stationary. Fortunately, in many cases, the data can be segmented into multiple, short, quasi-stationary segments with each subset of segments having the same properties. The new methods identify local time-invariant models for each quasi-stationary subset.

Finally, extensive simulation studies that mimicked important experimental conditions, tested these tools rigorously. When compared with other methods, the new methods gave more accurate estimates with lower variance and higher resistance to noise. This thesis also demonstrates the successful application of the new methods to experimental data. They provided accurate estimates of stiffness in a number of postural and movement tasks. They also unmasked important properties of the neuromuscular system and demonstrated how the reflex response is controlled by modulating both threshold and gain.

The new methods provide a better understanding on how the central nervous system modulates stiffness to perform a task. They also have important applications in assessment, diagnosis, treatment prescription and monitoring of a number of neuromuscular pathologies. Moreover, they are general and applicable to other biomedical systems with block oriented structures.

ABRÉGÉ

Cette thèse présente de nouveaux outils d'analyse et des méthodes pour l'identification des systèmes Hammerstein et parallèle-cascade qui revêtent un intérêt particulier pour l'étude de la rigidité articulaire dynamique. La rigidité articulaire joue un rôle essentiel dans le contrôle de la posture et du mouvement et a été largement utilisé pour décrire la biomécanique des articulations. Par conséquent, sa mesure précise est importante à de nombreux domaines de recherche. La rigidité dynamique peut être modélisée par un système en bloc avec deux voies parallèles: la rigidité intrinsèque qui est due aux propriétés mécaniques de l'articulation ainsi que des muscles et des tissus, et la rigidité réflexe générée par réflexe ostéotendineux.

Les méthodes objectives proposées avancent la capacité de quantifier la rigidité de trois manières principales. Tout d'abord, un cadre analytique est décrit pour la décomposition précise et efficace du moment de force articulaire en ses composants intrinsèque et réflexe. Ceci est important parce que ces composants existent et varient ensemble et ne peuvent pas être mesurés individuellement. Aussi, les anciens outils analytiques utilisent une approche itérative pour décomposer le moment de force qui ne réussit pas à converger face aux conditions expérimentales importantes. Ensuite, un nouveau modèle à représentation d'état de rigidité est conçu avec un nombre minimal de paramètres, chacun directement lié à un élément individuel de la rigidité. Cela facilite l'interprétation physiologique des résultats de l'identification étant donné que les paramètres des modèles précédents n'ont pas été explicitement liés à de tels éléments. Par conséquent, ces modèles font une prédiction précise du

moment de force mais ils ne sont pas capables de modéliser les composants individuels de rigidité.

Troisièmement, une solution est offerte qui permet de mesurer la rigidité de multiples courts segments de données quasi-stationnaires. Ainsi, au cours de tâches fonctionnellement importantes, les deux voies mentionnées ci-dessus deviennent variables en fonction du temps ou montrent un comportement de commutation et les données deviennent non-stationnaires. Heureusement, dans la plupart de ces tâches, les données peuvent être segmentées en plusieurs courts segments quasi-stationnaires avec des sous-ensembles de segments ayant les mêmes propriétés. Les nouvelles méthodes identifient les modèles invariants locaux pour chaque sous-ensemble des données quasi-stationnaires.

Enfin, les outils proposés sont rigoureusement vérifiés dans le cadre des études approfondies de simulation qui imitent les conditions expérimentales importantes. Les nouvelles méthodes donnent des estimations plus précises avec une variance plus faible et une plus grande résistance au bruit, par rapport des méthodes précédentes. Cette thèse démontre également l'application des nouvelles méthodes aux données expérimentales avec succès. Ces méthodes fournissent des estimations précises de rigidité dans un certain nombre de tâches posturales et de mouvement. Elles révèlent aussi des propriétés importantes du système neuromusculaire et démontrent comment la réponse réflexe est dirigée par modulation de seuil et de gain.

Les nouvelles méthodes permettent de mieux comprendre comment le système nerveux central module la rigidité afin d'effectuer une tâche. Elles ont également des applications importantes dans l'évaluation, le diagnostic, la prescription et le monitorage de certaines pathologies neuromusculaires. De plus, elles sont d'ordres généraux et applicables aux autres systèmes biomédicaux avec des structures en bloc.

ACKNOWLEDGMENTS

I wish to express my sincere gratitude to my advisor, Dr. Robert Kearney, for his invaluable support and advice on every stage of my PhD life. He has not only taught me joint stiffness and system identification but also indispensable life lessons.

Special thanks to my wife, Mina for all her moral and technical support. Not only she makes my life wonderful, she is also my best friend and colleague. She encouraged me all the time and never got tired of discussing system identification with me.

I would also like to thank my PhD committee members and especially Dr. Henrietta Galiana for providing me with excellent feedback on my research. I am also thankful to Dr. David Westwick for his insightful comments he provided at several conferences.

My gratitude extends to my lab colleague and friend Ehsan Sobhani with whom I had the opportunity to work closely. I enjoyed daily fruitful discussion with him and benefited greatly from his experience and knowledge. My appreciation also goes to other fellow REKlabers Abhishek, Alejandro, Carlos, Chris, Daniel, Diego, Ferryl, Lara, Mahsa and Pouya for making the lab my second home. Also, I would like to thank the department student affair officer, Pina, and graduate program coordinator, Nancy, for devoting their time to find solutions to my everyday questions.

I am grateful to have wonderful friends who made my life enjoyable: Arash, Mahsa, Hamid, Danial, Vahid and Iman.

Last, but not least, I would like to thank my parents, my brother and sister for their unconditional love and support.

The financial support of my research was provided by Canadian Institutes of Health Research (CIHR), Department of Biomedical Engineering, Fonds de recherche du Québec - Nature et technologies (FRQNT) and Natural Sciences and Engineering Research Council of Canada (NSERC).

TABLE OF CONTENTS

LIST OF TABLES

LIST OF FIGURES

CHAPTER 1
Introduction

Healthy humans perform motor tasks to take care of their bodies and/or to interact with the environment. Examples include bathing, dressing, eating, and community mobility [7]. These tasks may be performed without conscious thought but they involve multiple complex mechanisms, many of them still unknown, working together to accomplish the task. The neuromuscular system performs and controls these mechanisms. Thus, the central nervous system sends commands to the periphery that causes muscle contractions. It also constantly receives information about the state of the periphery, e.g. muscle kinematics (forces exerted on muscles, muscle lengths and their rates of changes), orientation of the body in space, etc, that it uses to regulate theses commands [8].

Humans must regulate their joint stiffnesses to effectively interact with the environment and to smoothly perform these motor tasks, [9]. This is because stiffness determines the resistance of the joint to an external perturbation before voluntary interventions in a postural task; it also defines the properties of the load and actuator that the central nervous system must control to perform a movement [10, 11, 12].

Regulation of joint stiffness is primarily achieved by two mechanisms. The first involves altering muscle activation or co-activation through neural commands. Thus, muscles exert forces on a joint to rotate it or maintain a posture. While the forces of agonist/antagonist muscles subtract with co-activation, it shifts the joint stiffness.

For example, in an arm wrestling match players strengthen their joint stiffnesses by engaging muscles and boosting their activations. The second mechanism is by selection of the joint posture, e.g. maintaining an open angle for the elbow joint during handwriting. Stiffness regulation can be achieved voluntarily when people deliberately select a posture or activation/co-activation level or involuntarily when stiffness is regulated through reflex arcs for fast corrections. The reflex mechanisms are also modulated with activation level and posture selection [10, 13, 14, 15, 16, 17, 18].

This thesis will focus on ankle joint stiffness. This joint is particularly important because during many activities of daily living, all interactions between the body and the environment are exerted as forces and moments at the ankle joint.

Our approach to understand how humans regulate ankle stiffness is by mathematical modelling. These models can describe the underlying system and simulating them can predict their behaviour. This is a non-invasive approach that can provide valuable insight into how the different elements of the neuromuscular system function individually and together. Moreover, these models provide objective methods for the diagnosis, assessment, treatment prescription and treatment monitoring of neuromuscular diseases that change muscle tone. They are also important to rehabilitation engineering works related to restoring function of lost or impaired limbs. Thus, a robot is designed to match the stiffness of the lost or impaired joint to a normal one. They are also important in the design of robots interacting with humans, biomimetic robots, and in sports for assessment purposes [19, 20, 21, 22, 23, 24, 25, 26, 27, 28, 29, 30, 31, 32].

One way to construct mathematical models of joint stiffness is to identify them from measurements of input-output data. This approach is called system identification which Lennart Ljung describes as “the art and science of building mathematical models of dynamic systems from observed input-output data. It can be seen as the interface between the real world of applications and the mathematical world...” [33]. This approach has been extensively used to obtain models of different neuromuscular systems [34, 35, 36].

Joint stiffness at the ankle joint can be modelled with a parallel-cascade structure with intrinsic and reflex pathways. Intrinsic stiffness results from the inertial properties of the limb and the viscoelastic properties of the joint surface, ligaments, connective tissues and active muscle fibers. Reflex stiffness is due to changes in muscle activation as a result of reflex mechanisms [37].

There are three major challenges in identification of the parallel-cascade model:

1. The intrinsic and reflex torques cannot be measured separately and only a noisy version of their sum can be measured as the net joint torque. Moreover, the intrinsic and reflex torques change together throughout the experiment. Consequently, the identification method must decompose the net torque to its intrinsic and reflex components before identification.
2. The joint posture and/or activation level has significant effects on both pathways and so the identified models must account for these modulations in a nonlinear or time-varying manner. Consequently, underlying dynamics are complex and requires complex nonlinear or time-varying methods.

3. The output noise is large so methods must be reliable and robust in the presence of noise.

The objectives of this thesis are to: (i) develop identification algorithms to effectively decompose the torque to the intrinsic and reflex torques and identify stiffness during a number of functionally important tasks; (ii) explore the performance of the methods using simulation studies mimicking realistic experimental conditions;(iii) demonstrate their utility with experimental data. The main contribution of this thesis is in the development of improved methods for system identification of the peripheral neuromuscular system. Nevertheless, these methods can be expected to provide novel findings and unmask important features of the neuromuscular system.

1.1 Thesis Outline

I present this thesis as a collection of four scholarly articles, 1 published journal paper, 1 journal paper currently under review and 1 journal article under preparation as well as 1 paper published in a conference proceeding. I am the first author of all four papers.

Chapter 2 describes the background materials. It starts by describing the anatomy and physiology of the neuromuscular system. It then describes the anatomy of the ankle joint, its bones, movements and muscles. Next, it presents background information for modelling and identification of biomedical systems. The background section is not intended to be comprehensive but rather to provide the reader with general understanding of the methods and mechanisms involved in identification of ankle joint stiffness.

Chapter 3 provides a critical review of the literature on experimental and analytical studies of joint stiffness. Next, it reviews the available methods in the literature for identification of block oriented nonlinear systems and it finally presents the thesis rationale.

The main complexity in the identification of ankle joint stiffness is related to the reflex pathway that has a Hammerstein structure, comprising a static nonlinearity and a dynamic linear system. Chapter 4 develops a state-space model for the Hammerstein structure and develops the *New SubSpace* (NSS) method for its identification. Simulations are used to demonstrate that the NSS method performs better than other methods described in the literature. Finally, the utility of the method is demonstrated by using it to identify the reflex EMG response in the plantarflexor muscles of the ankle. This chapter is published in IEEE Transactions on Biomedical Engineering authored by K. Jalalaleddini and R. E. Kearney, entitled "Subspace Identification of SISO Hammerstein Systems: Application to Stretch Reflex Identification" in 2013.

Chapter 5 extends the NSS method to support the identification from short segments of data. This was achieved by formulating multiple data segments (versus single data record of Chapter 4) by incorporating the initial conditions and identifying them together with other parameters. This will have important applications for time-varying or switched systems. It demonstrates the application of this method in identification of the EMG reflex response in the ankle plantarflexor muscles when subjects switched among different postural states during upright stance. This chapter is published in the proceedings of the IFAC System Identification Symposium authored by K. Jalalaleddini, F. Alley and R. E. Kearney, entitled “Identification of Hammerstein Systems from Short Segments of Data: Application to Stretch Reflex Identification” in 2012.

Chapter 6 extends the NSS method to the *Structural Decomposition SubSpace* (SDSS) method for the identification of ankle joint stiffness parallel-cascade model. The SDSS method decomposes the total measured torque to the intrinsic and reflex torques in a non-iterative way. It then fits an impulse response function to the intrinsic dynamics and uses the NSS method to identify the Hammerstein structure of the reflex pathway. This chapter also demonstrates the validity of the method by providing a comprehensive analysis in realistic simulation scenarios in comparison with available methods in the literature. It also demonstrates a successful application of the method in identifying stiffness as a function of muscle activation level from experimental data. This chapter is submitted to IEEE Transactions on Biomedical Engineering authored by K. Jalalaleddini, E. Sobhani Tehrani and R. E. Kearney, entitled “A Subspace Approach to the Structural Decomposition and Identification of Ankle Joint Dynamic Stiffness”.

Chapter 7 extends the SDSS method to identify stiffness models from short segments of data using an approach similar to that used in chapter 5. This would have important applications in many functional tasks when data are non stationary such as in upright stance, movement, etc. This chapter explores the validity of the method in comprehensive simulation studies that mimic realistic experimental conditions. The application of the method is also demonstrated in studying properties of stiffness during an imposed movement task. This chapter will be submitted to IEEE Transactions on Neural Systems and Rehabilitation Engineering authored by K. Jalalaleddini, and R. E. Kearney, entitled "Identification of Dynamic Joint Stiffness from Multiple Short Segments of Input-Output Data".

Chapter 8 summarizes the contributions of the findings of this thesis and provides a general discussion and suggestions for future developments, applications and improvements.

1.2 Contributions of Authors

Chapter 4:

K. J. designed the algorithm, simulation and experiments, performed the simulation and experiments, analyzed the data, interpreted the results, drafted the manuscript and prepared the final version. R. E. K. provided overall supervision and advice on the design of the algorithm, simulation and experimental studies, assisted in the interpretation of the result, and provided editorial input in writing the manuscripts.

Chapter 5:

K. J. designed the algorithm and simulation, analyzed the simulation data, interpreted the simulation data, drafted the manuscript and prepared the final version. F. A. designed the experiment, analyzed the experimental data and interpreted the experimental results. R. E. K. provided overall supervision and advice on the design of the algorithm, simulation and experimental studies, assisted in the interpretation of the result, and provided editorial input in writing the manuscripts.

Chapter 6:

K. J. designed the algorithm, simulation and experiments, performed the simulation and experiments, analyzed the simulation and experimental data, interpreted the simulation and experimental results, drafted the manuscript and prepared the final version. E. S. T. designed the algorithm and experiment and revised the manuscript. R. E. K. provided overall supervision and advice on the design of the algorithm, simulation and experimental studies, assisted in the interpretation of the result, and provided editorial input in writing the manuscripts.

Chapter 7:

K. J. designed the algorithm, simulation and experiments, performed the simulation and experiments, analyzed the data, interpreted the results, drafted the manuscript and prepared the final version. R. E. K. provided overall supervision and advice on the design of the algorithm, simulation and experimental studies, assisted in the interpretation of the result, and provided editorial input in writing the manuscripts.

CHAPTER 2
Background

This chapter presents some background information related to the dynamic joint stiffness identification problem. It starts by describing the physiology and anatomy of the neuromuscular mechanisms at the ankle joint. Finally, it introduces system modelling and identification and describes their usefulness in studying biomedical systems.

2.1 Physiology of the Neuromuscular Systems

2.1.1 Skeletal Muscles

Skeletal muscles are soft tissues and their role is to generate the forces needed to maintain a posture or perform a movement. They receive motor commands from the *Central Nervous System* (CNS) and respond by contracting to produce forces. The forces are transferred to bones via tendons. Muscles generate forces in one direction in which they shorten. Thus, they can only pull on their tendons. Consequently, each joint must be controlled by at least two antagonistic muscles working in opposite directions. Thus, by activating appropriate muscles, joints resist external forces or move [38].

A muscle is a bundle of thousands of muscle fibres working together in parallel. The muscle fibres thin and long cells (diameter as small as 10-100μm and length as long as 20cm). Each muscle fibre is a bundle of myofibrils that are 1-2 μm in diameter (Figure 2–1A). Each myofibril contains contractile proteins organized in a repeating pattern of thin and thick filaments to form sarcomeres (Figure 2–1B). A sarcomere is 1.5-3.5 μm long and are bounded by thin bands of protein called the Z disks. Thick filaments are composed of a contractile protein called myosin, each surrounded by 6 thin filaments. Thin filaments contain three major proteins: troponin, actin and tropomyosin (Figure 2–1C). The portion of the myosin that can interact with the thin filament is called the cross-bridge.

Forces are generated in muscles by the interaction of the thin and thick filaments in the presence of calcium ions. The muscle fibre membrane (sarcolemma) is an excitable membrane that can propagate action potentials using mechanisms similar to those used in neurons. When a muscle action potential is propagated along the fibre membrane, it releases calcium ions into the sarcoplasm that triggers a chain of events causing the thick and thin filaments to slide past each other and shorten the muscle. This mechanism is known as the cross-bridge cycle [3, 1, 39, 40, 41].

Motor Units

The CNS controls muscle fibres via *alpha* motor neurons. The cell bodies of the alpha motor neurons are located in the spinal cord and their axons exit the spinal cord from the ventral root and synapse with muscle fibres. When an alpha motor neuron fires, the entire innervated muscle fibers contract. The collection of motor units innervating a muscle is known as the *motor neuron pool* [42].

A motor unit consists of an alpha motor neuron and all the muscle fibres it innervates. It is the functional unit of the muscular system. All muscle fibres within a motor unit are located in the same muscle but are not necessarily adjacent to each other. Motor units vary in size from a few to thousands of muscle fibres. For example,

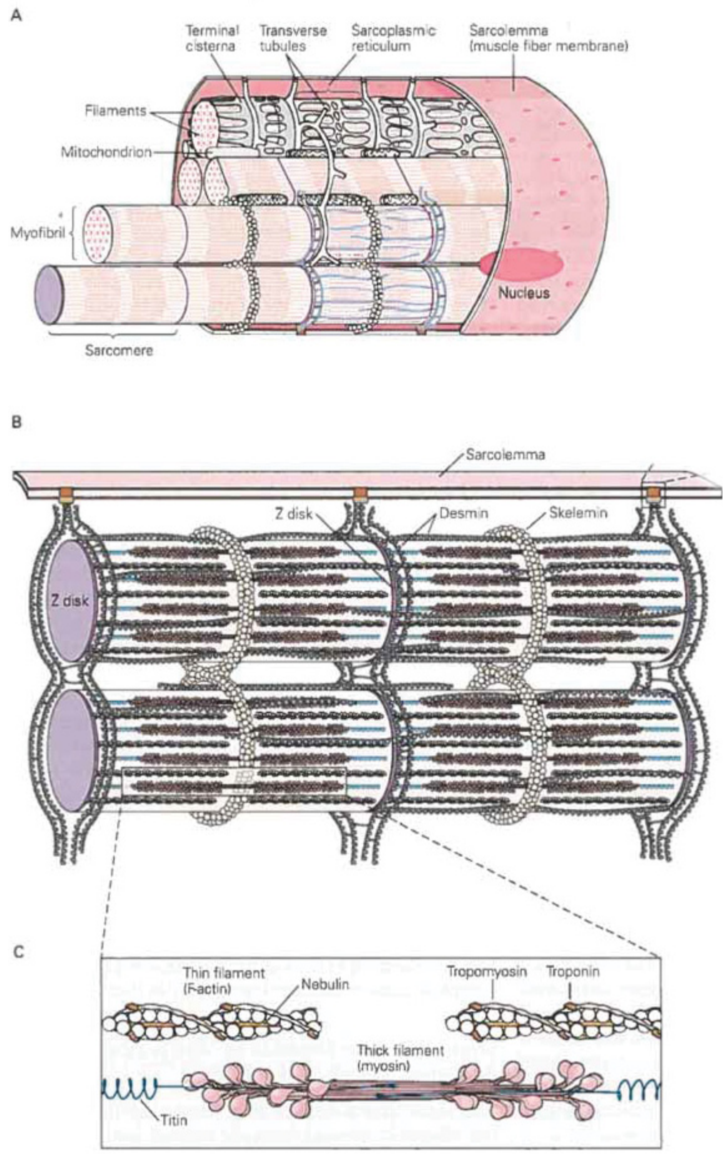

Figure 2–1: (A) A skeletal muscle is a bundle of muscle fibres working in parallel. Each muscle fibre is itself a bundle of myofibrils that are made of proteins organized as thin and thick filaments. (B) The special organization of filaments results in a repeating pattern of sarcomeres that are separated from each other at Z disks. (C) In each sarcomere, a thick filament is surrounded by thin filaments. Muscle contraction is achieved by interaction of the thin and thick filaments through the cross-bridge cycle that brings Z disks closer to each other and results, shortening the muscle. Adapted from [1].

in eye muscles (Rectus Lateralis) the average number of muscle fibres per motor unit is 5 [43] allowing delicate movements of the eye. The number is much larger in the leg muscles: 600 for the Tibialis anterior muscle and 1800 for the Gastrocnemius Medialis [44].

Mechanisms of Muscle Force Generation

A twitch is the response of a muscle to a single action potential. The time interval between its onset and end is the twitch contraction time; it ranges from 10 to 100ms. This time interval is closely related to the time history of the calcium ion concentration in the sarcoplasm which rises in response to an action potential and then decreases as it is recycled in the sarcoplasmic reticulum. This limits the muscle bandwidth and introduces a low-pass dynamic relation between the action potential firing rate and the generated force [45, 46, 2] (Figure 2–2).

Rate coding is the control of force by action potential firing rate. When the action potentials are fired faster, the twitch responses overlap and sum. At low firing rates, the response is oscillatory and is called the unfused tetanus response. However, at higher firing rates, the motor unit response saturates and is called the fused tetanus contraction (Figure 2–3).

The other mechanism for force generation is by recruitment of motor units progressively from the smallest to the largest. There is evidence that the membrane resistance of a motor neuron is inversely related to its surface area. Thus, a small motor neuron that innervates few muscle fibres has a small surface area and a low threshold and so is recruited earlier than a bigger motor neuron. De-recruitment follows the opposite order. This orderly recruitment/de-recruitment pattern is known as the size

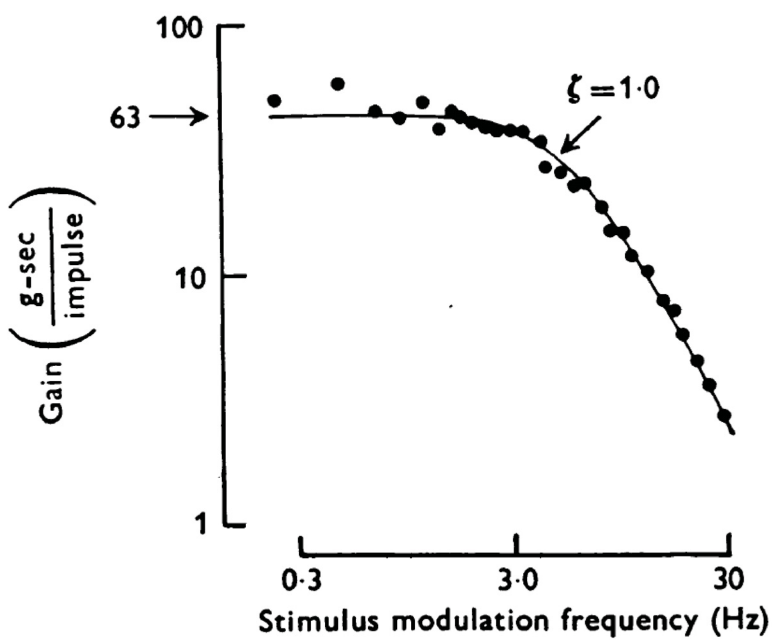

Figure 2–2: Muscles are sluggish and have limited bandwidth. The relation between the input action potential firing rate and output force can be characterized by a second-order low-pass filter. Adapted from [2].

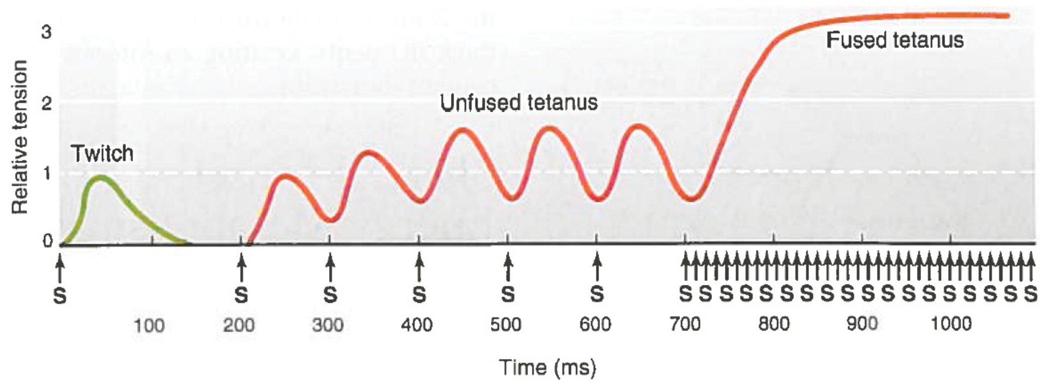

Figure 2–3: A twitch is the response of a motor unit to a single action potential. When the action potential firing rate increases, the twitch responses sum to increase the muscle force. This resultant force is oscillatory and called the unfused tetanus response. If the action potential firing rate is high enough, the motor unit reaches its force generation capacity and saturates; this is called the fused tetanus response. Adapted from [3].

principle, first proposed by Hennaman [47] and confirmed by others [48, 49, 50, 51, 52] (Figure 2–4).

Muscle Fibre Types

Small motor units have small thresholds and are recruited first. There are also other factors distinguishing small and large motor units. Generally, motor units can be categorized into two groups: type I units are slow and have a long twitch contraction time. They are highly resistant to fatigue and are nourished by blood supply since they have aerobic metabolism and so have a reddish color.

In contrast, type II motor units are large with many muscle fibres. They have a fast twitch contraction time, their tetanic force is large but they are prone to fatigue.

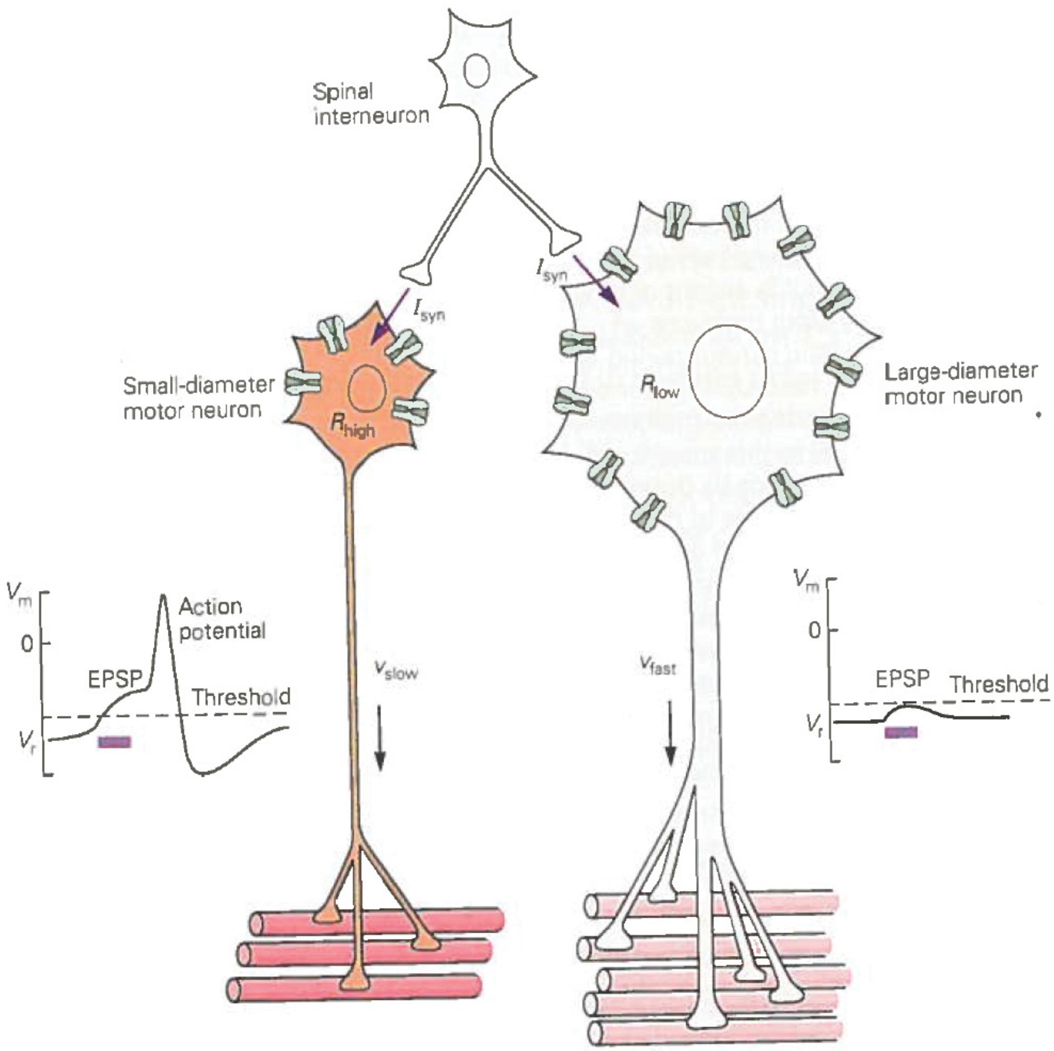

Figure 2–4: Muscle recruitment is achieved by progressive recruitment of additional motor units to increase muscle force. Motor neurons with smaller surface areas innervate fewer muscle fibres and have a lower threshold and are recruited easily. Adapted from [1].

They have anaerobic metabolism and rely on glycogen stored in their muscle fibres and have a white color [3, 1].

The proportion of motor unit types in a muscle depends on its function. Since type I units have lower thresholds, they are recruited first and are mainly used for low-intensity works such as providing muscle tone or in performing postural tasks. Type II units fatigue quickly so can provide short bursts of large force. For example, in the human soleus muscle which is mainly used for postural tasks such as providing muscle tone during upright stance, almost 70% of the units are type I while there is only 50% of type I units in the triceps branchii which can exerts bursts of large forces [44].

2.1.2 Muscle Spindles

A muscle spindle is a sensory organ lying in parallel with skeletal extrafusal muscle fibres. Consequently, they experience the same length change as the extrafusal muscle fibres. They provide the CNS with information about the muscle length and its rate of change. Muscle spindle is one of the main sensory organs providing proprioceptive feedback for sensorimotor regulation [53, 54, 55, 56].

Each muscle spindle has 3-12 specialized intrafusal muscle fibres (Figure 2–5). These fibres do not significantly contribute to the muscle force and their role is to adjust the sensitivity of the sensory organ. Muscle spindles have contractile polar regions and a non contractile central area. Thus, contraction of the polar regions pulls on the central region from both ends causing it to stretch and increase the firing rate of the afferents. The polar region is innervated by gamma motor neurons. Typically there are three types of intrafusal fibres inside a spindle capsule: a dynamic nuclear bag fibre, a static nuclear bag fibre and a number of shorter nuclear chain fibres. There are two types of gamma motor neurons: dynamic which innervates only the dynamic nuclear bag fibre, and static that innervates the static nuclear bag fibre and nuclear chain fibres. The afferents have a spiral form wrapped on the intrafusal muscle fibre. There are two types of afferents: primary (Ia) afferents are located in the central region of all intrafusal muscle fibre; secondary (II) afferent are located adjacent to the central region of the static nuclear bag and chain fibres [57, 58].

Originally, the primary (type Ia) afferents were thought to provide velocity information and the secondary (type II) afferents to provide length information. However, it is now known that both type Ia and II afferents provide velocity and length information. However, the type Ia afferents are the most sensitive and also provide acceleration information. An increase in the dynamic gamma motor neuron firing rate increases the dynamic response of type Ia afferents but has no effect on the type II response. In contrast, an increase in the static gamma activity, increases the static responses of both type Ia and II afferents but has no effect on their dynamic responses [59, 58, 56, 60, 57, 61, 62, 63, 54].

When a muscle shortens, the intrafusal muscle fibres shorten in parallel with the extrafusal muscle fibres causing the muscle spindles to become slack and insensitive to external perturbations. This can be prevented by activation of gamma motor neurons to stretch the intrafusal muscle fibres. This prevents slacking and maintains the tension. It has been hypothesized that since cell bodies of alpha and gamma motor neurons are adjacent, gamma motor neurons coactivate with alpha motor neurons to

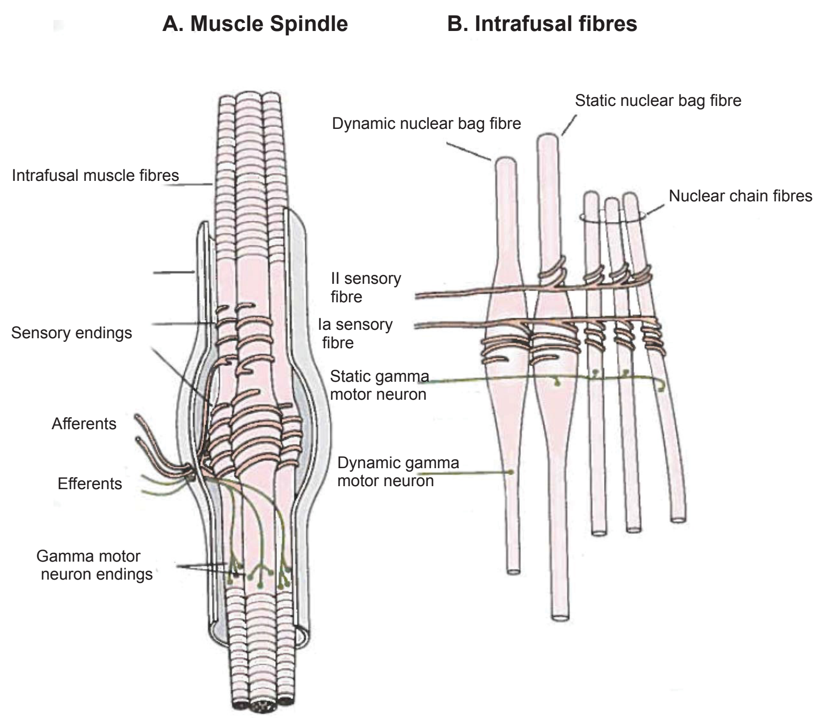

Figure 2–5: Muscle spindles are sensory organs located in a capsule structure and their role is to broadcast their parent muscle length and the rate of change in muscle length. Spindle nerves are wrapped on intrafusal muscle fibres. Each capsule has 3-12 intrafusal muscle fibers comprising a dynamic nuclear bag fibre, a static nuclear bag fibre and a number of shorter nuclear chain fibres. These fibres are innervated by gamma motor neurons. Adapted from [1].

ensure that information about the muscle length and velocity is continuously relayed to the CNS. This mechanism is known as the alpha-gamma coactivation [64].

2.1.3 Stretch Reflex

Stretch reflex is one of the spinal reflex mechanisms that is also known as the deep tendon reflex. In simplified terms, axons of muscle spindles enter the spinal cord from the dorsal roots. They make monosynaptic excitatory homonymous connections with the alpha motor neurons of their parent muscles. They also make monosynaptic excitatory heteronymous connections with other motor neuron pools that have similar functions. When a muscle is stretched, muscle spindles fire action potentials. If the stretch is large enough, the excitatory synapses produce action potentials in the alpha motor neurons that causes the muscle to contract. This mechanism is known as the stretch reflex and is illustrated in Figure 2–6 for the clinical knee jerk test. Muscle spindles also make inhibitory connections to the muscles of their antagonistic pair through polysynaptic pathways. The circuitry of the stretch reflex mechanism is very fast thanks to the monosynaptic connections but the information is still relayed with a significant time delay because of the limited actional potential propagation speed. For instance, this delay is in the order of 30-50ms at the ankle joint [65].

The circuitry of the stretch reflex arc is extensively studied and well understood in cats, normal and pathological humans [56, 66, 67]. However, its functional role in the neural control of movement is not very well understood and is a subject of debate.

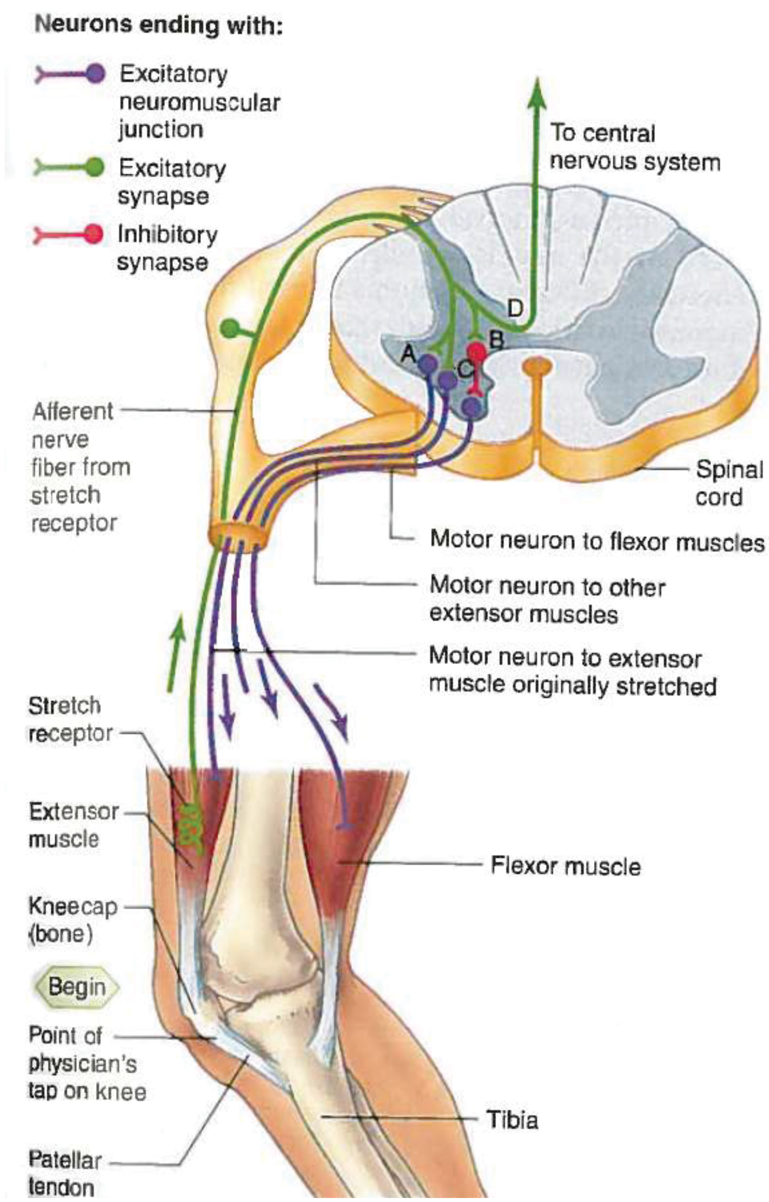

Figure 2–6: The stretch reflex arc: when a muscle is stretched, muscle spindles respond by generating action potentials. This response travels to the central nervous system and excites the alpha motor neurons of the muscles through monosynaptic connections and results in the contraction of those muscles. It also inhibits the antagonist muscle through polysynaptic connections. This reciprocal innervation results in decreased activation of the antagonist muscles. Adapted from [3].

2.2 Ankle Joint Anatomy

The lower extremity joints are extended from the trunk and their main function is to support body weight, maintain balance and perform movement. Figure 2–7 illustrates the regions and bones of the lower limbs. The main joints are at the hip, knee, ankle and toes. The interest of this thesis is on the ankle joint; so we will focus on its anatomy.

The ankle is a hinged synovial joint located between the distal ends of the tibia and fibula and the proximal end of the talus (Figure 2–8) [4].

2.2.1 Bones

The three main bones comprising the ankle joint are the tibia, fibula and talus. The tibia or shin bone is the second largest bone in the body, oriented vertically within the leg and its both ends are enlarged to provide efficient areas for articulation and weight transfer. The fibula lies posterolateral to the tibia but does not contribute to weight bearing. Its main function is to provide sites for muscle attachments (one muscle insertion and eight origins). The distal ends of both the tibia and fibula flare and are called the malleoli, the medial malleolus at the tibia and the lateral malleolus at the fibula (Figure 2–9). The talus has a body, neck and head. Its body articulates with the tibia and fibula; its superior surface articulates with the tibia at the medial malleolus and its lateral surface articulates with the fibula at the lateral malleolus (Figure2–7). It has no muscular or tendinous attachments and most of its surface is covered with articular cartilage.

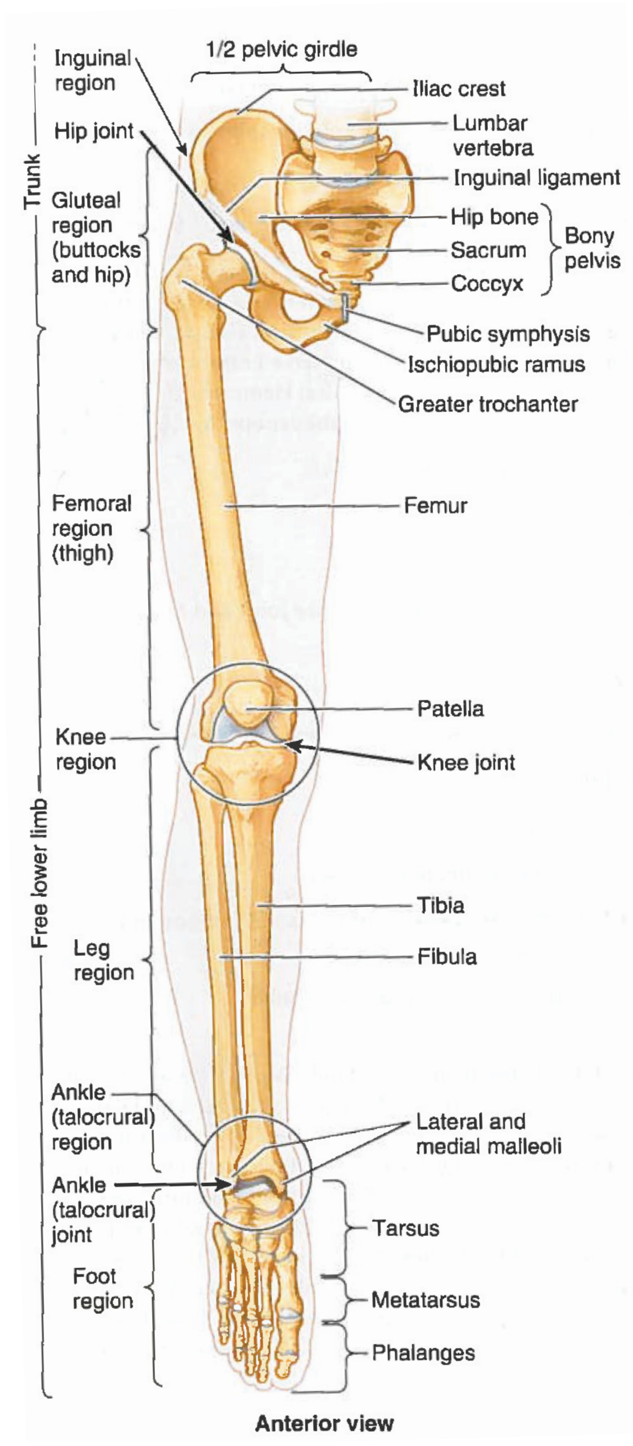

Figure 2–7: The anterior view of the regions and bones of the lower limbs. Adapted from [4].

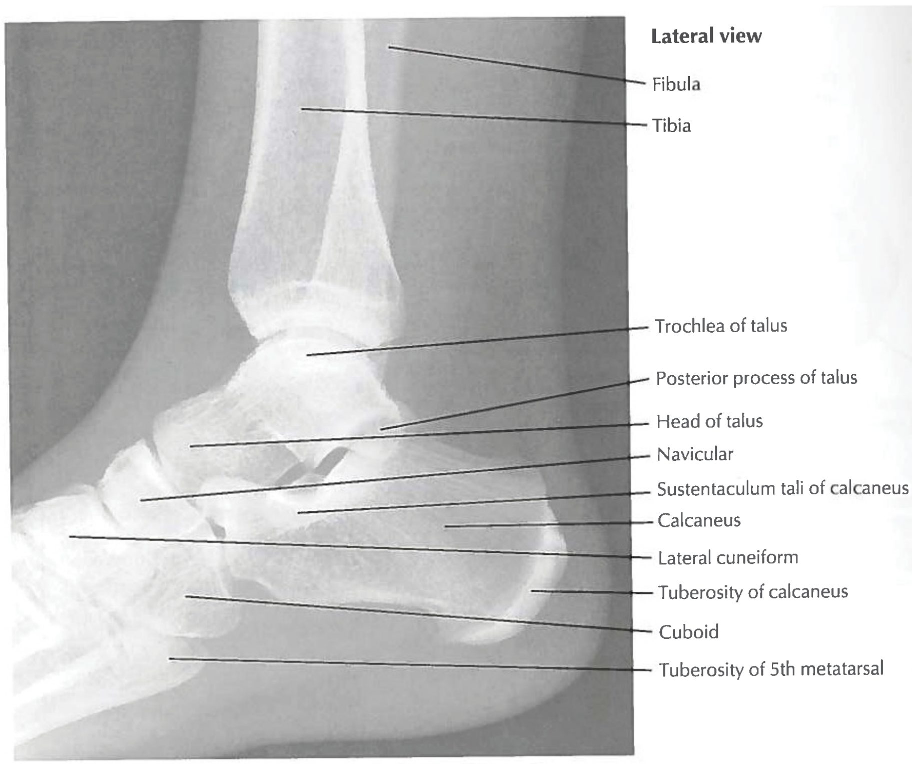

Figure 2–8: The lateral view of the ankle joint bones. Adapted from [5]
.

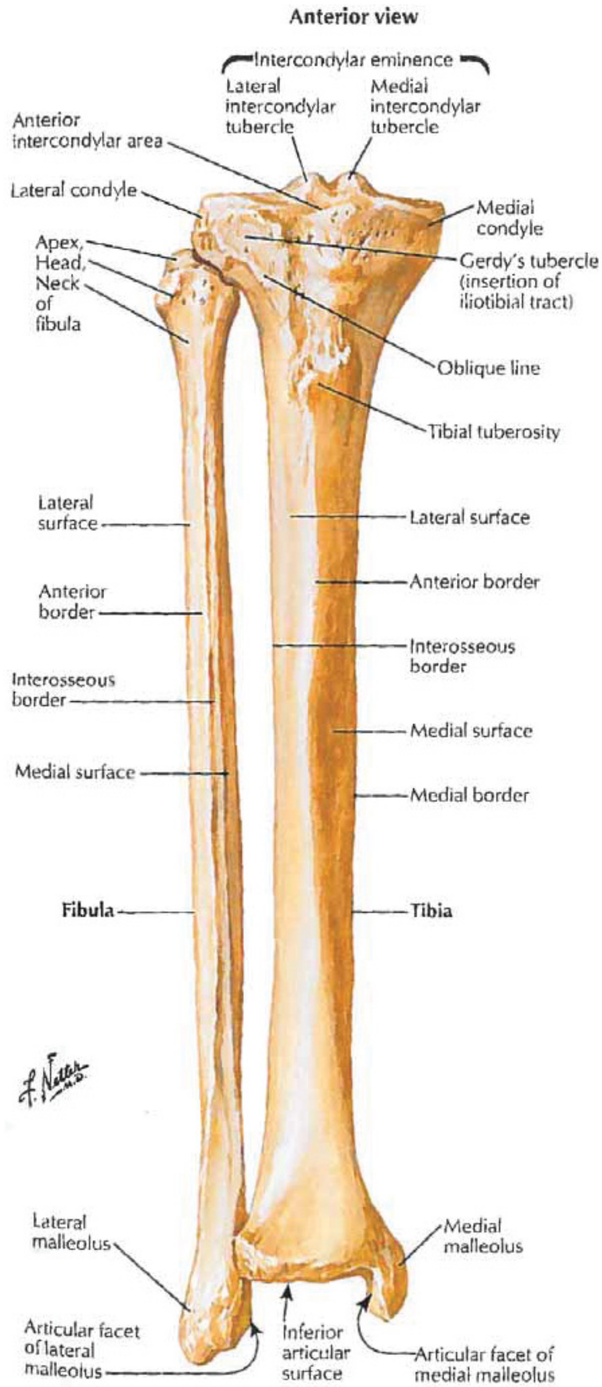

Figure 2–9: The anterior view of the tibia and fibula bones. Adapted from [5].

2.2.2 Movements

The main movements at the ankle joint are dorsiflexion and plantarflextion. Dorsiflexsion is flexion of the ankle joint, i.e. the toes are brought closer to the shin, e.g. walking on the heels, lifting the foot during walking. Plantarflexion is the opposite of dorsiflexion, e.g. pushing a car's gas pedal or standing on tiptoes (Figure 2–10).

The dorsiflexing range of motion of the ankle from its neutral position (foot positioned at a right angle to the shin) is smaller than its plantarflexion range. This is because of the resistance of the plantarflexor muscles to stretching and tension in the medial and lateral ligaments. Boone et al. examined the *range of motion* (ROM) of 56 male subjects aged between 19-54. The reported ROM average and standard deviations were $54.3(5.98)^\circ$ for plantarflexion and $12.2(4.1)^\circ$ for dorsiflexion [68]. Another study on 96 male Swedish subjects reported that ROM was $39.7(7.5)^\circ$ and $15.3(5.8)^\circ$ for plantarlexion and dorsiflexion respectively. [69]. Some studies have shown that the ankle ROM increased with passive stretching of the calf muscles [70, 71].

2.2.3 Muscles

The main muscle responsible for the ankle dorsiflexion is the *Tibialis Anterior* (TA). It lies against the lateral surface of the tibia and is innervated mainly from the fourth lumbar segment of the spinal cord [4]. The proximal attachment of the TA muscle is on the tibia. The distal attachment is through the long TA tendon whose origin is halfway down the leg and attaches to the medial side of the foot (Figure 2–11).

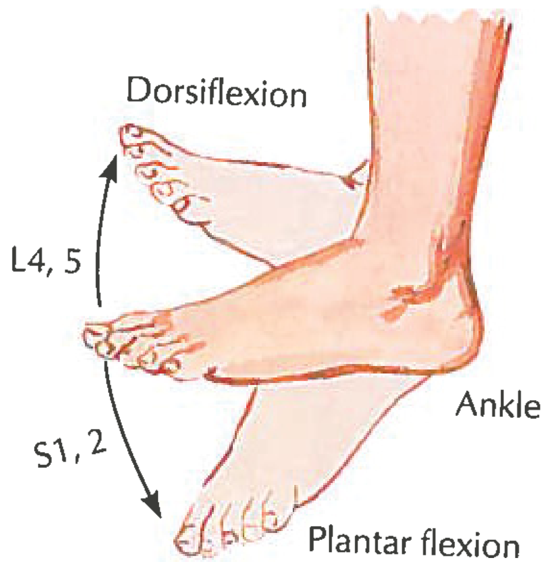

Figure 2–10: Dorsiflexion and plantarflexion movements of the ankle joint. Adapted from [5].

The main muscles responsible for the ankle plantarflexion are the Gastrocnemius and Soleus which are together called the *Triceps Surae* (TS) or calf muscle. The Gastrocnemius is a bi-articular muscle that attaches to the proximal side of the femur and has both medial and lateral heads (Figure 2–12). They share the calcaneal tendon with the soleus muscle at the distal side that is attached to the heel bone. The calcaneal tendon, also called the Achilles tendon, is the strongest tendon in the body. The TS is innervated mainly from the first and second sacral segments of the spinal cord.

The ankle dorsiflexor muscles lift the toes whereas the ankle plantarlexor muscles lift the whole body during upright stance or locomotion. Consequently, the ankle

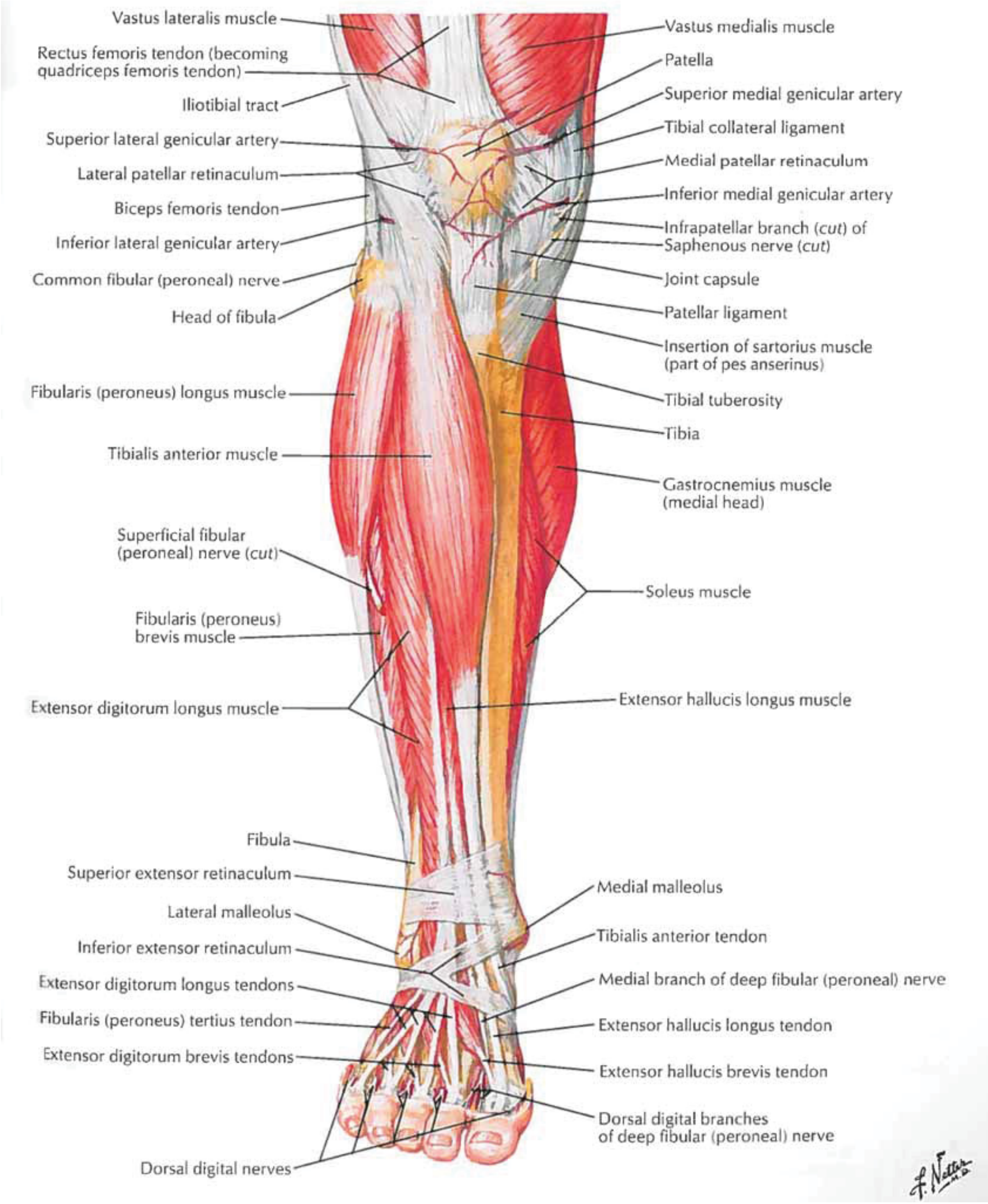

Figure 2–11: The anterior view of the lower leg muscles. Adapted from [5].

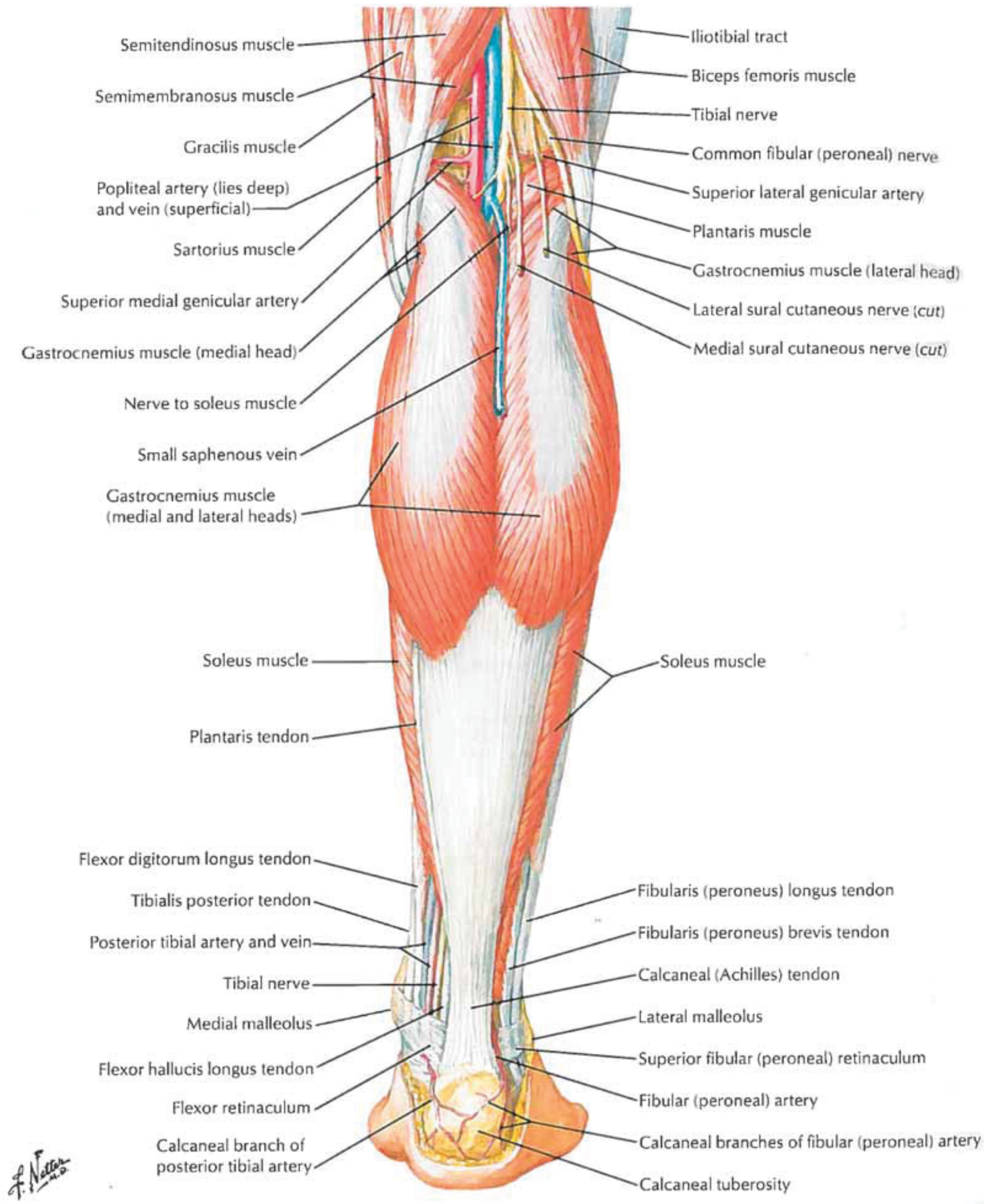

Figure 2–12: The posterior view of the lower leg muscles. Adapted from [5].

plantarflexor muscles are much stronger than their antagonists (almost four times stronger) [4].

2.3 Modelling and Identification of Biomedical Systems

One approach to the study of biomedical systems is through mathematical modelling. Mathematical models are useful since they can give insight on how the system works and may provide physiological interpretations. They predict the system output to the input used to train the model or to other novel inputs; they have important applications in simulations to make prediction about the system and in designing controllers. One approach to construct mathematical models is through identification of the model using input output data measurement.

2.3.1 System Modelling

There are two approaches in modelling biomedical systems. The bottom-up approach starts by modelling simple subsystems and piecing them together to give a more complex system. In this approach, each subsystem is modelled in details using known laws. These are then linked together according to the physics of the system until a complete top-level system is obtained [72]. For example, Niu et al. used models of the muscle spindle, spiking neurons, neural synapses and skeletal muscles to construct a model of the stretch reflex arc [73]. Each sub model was derived from previous studies of individual elements. This approach provides models with parameters that have physical significance and are directly related to the properties of the system. However, model development may be extremely difficult due to the detailed level of the analysis and complexity of the interactions between different subsystems. The models maybe heavily over-parameterized, i.e. many parameters cannot be measured or identified from the input-output data. Many parameters are lumped together to predict the final response so different sets of parameter values might give the same output. Furthermore, individual models of each subsystem identified from previous studies may not hold when that subsystem is interacting with others in function. Consequently, this approach has limited applications in studying biomedical systems.

The top-down approach, on the other hand, constructs models from measured experimental data, often using system identification techniques. These models have often fewer identifiable parameters and provide a concise description of the input-output data. However, the parameters may be more difficult to relate to the original properties of the system but they may provide an overall description of the underlying physiology. For example, the parallel-cascade model of the ankle joint stiffness is obtained from experimental data using a top-down approach [37]. Each parameter is not explicitly related to the actual physiology and is a combination of several parameters. However, this model has provided useful physiological interpretation of the overall role of the peripheral neuromuscular system in function [65].

In the context of system identification, there are two model structures: non-parametric and parametric models. A non-parametric model does not make a priori assumption about the underlying dynamics. It has been extensively used for modelling biomedical systems such as biomechanics of many human body joints (ankle, arm, trunk, wrist), intracellular calcium concentration in muscle fibres, bladder hydrodynamics, auditory system, vestibular ocular reflex system, lung tissue mechanics and many others [37, 74, 75, 76, 77, 78, 79, 80, 81, 82]. The main problem is that they may have large number of parameters. So, the routines used for their identifications deteriorate quickly in the presence of noise and this is inevitable when the data length is short and the number of unknown parameters is large [83].

Parametric models, on the other hand, require a priori information about the underlying system, e.g. model structure, order, etc, and often have few parameters. There is large body of work on parametric modelling primarily for modelling mechanical, electrical and economical systems where the model structure is known but the parameters are unknown. Thus, the main application of this approach has been in control engineering where the objective is to have a simple, concise and easily manipulated model to design an appropriate controller. However, this approach has been assumed to be less appropriate for biomedical systems because the modeller often does not have the necessary a priori information especially at the very first attempts. The two main parametric models of linear dynamic systems are *Transfer Functions* (TF) and *State-Space* (SS) models. In the sequel, we present different non-parametric and parametric model structures used for linear and nonlinear systems.

Models of Linear Dynamic Systems

In a dynamic system, current output depends not only on current input but also on previous values of input, i.e. the system has memory. In a *linear* system, the superposition and scaling principles hold.

Impulse Response Function (IRF) is the response of a system to a unit impulse; it is a non-parametric model. The impulse input is zero everywhere except at zero with an integral of one over the entire time. The response of a linear system to an arbitrary input can be predicted from its IRF using the convolution integral:

$$y_c(t) = h_c \ast u_c = \int_{t=-\infty}^{\infty} h_c(\tau) u_c(t-\tau) d\tau \tag{2.1}$$

where $u_c(t)$ and $y_c(t)$ are the continuous time input and output of the system and $h_c(t)$ is the IRF.

Since data are always recorded in discrete time in computers, the convolution sum gives the system output:

$$y_d(k) = h_d \ast u_d = \sum_{l=-\infty}^{\infty} h_d(l) u_d(k-l) \tag{2.2}$$

where $u(k)$ and $y(k)$ are the discrete time input and output signals and $h_d(k)$ is the discrete IRF.

In practice, the lower/upper limit of the convolution integral/sum of (2.1,2.2) is not infinity and bounded by the system memory. Consequently, the system memory determines the total number of model parameters. The IRF has proven to be a convenient way to model time-delayed, short memory and non-causal systems [72].

State-Space Models

Every realizable linear dynamic system has a *State-Space* (SS) representation which relates the system output to the input and state vectors by a set of first-order differential equations:

$$\begin{cases} \dot{\mathbf{X}}(t) & = A\mathbf{X}(t) + Bu(t) \\ y(t) & = C\mathbf{X}(t) + Du(t) \end{cases} \tag{2.3}$$

where $\mathbf{X}(t)$ is the state vector that might have a physical meaning (depending on the SS realization) and A, B, C, D are the state-space matrices (system parameters).

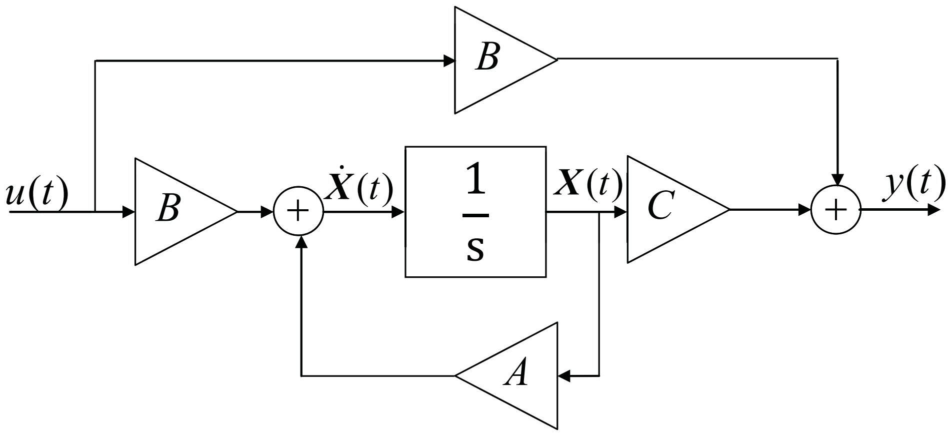

Figure 2–13: Signal flow graph of a linear state-space model.

The minimum number of state variables required to represent the system is the system order. The SS representation is a parametric model but has equal or more parameters than a transfer function but often fewer parameters than non-parametric models.

Figure 2–13 shows a block diagram representation of a state-space model that makes it clear that SS models can be easily converted to transfer functions:

$$H(s) = \frac{Y(s)}{U(s)} = C(sI - A)^{-1}B + D \tag{2.4}$$

The similarity transformation states that for an arbitrary full rank matrix T, the state-space model with matrices A_T, B_T, C_T, D_T is equivalent to (2.3) where:

$$\begin{cases} A_T &= T^{-1}AT \\ B_T &= T^{-1}B \\ C_T &= CT \\ D_T &= D \end{cases} \tag{2.5}$$

Consequently, the SS representation is not unique and the original A, B, C, D matrices cannot be recovered.

SS models for discrete time signals have the form:

$$\begin{cases} \mathbf{X}(k+1) &= A\mathbf{X}(k) + Bu(k) \\ y(k) &= C\mathbf{X}(k) + Du(k) \end{cases} \tag{2.6}$$

Models of Static Nonlinear Systems

The output of a static nonlinear system depends only on the current value of the input while superposition and scaling principles do not hold. A static nonlinearity can be modelled using a closed-form equation or using general basis expansions such as power, Tchebychev, etc polynomials. Polynomials provide a straight-forward tool to model static nonlinearities.

Power Polynomials

A power polynomial represents an arbitrary static nonlinearity using a sum of finite-order monomials of the input signal:

$$\hat{y}(k) = \lambda_0 + \lambda_1 u(k) + \cdots + \lambda_p u^p(k) = \sum_{j=1}^{p} \lambda_j u^j(k) \tag{2.7}$$

where p is the order of the power polynomials and λ_j is its coefficient. The power polynomials are not the best basis expansions to use since they are not orthogonal and their estimation may become prone to errors. Thus, the estimation methods may become ill conditioned, i.e. condition number of the least-squares regressor become large.

Tchebychev Polynomials

Tchebychev polynomials are orthogonalized over the input range $[-1, 1]$. A static nonlinearity is approximated with Tchebychev polynomials as follows:

$$\hat{y}(k) = \sum_{j=1}^{p} \lambda_j g_j(u(k)) \tag{2.8}$$

where $g_j(u(k))$ is the j-th Tchebychev polynomial defined as:

$$g_j(u(k)) = \frac{j}{2} \sum_{m=0}^{\lfloor \frac{j}{2} \rfloor} \frac{(-1)^m}{j-m} \begin{pmatrix} j-m \\ m \end{pmatrix} (2u(k))^{j-2m} \tag{2.9}$$

Tchebychev polynomials are frequently used to approximate static nonlinearities because they are orthogonalized, are easy to use and their estimations do not require complex mathematical analysis. However, Runge's phenomenon states that estimates oscillate at the edges of the input interval and even higher order polynomials do not improve the accuracy [84]. Oscillation of Tchebychev polynomials may hinder accurate identification of static nonlinearities, especially those with sharp transitions in their slopes. Consequently, the modeller cannot accurately recover the points of interests that may have physiological meanings.

Block Oriented Nonlinear Systems

Block Oriented NonLinear BONL structures are a class of nonlinear, dynamic systems constructed by combining linear dynamic and static nonlinear elements [85]. The linear element can be represented using parametric or non-parametric models. The nonlinear block can be represented in a closed form or using basis expansions.

A Hammerstein structure consists of a static nonlinearity followed by a linear dynamic system (Figure 2–14(A)). The Hammerstein structure was introduced by A. Hammerstein in 1930 [86] and became useful in modelling variety of physical systems including biomedical ones and is extensively used in this thesis. Examples include the reflex stiffness pathway of the human ankle joint [37], the neural integrator model of the human vestibular ocular reflex [87], the human smooth pursuit eye movement model [88], the visual cortex model for processing of image luminance and movement [89], the mechanical behaviour of lung tissues [81], chemical processes [90], the electrically stimulated muscles [91], aeroelastic systems [92] and many other biomedical and non-biomedical systems.

A Wiener structure is the cascade of a linear dynamic system and a static nonlinear element (Figure 2–14(B)). It was introduced by N. Wiener [93] in 1958 and has been used to model biomedical systems including models of neural processing [94], neural activity of semicircular canals [95], muscle mechanics [96], chemical processes [97] and many others.

Other class of BONL systems is sandwich structures. Thus, a Hammerstein-Wiener model consists of a static nonlinearity followed by a linear block followed by a second static nonlinearity (Figure 2–14(C)) and a Wiener-Hammerstein model consists of a linear dynamic system followed by a static nonlinearity followed by a second linear block (Figure 2–14(D)).

Parallel-cascade models are also an important class of BONL systems. Any finite-dimensional nonlinear dynamic system can be estimated with parallel paths of Wiener-Hammerstein structures [98]. Others showed that a structure with parallel paths of Wiener models can also estimate any system within an arbitrary small error [99, 100, 72]. Moreover, some biomedical systems have parallel-cascade structures in nature. For example, joint stiffness can be modelled with a linear pathway in parallel with a Wiener-Hammerstein system [37].

2.3.2 System Identification

System identification provides tools and methods to build mathematical models from measured input output data. It gives guidelines on the design of experiments to provide useful data. Typically, a model structure (non-parametric or parametric) is considered and a system identification routine tunes the parameters of the model to fit the data by optimizing certain cost functions. Identified models are then validated by inspecting the errors of the parameters, model residuals and their performance in response to novel inputs. If not satisfactory, previous steps must be revised. Thus, system identification is iterative with new discoveries at each iteration [101, 102].

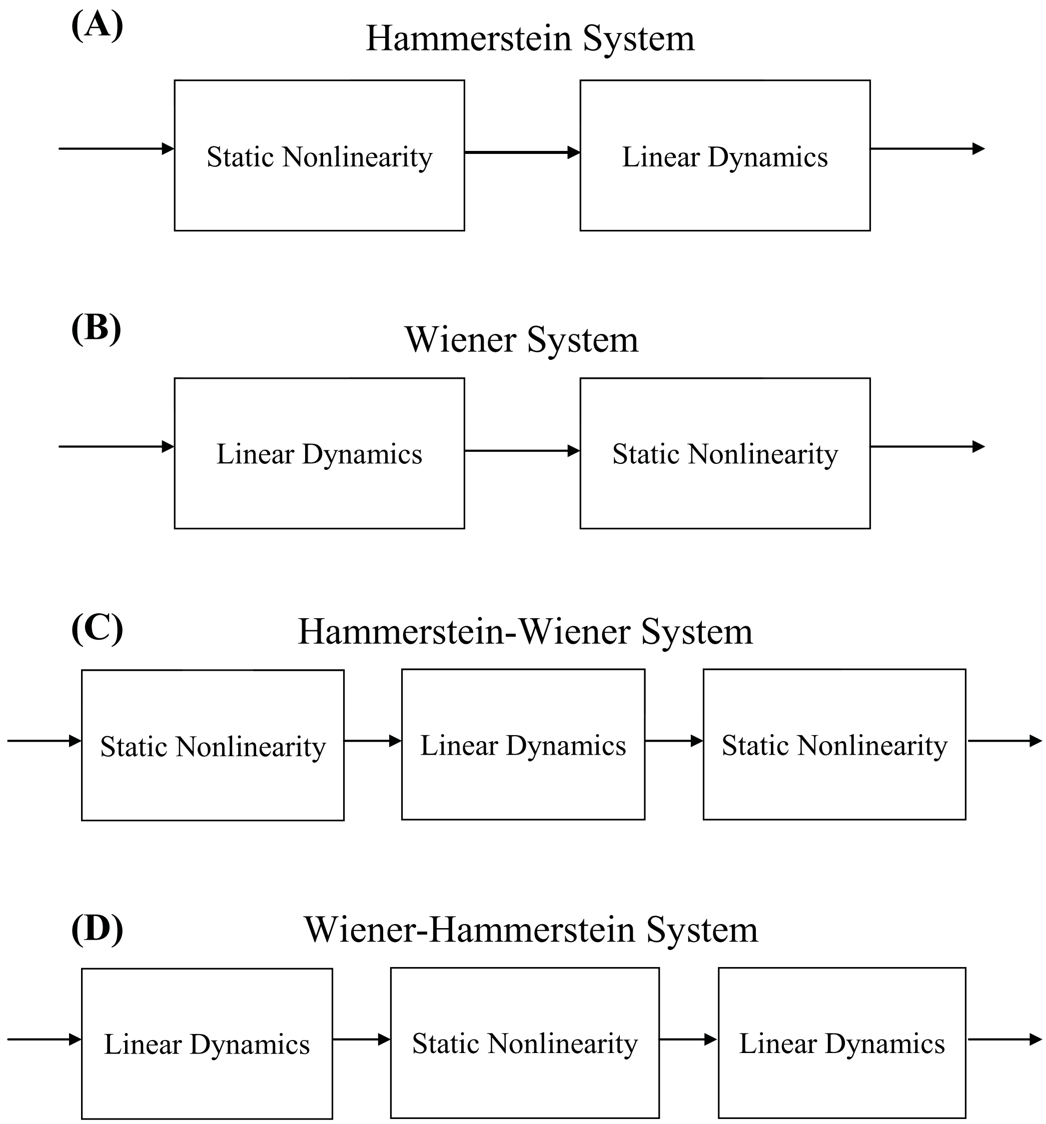

Figure 2–14: Models of block oriented nonlinear systems: (A) a Hammerstein structure consists of a static nonlinearity followed by a linear dynamic system; (B); a Wiener structure is the cascade of a linear dynamic system and a static nonlinear element; (C) a Hammerstein-Wiener model consists of a static nonlinearity followed by a linear block followed by a second static nonlinearity; (D) a Wiener-Hammerstein model consists of a linear dynamic system followed by a static nonlinearity followed by a second linear block.

Identification of biomedical systems is a challenging task since they are complex, nonlinear and time-varying in nature with little available a priori knowledge. For example, joint stiffness dynamics continuously change in time during upright stance [103] or subjects easily develop muscle fatigue if asked to provide large muscle contractions for a long period of time [104, 105].

Impulse Response Function

The difficulty in the identification of the IRF is that it is *not* physically possible to deliver an impulse to the system since impulse is not realizable. There are different approaches to identify IRF models. The least-squares regression is the most straightforward analytical approach but computationally expensive [72]. The correlation technique decreases the computational load by reducing the size of the least-squares regressor [106, 107]. The pseudo inverse approach is also useful with highly coloured inputs and at the same time robust to the output noise [108, 109, 110]. Most of the IRF identification routines suffer from biases when they are estimated from data recorded in the presence of a feedback, i.e. from a closed-loop system.

State-Space Models

Identification of *State-Space* (SS) models belongs to parametric identification methods and is the main focus of this thesis. SS models were introduced in the 1950's and became very popular after the development of Kalman filtering in the 1960's. Unlike transfer functions, identification of state-space models is a relatively young domain and started in the 1990's. There are different types of SS identification routines but since they all estimate a subspace and use that to estimate the state-space matrices, they are called the *subspace* methods [111].

Three popular subspace methods were developed in parallel in the 1990's: the *Canonical Variate Analysis* (CVA) method developed by Larimore in 1990 [112], *Multivariable Output-Error State-sPace* (MOESP) originally developed by Verhaegen and Dewilde in 1992 [113] and the *Numerical algorithms For Subspace state-space system IDentification* (N4SID) developed by Overschee and De Moor in 1994 [114]. Overschee and de Moor subsequently demonstrated that the differences of the methods are insignificant in the limit and they all represent cases of one unifying theorem [115].

In this thesis we chose to use the MOESP method because of a number of appealing features:

1. it estimates the order of the system before identification. This is critical for biomedical systems where a method requiring little *a priori* information is preferable.
2. The number of SS parameters is considerably less than non-parametric IRF models. This is expected to increase the method's precision in the presence of noise.
3. It is computationally efficient and available in the free SMI MATLAB toolbox [116, 117].
4. It has been extended to BONL structures, including Hammerstein [118] and Wiener systems [119].
5. With small modifications, it works well under closed-loop condition which is the case in identification of stiffness when a joint interacts with a compliant load [120].

6. It has been successfully applied to the joint stiffness identification problem for the intrinsic stiffness identification [121], and parallel-cascade model identification both in open-loop and closed-loop conditions [122].

MOESP uses *Instrumental Variables* (IV) to extract the system state-space matrices from the noisy data. The IVs need to satisfy two conditions: (*i*) full rank and correlated with the state vector; (*ii*) uncorrelated with the noise. Different IV candidates have been suggested for MOESP. The *Past Input* (PI) and *Past Output* (PO) IVs successfully identify the system from data recorded in open-loop [113, 123]. The reference input together with the PI and PO IVs successfully identify the system from data recorded in closed-loop [120].

MOESP works by first identifying the extended observability matrix. The column space of this matrix is equal to the column space of a matrix comprising the state vectors. Thus, a singular value decomposition estimates the minimum number of columns (system order) required to accurately estimate the state vector up to a similarity transform. Once the state vectors are identified, a two-stage algorithm estimates the state-space matrices. The first stage uses linear least-squares to estimate the A and C matrices (up to a similarity transform). These estimates of A and C are then used at the second stage to form a linear least-squares problem to identify the B and D matrices. For a full description of MOESP and its implementations refer to [102, 116].

CHAPTER 3
Literature Review

This focus of this thesis is on developing tools to identify dynamic joint stiffness. Consequently, this chapter starts by defining joint stiffness and explaining challenges in its measurement. It then presents a review of the experimental and analytical approaches that have been used to study joint stiffness. Next, it presents a mathematical model for joint stiffness and how this model is modulated in different experimental conditions. Then, it describes the strengths and weaknesses of the analytical methods that can be or have been used for identification of stiffness and ends by giving the thesis rationale.

3.1 Dynamic Joint Stiffness

3.1.1 Definition

Dynamic joint stiffness defines the dynamic relation between the position of a joint and the torque acting about it [19]. Joint stiffness is important because it determines the resistance of the joint to external perturbations before voluntary interventions during maintenance of a posture. It also defines the properties of the load and actuator that the central nervous system must control when performing movements [13, 19, 124, 125].

Dynamic joint stiffness has been used to describe joint biomechanics. However, a number of other terms have also been used and it is important to differentiate. Stiffness (versus dynamic stiffness) has been used to describe the static properties of joints, muscles, tendons and ligaments. Thus, stiffness refers to the elastic property and describes the elastic deformation and storage of elastic energy. Compliance is the inverse of stiffness and also describes only static properties [126]. Impedance defines the dynamic relation between the velocity (versus position) of a joint and its torque and admittance is its inverse [127, 128].

These terms have been used in various ways in the literature. Stiffness has been described as the ratio of torque (force) over length [10]. This relationship only gives one point on the force length curve and so is computing a response not a functional relationship. Even if stiffness were linear, at least two points would be required to estimate stiffness. Stiffness (compliance) has been used to explain the relationship between the position (torque) and torque (position) increments at different latencies during the time-course of position (torque) perturbations [129, 130, 20, 131]. Stiffness and compliance define only the static properties, those related to the elastic parameter at the steady-state, and their estimates during the time-course of the perturbations do not have a significant physical meaning. This value has also been referred to as the quasi-stiffness. This approach may predict the output correctly, but only to the very same input used for its estimation. Thus, this estimate must be given together with the input type and its characteristics, e.g. ramp-and-hold and its velocity. Impedance and admittance have also been used to describe the dynamic relation between the joint position (versus velocity as officially defined) and torque [132, 133, 134].

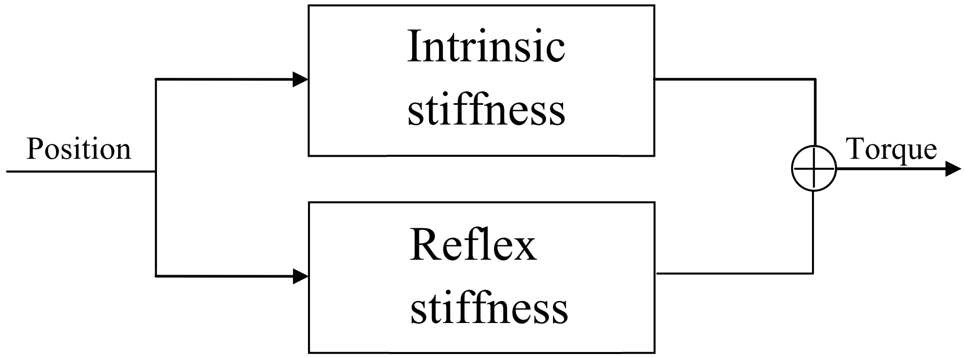

Figure 3–1: Joint stiffness can be modelled as a system with intrinsic and reflex stiffness pathways working in parallel.

Dynamic joint stiffness can be modelled as a system with intrinsic and reflex stiffness pathways [19]. Intrinsic stiffness arises from the mechanical (visco-elastic-inertial) properties of the joint, active muscles and passive tissues (tendons, ligaments, etc). Reflex stiffness arises from changes in the joint torque due to the activation of muscles by reflex mechanisms. When the stretch reflex mechanism (Section 2.1.3) is the main mechanism contributing to the reflex stiffness, it can be modelled as a feed forward pathway in parallel with the intrinsic stiffness pathway (Figure 3–1).

Dynamic joint compliance can also be modelled as a system with intrinsic and reflex stiffness pathways. When the stretch reflex mechanism is the main mechanism contributing to the reflex stiffness, it can be modelled as a feedback (Figure 3–2).

3.1.2 Decomposition of the intrinsic and reflex pathways

It is important to distinguish between the intrinsic and reflex mechanisms. In studying biomedical systems, the goal is to understand how the system functions.

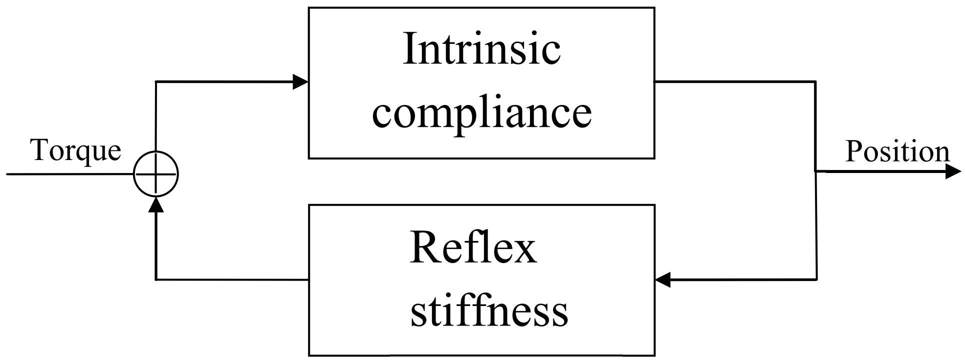

Figure 3–2: Joint compliance can be modelled as a system with intrinsic and reflex stiffness pathways with the reflex stiffness pathway as a feedback.

Thus, a model is preferred when it provides maximum insight about the underlying system.

Distinguishing the pathways is also significant when models are used for diagnosis purposes. For example, [135] showed that the reflex torque of spastic subjects was much larger than that of normal subjects while the intrinsic torque was not altered as much.

Accurate assessment of the increased stiffness and identification of its origins is important to prescribe a correct treatment. For example, injection of botulinum toxin-A is often the first-line treatment for spasticity which is attributed to the increased reflex response [136]. However, Aluhsaini et al. showed that this treatment did not help when the origin of the increased stiffness was mechanical [23]. Rather, other methods such as orthopedic surgery or orthotic management could be used [137, 138]. Accurate decomposition is also important to study the recovery patterns for treatment monitoring purposes [139].

The intrinsic and reflex torques change together and are not individually available for measurement. This makes the decomposition a challenging task. Thus, a number of experimental and analytical methods have been developed for this decomposition.

Two-Trials Experiments

Several experimental techniques have been implemented to separate intrinsic and reflex contributions using a two-trials experimental scheme: one with and one without reflex activity. Thus, identical position perturbations were delivered to the joint and difference between the measured torques of these two trials gives the reflex torque. Electrical stimulations [20, 140, 10, 141], ischemia induced by an inflated pneumatic cuff fitted around the limb [142, 143, 144], and vibration of muscle tendons have been used to suppress the reflex activity in the second trial [142, 145, 146]. These techniques have been applied to the ankle and knee.

Some animal studies performed on cats and monkeys cut the nerve supply [147, 10]. Muscle deafferentation also eliminated the reflex response while preserving the voluntary drive by cutting the corresponding dorsal spinal roots to remove the sensory input [148, 149, 150, 151].

These experimental approaches have several drawbacks:

It is extremely difficult to match muscle activation levels between the two trials. First of all, subjects might reach a different voluntary activation level in the presence of reflex response since the reflex response adds an offset to the final torque. Second, co-contraction is sometimes inevitable especially when electrical stimulations are applied to match the activation levels. Any mismatch between the activation levels of the two trials will bias the estimates.

Intrinsic and reflex pathways cannot be considered as independent pathways and must be studied together. This is because intrinsic stiffness is a function of the number of cross bridges which is increased by the reflex response [152, 15, 153]. For example, intrinsic stiffness was different in the two trials even when subjects were instructed to be relaxed [154].

Techniques such as muscle deafferentation and nerve blocking are invasive and not appropriate for human studies.

EMG Signals

EMG signal has been used as an intermediate signal to decompose the pathways. Since EMG is a measure of muscle activation, it is not affected by the intrinsic response. Thus, this signal has been used to guide the decomposition.

EMG signal has been used identify biomechanics of the arm [134, 155], ankle [156, 157, 158, 159, 132] and trunk [160]. In some cases, the relation between the joint position and EMG signals was referred to as the "reflex impedance" [133, 160]. Others used activation dynamics to estimate the reflex torque from EMG signals; this was achieved by (*i*) using *a priori* activation models from previous studies as a first or second-order low-pass filter [156, 134, 155]; (*ii*) identifying activation dynamics from EMG-torque in a separate trial by instructing the subject to perform isometric contractions at a range of activation levels [133].

Despite the utility of EMG signals, this approach has several drawbacks:

1. EMG does not represent the biomechanics of joints. Thus, the use of "reflex impedance" to described the position-EMG relationship cannot be justified.
2. The relationship between EMG and torque is complex and not well understood except for isometric conditions. Even this form of relationship is controversial and has been modelled as static, dynamic, linear and nonlinear systems in the literature [161, 162].
3. EMG is a spatial and temporal filtered version of the activation of the underlying motor units. Thus, electrode placement significantly changes the amplitude and dynamics of EMG [163, 164]. For example, it is not possible to relate changes in the reflex gain to the underlying dynamics or to the electrode location. Consequently, it is difficult to compare estimates among subjects or from controls to patients.
4. Cross-talk between EMG signals of the synergistic muscles or antagonistic muscles is inevitable [165]. This will deteriorate the confidence of the estimates.
5. Motor units are synchronized during the reflex response and this results in large EMG spikes [166]. Activation dynamics identified from *voluntary* isometric contractions might not hold for synchronized EMG reflex response.
6. EMG has two components when the joint is perturbed: (*i*) background noise that scales with the level of the voluntary drive and (*ii*) the response of the reflex mechanisms. Consequently, using EMG as the input of a system for identification purposes must be performed with extra caution since the very first assumption of many identification routines is a noise-free input [101].

Analytical Approaches

A number of system identification algorithms have been developed to decompose the intrinsic and reflex torques. Kearney et al. benefited from the delay of the reflex path. They used an IRF model for the intrinsic path whose length was smaller than the reflex delay. Thus, they proposed the use of an algorithm that fits the intrinsic and reflex pathways iteratively [37]. Despite its utility, this iterative method did not consistently converge to the true system [122]. Thus, Ludvig et al. proposed the use of a well designed position input signal that when excited the system, resulted in near zero correlation of the intrinsic and reflex torques. Thus, they could avoid the iteration and the convergence problems [167]. The method was limited to only that well designed input. Zhao et al. considered an a priori parametric model of the intrinsic stiffness and proposed a non-iterative subspace approach [168]. The main issue was that it could not capture complex dynamics of the intrinsic stiffness that arise because of the complex musculotendon structure or dynamics of the joint fixation to the actuator that delivers perturbations to the joint.

Accurate decomposition of the intrinsic and reflex torques is still an important open problem that I will address in this thesis. I will use an analytical approach to decompose the pathways. The main advantage of this approach is that it is noninvasive and can decompose the torque from its noisy measurement even when the intrinsic and reflex responses are changing together. It does not require an intermediate signal, e.g. EMG, and requires little a priori information.

3.1.3 Measurement of Joint Stiffness

Once the torque is decomposed to the intrinsic and reflex torques, the objective is to estimate the models. Accurate measurement of joint biomechanics is significant in a variety of research areas. It sheds light on the functional role of different circuitries and elements of the neuromuscular system. It provides objective tools for the diagnosis, assessment, treatment prescription and monitoring of neuromuscular diseases. It provides models to rehabilitation engineers to design orthotic or prosthetic robots for the purpose of dexterous interaction with the environment. Moreover, accurate models of stiffness play a key role for stable design of robots controlled remotely by human operators. Consequently, accurate measurement of stiffness is of interest to many fields. This section provides a critical review on the methods that have been used to measure joint stiffness in a variety of tasks and comments on their validities, strengths and weaknesses.

Ratio of Torque over Position Increments

The ratio of torque increment over position increment in the time-course of the perturbations, or at certain latencies after the onset of a perturbation (usually ramp-and-hold) has been used as a measure of joint stiffness [169, 129, 130]. Some calculated stiffness at a latency when the reflex response was insignificant [71, 170, 171]. If the reflex stiffness was also of interest this ratio was calculated at the latency when the reflex response was thought to be maximum [20, 131].

This approach has major drawbacks. First, the ratio of the torque over position increment at the steady-state (equilibrium) depends on the type of perturbation and changes dramatically with the type of the ramp-and-hold perturbation (velocity, amplitude). Moreover, division of the increments at a single point in time is prone to inaccuracies due to noise [129]. Consequently, using this approach, some studies reported negative values for stiffness that seems unreasonable [172, 173].

Linear Time-Invariant Identification Techniques

Linear techniques have been extensively used to characterize joint biomechanics. The basic assumptions are that the underlying dynamics are linear and time-invariant (stationary conditions). However, there is strong evidence that stiffness is time-varying and nonlinear. Thus, these techniques can be applied only in specially designed experiments where the assumptions can be satisfied.

The main challenge is measurement of the reflex stiffness. This is because of its highly nonlinear dynamics due to the the uni-directional rate sensitive muscle spindles. For example, stretching the ankle's plantarflexor muscles elicits a reflex response but there is little or no reflex when stretching the ankle dorsiflexor muscles [37]. Consequently, regardless of how close the system is to its operating point, reflex response stiffness is always nonlinear.

Linear identification techniques have been used to study stiffness in the absence of reflex activity when the joint is perturbed around its operating point. This technique estimates stiffness when the joint is interacting with both stiff and compliant loads. When the load is stiff, the joint torque in response to position perturbations cannot change the position. Since there is no feedback, this experimental condition has been referred to as the open-loop condition. This experimental condition can describe numerous functional postural and movement tasks (e.g. sitting or eccentric contraction of the arm, etc). Thus, any linear identification technique can estimate stiffness provided that perturbations persistently excite the dynamics. Both sinusoidal and stochastic perturbations have been applied to the ankle [174, 175, 176], jaw, elbow, knee and other joints using this approach [151, 177, 178, 179, 180].

When the load is compliant, the joint torque (in response to position perturbations and due to voluntary mechanisms) changes the joint position. This experimental condition has been referred to as the closed-loop condition. It describes many functional postural and movement tasks (e.g. upright stance, cycling, etc). Stiffness measurement is difficult since most of the methods are not designed to work for data gathered from closed-loop systems. The main problem is that the input and noise become correlated which violates the assumptions of many identification methods. Limited numbers of works have considered this condition with care. Kearney and Hunter first detected this possible problem and suggested a linear frequency response identification solution based on cross-spectra analysis [19]. One study quantified the bias error of open-loop identification techniques for closed-loop data and concluded that it is minimal for inertial loads and increases with the load elasticity [181]. The closed-loop frequency response approach has been successfully applied to the ankle joint with relaxed muscles [182] as well as the arm [74, 133]. A parametric transfer function approach was implemented in [183] and showed that the arm intrinsic stiffness did not change with the load damping [183, 184]. An impulse response function identification method has also been developed but no further experimental results have been reported from this group [185].

The linear, time-invariant identification technique has also been used to study stiffness in the presence of reflex response. This approach uses simple, parametric, linear models of the sensory organs (muscle spindle and golgi tendon organs) that feedback joint position, velocity, acceleration and force, each with a scalable gain, through activation dynamics to the torque. This approach has been used on both the arm and ankle joints [132, 133]. The main issue is that the reflex pathway is highly nonlinear and cannot be linearized especially at the ankle. So, the system parameters will be estimated incorrectly. For example, this approach identified ankle reflex parameters such that muscle spindles became inhibitory and golgi tendon organs became excitatory which is in contrast with the general belief of their role and physiology [132, 134].

The use of linear time-invariant techniques for stiffness identification is appropriate provided that these assumptions are satisfied. Thus, it can be used during quasi stationary conditions when the reflex response is insignificant or absent. When the reflex response is significant, the model becomes nonlinear and nonlinear techniques must be employed. Also, when changes in the joint operating point are large, the system exhibits nonlinear or time-varying behaviours and thus nonlinear and time-varying techniques must be employed.

Linear Time-Varying Identification Techniques

Linear time-varying techniques have been used to characterize intrinsic stiffness in conditions when changes in the operating point (position or activation level) are large, e.g. movement. Two types of conditions and techniques have been used in the literature: (*i*) the same time-varying behaviour can be repeated many times, i.e. periodic tasks; (*ii*) the time-varying nature is not periodic but changes as a function of a measurable signal such as the operating point. As with the linear time-invariant approach, these methods cannot quantify the reflex pathway either.

Lee and Hogan quantified intrinsic stiffness at the ankle during walking on a treadmill with a fixed speed [186]. Perturbations were delivered to the ankle joint using a wearable robot in the dorsiflexion/plantarflexsion and inversion-eversion directions. Since the joint operating point is periodic during walking with constant speed, the technique developed in [187, 188] estimated stiffness from ensembles of the input-output data records. Furthermore, they reported that there was no reflex activity and thus, the linear assumption was valid. Yangming and Hollerbach extended the ensemble method for parametric identification of human elbow joint [189]. Ludvig and Perreault improved the non-parametric ensemble method to efficiently deal with noise and short data segments [190]. They further improved their method by adding an instrumental variable to handle the closed-loop condition and reported how the elbow and knee intrinsic stiffness changed in the course of a sinusoidal movement [191, 192].

The main drawback of this approach is that it requires many ensembles of input-output realizations with the same time-varying nature. This might be difficult to obtain in real experiments and thus realizations must be inspected carefully and those with high variability must be discarded. It also requires many realizations to provide accurate estimates [193]. Furthermore, models identified from this approach cannot be used to predict stiffness in tasks with different time-varying natures.

If qualitative information on the time-varying nature of the system is known, *Linear Parameter Varying* (LPV) methods can be employed. This approach assumes that stiffness changes as a function of a signal called the scheduling variable which can be measured or estimated. Eesbeek et al. used an LPV method and measured wrist stiffness in an activation varying task [194]. Sobhani et al. used a similar approach to measure ankle stiffness in a position varying task [195].

The advantage of the LPV approach is that repeatability and periodicity is not required and estimates are accurate from a single trial provided that the scheduling variable has a rich amplitude distribution. It facilitates physiological interpretation by explicitly estimating the relationship between stiffness and the scheduling variable. Moreover, it provides models that can predict torques in novel time-varying tasks. This would have important applications in the design of neuroprosthesis. The main drawback is the choice of the scheduling variable which must be known as an a priori knowledge and sometimes is not trivial to find or estimate. For example, Ludvig and Perreault reported that a proper choice of scheduling variable was not found in estimating the knee stiffness in a position varying task [191].

Nonlinear Time-Invariant Identification Techniques

Some studies used nonlinear a priori models of different elements and used a nonlinear optimization to fit their parameters. These models were often taken from experimental studies performed on individual elements (e.g. muscles, muscle spindle, etc) in isolation. Thus, [196, 197] used a nonlinear model for the elastic parameter as a function of the wrist joint position and velocity and applied ramp and hold perturbations. They fit parameters to a small segment of the data after the perturbation onset and before the onset of the reflex activity to identify the intrinsic stiffness only. Others used nonlinear models of muscles and tendon (from force-length-velocity curves) and linear models of the muscle spindles and activation dynamics and applied ramp and hold perturbations [156, 21]. Due to the complexity of these models, a nonlinear optimization technique had to be used to fit the parameters to the measured data. While this approach estimates physiologically meaningful parameters, it has several weaknesses:

1. The slow ramp-and-hold input does not persistently excite the system to stimulate the dynamics for parameter estimation. Thus, several sets of different parameters might equally predict the output.
2. The optimization might converge to a local minimum. Thus, the estimated parameters are highly dependent on the values used to initialize the optimization search.
3. Since deterministic and slow perturbations are applied, subjects can learn the pattern and provide an anticipatory response.

Our lab extensively develops and applies nonlinear identification techniques to estimate stiffness using the top down approach. We developed a number of non-parametric and parametric time-invariant techniques to identify stiffness. The main idea is that given a persistently exciting input, the identification method decomposes the measured torque to the intrinsic and reflex torques and provides accurate and precise estimates of the parameters. Thus, Kearney et al. developed the *Parallel-Cascade* (PC) method that identified non-parametric (IRF) models of the stiffness [37]. Mirbagheri et al. successfully applied this methods to measure intrinsic and reflex contributions as a function of the joint operating points on normal human subjects [65]. Other studies applied this methods on spinal cord injured and stroke patients and showed that the reflex pathway was significantly altered in pathologies [135, 198]. Ludvig and Kearney extended the PC method for real-time estimation of stiffness [167] and showed that by providing subjects with a visual feedback of their reflex gain, they could voluntary modulate their reflexes [199]. Some studies used this method as an assessment tool [200, 201] to predict recovery patterns of patients [24]. Other labs applied this method to characterize intrinsic and reflex components of low-back stiffness [202, 203, 204]. The main issue with this approach is that it is difficult to relate the parameters to the physiological meaningful parameters, e.g it is impossible to relate the gain of the reflex pathway to the gain of the muscle spindles or motorneuron pool.

Nonlinear Time-Varying Identification Techniques

When changes in the joint operating point are large, the system is time-varying and time-varying identification techniques must be employed. A handful of studies considered the identification of the nonlinear stiffness model using time-varying identification techniques. Ludvig et al. developed the time-varying PC algorithm using ensembles of periodic but non-stationary data. Starret applied this method during isometric contractions with periodic variation in the activation level [205]. Sobhani et al. developed a subspace LPV approach to measure stiffness during imposed movement task [206].

The nonlinear, time-varying dynamic joint stiffness model would explain the biomechanics during a vast repertoire of functional tasks. Techniques have recently become available for identification of these complex dynamics and our lab is exploring them on the ankle joint during functional movements and postural tasks.

Multiple Joints/Multiple Degrees of Freedom

Joints often have more than one degree of freedom, e.g. inversion/eversion and plantarflexion/dorsiflexion of the ankle joint or flexion/extension and pronation/supination of the wrist. Moreover, several joints work together during many postural or movement tasks, e.g. postural control of the hand involve the elbow and shoulder joint movements [207, 208]. Furthermore, muscles are often connected to more than one joint. Thus, their contraction produces moments at several joints simultaneously [209]. Consequently, stiffness can be regarded as a *multiple-input, multiple-output* (MIMO) system.

Mussa-Ivaldi et al. and Shadmehr et al. considered the hand endpoint stiffness in the horizontal plane and measured restoring forces at the hand. They only measured the elastic parameter of the stiffness and showed it with ellipses illustrating its direction and magnitude. They reported how stiffness was modulated by the arm posture and activation level [16, 210]. Others complemented this approach by estimating dynamic part of the stiffness [211, 212, 213]. Perreault et al. used MIMO non-parametric frequency responses and impulse response functions [214]. They reported how stiffness at hand was modulated in the transverse plane with the activation level during a force regulation task [15]. de Velugt et al. enhanced this method for identification of MIMO stiffness for a closed-loop condition (compliant load) using cross-spectra techniques [74]. Thus, they described how stiffness ellipses change at different frequencies. Lee et al. used this approach and estimated the ankle stiffness in both inversion/eversion and plantarflexion/dorsiflexion directions simultaneously [182, 215, 216]. To this date, no study has considered estimating MIMO stiffness models with uni-direction rate sensitive reflex pathways.

To summarize, accurate measurement of joint stiffness is challenging. Dynamics are often nonlinear and time-varying in functional tasks. The feedback loops make the measurements even more challenging when joints interact with the body or environmental loads. Often, multiple joints function together and each has multiple degrees of freedom and this significantly increases the level of complexity.

3.1.4 Parallel-Cascade: A Model of Dynamic Stiffness

Kearney et al. developed the parallel-cascade model for dynamic stiffness [37]. This model is a data driven model obtained using the top-down approach. Consequently, it requires little a priori information. Its validity has been verified on both normal and pathological subjects and has successfully described dynamics of the ankle and trunk joints. This model has the intrinsic and reflex pathways. The intrinsic pathway has a quasi linear model and the reflex pathway has a BONL structure.

Intrinsic Stiffness

A quasi linear system with elastic (K), viscous (B) and inertia (I) parameters describe the intrinsic dynamics well:

$$tq_I(t) = Kpos(t) + Bvel(t) + Iacc(t) \tag{3.1}$$

where $tq_I(t)$ is the intrinsic torque, $pos(t)$ is the joint angular position, $vel(t)$ is the joint angular velocity and $acc(t)$ is the joint angular acceleration. This model has high-pass dynamics and has been successfully used to model the biomechanics of many joints including the ankle, elbow, knee and others. It can also be extended

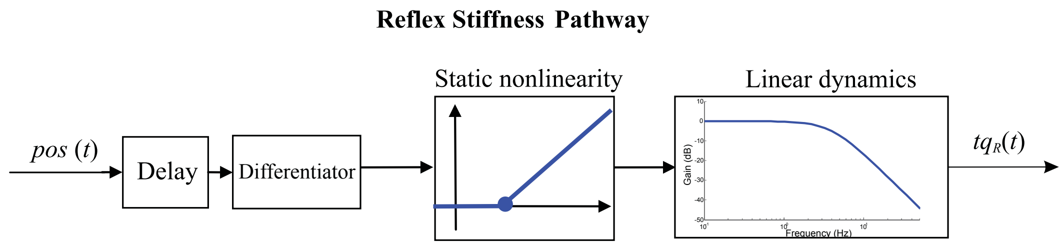

Figure 3–3: The reflex stiffness pathway has a block oriented nonlinear structure and is the cascade of a delay operator, a differentiator, a static nonlinearity followed by a linear dynamic system.

to joints with multiple degrees of freedom by replacing K, B, I with matrices with appropriate orders [182, 74, 176, 217, 218, 219, 220].

Reflex Stiffness

The reflex stiffness pathway can be modelled as a BONL structure comprising a differentiator followed by a delay operator followed by a static nonlinear element followed by a linear low-pass filter. At the ankle joint, the static nonlinearity resembles a half-wave rectifier because the stretch reflex mechanism is strong in the plantarflexor muscles and weak in the dorsiflexors [158, 159]. At other joints, stretches of both flexor and extensor muscles may elicit a stretch reflex response, so the static nonlinearity can look like a dead-zone with different slopes for positive and negative velocities [221]. Figure 3–3 illustrates the BONL structure of the reflex stiffness pathway for the ankle joint. This model was first proposed by Kearney et al. in [37] and since then has been widely used to characterize the reflex stiffness in the ankle and trunk joints of both normal and pathological subjects [202, 75, 222, 223, 76, 224, 225, 203, 226, 227, 201, 228].

Combination of the intrinsic and reflex pathways gives the parallel-cascade model for the joint stiffness (Figure 3–4). Thus, the total torque is the sum of the torque due to intrinsic mechanism and the torque generated due to the activation of muscles responding to the reflex mechanisms.

3.1.5 Stiffness Nonlinearities

The parallel-cascade model (Figure 3–4) is only valid for a specific operating point and small perturbations [65]. Thus, the parameters of the intrinsic (3.1) and reflex (Figure 3–3) models both change nonlinearly with the system operating point (position and activation level), task and instruction. In this section I will present some of these nonlinear properties.

Uni-directional Rate Sensitive Reflex Stiffness

The reflex pathway has a BONL structure. It consists of a differentiation block followed by a static nonlinearity and then a linear dynamic system. Thus, the obvious stiffness nonlinearity is the static nonlinearity of the reflex pathway. At the ankle, this resembles a half-wave rectifier reflecting a uni-directional rate sensitive reflex pathway. Thus, there is a response for large dorsiflexion velocities and little or no response for small dorsiflexion or plantarflexion velocities [229].

No one studied changes in the parameters of this nonlinearity. This is on one hand because of the lack of an accurate Hammerstein identification routine and on the other hand because of the input signal used in stiffness identification experiments. The frequently used input has been a realization of *Pseudo Random Binary Sequence* (PRBS) that does not evenly excite the input range of the nonlinearity. Therefore,

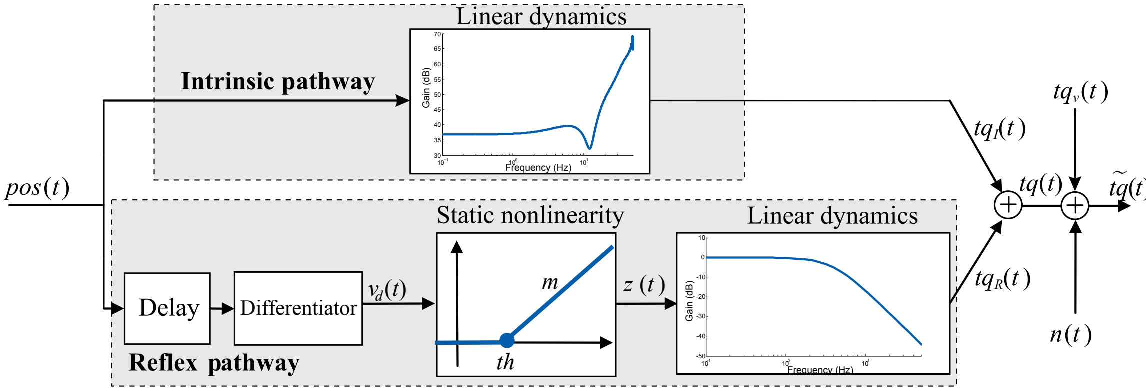

Figure 3–4: The Parallel-cascade structure of ankle joint dynamic stiffness.

accurate identification of the static nonlinearity becomes impossible even with an accurate identification routine. Consequently, this nonlinearity has often been assumed to be fixed as an a priori information with a threshold at zero [65, 135, 167]. Moreover, since the output of the nonlinearity is not measurable, the gain of the reflex pathway was attributed to its linear element as the reflex pathway gain. However, changes in the static nonlinearity can also change the reflex torque. For example, the reflex torque can be decreased by two different mechanisms: an increase in the threshold or a decrease in the slope (gain). Consequently, it is important to estimate both nonlinear and linear elements when measuring reflex stiffness.

Position Dependency

Intrinsic stiffness is a nonlinear function of the joint angular position. This has been studied during quasi stationary conditions. Zhang et al. found that the elastic and viscous parameters increased with knee extension [217]. MacKay et al. showed that the elastic parameter increased with elbow flexion [129]. Flash and Mussa-Ivaldi found that hand stiffness was strongly dependent upon arm configuration at rest. Weiss et al. studied this dependency at the ankle joint at rest and found that the elastic and viscous parameters increased as the joint was moved away from its neutral position [175]. Mirbagheri et al. also studied this nonlinearity during a torque regulating task in the presence of reflex activity and found similar patterns in both normal [65] and *Spinal Cord Injured* (SCI) subjects [135]. Thus, the ankle joint elastic parameter was minimal at the mid range of the ROM and increased toward plantar and dorsiflexion. They also found that the elastic and viscous parameters of the SCI subjects were larger than normal subjects.

Some groups studied the position dependency of intrinsic stiffness during imposed movement. Kirsch and Kearney demonstrated transient changes in stiffness during large, imposed movement of the ankle [152]. Sobhani et al. found modulation patterns of the intrinsic elastic parameter as a function of the ankle position during an imposed walking task; it was minimal at the mid range of the ROM and increased with both plantarflexion and dorsiflexion of the ankle [195]. Others showed that stiffness dropped at the movement initiation at the wrist [197, 196] and elbow [192].

Others studied the position dependency of intrinsic stiffness during voluntary joint movement. Thus, Bennett et al. studied the arm stiffness during sinusoidal movement and found that the elastic parameter was substantially lower than that during posture [230]. Lee and Hogan showed that the ankle joint elastic and viscous parameters were modulated strongly in the course of walking. Thus, both decreased from the pre-swing phase to the initial swing phase, stayed almost invariant during the swing phase and increased again at the early stance phase. Stiffness rapidly changed at heal-strike and toe-off instants [186].

Mirbagheri et al. studied changes in the ankle reflex stiffness as a function of the joint position during quasi stationary conditions [65, 135]. They found that the only parameter that significantly changed was the reflex stiffness gain. Thus, the gain was small when the ankle was plantarflexed and increased significantly as the joint was dorsiflexed. SCI subjects had similar patterns but their reflex stiffness gain was substantially larger than normal subjects. Sobhani et al. found similar patterns during imposed movement of the ankle joint [206].

Activation Dependency

Intrinsic stiffness is minimum at rest and increases with muscle activation and with antagonistic muscle co-contraction. This has been shown at the ankle, hand, knee and other joints during quasi stationary conditions [15, 217, 174, 231, 140, 153].

MacNeil et al. studied the time-varying properties of the ankle intrinsic stiffness during a rapid, voluntary, isometric contraction task where subjects were instructed to switch between two activation levels. They found that during the transient phase of the contraction, the elastic parameter decreased [232]. Starret Visser improved this work by considering both intrinsic and reflex pathways simultaneously and using a continuous sinusoidal activation varying task. She showed that the ankle elastic parameter was modulated proportional to the voluntary torque and the reflex gain showed two peaks at the lowest and highest activation level [205].

Mirbagheri et al. studied the effect of the ankle plantarflexor activation level on reflex stiffness during quasi stationary conditions [65]. They found that the reflex gain increased from rest to the minimum activation level (5% of maximum voluntary contraction) and decreased with further increase in the activation level. Other researchers found that the maximum reflex gain happened at around 50% of the maximum voluntary contraction [233, 140].

Lang and Kearney showed that the intrinsic and reflex parameters modulated during quite stance as a function of the postural sway. Thus, the elastic parameter was minimal at the mid range of the sway torque. It increased when subjects switched to forward or backward lean postural states. Modulation of the reflex gain was complementary to the intrinsic response. Thus, it was large when the elastic parameter was small and small when the elastic parameter was large [103].

Input Dependency

Joint stiffness changes with the characteristics of the perturbations used for their identification. Thus, both the elastic parameter and reflex gain decreased with position perturbation amplitude. This has been observed at the ankle [195, 152, 234, 235], elbow [230], knee [191] and wrist [197] joints; and the rate of decrease increased with joint velocity [196].

Reflex stiffness also changes with the input characteristics. The ankle reflex stiffness (*i*) saturated with increasing position perturbations amplitude [229]; (*ii*) decreased with increasing perturbation mean absolute velocity [229]; (*iii*) decreased with increasing input bandwidth [134, 133].

Other Dependencies

Some groups found that joint stiffness decreases with static stretching [71, 70, 236]. Others reported that intrinsic stiffness is invariant with muscle fatigue while reflex stiffness gain decreases [105]. Studies at the ankle joint have shown that the elastic parameter decreases and the reflex stiffness gain increases with muscle fatigue [237]. Some groups studied tasks dependencies; Thus, stiffness changes with the task, e.g. cycling vs walking vs running [238, 239, 240]. Others found that task instructions has significant effect on both intrinsic and reflex stiffness, e.g. resist versus do-not-intervene [160, 241, 242, 199].

To conclude, joint stiffness is a complex and highly nonlinear system. Some of these nonlinearities can be relaxed for example by fixing the system at an operating point, i.e. keeping the activation level and position operating points constant throughout the experiment. Moreover, the system can also be assumed time-varying instead of nonlinear when there are large changes in the position/activation level.

3.2 System Identification

This section provides a critical review of the system identification techniques that have been or can be used to the joint stiffness identification problem. It starts by reviewing Hammerstein identification methods applicable to the identification of the reflex pathway. Next, it reviews identification methods that have been developed to identify the parallel-cascade model of joint stiffness during various experimental conditions.

3.2.1 Hammerstein Models

Any identification method for the parallel-cascade model requires a Hammerstein identification routine to estimate the reflex stiffness pathway. Consequently, in this thesis we always start by identifying the Hammerstein structure and then extend it to the full parallel-cascade model. Identification of Hammerstein structure is also significant for other important biomedical systems such as the human vestibular ocular reflex, the visual cortex model, the mechanical behaviour of lung tissues and the electrically stimulated muscles.

Non-Iterative Techniques

Stochastic methods estimate the Hammerstein cascade with no *a priori* knowledge. They fit polynomials to the static nonlinearity and a discrete or continuous-time IRF to the linear element in a non-iterative manner using cross correlation techniques [243, 244, 245, 246]. The severe limitation is that both input and noise must be white and Gaussian. These conditions cannot be realized in experiments on biomedical systems so their application cannot be justified. For example, in stiffness identification experiment, the actuator has a limited bandwidth and delivers non-white position perturbations and noise is also colored [247].

Verhagen and Westwick extended the linear MOESP method to Hammerstein structures [118]. The method works by expanding the input signal using basis expansions to transform the *Single-Input-Single-Output* (SISO) Hammerstein cascade into a MISO linear SS model. Thus, MOESP identifies the linear MISO SS model. This method is robust, accurate and non-iterative and so does not have convergence problems. It inherits all appealing features of the MOESP method. However, it is not straightforward to convert the resulting MISO system to models of the static nonlinearity and the linear element. Consequently, while this approach is useful to predict the output in control applications, it fails in biomedical applications where the purpose of the model is to provide insight into the system.

Iterative Techniques

Other Hammerstein identification methods are iterative. Non-parametric methods iterate between estimating the static nonlinearity and the linear element. The *Hunter-Korenberg* (H-K) method is based on the Bussgang's theorem [96] which states that the cross correlation between input and output of a Hammerstein structure is proportional to the cross-correlation of the input and output of the linear element. Thus, the H-K algorithm approximates the nonlinearity with polynomials and the linear element with an IRF using cross-correlation techniques. It has been applied to study reflex stiffness [158, 248] and lung tissue mechanics [81]. This method does not require the input to be white but it must be Gaussian for the Bussgang theorem to hold. Thus, [249] showed that the H-K method does not converge when the input is non-Gaussian and non-white. However, if the input is non-Gaussian or non-white (not both), the estimates are unbiased.

Westwick and Kearney developed the *Separable Least Squares*(SLS) method that is iterative, non-parametric and correlation-based and identifies a basis expansion for the nonlinear element and an IRF for the linear element. They showed that SLS is superior to H-K because it does not depend on the Bussgang theorem and so does not require the input to be Gaussian. They compared the two methods using experimental data from the ankle stretch reflex model and showed that the H-K estimates were biased and the IRF had a large oscillatory component whereas the structure was identified more accurately using SLS [249]. In the SLS formulation, the cost function, defined as the sum of squared errors, is highly nonlinear in terms of its unknown parameters: coefficients of the nonlinearity and IRF weights. The

SLS method separates the unknown parameters into two sets: one that is easy to solve (using least-squares) and one that is more difficult to solve (using a nonlinear optimization). The SLS method works by iterating between solving each parameter set. The convergence of the SLS method cannot be established analytically because the nonlinear optimization might not converge to the global minimum and the cost function might not decrease with incrementing iterations. Nevertheless, the SLS method has been extended to identify cubic spline models of the static nonlinearity [250] which would have important applications in hard nonlinearities with sharp changes in their slopes, e.g. half-wave rectifier of the stretch reflex mechanism. Le et al. successfully used this approach to identify models of the electrically stimulated muscles in stroke patients [251].

Bai and Li separated the Hammerstein structure parameters into two sets. They showed that the output is a linear function of each parameter set provided that the other set is held fixed [252]. Thus, they simplified the solution by proposing an algorithm iterating between two least-squares problems. They showed that their algorithm converges if the two parameter sets are normalized at each iteration and if the algorithm starts from a certain set of initial conditions. Consequently, this work improved on Westwick and Kearney's work since no nonlinear optimization was involved and the convergence of the algorithm was guaranteed.

Another class of iterative Hammerstein identification methods identifies parametric models of the linear element, e.g. transfer function. Narendra and Gallman separated the Hammerstein parameters into two sets, one for the coefficients of the static nonlinearity and one for the parameters of the linear transfer function [253].

They showed that the output is a linear function of each parameter set provided the other set is held fixed. So, they proposed iterative methods solving two least-squares at each iteration and showed that the convergence occurs very fast. Later, Stoica found a counterexample where this iterative method failed to converge [254]. Consequently, the convergence became an open problem until Bai proposed two solutions: a two-stage identification approach and a normalized iterative approach. The two-stage approach overparameterizes the problem by defining a new parameter set containing all combinations of the products of the nonlinear and linear parameters. Thus, the output becomes a linear function of the augmented parameter set. At the first stage, a linear least-squares identifies this parameter set. At the second stage, a singular value decomposition separates and identifies parameters of the static nonlinearity and linear elements [255]. The normalized iterative method was first proposed in [252] for non-parametric identification of Hammerstein structure that adds an initialization stage before the iteration and a normalization stage at each iteration of Narendra and Gallman's method. Thus, [252] proved that the iteration converges to the global minimum. Later, Liu and Bai extended the convergence analysis for non-smooth nonlinearities [256] and Li and Wen proved that the convergence will be established for any arbitrary non-zero initial condition [257]. Jalaleddini and Kearney used Monte-Carlo simulations and showed that the iterative method is more robust to noise and gives more reliable estimate with highly colored inputs compared to the two-stage approach [258].

To conclude, identification of Hammerstein systems is a relatively mature domain and many techniques have been developed for different system structures (e.g., transfer function, IRF, FRF, state-space models) under different conditions (e.g., white Gaussian input, colored input, white output noise, colored output noise). In identification of biomedical systems, however, a method is desired that: (i) is robust to noise; (ii) is guaranteed to converge; (iii) requires minimum a priori information; (iv) provides consistent estimates for non-white inputs with arbitrary amplitude distribution; (v) provides consistent estimates for non-white output noises with arbitrary amplitude distributions. Consequently, we aimed to use the MOESP subspace method that satisfies all these conditions. However, the current MOESP Hammerstein method suffers from the fact that it does not separate the static nonlinearity from the linear dynamics. Consequently, as it currently stands, its application is less appropriate for biomedical systems where the objective is to acquire information about the underlying system.

3.2.2 Parallel-Cascade Models

Both non-parametric and parametric methods have been developed to identify the parallel-cascade model. The first was the *Parallel-Cascade* (PC) method proposed by Kearney et al. [37]. It is a non-parametric method that iterates between estimating the intrinsic and reflex pathways. They modelled the intrinsic pathway using a short two sided IRF whose length was shorter than the reflex delay. This prevented the intrinsic model from capturing any of the reflex pathway dynamics. They used the H-K method to identify the reflex pathway so this version was called the PC-HK method. This method had two types of iteration. The first is the iteration between the identification of intrinsic and reflex pathways. The second is the H-K iteration in estimating the reflex Hammerstein elements. None of these iterations are guaranteed to converge. Indeed, it has been frequently observed that the algorithm does not converge and the cost function becomes non-decreasing.

The H-K method was not the most appropriate choice because it required the velocity input to be Gaussian. However, one of the frequently used input is *Pseudo Random Binary Sequence* (PRBS) with a velocity profile far from a Gaussian distribution. Consequently, two other variations of the PC method were implemented: (*i*) PC-HR which assumed a fixed half-wave rectifier nonlinearity; the reflex path identification was simplified as an IRF estimation between the half-wave rectified velocity and the reflex torque; (*ii*) PC-SLS which replaced the H-K by the SLS method.

The PC-HR method was the most popular because of its simplicity. It was extensively used to explore stiffness in quasi stationary conditions [65, 135, 198]. A real time version of the PC-HR was also developed [199, 167].

Time-Varying (TV) versions were also developed. One approach is using ensemble based methods. Lortie and Kearney developed the TV-IRF method using correlation techniques. They extended it to identify TV Hammerstein structures with a TV nonlinear element and a TV linear element [187]. Finally, Ludvig et al. combined the two TV linear and Hammerstein approach and developed the TV-PC method. They validated the TVPC method using simulation, [193], and experimental data [205].

Kukreja et al. developed a parametric model of the parallel-cascade structure and a method for its identification [259]. Their model was based on a *Nonlinear AutoRegressive Moving Average with eXogenous input* (NARMAX) structure with a fixed static nonlinearity. They showed that their proposed scheme works using some experimental data. Guarin et al. later showed that the NARMAX model and its identification method is not accurate under realistic conditions because first the nonlinearity limited to be fixed and second the method fails in the presence of colored noise and third the identified discrete-time parameters were very difficult to interpret and relate to the original parallel-cascade model [260]. Thus, they formulated the nonlinearity to be identified as part of the identification procedure and they considered a *Multiple-Input-Multiple-Output* MISO *Box Jenkins* (BJ) model with an arbitrary colored output noise. They developed an iterative method with instrumental variables that gave unbiased and accurate estimates. Similar to the PC, this method iterated between estimating the two pathways [261].

Zhao et al. developed a linear MISO SS model for the parallel-cascade structure [122]. Similar to the Hammerstein MOESP, they used the MOESP linear method for identification of the linear MISO SS model. They performed simulation analysis and showed that the method gave more accurate estimates than the PC method. They demonstrated that the method was consistent in both open-loop and closed-loop conditions. I identified that this study has several issues which might limit its applications in practice:

1. The method was not validated with experimental data. The results were given for only one subject and one trial.
2. The parametric structure of the intrinsic pathway (elastic-viscous-inertia) does not represent the reality. More complex dynamics that arise from complex musculotendon dynamics or the joint-actuator contact dynamics must be considered.

3. MOESP estimates a linear MISO SS model of the stiffness. However, it is not straightforward to implement continuous-time models of individual elements of the parallel-cascade structure from the SS model.
4. It is over-parameterized, so it is expected to be less robust in the presence of noise.

3.3 Thesis Rationale

This thesis develops novel identification algorithms that efficiently unmask properties of stiffness during functionally important tasks. Detection of previously masked properties can result from such developments. Moreover, such methods will be useful for identification of other biomedical systems with linear, Hammerstein or parallel-cascade structures.

Identification of Hammerstein structure is important in estimating joint stiffness. The methods that have been used for this application are the linear, HK, SLS and subspace methods. The linear method assumes a fix static nonlinearity (a half wave rectifier) which assumes a priori information that might not be a correct representation of the underlying system. The HK method does not converge when the input to is non-white and non-Gaussian which is very limiting in practice. The SLS method is not guaranteed to converge either. The current subspace method seems promising but it does not separate the static nonlinearity and the linear dynamics from the identified MISO model. Thus, it is not possible to detect changes in the threshold or slope of the static nonlinearity from the gain of the linear element. Consequently, in chapter 4, I answer two questions: (i) how we can improve the subspace method to give direct estimates of the static nonlinearity and the linear dynamics;

(*ii*) whether the reflex stiffness is regulated by changes in both the static nonlinearity and the linear dynamics as a function of muscle activation.

Stiffness has a parallel-cascade model but accurate decomposition of the torque and identification of the parameters remains an important open problem. All versions of the iterative PC methods (PC-HR, PC-HK, PC-SLS) do not consistently converge to the true system. Moreover, they will give biased results when the joint is interacting with a compliant load. The subspace method, on the other hand, does not have convergence problems and it gives accurate estimates for compliant loads. However, it considers an a priori structure for the intrinsic pathway that might not accurately represent the complex underlying dynamics. It gives an over-parameterized MISO state-space model but it is not straightforward to relate its parameters to the individual elements of the parallel-cascade structure. Furthermore, all previous experimental studies ignored changes in the static nonlinearity of the reflex pathway and assigned all changes to the linear element. This was because of the lack of an accurate Hammerstein identification method and also because of the non-informative input signal that was used for identification. Consequently, in chapter 6, I address four important questions: (*i*) how we can implement a non-parametric model of the intrinsic stiffness in the state-space model; (*ii*) how we can analytically decompose the torque to the intrinsic and reflex torques by assuming minimal a priori information; (*iii*) how we can improve the subspace method to give direct estimates of all elements of the parallel-cascade model; (*iv*) how we can use a more informative input signal for more accurate identification of the static nonlinearity.

It is challenging to obtain long stationary data as stiffness shows time-varying or switching behaviour. This could happen in a variety of functional conditions such as movement when the joint operating point is not fixed, during upright stance when subject switches between different postural states, or in maintaining high activation levels because muscle fatigue is inevitable. One approach is to segment the nonstationary data record into multiple, short, stationary data segments and then identify local time-invariant models from subsets of segments having the same properties. Consequently, I extend the Hammerstein method in Chapter 5 and the parallel-cascade method in Chapter 7 to support multiple short data segments.

CHAPTER 4
Subspace Identification of SISO Hammerstein Systems: Application to Stretch Reflex Identification

4.1 Abstract

This paper describes a new subspace-based algorithm for identification of Hammerstein systems. It extends a previous approach which described the Hammerstein cascade by a state-space model and identified it with subspace methods that are fast and require little *a priori* knowledge. The resulting state-space models predict the system response well but have many redundant parameters and provide limited insight into the system since they depend on both the nonlinear and linear elements. This paper addresses these issues by reformulating the problem so that there are many fewer parameters, and each parameter is related directly to either the linear dynamics or the static nonlinearity. Consequently, it is straightforward to construct the continuous-time Hammerstein models corresponding to the estimated state-space model. Simulation studies demonstrated that the new method performs better than other well-known methods in the non-ideal conditions that prevail during practical experiments. Moreover, it accurately distinguished changes in the linear component from those in the static nonlinearity. The practical application of the new algorithm

was demonstrated by applying it to experimental data from a study of the stretch reflex at the human ankle. Hammerstein models were estimated between the velocity of ankle perturbations and the EMG activity of triceps surae for voluntary contractions in the plantarflexing and dorsiflexion directions. The resulting models described the behavior well, displayed the expected uni-directional rate sensitivity, and revealed that both the gain of the linear element and the threshold of the nonlinear changed with contraction direction.

4.2 Introduction

A Hammerstein system as shown in Fig. 4–1 consists of a zero memory static nonlinearity followed by a linear dynamic system [96]. Many physical and biological systems can be modeled with the Hammerstein structure; biological examples include the reflex stiffness of human ankle joint [37], the neural integrator model of the human *vestibular-ocular reflex* [87], and the mechanical behavior of lung tissue [81].

A variety of methods have been developed to identify Hammerstein systems. Stochastic methods estimate the linear and nonlinear components of the Hammerstein cascade with no *a priori* knowledge of the system. However, they require the input to be white [245], [244] - a severe limitation since in practice it is rarely feasible to generate white inputs experimentally.

Another category of Hammerstein system identification algorithm uses iterative approaches. Hunter and Korenberg [96] described a method that first estimates the linear dynamics using cross-correlation based methods. It estimates the nonlinearity's output using the inverse dynamics of the linear component, and then uses this predicted output to estimate the nonlinearity. The linear dynamics are then re-estimated using the output predicted by the estimated nonlinearity and the iteration repeated. The method does not require the input to be white but the input distribution needs to be Gaussian. Westwick and Kearney presented a method that formulates the output of the system as a linear function of some parameters and nonlinear function of the others [249]. *Separable least-squares* (SLS) optimization was then used to estimate the linear and nonlinear elements. This method does not require the input to be either white or Gaussian.

Another class of iterative algorithms separated the parameters into two sets: one corresponding to the static nonlinearity and the second to the linear element [253]. The output is a linear function of each parameter set provided the other set is held constant. In the first step, one set of parameters is held fixed and the other set is estimated using least-squares. The parameter sets are then interchanged and the same procedure is used to estimate the optimal value for the second set. The algorithm iterates until it converges to the optimal parameter values. Convergence can be assured by 1) normalizing the parameter estimates at each iteration and 2) setting the initial point for the optimization search correctly [252, 262, 257].

Most non-parametric approaches for identification of Hammerstein systems, model the linear component as an *impulse response function* (IRF) [96], [253], [249]. This has the advantage of requiring little a priori knowledge of the system but may result in models with many parameters if the system has a long memory. For instance, describing a low-pass filter with a very low break frequency requires a long IRF, i.e., introducing many unknown parameters [72]. This can result in less accurate estimation when the noise level is high.

In contrast, parametric approaches can provide parsimonious models but require accurate *a priori* information about the system structure, i.e. system order, noise model, etc [72]. Moreover, using a parametric method with an incorrect model will give misleading results [154]. What is desired is an identification approach that yields parsimonious models while requiring minimal *a priori* information. The subspace method described in this paper achieves this.

Subspace methods were originally developed to estimate state-space models for *multiple-input/multiple-output* (MIMO) linear systems; they require little *a priori* knowledge since the order of the state-space model is determined as part of the estimation procedure [113], [123]. They are efficient computationally, and can be extended to identify systems with both input and output noise [116]. Moreover, as Verhaegen and Westwick [118] showed, the *Multivariable output error state-space* (MOESP) subspace algorithm can be used to identify Hammerstein models by transforming the *single-input/single-output* (SISO) nonlinear Hammerstein model into a *multi-input/single-output* (MISO) linear state-space model and identifying it with MOESP. Models estimated with this approach have excellent predictive capabilities but, as a result of the transformation to MISO, their parameters are not directly related to those of the SISO system. This causes two problems. First, many of the MISO model parameters are redundant and the resulting over-parameterization can be expected to reduce the identification robustness. Secondly, each MISO parameter depends on the properties of both the nonlinear and the linear dynamic elements. Consequently, it is difficult to relate changes in the state-space model parameters to those of the original Hammerstein model. For example, in studying the stretch

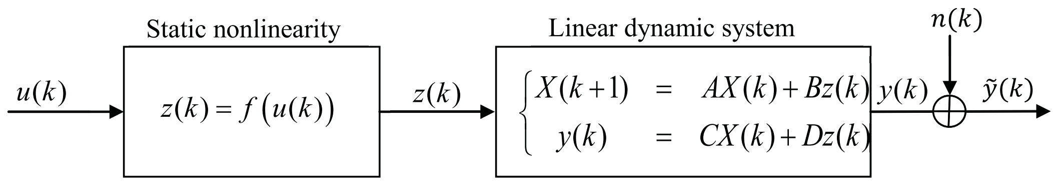

Figure 4–1: The Hammerstein system model comprises a static nonlinearity followed by a linear system. The input signal is $u(k)$, $z(k)$ is the output of the nonlinearity and the input to the linear system, $y(k)$ is the noise free output. $n(k)$ is additive noise, and $\tilde{y}(k)$ the noisy output. The only signals available for identification are $u(k)$ and $\tilde{y}(k)$.

reflex it is important to distinguish changes in the linear dynamics from those of the static nonlinearity. Thus, when we used the method described in [118] to estimate a state-space model for joint stiffness, additional steps were required to recover the underlying nonlinearity and linear dynamics [122].

The paper is organized as follows. Section 4.3, formulates the state-space model for Hammerstein system. Section 4.4 describes the new identification algorithm which extends Verhaegen's algorithm [118] to estimate directly the coefficients of the basis function expansion of the nonlinearity and the state-space model of the linear component. Section 4.5 presents the results of simulation studies that validate and evaluate the performance of the new algorithm. It compares the new method with the original subspace method [118], which is a parametric approach, and two non-parametric identification methods: *Hunter-Korenberg* H-K [96] and *separable least-squares* SLS algorithms [249]. Section 4.6 gives experimental results and Section 4.7 provides a discussion and some concluding remarks.

4.3 Problem Formulation

This section first formulates the state-space model for a Hammerstein structure as developed in [118]. The SISO, nonlinear Hammerstein system is transformed into a MISO linear model whose inputs are constructed from a basis function expansion of the static nonlinearity. Then, it shows how the static nonlinearity and the linear system parameters appear individually in data equations. Throughout this paper, vectors, matrices and scalars are indicated by bold-face uppercase, uppercase and lowercase letters respectively.

Consider a SISO Hammerstein discrete-time system shown in Fig. 4–1 consisting of a static nonlinear block followed by a linear dynamic system. Define $z(k)$ to be the output of the nonlinear component - an intermediate signal that cannot be observed. Approximate the nonlinearity by an orthogonal basis function expansion (e.g. Tchebyshev, Hermite, ...):

$$z(k) = f\left(u(k)\right) \simeq \sum_{i=1}^{n} \omega_i g_i\left(u(k)\right) \tag{4.1}$$

where, $g_i(\cdot)$ is the i^{th} basis function, n is the order of the expansion and ω_i is its coefficient. Assume that N_s samples of $u(k)$, the input of the Hammerstein structure, and $y(k)$, its output are recorded.

Assume the linear component is stable and can be represented by a state-space model:

$$\begin{cases} \boldsymbol{X}(k+1) & = A\boldsymbol{X}(k) + \boldsymbol{B}z(k) \\ y(k) & = C\boldsymbol{X}(k) + Dz(k) \end{cases} \tag{4.2}$$

where, $\boldsymbol{X}(k)$ is a $m \times 1$ state vector while, $A_{m\times m}$, $\boldsymbol{B}_{m\times 1}$, $C_{1\times m}$ and $D_{1\times 1}$ are the state-space model matrices. Represent the elements of $\boldsymbol{B}$ and D by:

$$\begin{aligned} \boldsymbol{B} &= [b_1, \cdots, b_m]^T \\ D &= [d] \end{aligned} \tag{4.3}$$

Assume the measured output $\tilde{y}(k)$ is contaminated with additive noise, $n(k)$ that is zero mean and uncorrelated with the input signal $u(k)$. Define the vectors:

$$\boldsymbol{\Omega} = [\omega_1, \cdots, \omega_n]^T \tag{4.4}$$

$$\boldsymbol{U}(k) = [g_1(u(k)), \cdots, g_n(u(k))]^T \tag{4.5}$$

Substitute (4.4) and (4.5) in (4.2) to yield:

$$\begin{cases} \boldsymbol{X}(k+1) & = A\boldsymbol{X}(k) + B_\Omega \boldsymbol{U}(k) \\ y(k) & = C\boldsymbol{X}(k) + D_\Omega \boldsymbol{U}(k) \end{cases} \tag{4.6}$$

where:

$$B_\Omega = \boldsymbol{B}\boldsymbol{\Omega}^T = \begin{bmatrix} b_1\omega_1 & \cdots & b_1\omega_n \\ \vdots & \ddots & \vdots \\ b_m\omega_1 & \cdots & b_m\omega_n \end{bmatrix} \tag{4.7}$$

$$D_\Omega = D\boldsymbol{\Omega}^T = \begin{bmatrix} d\omega_1 & \cdots & d\omega_n \end{bmatrix} \tag{4.8}$$

Note that this parameterization is not unique since for any arbitrary scalar β, the vectors $\beta\boldsymbol{B}$, βD and $\beta^{-1}\boldsymbol{\Omega}$ will generate the same matrices B_Ω and D_Ω.

Consequently, to provide a unique solution we will require that the first non-zero element of the vector $\mathbf{\Omega}$ be positive and $||\mathbf{\Omega}|| = 1$, where $|| \cdot ||$ is the two norm.

Note that (4.6) models the total Hammerstein system as a MISO system whose input is $\boldsymbol{U}(k)$, a $n \times 1$ vector constructed from the basis function expansion of the input to the SISO system. Thus, the estimated state-space matrices have the following structure:

$$\begin{cases} \hat{\boldsymbol{X}}^S(k+1) & = \hat{A}^S \hat{\boldsymbol{X}}^S(k) + \hat{B}^S \boldsymbol{U}(k) \\ \hat{y}(k) & = \hat{C}^S \hat{\boldsymbol{X}}^S(k) + \hat{D}^S \boldsymbol{U}(k) \end{cases} \tag{4.9}$$

where, the superscript $(\cdot)^S$ indicates that the identification is achieved up to a similarity transform. One can show that given the matrix S as the similarity transform, the matrices $\hat{B}^S$ and $\hat{D}^S$ can be written as follows:

$$\hat{B}^S \simeq S^{-1} B_\Omega = \begin{bmatrix} b_1^S \omega_1 & \cdots & b_1^S \omega_n \\ \vdots & \ddots & \vdots \\ b_m^S \omega_1 & \cdots & b_m^S \omega_n \end{bmatrix} \tag{4.10}$$

$$\hat{D}^S \simeq D_\Omega = \begin{bmatrix} d\omega_1 & \cdots & d\omega_n \end{bmatrix} \tag{4.11}$$

Remark 1 *The vector $\boldsymbol{B}^S = \left[b_1^S, \cdots, b_m^S\right]^T$ incorporates the effect of the similarity transform i.e, $\boldsymbol{B}^S = S^{-1}\boldsymbol{B}$. Thus, the similarity transform has no effect on the parameter set $\mathbf{\Omega}$ but does alter the parameters corresponding to the linear component, i.e. $b_1, \cdots, b_m, d$. Also note that the rows of the matrices B_Ω and D_Ω are linearly dependent.*

4.4 Algorithm

The first step of the new algorithm uses MOESP to estimate the order of the linear component and the $\hat{A}^S$ and $\hat{C}^S$ state-space matrices from the constructed input (4.5) and the measured noisy output $\tilde{y}(k)$. MOESP is described in [113], [123], [116], [118] and is not repeated here. We used MOESP automatic order selection method which is described in [117, 116].

It remains to estimate the vector $\boldsymbol{B}^S$ and the scalar d, which define the linear dynamics, and the vector $\hat{\boldsymbol{\Omega}}$ which contains the coefficients of the basis function expansion of the nonlinear block. The output of (4.9) can be expressed as [116]:

$$\begin{aligned}\hat{y}(k) = &\left[\sum_{\tau=0}^{k-1} \boldsymbol{U}^T(\tau) \otimes \hat{C}^S \hat{A^S}^{k-1-\tau}\right] \mathrm{vec}\left(\hat{B}^S\right) \\ &+ \left[\boldsymbol{U}^T(k)\right] \mathrm{vec}\left(\hat{D}^S\right) + n(k)\end{aligned} \tag{4.12}$$

where the operator vec$(\cdot)$ stacks the columns of a matrix $(\cdot)$ on top of each other in a tall vector and $\otimes$ is the Kroncker product. Define the following matrices:

$$\begin{aligned}\boldsymbol{Y} &= \left[\tilde{y}(0), \cdots, \tilde{y}(N_s-1)\right]^T \\ \Delta_{N_s} &= \left[0, \cdots, \sum_{\tau=0}^{N_s-2} \boldsymbol{U}^T(\tau) \otimes \hat{C}^S \hat{A^S}^{N_s-2-\tau}\right]^T \\ \Phi_{N_s} &= \left[\boldsymbol{U}^T(0), \cdots, \boldsymbol{U}^T(N_s-1)\right] \\ \bar{\boldsymbol{B}} &= \mathrm{vec}(\hat{B}^S) \\ \bar{\boldsymbol{D}} &= \mathrm{vec}(\hat{D}^S) \\ \boldsymbol{E} &= \left[\begin{array}{cccc} n(0) & n(1) & \cdots & n(N_s-1) \end{array}\right]^T\end{aligned} \tag{4.13}$$

Rewrite (4.12) as the matrix equation:

$$\boldsymbol{Y} = \Psi\boldsymbol{\Theta} + E \tag{4.14}$$

where, Ψ is the $N_s \times n(m+1)$ data matrix constructed only from the known or estimated elements:

$$\Psi = [\Delta_{N_s}, \Phi_{N_s}] \tag{4.15}$$

Let the columns of Ψ be $\boldsymbol{\Psi}_1, \boldsymbol{\Psi}_2, \cdots, \boldsymbol{\Psi}_{n(m+1)}$. The vector $\boldsymbol{\Theta}$ contains the unknown parameters stacked in a single vector:

$$\boldsymbol{\Theta} = \begin{bmatrix} \bar{\boldsymbol{B}} \\ \bar{\boldsymbol{D}} \end{bmatrix} = \begin{bmatrix} \mathrm{vec}(B) \\ \mathrm{vec}(D) \end{bmatrix} \tag{4.16}$$

For normal linear MISO identification, the remaining system parameters are estimated by solving the least-squares problem defined by (4.14). However, for the Hammerstein model, the parameters of interest appear as nonlinear combinations:

$$\begin{aligned} \boldsymbol{\Theta} =& [b_1^S\omega_1,\ \cdots,\ b_m^S\omega_1,\ b_1^S\omega_2,\ \cdots,\ b_m^S\omega_2,\ \cdots \\ & b_1^S\omega_n,\ \cdots,\ b_m^S\omega_n,\ d\omega_1,\ \cdots,\ d\omega_n]^T \end{aligned} \tag{4.17}$$

Consequently, the parameters $\{b_1^S, \cdots, b_m^S, \omega_1, \cdots, \omega_n, d\}$ cannot be estimated directly by linear least-squares solution.

Note that the parameters in the vector $\boldsymbol{\Theta}$ are combinations of a smaller number of independent parameters that may be divided into two subsets: the coefficients of the nonlinearity $\{\omega_1, \cdots, \omega_n\}$ and the parameters of linear system's state-space model $\{b_1^S, \cdots, b_m^S, d\}$. These parameters can be estimated separately using the iterative approach suggested in [252, 262, 257] as follows: Assume an initial set of values for the nonlinear coefficients $\{\omega_1, \cdots, \omega_n\}$, and estimate the parameters of the linear dynamics using ordinary least-squares. Then, fix these parameters $\{b_1^S, \cdots, b_m^S, d\}$, and estimate the parameters of the nonlinearity using an ordinary least-squares solution. Repeat the procedure until it converges to optimal values.

To use this approach, the data equation (4.14) must be reformulated so that if the coefficients of the basis function expansion of the static nonlinearity ($\mathbf{\Omega}$) are known, then the output vector $\boldsymbol{Y}$ is a linear function of the unknown parameters $\left[b_1^S \; b_2^S \; \cdots \; b_m^S \; d\right]^T$. To do so, group the linear system parameters as follows:

$$
\begin{aligned}
\boldsymbol{Y} &= \left(\boldsymbol{\Psi}_1\omega_1 + \boldsymbol{\Psi}_{m+1}\omega_2 + \cdots + \boldsymbol{\Psi}_{m(n-1)+1}\omega_n\right) b_1^S \\
&\quad + \cdots\cdots \\
&\quad + \left(\boldsymbol{\Psi}_m\omega_1 + \boldsymbol{\Psi}_{2m}\omega_2 + \cdots + \boldsymbol{\Psi}_{mn}\omega_n\right) b_m^S \\
&\quad + \left(\boldsymbol{\Psi}_{mn+1}\omega_1 + \boldsymbol{\Psi}_{mn+2}\omega_2 + \cdots + \boldsymbol{\Psi}_{mn+n}\omega_n\right) d' + \boldsymbol{E}
\end{aligned}
\tag{4.18}
$$

Write this equation in matrix form:

$$
\boldsymbol{Y} = \Psi_\Omega \begin{bmatrix} b_1^S \\ \vdots \\ b_m^S \\ d \end{bmatrix} + \boldsymbol{E} \tag{4.19}
$$

where it is evident from (4.18) and (4.14) that Ψ_Ω is:

$$\Psi_\Omega = \Psi \begin{bmatrix} \omega_1 & \cdots & 0 & 0 \\ \vdots & \ddots & \vdots & \vdots \\ 0 & \cdots & \omega_1 & 0 \\ \vdots & \vdots & \vdots & \vdots \\ \omega_n & \cdots & 0 & 0 \\ \vdots & \ddots & \vdots & \vdots \\ 0 & \cdots & \omega_n & 0 \\ 0 & \cdots & 0 & \omega_1 \\ \vdots & \ddots & \vdots & \vdots \\ 0 & \cdots & 0 & \omega_n \end{bmatrix} \tag{4.20}$$

The second requirement is to find a formulation that relates the output $\boldsymbol{Y}$ linearly to the unknown vector $\boldsymbol{\Omega}$ given the state-space parameters $b_1^S, b_2^S, \cdots, b_m^S$ d are known. To do so, collect the terms associated with each nonlinear parameter to give:

$$\begin{aligned} \boldsymbol{Y} &= \left(\boldsymbol{\Psi}_1 b_1^S + \boldsymbol{\Psi}_2 b_2^S + \cdots + \boldsymbol{\Psi}_m b_m^S + \boldsymbol{\Psi}_{mn+1} d\right) \omega_1 \\ &+ \cdots + \left(\boldsymbol{\Psi}_{m(n-1)+1} b_1^S\right) \omega_n \\ &+ \left(\boldsymbol{\Psi}_{m(n-1)+2} b_2^S + \cdots + \boldsymbol{\Psi}_{mn} b_m^S + \boldsymbol{\Psi}_{mn+n} d\right) \omega_n + \boldsymbol{E} \end{aligned} \tag{4.21}$$

Write this in matrix form as:

$$\boldsymbol{Y} = \Psi_{bd} \begin{bmatrix} \omega_1 \\ \vdots \\ \omega_n \end{bmatrix} + \boldsymbol{E} \tag{4.22}$$

where from (4.21) and (4.14) it can be seen that Ψ_{bd} is :

$$\Psi_{bd} = \Psi \begin{bmatrix} b_1^S & 0 & \cdots & 0 \\ \vdots & \vdots & \ddots & \vdots \\ b_m^S & 0 & \cdots & 0 \\ \vdots & \vdots & \vdots & \vdots \\ 0 & 0 & \cdots & b_1^S \\ \vdots & \vdots & \ddots & \vdots \\ 0 & 0 & \cdots & b_m^S \\ d & \cdots & \cdots & 0 \\ \vdots & \ddots & & \vdots \\ \vdots & & \ddots & \vdots \\ 0 & \cdots & \cdots & d \end{bmatrix} \tag{4.23}$$

Algorithm: The following algorithm uses these two formulations to estimate the unknown parameters $b_1^S, \cdots, b_m^S, d, \omega_1, \cdots, \omega_n$. The algorithm is iterative so variables will be indexed according to the iteration number j.

(1) Initialization:

Let $j = 1$ and $\hat{\mathbf{\Omega}}(0) = [1, \cdots, 1]_{n\times 1}^T$.

(2) Construct the matrix $\Psi_{\hat{\Omega}(j-1)}$ using (4.20).

(3) Estimate $[b_1^S, \cdots, b_m^S, d]^T$ by solving the least-squares problem defined in (4.19) to give :

$$\hat{\boldsymbol{bd}}(j) = \begin{bmatrix} \hat{b}_1^S(j) \\ \vdots \\ \hat{b}_m^S(j) \\ \hat{d}(j) \end{bmatrix} = \left(\Psi_{\hat{\Omega}(j)}\right)^{\dagger} \boldsymbol{Y} \tag{4.24}$$

where † is the pseudo inverse.

(4) Construct the matrix $\Psi_{\hat{bd}(j)}$ using (4.23).

(5) Estimate $[\omega_1, \cdots, \omega_n]^T$ by solving the least-squares problem (4.22) to give:

$$\hat{\boldsymbol{\Omega}}(j) = \begin{bmatrix} \hat{\omega}_1(j) \\ \vdots \\ \omega_n(j) \end{bmatrix} = \left(\Psi_{\hat{bd}(j)}\right)^{\dagger} \boldsymbol{Y} \tag{4.25}$$

(6) Let s be the sign of first non-zero element of $\hat{\boldsymbol{\Omega}}(j)$:

$$s = \operatorname{sgn}\left(\hat{\omega}_1(j)\right) \tag{4.26}$$

Perform the normalization:

$$\begin{aligned} \hat{\boldsymbol{bd}}(j) &\leftarrow \hat{\boldsymbol{bd}}(j) s \left\| \hat{\boldsymbol{\Omega}}(j) \right\| \\ \hat{\boldsymbol{\Omega}}(j) &\leftarrow \frac{\hat{\boldsymbol{\Omega}}(j) s}{\left\| \hat{\boldsymbol{\Omega}}(j) \right\|} \end{aligned} \tag{4.27}$$

(8) Compute the *sum of squared error* (SSE) between the predicted output and the measured output.

(9) Terminate if SSE satisfies the following condition; otherwise replace j by $j+1$ and go to step (2).

$$\frac{\mathrm{SSE}(j) - \mathrm{SSE}(j-1)}{\mathrm{SSE}(j-1)} \leqslant \text{threshold} \tag{4.28}$$

Considering SSE as a cost function, it is strictly convex at each iteration [252], and so there will be a unique global minimum at each step. In addition, the cost function will decrease with each iteration. Moreover, the algorithm will converge after at most two steps to the true values of the parameters in the limit, i.e. provided enough samples are available [252].

The threshold value for the stopping criteria is adjustable. However, the algorithm converges very quickly with improvements in the SSE becoming very small after a relatively few iterations. In the results presented here, we used a threshold of 10^{-10} and the algorithm converged after 6-8 iterations.

4.5 Simulation Results

4.5.1 Methods

The performance of the algorithm was evaluated using simulated data from the stretch reflex stiffness model of the human's ankle shown in Fig. 4–2. In this model, the input, $u(k)$ joint velocity, first passes through a static nonlinearity and then through a linear component consisting of a delay and a second-order low-pass filter to generate the output torque. This model describes reflex behavior well and has been used extensively to explore the human stretch reflex [37], [65], [122]. The nonlinear element accounts for two experimentally observed phenomena: strong unidirectional rate sensitivity is modeled as a threshold at p_1 [229]; a saturation of the response

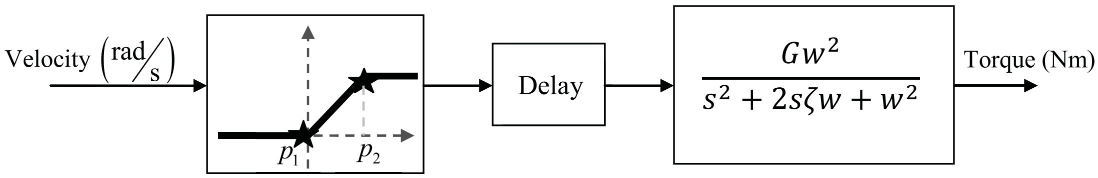

Figure 4–2: Hammerstein model of reflex stiffness.

at high velocities is modeled with a saturation at p_2 [229]. This nonlinearity can be described analytically as:

$$f(u(k)) = \frac{(u(k) - p_1) + (u(k) - p_1)\mathrm{sgn}(u(k) - p_1)}{2} - \frac{(u(k) - p_2) + (u(k) - p_2)\mathrm{sgn}(u(k) - p_2)}{2} \tag{4.29}$$

where sgn is the sign function. The continuous-time transfer function of the linear component is:

$$H(s) = \frac{e^{-\tau s} G w^2}{s^2 + 2s\zeta w + w^2} \tag{4.30}$$

where s is the Laplace variable, G is the gain, ζ is the damping parameter, w is the natural frequency, and τ is the delay in seconds. Nominal values of these parameters were based on those described previously [65]:

$$\begin{cases} G & = 25 \left(\frac{Nms}{rad}\right) \\ \zeta & = 0.98 \\ w & = 20 \left(\frac{rad}{s}\right) \\ \tau & = 0.04(s) \\ p_1 & = 0 \left(\frac{rad}{s}\right) \\ p_2 & = 1.5 \left(\frac{rad}{s}\right) \end{cases} \tag{4.31}$$

To avoid aliasing due to the nonlinearity, the model was simulated using MATLAB Simulink at 1KHz for sixty seconds. Signals were then filtered with an eight-order low-pass filter with cutoff frequency of 40 Hz and decimated to 100 Hz before analysis. Gaussian, white noise was added to the decimated output to simulate experimental noise; the amplitude of the noise was adjusted to generate the required *signal to noise ratio* (SNR) defined as:

$$\text{SNR (dB)} = 20\log_{10}\left(\frac{\text{RMS}_{\text{signal}}}{\text{RMS}_{\text{noise}}}\right) \tag{4.32}$$

The model used by SLS and H-K had 50 unknown parameters for the IRF and 12 parameters for the static nonlinearity for a total of 62 free parameters while the Hammerstein state-space model used in OSS algorithm had 42 unknown parameters. In comparison, the NSS algorithm had 3 parameters for the state-space matrices B and D, 6 parameters for the state-space matrices A and C, and 12 parameters for the static nonlinearity, for a total 21 free parameters. Consequently, the NSS describes the same dynamics with fewer parameters than the other methods which should make its estimates more robust.

The similarity of the predicted $\hat{y}$ to the noise free simulated reflex torque, y was quantified in terms of percentage *variance accounted for* (%VAF):

$$\%\mathrm{VAF} = 100\left(1 - \frac{\mathrm{var}(\hat{y} - y)}{\mathrm{var}(y)}\right) \tag{4.33}$$

To derive confidence intervals on the prediction %VAF, we used Monte-Carlo simulations with 1000 trials in which each trial involved a new realization of input signal and noise sequence. The distributions of the %VAFs for the different methods were not Gaussian, so we used a non-parametric approach to estimate the significance of differences between methods. Thus, for each trial we computed the difference between the %VAF of the new method and each of three other methods. Then, we computed the *cumulative distribution function* (CDF) of this difference for the 1000 trials. The value of this CDF at zero (p) gives the probability that the %VAF of NSS was equal to or smaller than that of the other method. Thus, the lower this probability, the greater confidence that the NSS method is more accurate. Fig. 4–3 shows the CDFs for Monte-Carlo simulations at SNR levels of -15 and +15 dB. For the low SNR of -15dB, $p < 0.02$ for all three comparisons. Consequently, NSS was more accurate than others at this SNR level. The difference was, however, not significant at +15dB in comparison to the original subspace ($p = 0.40$) and SLS ($p = 0.18$) methods, however, the new method was still significantly more accurate than H-K at this SNR level ($p = 0$).

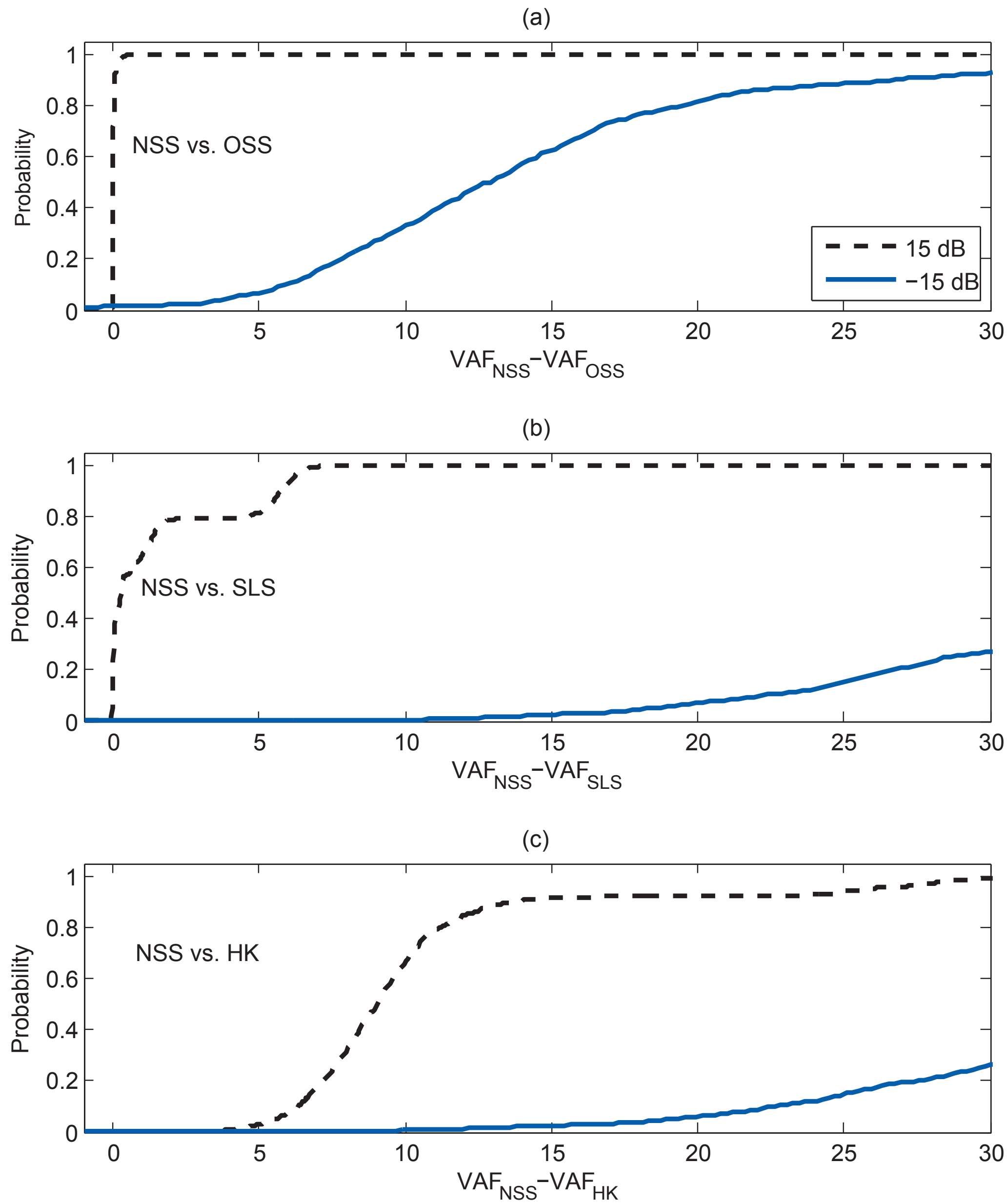

Figure 4–3: *Cumulative distribution function* (CDF) of the difference between %VAF of the NSS method and those of (a) OSS; (b) SLS; (c) H-K. Results are shown for SNRS of -15dB and + 15dB.

4.5.2 Input Design

The position input often used in identification of reflex stiffness is *pseudo random binary sequence* (PRBS) of low amplitude displacements around an operating point. The histogram of the velocity of this input has three major peaks corresponding to zero, positive, and negative velocities [229]. As a result, while the PRBS input excites the linear system well, its amplitude distribution is not well suited to estimate the static nonlinearity since an infinite number of polynomials can be fit between these three levels. To address this, we used a velocity input generated by sampling a uniform distribution at 250 ms intervals. For simulation purposes we integrated the velocity signal to produce the desired angular position signal. Position was then filtered with a second-order, low-pass, Butterworth filter, with break frequency of 15.9 Hz to represent actuator dynamics. Fig. 4–4 shows one realization of the resulting position input, the corresponding velocity, its distribution and power spectrum. The amplitude histogram of the velocity shows that it is distributed over the whole range of possible values and so this input provides a much richer set of values with which to estimate the static nonlinearity. The frequency spectrum of the simulated actuator velocity is not white but does contain power up to 30 Hz suitable for identification.

4.5.3 Results

We compared the predictive ability of the models produced by the different methods in a Monte-Carlo validation where the SNR was varied between -15 to 15 dB at 10 db increments. We first estimated a model using half of the data points. Then, we quantified the results in terms of the %VAF between the true output and predicted output using the second half of the data points.

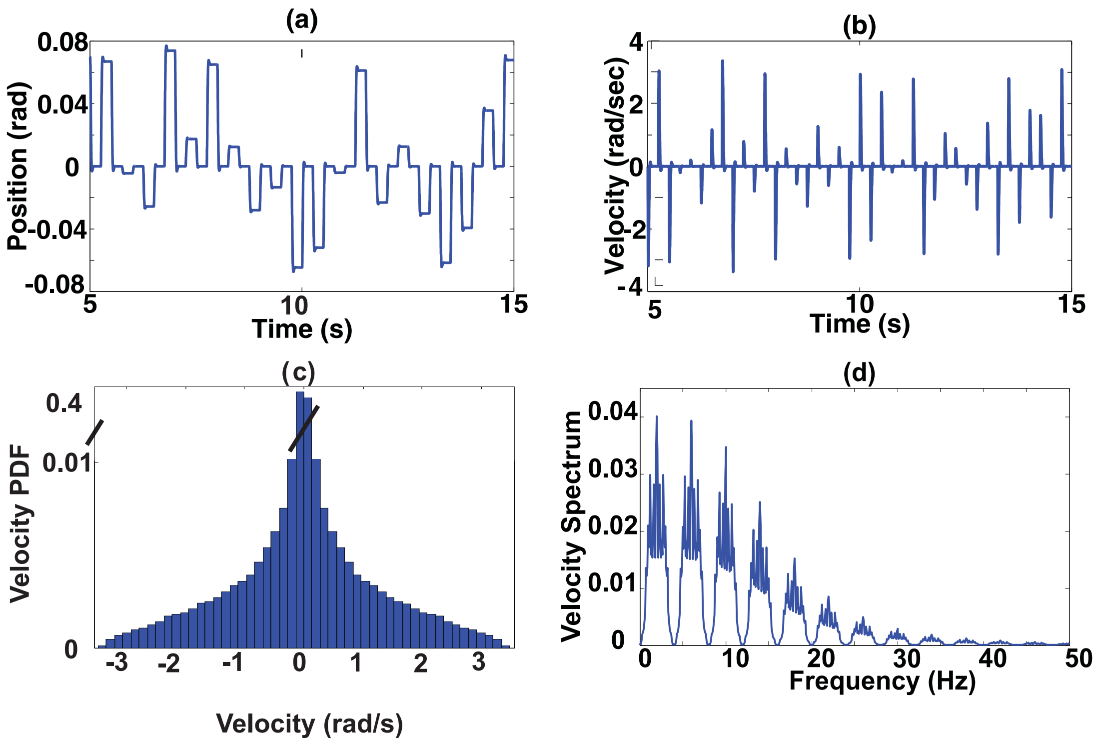

Figure 4–4: Input signal used for simulation: (a) a realization of the position; (b) a realization of the velocity; (c) amplitude distribution of the input; (d) Power spectrum of velocity.

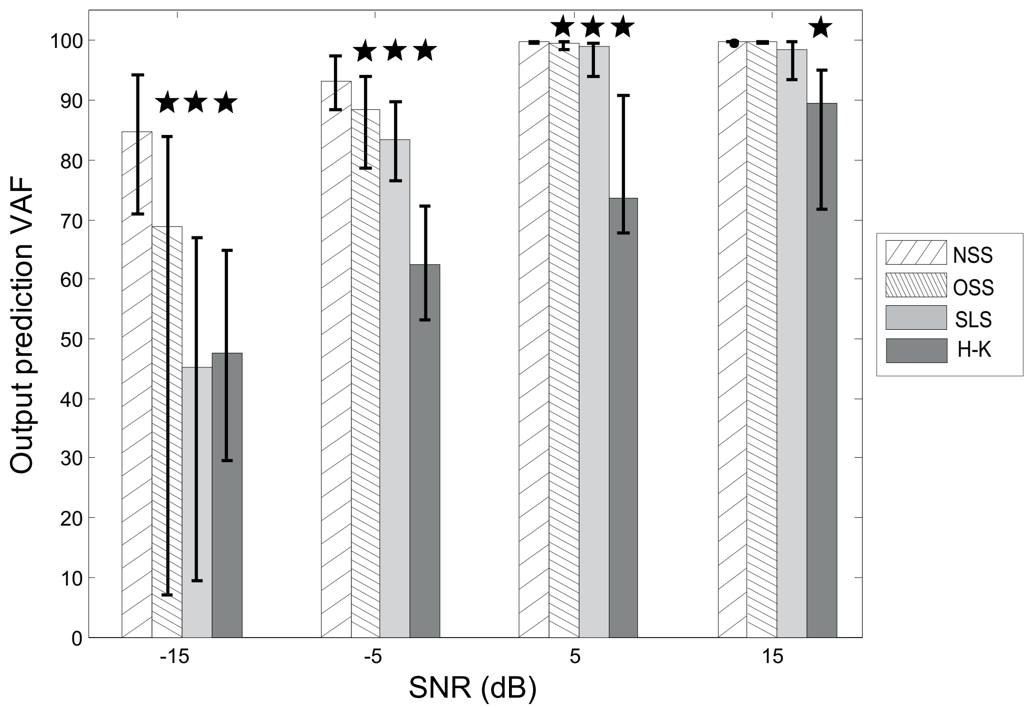

Figure 4–5: Mean output prediction (%VAF) bracketed by 95% range, i.e. [2.5% – 97.5%] percentiles, for all four methods. Stars indicate cases where the %VAFs were less than those of NSS in ¿ 95% of trials.

First, we studied the output prediction accuracy of the new method in comparison to other methods. Fig. 4–5 shows the %VAF and its statistics for each method at different noise levels. It shows that the output predictions from the new method were significantly more accurate than those from all other methods at SNRs of -15, -5 and 5 dB. At +15 dB, the only significant difference was for H-K.

Second, we examined the accuracy with which the nonlinear and linear elements of the Hammerstein model were estimated by NSS in comparison to the H-K and SLS algorithms. Note that, as indicated in the introduction, the original state

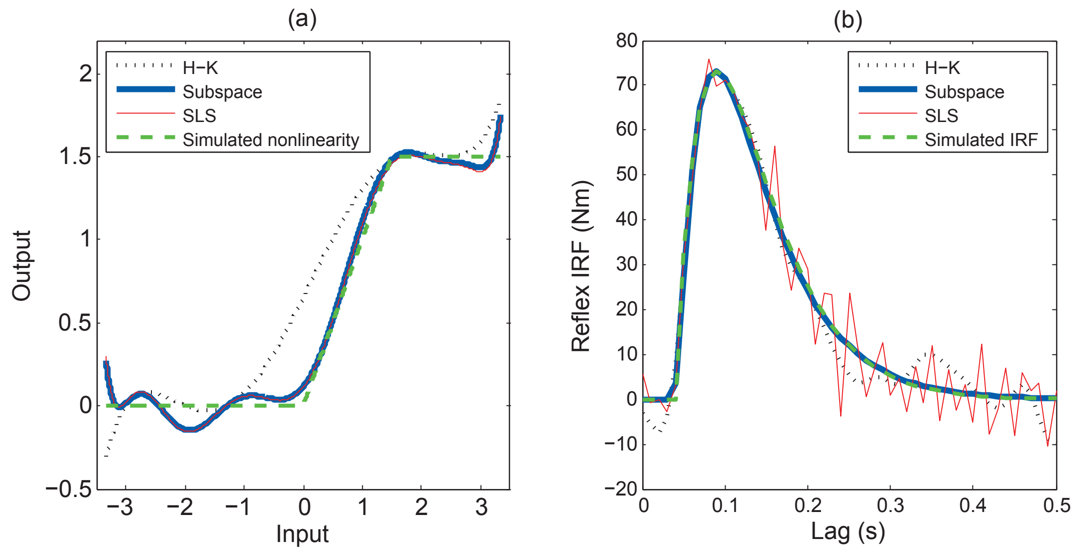

Figure 4–6: Hammerstein models of stretch reflex identified from simulation data (SNR=5 dB). (a) Static Nonlinearity (b) IRF.

space method does not yield direct estimates of the static nonlinearity or linear dynamic elements of the Hammerstein systems. Consequently, no results are shown in Fig. 4–6 and 4–7 for this method. For this comparison we used the nominal linear model, a nonlinearity with fixed value for threshold ($p_1 = 0\left(\frac{rad}{s}\right)$) and saturation ($p_2 = 1.5\left(\frac{rad}{s}\right)$) and a SNR level of 5 dB. The nonlinear elements were evaluated by comparing their shapes over the input range. The nonlinearities estimated using SLS and subspace were very similar to that simulated. As shown in Fig. 4–6(a), the nonlinearity estimated with H-K was, however, wrong.

The linear dynamics estimated by the different methods were compared in terms of their impulse response functions. Both SLS and H-K methods estimate IRFs directly; the IRF of the state-space model was determined by simulating its response to unit impulse. As shown in Fig. 4–6(b), the IRF estimated by the subspace method was almost identical to that simulated. The IRFs estimated by both SLS and HK had considerable noise.

The subspace and SLS algorithms both predicted the noise free torque well (%VAF of 99.7%, 99.4% respectively) while the prediction of the H-K method was poor (%VAF = 81.2%).

We studied the robustness of the different methods, further by using a Monte-Carlo simulation to examine how well the linear dynamics were estimated as the SNR level changed. To do so, the gain, threshold and saturation were held fixed at the same values ($p_1 = 0\left(\frac{rad}{s}\right)$ and $p_2 = 1.5\left(\frac{rad}{s}\right)$) while the SNR was varied from 0 to 20 dB. A Monte-Carlo simulation of 1000 trials was performed at each SNR (each with different realization of input and noise signals) and the estimated IRF was compared to that simulated in terms of %VAF. Similar to Fig. 4–5, Fig. 4–7 shows the mean value of the %VAF bracketed by its 95% range as a function of SNR. It also shows the statistical test results as a star on the bar plot if the new subspace method was significantly more accurate. The new subspace algorithm performed the best - it had the highest mean %VAF with lowest variation at all SNRs. Moreover, the IRF was significantly more accurately identified at all levels.

There are physiological reasons to expect both the linear and nonlinear elements may change independently. Consequently, it is important for an identification algorithm to distinguish between changes in the linear and nonlinear elements. To examine this, Monte Carlo simulations were done to assess the ability of the algorithm to distinguish between changes in gain and threshold. Systematic changes in the linear system gain G (10 to 30) and nonlinearity threshold (-0.8 to 0.2) were

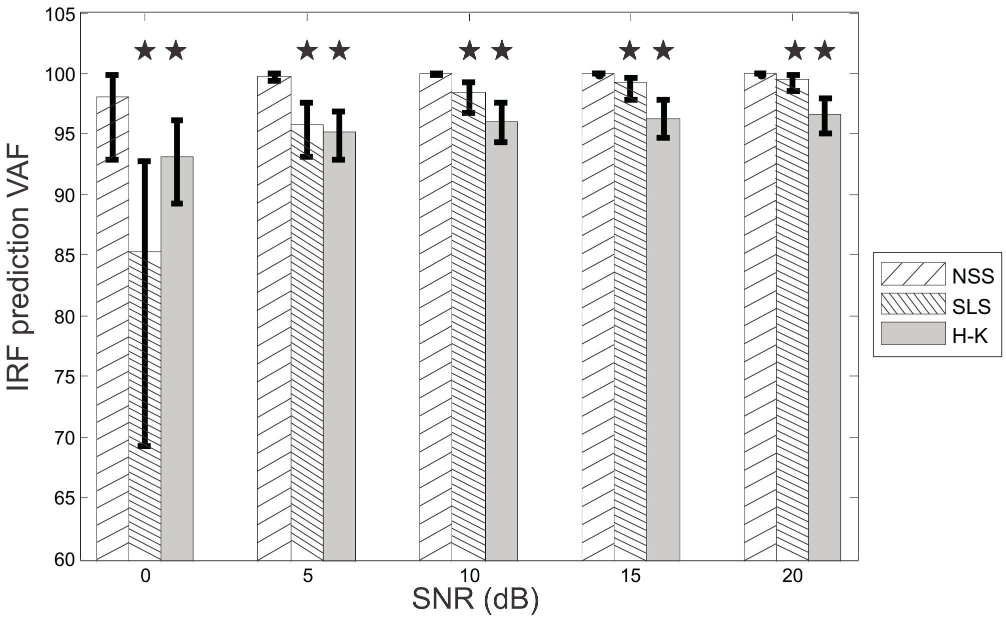

Figure 4–7: Mean IRF estimation accuracy (%VAF) bracketed by 95% range. Stars indicate cases with %VAFs less than those of NSS in 95% of trials.

made and 100 trials were simulated at each threshold/gain combination, each with different realizations of noise and input sequence. The results of identifying each trial were parameterized by: (i) fitting equations (4.29) to the estimated nonlinearity and (b) fitting under-damped second-order IRF (4.34) to the estimated IRF. Fits were done using Levenberg-Marquardt method in MATLAB curve fitting toolbox.

$$h(t) = \frac{Gw}{\sqrt{1-\zeta^2}} e^{-\zeta w(t-\tau)} \sin\left(w\sqrt{1-\zeta^2}(t-\tau)\right) \tag{4.34}$$

Fig. 4–8(a) shows the mean value of the estimated gain as a function of the simulated gain and threshold. Fig. 4–8(b) shows the coefficient of variation CV of the gain estimates. Fig. 4–8(c) and (d) show the results for the identification of the threshold in a similar manner.

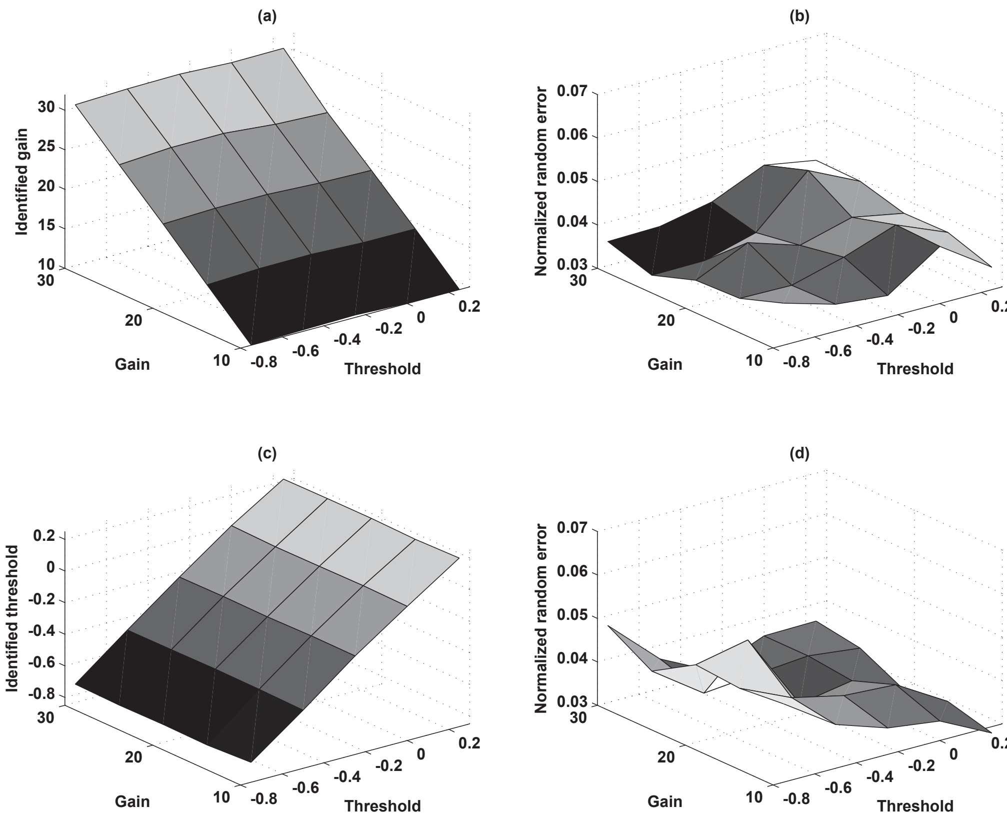

Figure 4–8: Estimation accuracy of the Hammerstein model; (a) mean value of the predicted gains (b) CV associated with the estimation of gain; (c) mean value of the predicted thresholds (d) CV associated with the estimation of threshold.

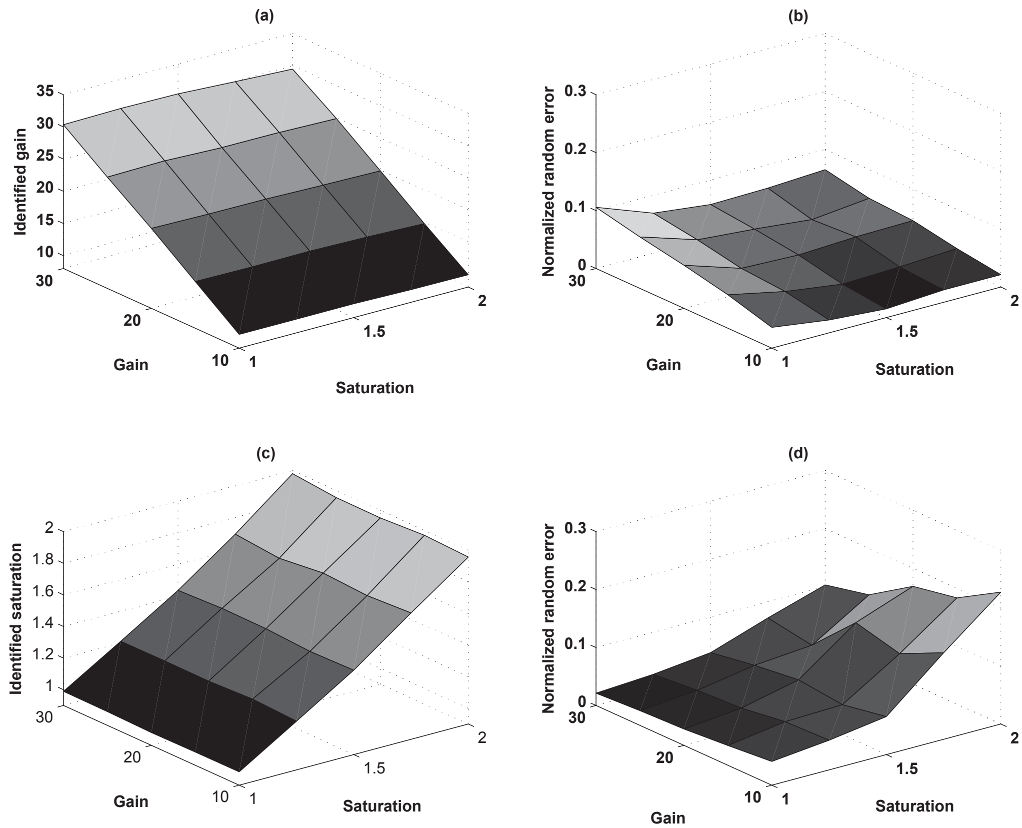

Figure 4–9: Estimation accuracy of the Hammerstein model; (a) mean value of the predicted gain; (b) CV associated with the estimation of gain; (c) mean value of the predicted saturation; (d) CV associated with the estimation of saturation.

In another set of simulations, the gain and saturation parameters were varied systematically between [10 to 30] and [1 to 2] while the threshold was held constant which is shown in Fig. 4–9. Fig. 4–8 and Fig. 4–9 show that the new method tracked the changes accurately in the shape of the nonlinearity from changes in the linear component.

To evaluate the quality of the tracking we fitted planes to the data from Fig. 4–8 and 4–9. Ideally, the estimated thresholds, saturations and gains should be equal to

Table 4–1: Estimation accuracy for varying gain and threshold values

		NSS	SLS	H-K
Gain	Slope	1.00	0.94	0.72
	R-square	0.98	0.94	0.95
Threshold	Slope	0.95	0.86	-0.12
	R-square	0.98	0.96	0.20

Table 4–2: Estimation accuracy for varying gain and saturation values

		NSS	SLS	H-K
Gain	Slope	1.00	1.00	0.97
	R-square	0.98	0.98	0.98
Saturation	Slope	0.97	0.95	0.43
	R-square	0.88	0.86	0.66

those simulated and the fitted planes would have a slope of 1. The fit results are summarized in Table 1 for threshold/gain and in Table 2 for saturation/gain. For the NSS method the slopes were close to one and the r-squared values were large indicating that changes in the gain, threshold and saturation were distinguished accurately. Results from SLS were also very good, although slightly less accurate, while the H-K results were much worse.

In all the Monte-Carlo simulations we used MOESP automatic order selection method which is described in [117], [116]. The order of the linear system was always selected correctly as 2, however, as also stated in [117], [116], manual inspection must always be performed.

Simulation studies validate the new method for identification of stretch reflex model and shows that it is more reliable compared to the other non-parametric algorithms and the original subspace method for systems of this type. In the future it will be of interest to determine whether this improved performance is also observed for different types of dynamics (e.g. band-pass, high pass).

4.6 Experimental Results

4.6.1 Methods

We evaluated the performance of the algorithm under practical conditions by using it to estimate the dynamic relation between ankle velocity and reflex EMG in the *triceps surae* TS muscle. This relation has been modeled previously as a Hammerstein system involving a unidirectional, rate sensitive nonlinearity [158].

EMGs were recorded using single differential surface Delsys electrodes supplied with the Bagnoli Systems. The reference electrode was a DermaSport placed on the subject's left knee which was immobilized during the experiment. EMG signal was amplified 1000 times and then band-passed at 20-2000 Hz using a custom-made filter to remove artifacts. EMG as well as position signals were recorded using NI-4472 A/D card. Data were filtered to avoid aliasing and then sampled at 1000 Hz for 60 seconds. The anti-aliasing filter of the module filtered data at 486.3 Hz.

The experimental methods were similar to those described in [37], [65], [249] except that we used the input signal described in Section V. Five subjects were recruited and gave informed consent to the experimental procedures, which had been reviewed and approved by McGill University Institutional Review Board. The ankle joint was slightly dorsiflexed from the neutral position (+0.2 rad). The subject was asked to maintain a constant torque aided by the visual feedback of low-pass filtered ankle torque.

Data were acquired at two voluntary torque directions corresponding to: PF (5% of the Maximum Voluntary Contraction (MVC) in the plantarflexing direction, i.e., a low level contraction of the (TS)) and DF (5% of the MVC in the doresiflexing direction, i.e., a low level contraction of the *tibialis anterior* TA). Prior to analysis, we verified the recorded data to be stationary by inspecting the EMG background levels. We full-wave rectified EMG signals and removed their means. Simliar to the simulation section, we decimated all data to 100 Hz for analysis purposes.

In the Hammerstein cascade, the distribution of the gain is arbitrary between the static nonlinearity and the linear element [252]. We opted to assign the gain to the linear element and fix the gain of the nonlinearity to one. This was achieved by fitting the nonlinear element with (4.29) to give estimates of threshold and slope. Next, we divided the coefficients of the nonlinearity by the slope of the nonlinearity and multiplied the gain of the linear element by the slope of the nonlinearity. We then calculated the gain of the linear system by integrating the IRF. Consequently, we parameterized the Hammerstein cascade by two important parameters: the threshold of the nonlinearity and overall gain of the cascade.

4.6.2 Results

Fig. 4–10 shows the Hammerstein systems estimated between the velocity and EMG for a typical subject with the new algorithm. Qualitatively, the estimated models were similar to previous results - the nonlinearities both demonstrate a uni-direction rate sensitivity while the IRFs were dominated by a sharp peak at about 40 ms [158].

The estimated order of the linear system was 6 for 3 trials and 5 for the other 7 trials. The %VAF of the identification was 90% for PF and 54% for DF for this subject. The identification %VAF was 84 ± 7% and 66 ± 9% for PF and DF conditions respectively for all five subjects. We attribute the decreases in %VAF in DF to the lower gain and increased threshold associated with the changes from PF to DF. As a result of these changes, the responses became much smaller; indeed the power of the predicted output for PF was more than 13 times larger than that for DF. Consequently, the effect of noise and non-reflex EMG activity would become relatively more important. It is unlikely that the decrease resulted from un-modelled dynamics since fitting a parallel-cascade model [99] to the residuals did not account for any variance.

The previous studies modeled reflex EMG nonlinearity with a half-wave rectifier, i.e., a threshold at zero [158]. Consequently, we also calculated the prediction %VAF of a Hammerstein model whose nonlinearity is a half-wave rectifier to validate our new models. The prediction %VAF was comparable to the identified nonlinearities for PF condition which shows that in this case, the reliability of the half-wave rectifier and the identified nonlinearity is almost similar. However, in DF condition, the prediction %VAF of the half-wave rectifier was always smaller than our identified models.

What is of most interest is the changes observed with the torque direction. During plantarflexing contractions, when TS was active, the threshold was close to 0 and the IRF amplitude was large which is consistent with previous findings [65]. In contrast, during dorsiflexing contractions, when TA was active, the amplitude of

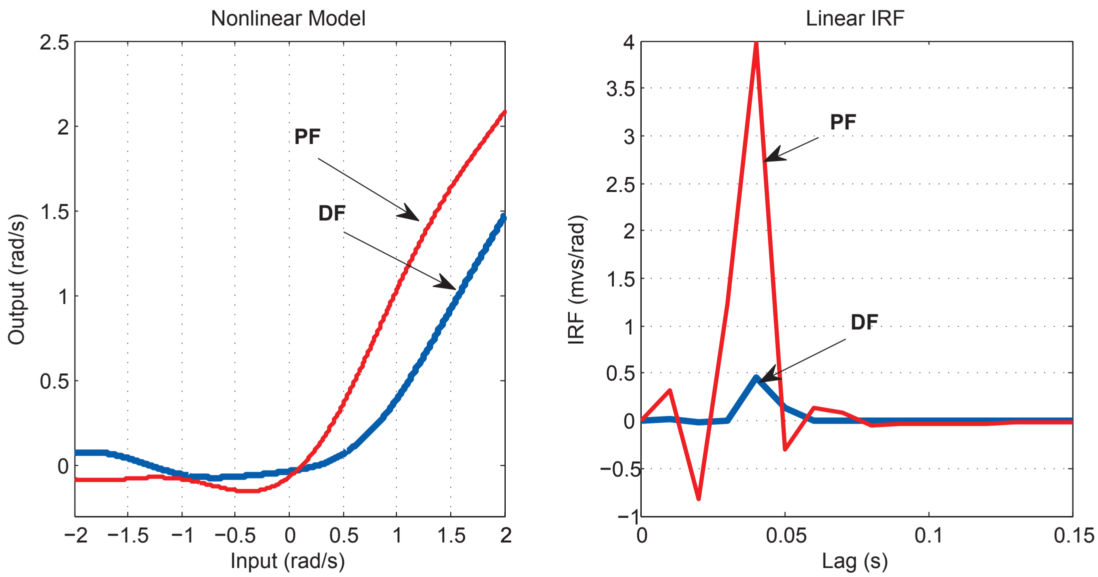

Figure 4–10: Hammerstein models estimated from reflex EMG at two different torque directions.

the IRF decreased and the threshold was higher than during the TS contraction. Fig. 4–11 shows the result. It is evident that the threshold was always larger in DF condition and the gain was always smaller compared to PF for all subjects.

4.7 Discussion and Conclusion

This paper describes a new MOESP-based algorithm for identification of Hammerstein systems. Its major advantage over previous Hammerstein MOESP-based algorithms [118], [122], is that it yields independent estimates of the linear dynamics and the static nonlinearity. This gives explicit information on the coefficients of nonlinearity and the state-space model of the linear component. Consequently, it is straightforward to compute the shape of the nonlinearity and the IRF of the linear dynamics which are needed to interpret the significance of parameter changes.

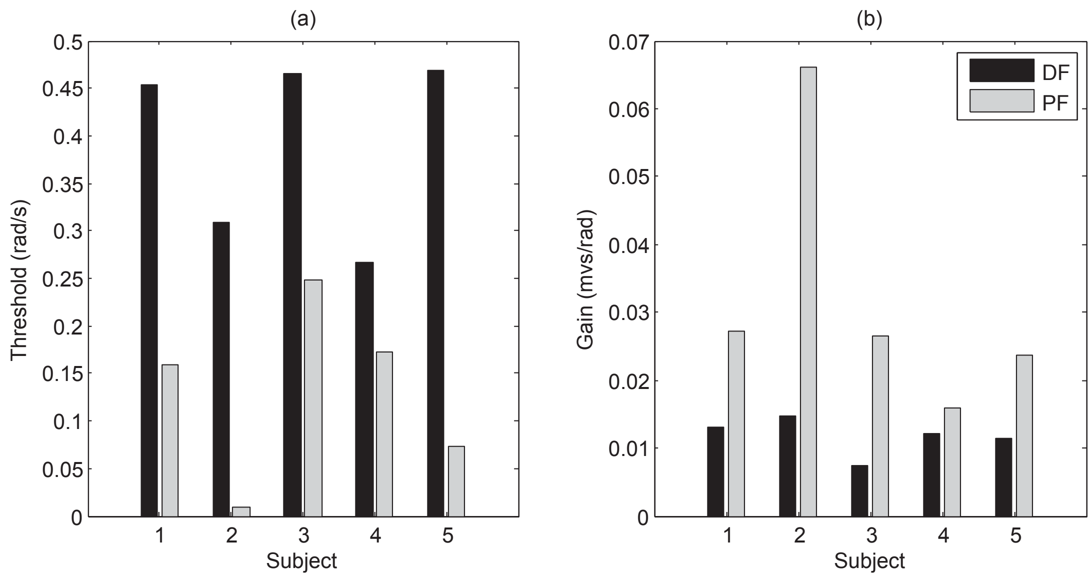

Figure 4–11: Changes in threshold and gain in PF and DF operating point: (a) threshold; (b) gain.

One of the advantages of the MOESP over other parametric identification approaches is that it estimates the linear system order prior to the parameter identification. Consequently, in MOESP the only required *a priori* information about the system is an upper-bound on its order.

The simulation results demonstrated that the new algorithm successfully distinguished changes in the threshold and saturation of the nonlinearity from changes in the gain of the linear subsystem (see Fig. 4–8 and 4–9). They further demonstrated that the NSS method was more robust to additive output noise than OSS, SLS and H-K Hammerstein algorithms. Thus, the subspace estimates were more accurate and had lower variances (i.e. lower biases and less noisy, Fig.4–5 and 4–7) especially at low SNRs. The SLS also gave good results at at high SNRs (Fig. 4–5). However, SLS solves a nonlinear optimization and it is not guaranteed to converge. Indeed, the Monte-Carlo studies showed that this was the case; the %VAF had a bimodal distribution; one mode corresponding to large values of %VAF with high probability and a second mode to lower %VAFs corresponding to trials where the algorithm did not converge. In contrast, NSS always converged and the %VAF distribution was unimodal.

Our simulation results demonstrated that the NSS method performed much better than other methods for SNRs less than 0 dB. SNRs as low as this may be infrequent for single input systems but will occur frequently for multiple input systems since when estimating the response to one input, the responses to the other inputs will appear as noise. For example, in the identification of reflex stiffness at the ankle, torques generated as a result of intrinsic mechanisms will appear as noise [37] resulting in effective SNRs of much lower than 0dB.

Thus, the new method was more robust than other methods; this is likely because it has fewer free parameters to estimate in the case of reflex stiffness identification. We described the linear component of the Hammerstein system with a state-space model whose number of parameters depends on the system order. In contrast, non-parametric methods modeled it as an IRF whose length depends on the system memory. The original subspace algorithm used an over-parameterized model which will always have more parameters compared to our minimal formulation. The total number of unknown parameters in our model is $(m+1)^2+n$ whereas for the original subspace method is $m^2+m+mn+n$. Thus, the new formulation reduced the number of parameters by $mn-m-1$. The total number of unknown parameters in the SLS formulation is $n_{\text{lags}}+n$, where n_{lags} is the memory of the system. The difference of $n_{\text{lags}} - (m+1)^2$ between number of parameters in SLS and NSS formulation is significant for a low-pass filter with relatively large memory compared to its order.

The new method presented here modeled the static nonlinearity by a polynomial. Future work is required to develop a method for determining which expansion to use and the optimal order for the nonlinearity.

The experiment studies in this paper were intended as proof-of-principle experiments. We did not examine reflex stiffness directly since the reflex torque cannot be measured directly (only the sum of the voluntary, reflex and intrinsic torques can be measured). Consequently, we used EMG as the output since it is an indicator of muscle activity and is not related to the intrinsic response. The results showed that the method works well with experimental data and gave results consistent with previous EMG studies [158], [65].

Previous studies have shown that reflex stiffness changes dramatically with the operating point defined by mean ankle position and muscle activation level [65]. In these experiments the nonlinearity was assumed to be constant so all changes were modeled as changes in the parameters of the linear component. Here, the results show that the nonlinearity also changes as a function of the operating point, in this case the muscle activation. The amplitude of the IRF changed with torque level as expected - it was the larger when TS was active, and lower when TA was active. Interestingly, the threshold behaved differently, it was low when TS was active and high when TA was active. At least in this case, it appears the the reflex gain and threshold varied independently and consequently, characterizing the reflex by its gain alone may not be appropriate. Much additional work on the identification of stretch reflex (position-EMG system) needs to be carried out to map out how the gain and threshold change with operating point; the new algorithm provides the means to do so.

An important application of this work will be to incorporate it into our parallel-cascade methods for the identification of systems with parallel-cascade structures. We demonstrated its utility for reflex stiffness in our simulations. However, since the reflex torque cannot be measured independently, a parallel-cascade method is required to decompose the intrinsic and reflex components prior to the identification of parameters [37]. In theory, by incorporating the intrinsic path into the system model, one can integrate this method into the identification of the parallel-cascade structures. This will become useful in studying joint stiffness with a compliant load. Previous studies have shown that subspace method has the great advantage of providing accurate estimates in the presence of feedback and/or input noise, conditions under which other correlation based methods give biased results [122].

Implementation of the new method is straightforward. The MOESP method that we used is well-known to the system identification community and an implementation is available as part of the SIM toolbox, Delft University of Technology [117]. The remainder consists of solving two least-squares in an iterative manner followed by normalization. The MATLAB routine for the new method can be downloaded from our website as part of the new release of NLID toolbox.

The new method has some limitations too. It is difficult to include delay in a state-space model. Thus, for the subspace identification methods to work, the value of the delay has to be known. Moreover, we showed that since the IRF model has many parameters, its identification is less robust than the state-space identification. However, for a complex linear dynamics with short memory, the IRF might have fewer parameters than the state-space model and its identification might be more robust. This is because the number of parameters in the state space model grows rapidly with the system order.

CHAPTER 5
Identification of Hammerstein Systems from Short Segments of Data: Application to Stretch Reflex Identification

This paper was originally published in IFAC-PapersOnline, DOI: 10.3182/20120711-3-BE-2027.00386, from Kian Jalaleddini, Ferryl Alley, and Robert E. Kearney, 16th IFAC Symposium on System Identification, pp. 798-803, July 2012.

In Chapter 4, I developed the NSS method that identified a Hammerstein cascade from a single, stationary, long data record. In this chapter, I extend the NSS method to identify a Hammerstein cascade from multiple, short, stationary data segments. I show an application to identify reflex EMG response in ankle plantarflexor muscles during stance. This chapter is a conference paper published in the Proceedings of 16th IFAC Symposium on System Identification.

Authors: Kian Jalaleddini, Ferryl Alley, Robert E. Kearney

Proceedings: 16th IFAC Symposium on System Identification, pp. 798-803, July 2012.

5.1 Abstract

It is not trivial to acquire data under stationary conditions from biomedical systems since they frequently show time-varying/switching behaviour. It is often possible to acquire short transients of stationary data and repeat the experiment many times. However, initial conditions may contribute substantially to transient response and must therefore be accounted for explicitly. This paper presents a subspace algorithm for identification of Hammerstein systems from short transients of data that estimates the initial condition of each transient and the parameters of the nonlinearity, as well as a state-space model for the linear part. A previously developed subspace short transient algorithm suffers from two issues. Firstly, all transients had to be equal lengths, and secondly the algorithm provided an over-parameterized model of the Hammerstein system rather than an individual model for each component of the cascade. We resolved the first issue by introducing a new formulation of the problem and the second one by developing an iterative method to separate the estimated parameters. Simulation results on Hammerstein model of reflex joint stiffness show the algorithm is capable of identifying an acceptable model even with corrupted noisy data. We also use this algorithm on a set of experimental data acquired from one subject.

5.2 Introduction

A Hammerstein system consists of a static memory-less nonlinear system followed by a linear dynamic. Many biologicals systems have a Hammerstein structure such as ankle joint stretch reflex stiffness and neural integrator model of the human *vestibular-ocular reflex* (VOR). For more detailed structure of the models see [37] and [87].

Identification of a Hammerstein system is an important problem and has been extensively investigated in the past years. Some methods model the nonlinear part with a polynomial and the linear part with an *impulse response function* (IRF). The algorithm then iterates between estimation of these two subsystems until it converges to the optimum minimum, [249], [252], [96] and [253]. Other algorithms model the nonlinearity by a spline which are found to be useful in presence of hard nonlinearities, and the linear part by an IRF [92] [250]. Another class of algorithms formulates the nonlinear element by a polynomial and the linear part by a state-space model. [118], [263] developed subspace algorithms to estimate this structure formulation. The algorithm proposed in [118] works by transforming the *single-input-single-output* SISO Hammerstein system to a *multi-input-single-output* MISO linear system and then uses linear subspace method to estimate a state-space model for the Hammerstein structure.

Most system identification methods use a single data record. During the whole length of recorded data, the system is assumed to be stationary, i.e. time-invariant. The general rule is that the longer the data record, the more the identification will be accurate in the presence of noise. However, in biomedical systems, it is difficult to maintain stationary conditions for long periods. The system may show time-varying behaviour, for example stretch reflex dynamic parameters change with postural sway during quite stance [264]. Other systems such the vestibulo-ocular reflex (VOR) switch between two different modes at random times [265]. As a result while it is difficult to obtain long data record under stationary condition, often it is possible to obtain many short data records during which the system is stationary. It may also be possible to break a long data record displaying time-varying behaviour, into a series smaller segments during which the system is time-invariant.

Initial conditions are an important issue to the system response for short transients, [266]. Depending on the memory of the system, the effect of initial conditions will die out after some time. It is a standard practice in identification of biological systems to consider the system in steady state mode and neglect the effect of initial conditions. However, when only short transients of data are recorded, the effect of initial condition must be considered since they play an important role at the onset of recording.

Our laboratory has extended the Hammerstein identification proposed in [118] to estimation of the parallel-cascade model of joint stiffness from short transients of data (see [267]). This algorithm requires all transients of data to be the same length (a condition that is often difficult to meet). It then identifies a state-space model for the total Hammerstein system in which each parameter of the state-space model is dependent on both the nonlinearity and the linear component. This model predicts the output very well but is unable to describe each individual element of the Hammerstein model. Therefore, after identification, the input and noise free

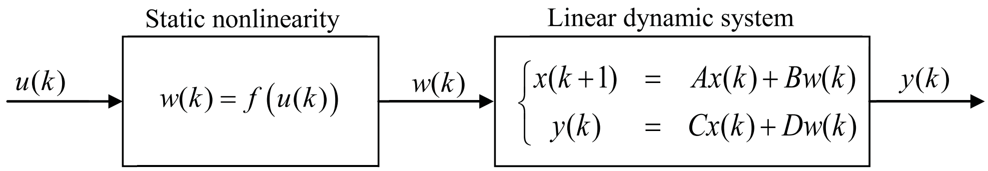

Figure 5–1: Hammerstein system model.

predicted output was analyzed using other Hammerstein algorithms to acquire insight about each component of the system.

In this paper, we introduce a new formulation of the problem where each transient may have different length. We then use the results of [253] and [252] to develop separation and estimation the unknown parameters which are the initial condition of each transient, the coefficients of the polynomial nonlinearity, and the state-space model of the linear system.

The plan of the paper is as follows: Section 5.3 formulates the Hammerstein model and define the optimization problem. Section 5.4 presents the new identification algorithm. Section 5.5 provides some simulation results on a model of stretch reflex. Section 5.6 describes its application to an experiment on identification of velocity/EMG system. Section 5.7 gives a summary and some concluding remarks.

5.3 Problem Formulation

This section presents a formulation for the Hammerstein cascade where the nonlinearity is approximated by finite-order polynomial and the linear system by its state-space model.

Consider the SISO Hammerstein system shown in Fig. 5-1. The output to the system is $u(k)$, the output of the nonlinearity is $w(k)$ and the output of the system is $y(k)$. We can represent any static nonlinearity with a finite-order polynomial with a given accuracy as follows, [5]:

$$w(k) = f\left(u(k)\right) \simeq \sum_{i=1}^{n} \alpha_i g_i\left(u(k)\right) \tag{5.1}$$

where $g_i(\cdot)$ is the i^{th} basis function and α_i is the corresponding coefficient.

We further assume p transients of input-output data is recorded where each transient has a distinct number of data points, i.e., the j^{th} transient $(j \in 1, \cdots, p)$ has t_j samples:

$$u_j = [u_j(0), \cdots, u_j(t_j - 1)]$$
$$y_j = [y_j(0), \cdots, y_j(t_j - 1)]$$

where $u_j(k)$ and $y_j(k)$ are the input and output of the j^{th} transient at discrete time k.

Assume that the linear component is stable and of order m so that it can be described by the state-space model for the data in the j^{th} transient:

$$\begin{cases} x_j(k+1) & = Ax_j(k) + Bw_j(k) \\ y(k) & = Cx_j(k) + Dw_j(k) + v_j(k) \end{cases} \tag{5.2}$$

where, $x_j(k) \in \mathbb{R}^m$ is the state vector and, $A_{m\times m}$, $B_{m\times 1}$, $C_{1\times m}$ and $D_{1\times 1}$ are the corresponding matrices and $v_j(k)$ is the additive noise signal which is uncorrelated with the input. Let the elements of B and D be:

$$B = [b_1, \cdots, b_m]^T$$
$$D = [d] \tag{5.3}$$

Define the vectors:

$$\alpha = [\alpha_1, \cdots, \alpha_n]^T \tag{5.4}$$

$$U_j(k) = [g_1(u_j(k)), \cdots, g_n(u_j(k))]^T \tag{5.5}$$

Substitute (4.4) and (5.5) in (5.2) to yield:

$$\begin{cases} x_j(k+1) & = Ax_j(k) + B_\alpha U_j(k) \\ y_j(k) & = Cx_j(k) + D_\alpha U_j(k) \end{cases} \tag{5.6}$$

where:

$$B_\alpha = \begin{bmatrix} b_1\alpha_1 & \cdots & b_1\alpha_n \\ \vdots & \ddots & \vdots \\ b_m\alpha_1 & \cdots & b_m\alpha_n \end{bmatrix} \tag{5.7}$$

$$D_\alpha = \begin{bmatrix} d\alpha_1 & \cdots & d\alpha_n \end{bmatrix} \tag{5.8}$$

The parameterization (5.7) and (5.8) is not unique and has one degree of freedom, i.e, for any arbitrary scalar β, the vectors βB, βD and $\beta^{-1}\alpha$ will generate the same matrices B_α and D_α. Consequently, to provide a unique solution we will require that the first non-zero element of the vector α is positive and:

$$|| [\alpha_1, \cdots, \alpha_n]^T || = 1 \tag{5.9}$$

where $|| \cdot ||$ is the two norm.

The state vector of the j^{th} transient at discrete time k is given by:

$$x_j(k) = A^k x_j(0) + \sum_{\tau=0}^{k-1} A^{k-1-\tau} BU_j(\tau) \tag{5.10}$$

The first term of (5.10) reflects the initial conditions while the second term states how the past input signal accumulated in the memory of the system. Substituting (5.10) in the state-space model (5.6), gives the output of the system at time k, [116]:

$$y_j(k) = CA^k x(0) + \sum_{\tau=0}^{k-1} A^{k-1-\tau} BU_j(\tau) + DU_j(k) + v(k) \tag{5.11}$$

Definition 1 *A Hankel matrix constructed from a discrete signal $o(k)$ has constant block anti diagonal shape:*

$$O_{i,j,k} = \begin{bmatrix} o(i) & \cdots & o(i+k-1) \\ \vdots & & \vdots \\ o(i+j-1) & \cdots & o(i+j+k-2) \end{bmatrix} \tag{5.12}$$

Using this, (5.11) can be cast into the following data equations:

$$\begin{aligned} Y_{0,s,N_j} = & \underbrace{\begin{bmatrix} C \\ CA \\ \vdots \\ CA^{s-1} \end{bmatrix}}_{\text{Extended observability}} [x_j(0) \cdots x_j(N_j-1)] \\ & + \begin{bmatrix} D & 0 & \cdots & 0 \\ CB & D & \cdots & 0 \\ \vdots & \vdots & \ddots & \vdots \\ CA^{s-2}B & CA^{s-3}B & \cdots & D \end{bmatrix} U_{0,s,N_j} + V_{0,s,N_j} \end{aligned} \tag{5.13}$$

where, U_{0,s,N_j}, Y_{0,s,N_j} and V_{0,s,N_j} are the Hankel matrices of the j^{th} transient input, output and the noise signals. s is the Hankel size which must be greater than the linear system order and N_j is defined according to cover all the recorded data points:

$$N_j = t_j - s + 2 \tag{5.14}$$

The data equation (5.13) for each transient record can be generalized for all the recorded transients as follows:

$$\begin{aligned} Y_{0,s,N_1,\cdots,N_p} &= \begin{bmatrix} Y_{0,s,N_1} & \cdots & Y_{0,s,N_p} \end{bmatrix} \\ &= \begin{bmatrix} C \\ CA \\ \vdots \\ CA^{s-1} \end{bmatrix} [x_1(0) \cdots x_1(N_1-1) \cdots x_p(0) \cdots x_p(N_p-1)] \\ &+ \begin{bmatrix} D & 0 & \cdots & 0 \\ CB & D & \cdots & 0 \\ \vdots & \vdots & \ddots & \vdots \\ CA^{s-2}B & CA^{s-3}B & \cdots & D \end{bmatrix} U_{0,s,N_1,\cdots,N_p} + V_{0,s,N_1,\cdots,N_p} \end{aligned} \tag{5.15}$$

Concatenate all the recorded transients:

$$U = [U_1(0) \cdots U_1(t_1) \cdots U_p(0) \cdots U_p(t_p - 1)] \tag{5.16}$$

$$Y = [y_1(0) \cdots y_1(t_1) \cdots y_p(0) \cdots y_p(t_p - 1)] \tag{5.17}$$

5.4 Identification Algorithm

The *past-input multivariable Output Error State Space* PI-MOESP algorithm estimates the linear system order and the A and C state-space matrices from the constructed input signal U and the measured output Y. The PI-MOESP algorithm works by first eliminating the effect of the input signal from the data equation (5.15) leaving only the observability matrix and the noise term. This is achieved by right multiplying the data equation (5.15) by the orthogonal complement of the input signal. The past input signal is a good candidate for *instrumental variable* (IV) since it is not correlated with the noise signal but is correlated with the rest of the data equation. Right multiplying the data equation with this IV leaves only the extended observability matrix which can be used to estimate A and C matrices. For details of the MOESP algorithm see [102].

The goal of the identification is now to estimate the remaining state-space matrices (B and D), the initial conditions ($x_j(0)$, $j \in 1 \cdots p$), and the parameters of the nonlinearity (α). Using the Kronecker product, the output of the j^{th} transient (5.11) is ([116]):

$$\begin{aligned} y_j(k) = &\underbrace{\left[\sum_{\tau=0}^{k-1} U_j^T(\tau) \otimes CA^{k-1-\tau}\right]}_{\Lambda_j(k)} \operatorname{vec}(B_\alpha) \\ &+ \left[U_j^T(k)\right] \operatorname{vec}(D_\alpha) + CA^k x_j(0) + v_j(k) \end{aligned} \tag{5.18}$$

where vec$(\cdot)$ generates a vector by stacking the columns of the matrix $(\cdot)$:

$$\begin{aligned} \operatorname{vec}(B_\alpha) &= \left[b_1\alpha_1 \cdots b_m\alpha_1 \cdots b_1\alpha_n \cdots b_m\alpha_n\right]^T \\ \operatorname{vec}(D_\alpha) &= \left[d\alpha_1 \cdots d\alpha_n\right]^T \end{aligned} \tag{5.19}$$

Define the matrix $\Gamma = [\Gamma_1 \cdots \Gamma_p]$ as follows:

$$\Gamma_1 = \begin{bmatrix} C \\ \vdots \\ CA^{t_1-1} \\ 0 \\ \vdots \\ 0 \end{bmatrix},\ \Gamma_2 = \begin{bmatrix} 0 \\ \vdots \\ 0 \\ C \\ \vdots \\ CA^{t_1-1} \\ 0 \\ \vdots \\ 0 \end{bmatrix}, \cdots \Gamma_p = \begin{bmatrix} 0 \\ \vdots \\ 0 \\ C \\ \vdots \\ CA^{t_1-1} \end{bmatrix} \tag{5.20}$$

Define matrix Λ as follows:

$$\Lambda = \begin{bmatrix} 0 \\ U_1(0)C \\ \vdots \\ \sum_{\tau=0}^{t_1-2} U_1(\tau)CA^{t_1-2-\tau} \\ 0 \\ U_p(0)C \\ \vdots \\ \sum_{\tau=0}^{t_p-2} U_p(\tau)CA^{t_p-2-\tau} \vdots \end{bmatrix} \tag{5.21}$$

Now, the data equation (5.18) can be expressed in the following matrix form:

$$Y = \Phi\theta \tag{5.22}$$

where θ contains the unknown parameters:

$$\theta = [x_1(0) \ \cdots \ x_p(0) \ \mathrm{vec}\,(\mathrm{B}) \ \ \mathrm{vec}\,(\mathrm{D})]^{\mathrm{T}} \tag{5.23}$$

and the regressor Φ is constructed from Γ and Λ:

$$\Phi = [\Gamma_1 \ \Gamma_2 \ \cdots \ \Gamma_p \ \Lambda \ U] \tag{5.24}$$

The unknown parameter θ set can be re-written as follows:

$$\theta = [\zeta_1 \ \cdots \ \zeta_p \ b_1\alpha_1 \ \cdots \ b_m\alpha_1 \ \cdots \ b_1\alpha_n \ \cdots \ b_m\alpha_n \ d\alpha_1 \ \cdots \ d\alpha_n]^T \tag{5.25}$$

Assuming α_i is non-zero, ζ_i is:

$$\zeta_i = \frac{x_i(0)}{\alpha_1} \tag{5.26}$$

It is evident that the least-squares problem (5.22) is not a linear least-squares problem. Therefore, the iterative algorithm suggested in [252] is applied to separate and estimate the unknown parameters. This iterative algorithm separates the unknown parameters into two sets:

$$\begin{aligned} \theta_A &= [\alpha_1 \ \cdots \ \alpha_n]^T \\ \theta_B &= [\zeta_1 \ \cdots \ \zeta_p \ b_1 \ \cdots \ b_m \ d]^T \end{aligned} \tag{5.27}$$

Now, if the set θ_A is held fixed, the output is a linear function of the other set θ_B and similarly, if the set θ_B is held fixed, the output is again a linear function of the parameter set θ_A. In other words, we break the problem of separation and estimation of the unknown parameters into two linear least-squares problem which are solved iteratively. Suppose the iteration index is k. Below, we state these two problems:

Problem I: Suppose the parameter set θ_A^k is known and fixed. The following problem states the linear dependency of the output on θ_B^k:

$$Y = \Phi \underbrace{\begin{bmatrix} \alpha_i^{k-1} & & 0 & 0 & \cdots & 0 & 0 \\ \vdots & \ddots & \vdots & \vdots & \ddots & \vdots & \vdots \\ 0 & & \alpha_i^{k-1} & 0 & \cdots & 0 & 0 \\ 0 & \cdots & 0 & \alpha_1^{k-1} & \cdots & 0 & 0 \\ \vdots & \ddots & \vdots & \vdots & \ddots & 0 & 0 \\ 0 & \cdots & 0 & 0 & \cdots & \alpha_1^{k-1} & 0 \\ & \vdots & & & \vdots & & \vdots \\ 0 & \cdots & 0 & \alpha_n^{k-1} & \cdots & 0 & 0 \\ \vdots & \ddots & \vdots & \vdots & \ddots & 0 & 0 \\ 0 & \cdots & 0 & 0 & \cdots & \alpha_n^{k-1} & 0 \\ 0 & & & \cdots & & 0 & \alpha_1^{k-1} \\ & & & & & & \vdots \\ 0 & & & \cdots & & 0 & \alpha_n^{k-1} \end{bmatrix}}_{\Phi_B^{k-1}} \underbrace{\begin{bmatrix} \zeta_1^k \\ \vdots \\ \zeta_p^k \\ b_1^k \\ \vdots \\ b_m^k \\ d^k \end{bmatrix}}_{\theta_B^k} \tag{5.28}$$

The following linear least-squares estimates θ_B^k:

$$\theta_B^k = \left[(\Phi\Phi_B^{k-1})^T (\Phi\Phi_B^{k-1}) \right]^{-1} (\Phi\Phi_B^{k-1}) Y \tag{5.29}$$

Problem II: Suppose the parameter set θ_B^k is known and fixed. The following problem states the linear dependency of the output on θ_A^k:

$$Y = \Phi \underbrace{\begin{bmatrix} \zeta_1^{k-1} & \cdots & 0 \\ \vdots & \vdots & \vdots \\ \zeta_p^{k-1} & \cdots & 0 \\ b_1^{k-1} & \cdots & 0 \\ \vdots & \vdots & \vdots \\ b_m^{k-1} & \cdots & 0 \\ \vdots & \vdots & \vdots \\ 0 & \cdots & b_1^{k-1} \\ \vdots & \vdots & \vdots \\ 0 & \cdots & b_m^{k-1} \\ d^{k-1} & \cdots & 0 \\ & \ddots & \\ 0 & \cdots & d^{k-1} \end{bmatrix}}_{\Phi_{\alpha^{k-1}}} \underbrace{\begin{bmatrix} \alpha_1^k \\ \vdots \\ \alpha_n^k \end{bmatrix}}_{\theta_A^k} \tag{5.30}$$

The following linear least-squares estimates θ_B^k:

$$\theta_A^k = \left[(\Phi\Phi_A^k)^T (\Phi\Phi_A^k) \right]^{-1} (\Phi\Phi_A^k) Y \tag{5.31}$$

Identification Algorithm: The identification algorithm iterates between problem 1 and problem 2 to estimate the model parameters. If the initial point is set properly, the global convergence of the algorithm is guaranteed:

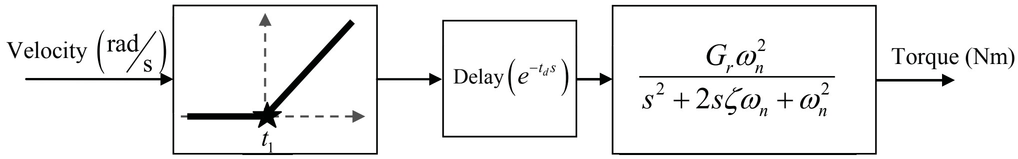

Figure 5–2: Hammerstein model of reflex stiffness.

1. Set $k = 1$ and $\theta_A^0 = \begin{bmatrix} 1 & \cdots & 1 \end{bmatrix}^T$.
2. Construct the matrix Φ_B^{k-1} and following (5.29), solve problem 1.
3. Construct the matrix Φ_α^k and following (5.31), solve problem 2.
4. Let q be the sign of the first non-zero element of θ_A^k, i.e., $s = \text{sgn}\left(\alpha^{\text{k}}\right)$ and perform the following normalization:

$$\begin{aligned}\theta_A^k &\leftarrow \frac{\theta_A^k s}{\left\|\theta_A^k\right\|} \\ \theta_B^k &\leftarrow \theta_B^k s \left\|\theta_A^k\right\| \end{aligned} \tag{5.32}$$

5. Evaluate the *sum of squared errors* $(\text{SSE})^{\text{k}}$ between the predicted output and the recorded output. If the relative improvement in SSE is greater than a threshold, replace k by $k + 1$ and go to step 2. Otherwise, terminate.

5.5 Simulation Results

We assessed the algorithm's performance using a small signal model of the stretch reflex stiffness of the human ankle joint (Fig. 5-2). The input to this model is joint angular velocity and the output is the reflex torque. Previous studies modeled this stretch response by a Hammerstein system. The nonlinearity resembles a threshold and the linear component is modeled by a second-order (or sometimes third-order) low-pass filter, [65] and [37].

To generate the velocity input signal, we sampled a uniform distribution with minimum and maximum of $[-20,\ 20]$ (rad/s) at each 150 ms. We integrated this desired input signal to derive the desired angular position. The desired position signal was then passed through a low pass filter with cut-off frequency of 20Hz to mimic the actuator dynamics. We then calculated the derivative of the output of the actuator as the simulated velocity input signal to the model.

We simulated this model in MATLAB Simulink at 1 KHz and the resulting signals were decimated to 100 Hz before further analysis. We simulated 20 transients of input-output where the length of each transient was selected from a random distribution with the mean of 1000 ms. The initial condition of each transient was set to be a random as well. Realizations of Gaussian, white noise were added to the output to simulate experimental noise; the amplitude of the noise was adjusted to generate the 10dB *signal to noise ratio* (SNR).

Fig. 5-3 shows the simulated input-output data for 4 transients along with the predicted output using the algorithm and Fig. 5-4 shows the identified Hammerstein system. The *variance accounted for* (VAF) was 95.6% with respect to the noise free output which shows an excellent consistency between the predicted torque and the simulated one.

5.6 Experimental Results

We studied the behaviour of the stretch reflex during normal upright standing when the subject is unconstrained. During upright standing, a subject sways forwards and backwards freely, in a random, time-varying pattern. The general pattern of a subject's postural sway was identified by low pass filtering the ankle torque at

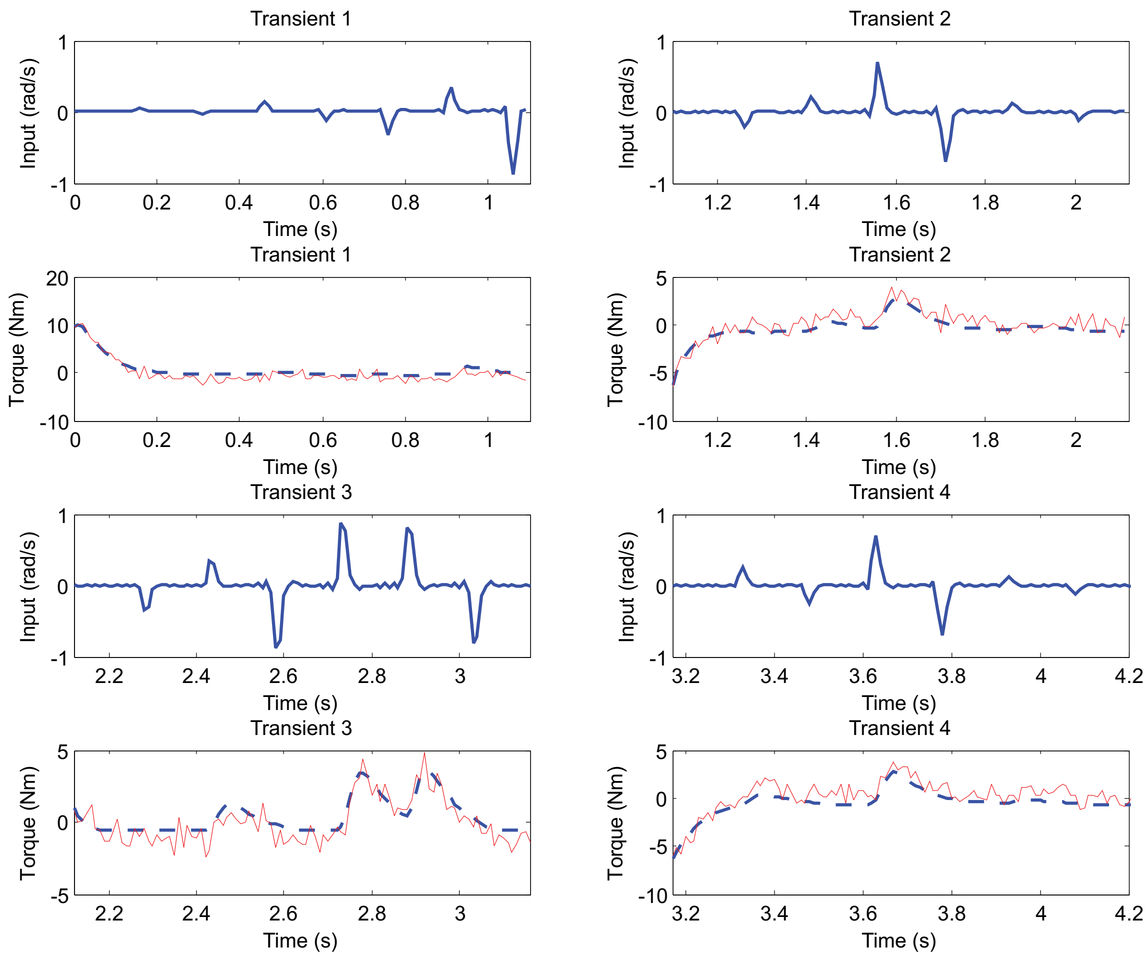

Figure 5–3: Simulated input-output of 4 transients along with the predicted output.

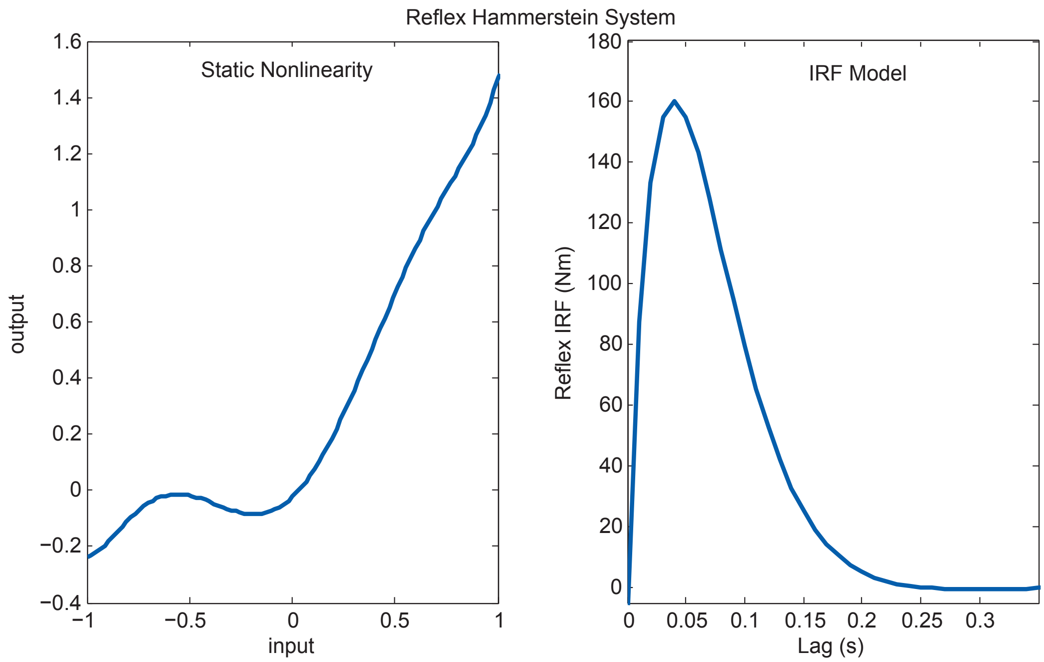

Figure 5–4: Identified Hammerstein system model.

1Hz. Several postural states were identified for which the ankle torque was at different levels. We expect that the postural state of a subject will affect the ankle joint operating point; during a forward lean state, the subject's *triceps surae* (TS) are stretched and will contract. In contrast, during a backward lean, the TS are relaxed. The state of the ankle joint will affect the behaviour of the stretch reflex response.

The experiment paradigm is described elsewhere but both feet were perturbed with two uncorrelated PRBS position input signals, [268]. Fig. 5-5(a) shows the postural torque for a typical subject, where two different states were identified as a postural forward lean, state A, occurring at mean postural torques less than -2Nm, and a postural backward lean, state B, occurring at mean postural torques greater than +2Nm. From the full data record, several state transients were identified, each having a different length and occurring at several points during the record length.

The stretch reflex response has been described in terms of its reflex stiffness; however, it can also be described in terms of the muscle activation EMG response. This reflex EMG response can be represented by a Hammerstein system between input velocity and output EMG recorded from the TS muscle, [158]. Therefore, to determine the stretch reflex system at each postural state, the input velocity, Fig. 5-5(b), and the output EMG, Fig. 5-5(c), were segmented according to the selected transients from each postural State. Fig. 5-5 (b-1) and (c-1) illustrate a single transient, where we have identified a segment of input velocity and output EMG, respectively, according to the duration of the forward lean state A identified from the postural torque. We identified three transients from state A and four transients from state B, each with a different duration.

We used the algorithm presented herein to estimate the stretch Hammerstein system for each state. The predicted models for state A (53.5%VAF) and state B (62.8%VAF) are both presented in Fig. 5-6. The Hammerstein system identifies a static nonlinearity resembling a half wave rectifier and a linear impulse response function with a peak occurring at 40ms. The half-wave rectifier is consistent with the physiological stretch reflex response, which is activated by positive input velocities, or by inputs that stretch the TS muscle. Furthermore, the peak of the impulse response function is consistent with the neural conduction delay of the reflex monosynaptic pathway presented in previous literature. Comparing each state's linear impulse response function, state A has a higher peak than state B. This indicates that the reflex response is stronger when the subject has a postural forward lean, which is consistent with prior ankle joint dynamic stiffness studies while subjects were at supine position, [65].

5.7 Conclusions

We developed a subspace method to identify a Hammerstein model from short transients of input-output data record. Compared to previous methods, it has two advantages. First, we can now apply it to transients with different lengths and second, it fully separates the parameters of the nonlinearity from the linear component model. These two features make the algorithm a powerful tool for analysis of biomedical systems where the system dynamics change/switch during the data record. Simulation analysis show excellent identification in presence of additive noise. Experimental results show that the algorithm was able to identify the half-wave rectifier static nonlinearity and linear dynamic structure. This is consistent with results presented in previous stretch reflex studies using alternative methods, [249]. Note that the example presented here used only two states but the same principle can be applied to distinguish many different states of the system.

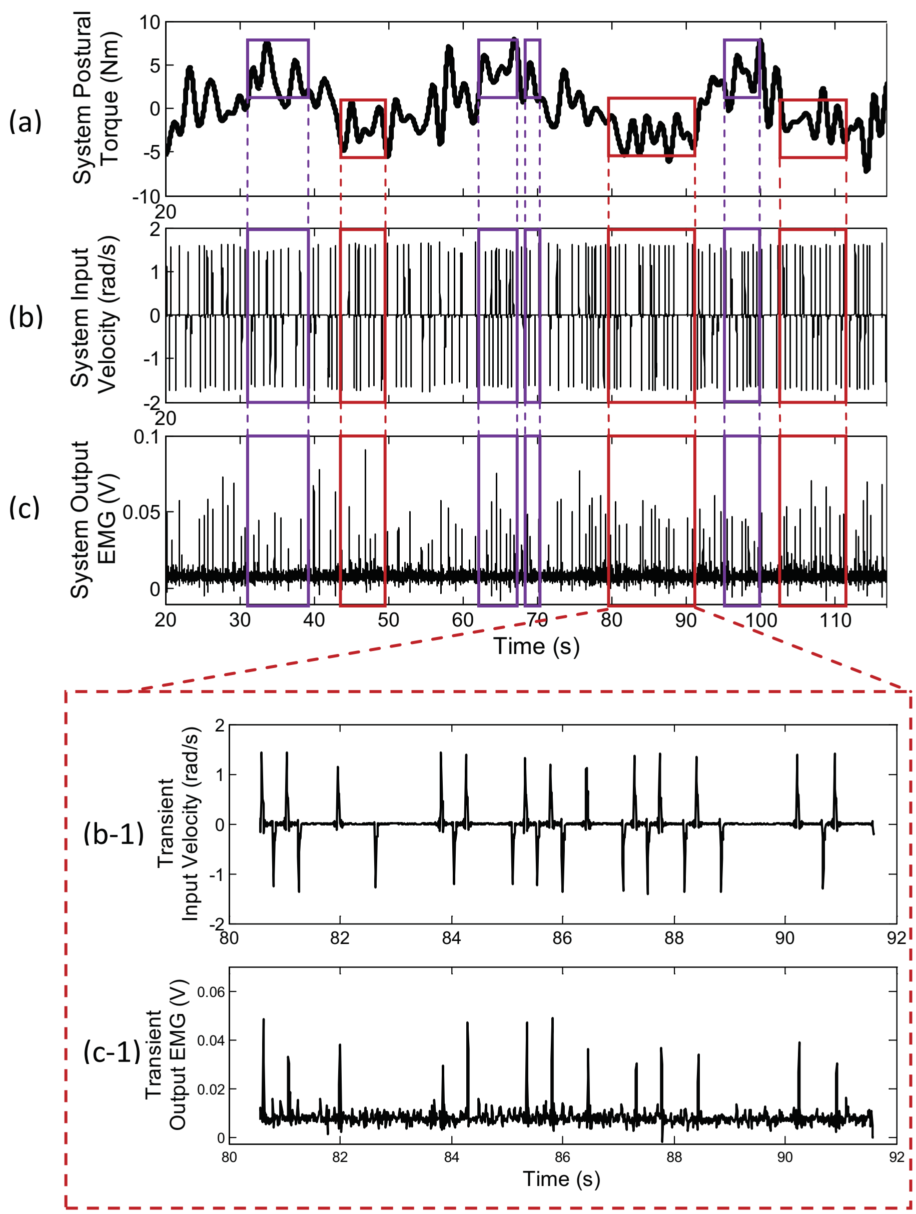

Figure 5–5: (a) System's postural torque; (b) system input velocity; (c) system output lateral Gastrocnemius EMG.

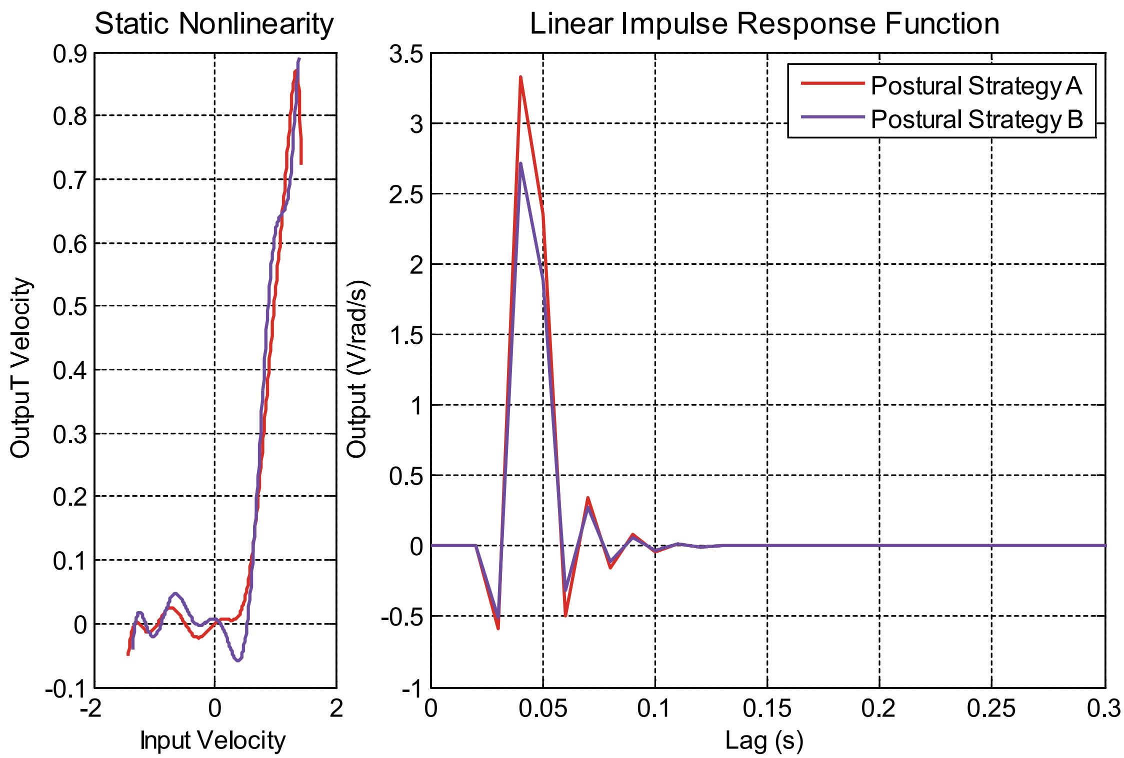

Figure 5–6: Estimated stretch reflex EMG system between input velocity and output lateral Gastrocnemius EMG; State A corresponds to a forward lean postural state and State B corresponds to a backward lean postural state

CHAPTER 6
A Subspace Approach to the Structural Decomposition and Identification of Ankle Joint Dynamic Stiffness

In Chapter 4 and 5, I developed methods for identification of Hammerstein structures. In this chapter, I extend the Hammerstein identification method to the full parallel-cascade model of joint stiffness from a single, stationary, long data record. I show an application to identify stiffness at the ankle joint as a function of activation direction. This chapter is a journal paper that has been submitted to the IEEE Transactions on Biomedical Engineering.

Authors: Kian Jalaleddini, Ehsan Sobhani Tehrani and Robert E.Kearney

Journal: Submitted to IEEE Transactions on Biomedical Engineering.

6.1 Abstract

This paper presents a Structural Decomposition SubSpace (SDSS) method for the identification of ankle joint dynamic stiffness, modelled as a parallel-cascade structure with intrinsic and reflex pathways. First, it formulates a novel state-space representation for the parallel-cascade structure with a concise parameter set that provides a direct link between the state-space representation matrices and the parallel-cascade parameters. Secondly, it presents a subspace method for the identification of the new state-space model that involves two steps: (*i*) the decomposition of the intrinsic and reflex pathways contributions; (*ii*) the identification of an impulse response model of the intrinsic pathway and a Hammerstein model of the reflex pathway. Extensive simulation studies demonstrate that SDSS has significant performance advantages over other methods. Thus, SDSS was more robust under high noise conditions, converging where other methods failed; it was more accurate, giving estimates with lower bias and random errors than other methods. The practical application of SDSS was demonstrated by applying it to experimental data from human subjects at three muscle activation levels. Together, the simulation and experimental results demonstrate that SDSS accurately decomposes the intrinsic and reflex torques and provides accurate estimates of physiologically meaningful parameters. It should be a valuable tool for studying joint stiffness under functionally important conditions.

6.2 Introduction

Joint dynamic stiffness defines the dynamic relation between the position of a joint and the torque acting about it [19]. It plays an important role in control of posture since it determines the resistance to external perturbations. Moreover, it is important in movement since it defines the load the *central nervous system* (CNS) must control [269, 10, 11, 12]. Consequently, its identification is of great importance and has been extensively investigated [230, 37, 221, 65, 270, 185, 75].

Kearney et al. proposed a parallel-cascade model for ankle joint stiffness [37], that was valid for small variations of position and torque about fixed operating points. The model comprises two parallel pathways: intrinsic stiffness modelled as a linear dynamic system and reflex stiffness modelled as a *block oriented nonlinear* (BONL) structure consisting of the cascade of linear dynamic and a static nonlinear blocks [85]. The total joint torque is the sum of intrinsic and reflex torques (Fig.6–1).

Identification of the parallel-cascade stiffness model is challenging since there is no access to the intrinsic and reflex torques separately, i.e. only their sum can be measured. Thus, intrinsic and reflex torques must be decomposed from the measured torque as part of the identification procedure. Moreover, the noise is large and colored since during the estimation of one pathway, the output of the other pathway appears as noise in addition to measurement noise.

The *parallel-cascade* (PC) method described in [37] decomposes the torques iteratively by estimating the intrinsic and reflex pathways alternatively using non-parametric techniques. Our laboratory has successfully employed PC to study ankle joint stiffness in both healthy and pathological subjects and showed how intrinsic and reflex stiffnesses modulate with the operating point [65, 135]. A real-time implementation of the PC was used to demonstrate that subjects could voluntarily modulate their stiffness [167].

Despite its utility, the PC method has some shortcomings. First, it is based on an iterative procedure that is not guaranteed to converge; indeed it does fail when the noise is large. Second, the Impulse Response Function (IRF) used to model the reflex linear dynamics has many free parameters which reduces the method's robustness to noise [271]. Third, it is a correlation based method and so will give biased results when position and torque are connected via a feedback, as will be the case when the joint interacts with a compliant load [185, 272].

To address these issues, we have explored the use of state-space models and a parametric, subspace identification method, *Multivariable Output Error State-sPace* MOESP. Zhao et al. formulated a state-space model for the parallel-cascade stiffness structure and showed how it could be identified using the MOESP method [122]. This method which we will call original *SubSpace* (SS) throughout this paper, is not iterative, gives reliable results with both open- and closed-loop data, and produces models with excellent predictive abilities.

However, this state-space representation: (*i*) was over-parameterized which reduces the robustness of the identification procedure to noise [273]; (*ii*) parameters were not directly related to the elements of the parallel-cascade model which makes it difficult to interpret the physiological significance of the identified models [271]; and

(iii) modelled the intrinsic stiffness pathway with a simple second-order mass-spring-damper (IBK) structure that could not capture more complex dynamics that might arise from the muscle tendon complex structure and/or fixation dynamics [206].

This paper addresses these limitations by extending Zhao's method in three ways. Firstly, it reformulates the state-space model based on our previous work on Hammerstein systems ([271]), to have many fewer parameters, each directly related to the underlying parallel-cascade elements. Secondly, it represents the intrinsic dynamics by a two-sided IRF to account for more complex dynamics of this pathway. Thirdly, it develops a *Structural Decomposition SubSpace* (SDSS) method that estimates all elements of the parallel-cascade model individually.

The paper plan is as follows: Section 6.3 formulates the problem. Section 6.4 develops the SDSS identification algorithm. Section 6.5 evaluates the SDSS method using simulation data that closely mimic actual experimental conditions and compares its performance to those of the SS and PC methods. Section 6.6 demonstrates successful application of SDSS to experimental data. Section 6.7 provides a discussion and concluding remarks. A part of this work has been subject of a conference presentation [274].

6.3 Problem Formulation

This section formulates a state-space model for the ankle stiffness and demonstrates how each element of the parallel-cascade structure contributes to it.

Throughout this paper, vectors, matrices and scalars are shown in roman boldface uppercase, uppercase and lowercase letters respectively, the continuous time

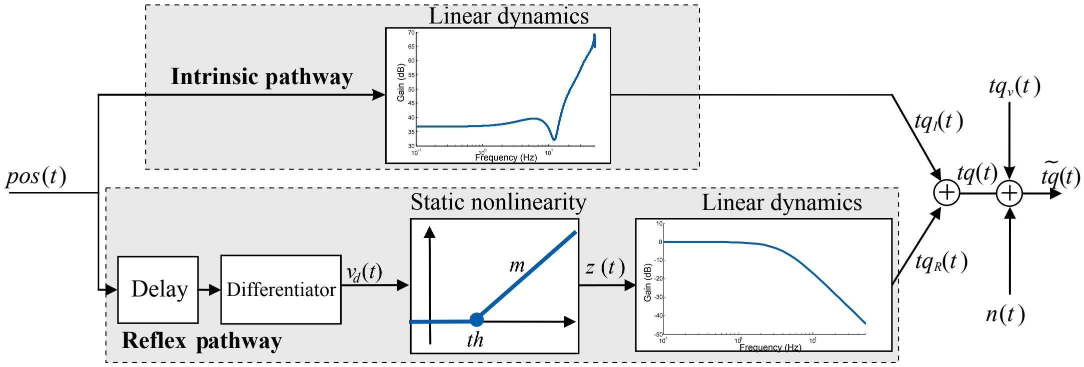

Figure 6–1: Parallel-cascade model of the ankle joint stiffness. The input is joint angular position ($pos(t)$) and the output is the joint total torque ($\tilde{tq}(t)$). The intrinsic pathway is modelled by a linear system (high-pass filter), and the reflex pathway modelled as a cascade of a delay operator, a differentiator, a static nonlinear element (threshold-slope) followed by a linear element (low-pass filter). The measured output torque ($\tilde{tq}(t)$) is the sum of intrinsic ($tq_I(t)$), reflex ($tq_R(t)$) and voluntary ($tq_v(t)$) torques and measurement noise ($n(t)$).

argument by t, the discrete time argument by k. The symbol $\tilde{(\cdot)}$ indicates the value of $(\cdot)$ contaminated by additive noise, and $\hat{(\cdot)}$ is its estimate.

Fig. 6–1 shows the parallel-cascade model of ankle joint stiffness which is a *single-input-single-output* (SISO) nonlinear structure. We will use this model in discrete time and transform it to a *multi-input-single-output* (MISO) linear system to take advantage of linear identification techniques.

6.3.1 Intrinsic stiffness

Model the intrinsic stiffness pathway with a two-sided IRF, $h_i(\tau)$, whose length, T_{Max}, is less than the reflex delay, which is assumed to be known: $T_{Max} \leqslant \Delta$ samples.

Thus, the convolution sum gives the intrinsic torque $tq_I(k)$:

$$
\begin{aligned}
tq_I(k) &= \sum_{\tau=-T_{Max}}^{T_{Max}} h_i(\tau) pos(k-\tau) = \mathbf{\Theta}_I^T \mathbf{U}_I^T(k) \\
\mathbf{\Theta}_I &= \begin{bmatrix} h_i(-T_{Max}) & \cdots & h_i(T_{Max}) \end{bmatrix}^T \\
\mathbf{U}_I(k) &= \begin{bmatrix} pos(k-T_{Max}) & \cdots & pos(k+T_{Max}) \end{bmatrix}
\end{aligned}
\tag{6.1}
$$

where, $\mathbf{U}_I(k)$ is constructed from the sampled position input, and $\mathbf{\Theta}_I$ comprises the unknown IRF coefficients.

6.3.2 Reflex Stiffness

Reflex stiffness has a BONL structure consisting of a differentiator, a delay operator (Δ samples), followed by a Hammerstein model, i.e. a cascade of a static nonlinearity and a dynamic linear system. The static nonlinearity is often modelled by a rectifier and the linear component by a second-order ([37]) or third-order ([65, 135]) low-pass filter.

Numerically, calculate the delayed velocity $v_d(k)$ from the recorded sampled position and approximate the output of the nonlinearity, $z(k)$, using a basis function expansion of order p on $v_d(k)$:

$$
\begin{aligned}
z(k) &= \sum_{j=1}^{p} \lambda_j g_j\left(v_d(k)\right) = \mathbf{\Lambda}^T \mathbf{U}_R^T(k) \\
\mathbf{\Lambda} &= \begin{bmatrix} \lambda_1 & \cdots & \lambda_p \end{bmatrix}^T \\
\mathbf{U}_R(k) &= \begin{bmatrix} g_1\left(v_d(k)\right) & \cdots & g_p\left(v_d(k)\right) \end{bmatrix}
\end{aligned}
\tag{6.2}
$$

where $\mathbf{U}_R(k)$ is constructed based on the basis expansion terms, and $\mathbf{\Lambda}$ comprises its unknown weights.

Represent the reflex linear dynamics by a state-space model of unknown order (m) with the unknown state-space matrices $A_R \in \mathbb{R}^{m\times m}$, $B_R \in \mathbb{R}^{m\times 1}$, $C_R \in \mathbb{R}^{1\times m}$ and $D_R \in \mathbb{R}^{1\times 1}$:

$$\begin{cases} \mathbf{X}_R(k+1) & = A_R\mathbf{X}_R(k) + \mathbf{B}_R z(k) \\ tq_R(k) & = C_R\mathbf{X}_R(k) + \mathbf{D}_R z(k) \end{cases} \tag{6.3}$$

where $\mathbf{X}_R(k)$ is the state vector and:

$$\mathbf{B}_R = \begin{bmatrix} b_1 & \cdots & b_m \end{bmatrix}^T$$
$$\mathbf{D}_R = [d] \tag{6.4}$$

Using (6.2) and (6.3), the MISO state-space model for the reflex pathway is [271]:

$$\begin{cases} \mathbf{X}_R(k+1) & = A_R\mathbf{X}_R(k) + B_{\lambda R}\mathbf{U}_R(k) \\ tq_R(k) & = C_R\mathbf{X}_R(k) + D_{\lambda R}\mathbf{U}_R(k) \end{cases} \tag{6.5}$$

where:

$$B_{\lambda R} = \begin{bmatrix} b_1\lambda_1 & \cdots & b_1\lambda_p \\ \vdots & & \vdots \\ b_m\lambda_1 & \cdots & b_m\lambda_p \end{bmatrix}$$
$$D_{\lambda R} = \begin{bmatrix} d\lambda_1 & \cdots & d\lambda_n \end{bmatrix} \tag{6.6}$$

6.3.3 Total Stiffness

The MISO linear state-space model for the total ankle joint stiffness is:

$$\begin{cases} \mathbf{X}_R(k+1) & = A_T \mathbf{X}_R(k) + B_T \mathbf{U}_T(k) \\ \tilde{tq}(k) & = C_T \mathbf{X}_R(k) + D_T \mathbf{U}_T(k) + tq_v(k) + n(k) \end{cases} \tag{6.7}$$

where $\tilde{tq}(k)$ is the recorded total torque. The intrinsic model has no state variables, so $A_T = A_R$ and $C_T = C_R$. B_T is an $m \times (p+2\Delta+1)$ matrix and D_T is a $1 \times (p+2\Delta+1)$ vector:

$$B_T = \begin{bmatrix} B_{\lambda R} & 0 & \cdots & 0 \end{bmatrix} \tag{6.8}$$

$$D_T = \begin{bmatrix} D_{\lambda R} & \mathbf{\Theta}_I^T \end{bmatrix} \tag{6.9}$$

The constructed input is:

$$\mathbf{U}_T(k) = [\mathbf{U}_R(k) \ \mathbf{U}_I(k)] \tag{6.10}$$

The sum of voluntary torque ($tq_v(k)$) and measurement noise ($n(k)$) is considered as the system's noise which is not white.

6.4 Identification Algorithm

First, use PI-MOESP with *past input* to estimate the order of the reflex dynamics and the matrices $\hat{A}_R$ and $\hat{C}_R$ using $\mathbf{U}_T(k)$ as the input, and $\tilde{tq}(k)$ as the output. This method is available in the SMI toolbox [117] and gives unbiased estimates [113].

It remains to estimate $\mathbf{\Theta}_I$, $\mathbf{B}_R$, $\mathbf{D}_R$ and $\mathbf{\Lambda}$. Express the output of the state-space model (6.7) as [116]:

$$\tilde{tq}(k) = \left[\sum_{\tau=0}^{k-1} \mathbf{U}_T^T(\tau) \otimes \hat{C}_R \hat{A}_R^{k-1-\tau}\right] vec(B_T) \qquad (6.11)$$
$$+\mathbf{U}_T^T(k) vec(D_T) + tq_v(k) + n(k)$$

where the operator vec stacks the columns of a matrix vertically and $\otimes$ is the Kronecker product. Rewrite (6.11), the data equation, for all samples:

$$\tilde{\mathbf{TQ}} = \Psi\mathbf{\Theta} + \mathbf{N} \qquad (6.12)$$

where:

$$\Psi = \begin{bmatrix} 0 & \mathbf{U}_T^T(0) \\ \vdots & \vdots \\ \sum_{\tau=0}^{N-2} \mathbf{U}_T^T(\tau) \otimes \hat{C}_R \hat{A}_R^{N-2-\tau} & \mathbf{U}_T^T(N-1) \end{bmatrix}$$

and:

$$\tilde{\mathbf{TQ}} = \begin{bmatrix} \tilde{tq}(0) & \cdots & \tilde{tq}(N-1) \end{bmatrix}^T$$
$$\mathbf{N} = \begin{bmatrix} tq_v(0) + n(0) & \cdots & tq_v(N-1) + n(N-1) \end{bmatrix}^T$$
$$\mathbf{\Theta} = [\ b_1\lambda_1 \ \cdots \ b_m\lambda_1 \ \cdots \ b_1\lambda_n \ \cdots \ b_m\lambda_n$$
$$\cdots \ d\lambda_1 \ \cdots \ d\lambda_n \ \ h_i(-T_{max}) \ \cdots \ h_i(T_{max}) \ ]^T$$

Separate the intrinsic and reflex parameter sets ($\mathbf{\Theta}_I$, $\mathbf{\Theta}_R$) and their regressors (Ψ_I, Ψ_R):

$$\tilde{\mathbf{TQ}} = \mathbf{TQ}_I + \mathbf{TQ}_R + \mathbf{N} = \Psi_I\mathbf{\Theta}_I + \Psi_R\mathbf{\Theta}_R + \mathbf{N} \qquad (6.13)$$

where:

$$\Psi_I = \begin{bmatrix} \mathbf{U}_I^T(0) \\ \vdots \\ \mathbf{U}_I^T(N-1) \end{bmatrix}, \ \mathbf{\Theta}_I = \begin{bmatrix} h_i(-T_{max}) \\ \vdots \\ h_i(T_{max}) \end{bmatrix}$$

$$\Psi_R = \begin{bmatrix} 0 & \mathbf{U}_R^T(0) \\ \vdots & \vdots \\ \sum_{\tau=0}^{N-2} \mathbf{U}_R^T(\tau) \otimes \hat{C}\hat{A}^{N-2-\tau} & \mathbf{U}_R^T(N-1) \end{bmatrix} \tag{6.14}$$

$$\mathbf{\Theta}_R = \begin{bmatrix} b_1\lambda_1 & \cdots & b_m\lambda_n & d\lambda_1 & \cdots & d\lambda_n \end{bmatrix}^T$$

6.4.1 Decomposition

Use orthogonal projections to decompose the total torque into its intrinsic and reflex components. Fig. 6–2 demonstrates the decomposition geometrically, in 2D for simplicity. The total torque is the vector sum of intrinsic and reflex torques, and noise. R_I is the range (column space) of the intrinsic torque and $R_I^{\perp}$ is its perpendicular complement. Similarly, R_R is the range of the reflex torque and $R_R^{\perp}$ is its perpendicular complement.

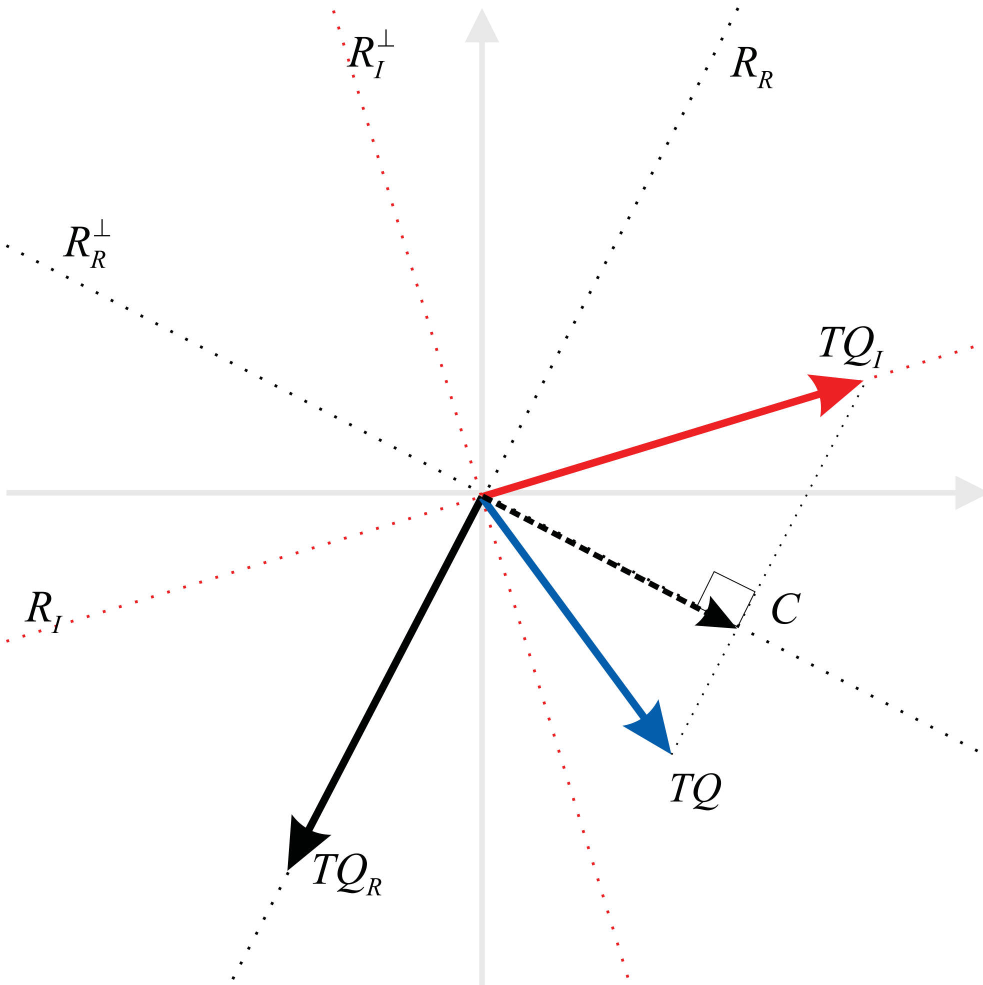

Figure 6–2: 2D geometrical representation of intrinsic, reflex and total torques and their spaces used for the decomposition of the pathways. R_I is the column space of the intrinsic torque and $R_I^\perp$ is its perpendicular complement. R_R is the column space of the reflex torque and $R_R^\perp$ is its perpendicular complement. Projections of both intrinsic and total torques onto $R_R^\perp$, the perpendicular complement of the reflex space ($R_R^\perp$), are equal to C.

Define orthogonal projection operators[1] on R_I, $R_I^{\perp}$, R_R, $R_R^{\perp}$:

$$\begin{cases} P_I & = \Psi_I \Psi_I^{\dagger} \\ P_R & = \Psi_R \Psi_R^{\dagger} \end{cases} \quad \begin{cases} P_I^{\perp} & = I - P_I \\ P_R^{\perp} & = I - P_R \end{cases}$$

where I is the identity matrix.

Fig. 6–2 makes it evident that the projection of the total torque on $R_R^{\perp}$ is equal to the projection of the intrinsic torque on $R_R^{\perp}$:

$$C = P_R^{\perp} \mathbf{T} \mathbf{Q}_I = P_R^{\perp} \tilde{\mathbf{T}\mathbf{Q}} \tag{6.16}$$

Project C on R_I:

$$P_I \left(I - P_R\right) \mathbf{T} \mathbf{Q}_I = P_I \left(I - P_R\right) \tilde{\mathbf{T}\mathbf{Q}} \tag{6.17}$$

---

[1] If the matrix A is full rank, then P_A is an orthogonal projection onto the column space of A [275]:

$$P_A = AA^{\dagger} \tag{6.15}$$

where $(\cdot)^{\dagger}$ is the pseudo-inverse operator. Any arbitrary vector $\mathbf{X}$ has a component that lies in the columns space of A, and a component that is perpendicular to this space, i.e. $\mathbf{X} = \mathbf{X}^{||} + \mathbf{X}^{\perp}$. Thus, projection of $\mathbf{X}$ on the column space of A is:

$$P_A \mathbf{X} = \mathbf{X}^{||}$$

The projection on the orthogonal complement is:

$$P_A^{\perp} = I - P_A, \; P_A^{\perp} \mathbf{X} = \mathbf{X}^{\perp}$$

where I is the identity matrix of appropriate order.

The projection of $\mathbf{TQ}_I$ on R_I is equal to itself ($P_I\mathbf{TQ}_I = \mathbf{TQ}_I$), so (6.17) becomes:

$$(I - P_I P_R)\,\mathbf{TQ}_I = P_I(I - P_R)\tilde{\mathbf{TQ}} \tag{6.18}$$

Replace $\mathbf{TQ}_I$ by $\Psi_I \mathbf{\Theta}_I$:

$$\underbrace{(I - P_I P_R)\,\Psi_I}_{F}\,\mathbf{\Theta}_I = P_I(I - P_R)\tilde{\mathbf{TQ}} \tag{6.19}$$

Now, estimate the intrinsic parameters using least squares:

$$\hat{\mathbf{\Theta}}_I = F^{\dagger} P_I(I - P_R)\tilde{\mathbf{TQ}} \tag{6.20}$$

Use $\hat{\mathbf{\Theta}}_I$ to estimate the intrinsic and reflex torques:

$$\begin{aligned}\hat{\mathbf{TQ}}_I &= \Psi_I \hat{\mathbf{\Theta}}_I \\ \hat{\mathbf{TQ}}_R &= \tilde{\mathbf{TQ}} - \hat{\mathbf{TQ}}_I\end{aligned} \tag{6.21}$$

This has decomposed the intrinsic and reflex torques besides estimating the intrinsic IRF.

Remark 2 *The decomposition is unbiased to the noise $tq_v(k) + n(k)$ if it is not correlated with the input signal. This is a realistic assumption because the system operates in open-loop. So, the noise vector is perpendicular to the intrinsic and reflex spaces and their perpendicular complements. Projecting the noisy torque ($\tilde{\mathbf{TQ}}$) in (6.16) on to $R_R^{\perp}$ and R_I will eliminate the effects of noise.*

6.4.2 Identification

Use the subspace Hammerstein method described in [271] to estimate the reflex pathway using $v_d(k)$ as input and $\hat{\mathbf{TQ}}_R$ as output. This method divides the parameter set $\mathbf{\Theta}_R$ into two subsets: the coefficients of the nonlinearity $\mathbf{\Lambda}$, and the parameters of linear system's state-space model $\mathbf{BD} = \{b_1 \ \cdots \ b_m \ d\}^T$. These are estimated iteratively as follows: For the i^{th} iteration, fix $\mathbf{\Lambda}$ and estimate $\mathbf{BD}$ using ordinary least-squares [271]:

$$\hat{\mathbf{T}}\mathbf{Q}_R = \Psi_R \underbrace{\begin{bmatrix} \lambda_1^i & \cdots & 0 \\ 0 & \ddots & 0 \\ 0 & \cdots & \lambda_1^i \\ \vdots & \ddots & \vdots \\ \lambda_p^i & \cdots & 0 \\ 0 & \ddots & 0 \\ 0 & \cdots & \lambda_p^i \end{bmatrix}}_{\Psi_{RBD}} \underbrace{\begin{bmatrix} b_1^{i+1} \\ \vdots \\ b_m^{i+1} \\ d^{i+1} \end{bmatrix}}_{\mathbf{BD}^{i+1}} \tag{6.22}$$

$$\hat{\mathbf{BD}}^{i+1} = \Psi_{RBD}^{\dagger} \hat{\mathbf{T}}\mathbf{Q}_R \tag{6.23}$$

Fix **BD** and estimate $\mathbf{\Lambda}$ using ordinary least-squares:

$$\mathbf{T\hat{Q}}_R = \Psi_R \underbrace{\begin{bmatrix} b_1^{i+1} & 0 & \cdots & 0 \\ \vdots & 0 & \cdots & 0 \\ b_m^{i+1} & 0 & \cdots & 0 \\ d^{i+1} & 0 & \cdots & 0 \\ \vdots & \ddots & \ddots & \vdots \\ 0 & 0 & \cdots & b_1^{i+1} \\ 0 & 0 & \cdots & \vdots \\ 0 & 0 & \cdots & b_m^{i+1} \\ 0 & 0 & \cdots & d^{i+1} \end{bmatrix}}_{\Psi_{R\lambda}} \underbrace{\begin{bmatrix} \lambda_1^{i+1} \\ \vdots \\ \lambda_p^{i+1} \end{bmatrix}}_{\mathbf{\hat{\Lambda}^{i+1}}} \tag{6.24}$$

$$\mathbf{\hat{\Lambda}^{i+1}} = \Psi_{R\lambda}^{\dagger} \mathbf{T\hat{Q}}_R \tag{6.25}$$

Normalize the parameters to the norm of $\mathbf{\Lambda}$ to ensure the iteration's convergence.

6.4.3 Algorithm

The following Algorithm summarizes the decomposition and identification steps.

1. Record N samples of position input and total torque output.
2. Construct the input signal $\mathbf{U}_T(k)$ using (6.10).
3. Use PI-MOESP with $\mathbf{U}_T(k)$, as the input and noisy torque, $\tilde{tq}(k)$, as the output to estimate the order of the reflex system m and the state-space matrices $\hat{A}_R$ and $\hat{C}_R$.
4. Construct the regressors Ψ_I and Ψ_R by using the estimated $\hat{A}_R$ and $\hat{C}_R$ in (6.14).

5. Estimate the intrinsic parameters ($\hat{\mathbf{\Theta}}_I$) using (6.20).
6. Estimate $\hat{\mathbf{TQ}}_R$ using (6.21).
7. Choose an arbitrary non-zero $\mathbf{\Lambda}^0$ and set $i = 0$.
8. Use linear least squares to estimate the elements of B_R and D_R (i.e. $\hat{\mathbf{BD}}^{i+1}$) from (6.23).
9. Use linear least squares to estimate the nonlinearity's coefficients (i.e. $\hat{\mathbf{\Lambda}}^{i+1}$) from (6.25).
10. Normalize the estimates to ensure convergence:

$$
\begin{aligned}
\hat{\mathbf{\Lambda}}^{i+1} &:= \frac{\hat{\mathbf{\Lambda}}^{i+1}}{||\hat{\mathbf{\Lambda}}^{i+1}||} \\
\hat{\mathbf{BD}}^{i+1} &:= \hat{\mathbf{BD}}^{i+1}||\mathbf{\Lambda}^{i+1}||
\end{aligned}
\tag{6.26}
$$

11. Simulate the model (6.22) or (6.24) with the estimated parameter sets $\hat{\mathbf{\Lambda}}^{i+1}$ and $\hat{\mathbf{BD}}^{i+1}$ to predict the reflex torque $\hat{\mathbf{TQ}}_{PR}$.
12. Terminate if there is no significant improvement in the *sum of squared errors* (SSE):

$$
\text{SSE} = \sum_{k=0}^{N-1} (\hat{tq}_{PR}(k) - \hat{tq}_R(k))^2 \tag{6.27}
$$

Otherwise, $i := i + 1$ and go to step 8.

6.5 Simulation Studies

6.5.1 Methods

The performance of the new SDSS method was evaluated using data from simulations designed to replicate important experimental conditions: realistic model and input noise sequences.

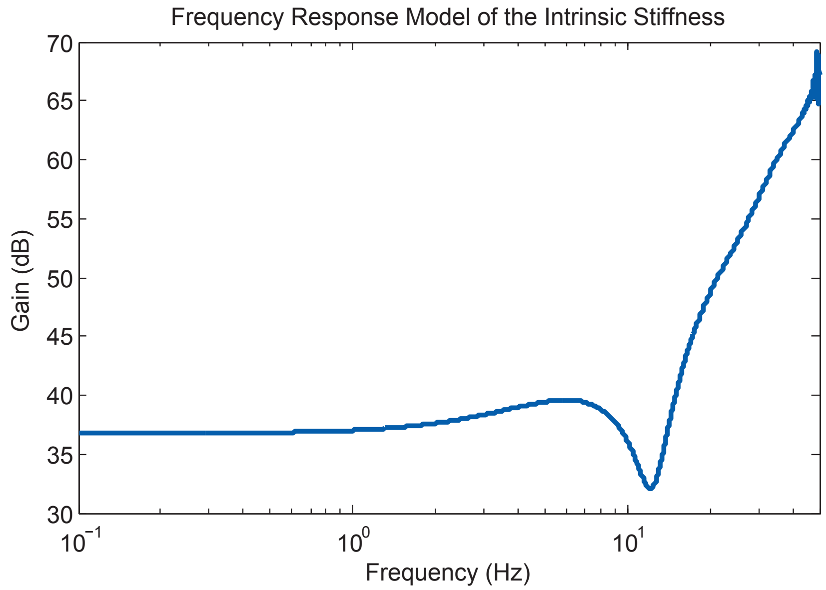

Figure 6–3: The gain of the frequency response function of the intrinsic stiffness model used in simulation studies.

Model

The model shown in Fig. 6–1 was simulated in MATLAB Simulink. The intrinsic pathway was an IRF from previous work [206] where Fig. 6–3 shows the gain of its frequency response. The reflex pathway parameters were based on those from [260]; the nonlinear element was a threshold at 0.75 rad/s, and the linear element was the second-order low-pass filter:

$$H = \frac{3347.7}{s^2 + 16.8s + 184.9} \tag{6.28}$$

Experimental Input

Characteristics of the input signal will strongly influence identification performance. Consequently, we built a library of realistic inputs by recording the position perturbations resulted when different realizations of a *piecewise constant pseudo random arbitrary level distributed signal* (PRALDS) were input to a hydraulic actuator while subjects maintained an isotonic contraction. PRALDS switches between random position levels at time intervals drawn from a uniform distribution ranging from 100 to 200ms. Thus, this input has a broad distribution of velocities needed to accurately estimate the static nonlinearity of the reflex pathway. Fig. 6–4A shows a 10s segment of a PRALDS realization. The input library contained 210 realizations, each 60s long.

Experimental Noise

Output noise is often treated as white and Gaussian when evaluating the performance of identification algorithms. However, the noise associated with the torque in stiffness identification experiments is neither white nor Gaussian [247]. Rather, it comprises (*i*) a white Gaussian component due to electronics and signal conditioning circuitries and (*ii*) a low-pass non-Gaussian component due to variations in the voluntary torque.

Consequently, to ensure that our simulations represented noise realistically, we built a library of noise signals by recording the torque generated while subjects attempted to maintain a constant muscle contraction with no position perturbation. This record will have both components of the noise. Fig. 6–4B shows a typical noise realization. The noise library comprised 210 records of voluntary torque, each 60s long.

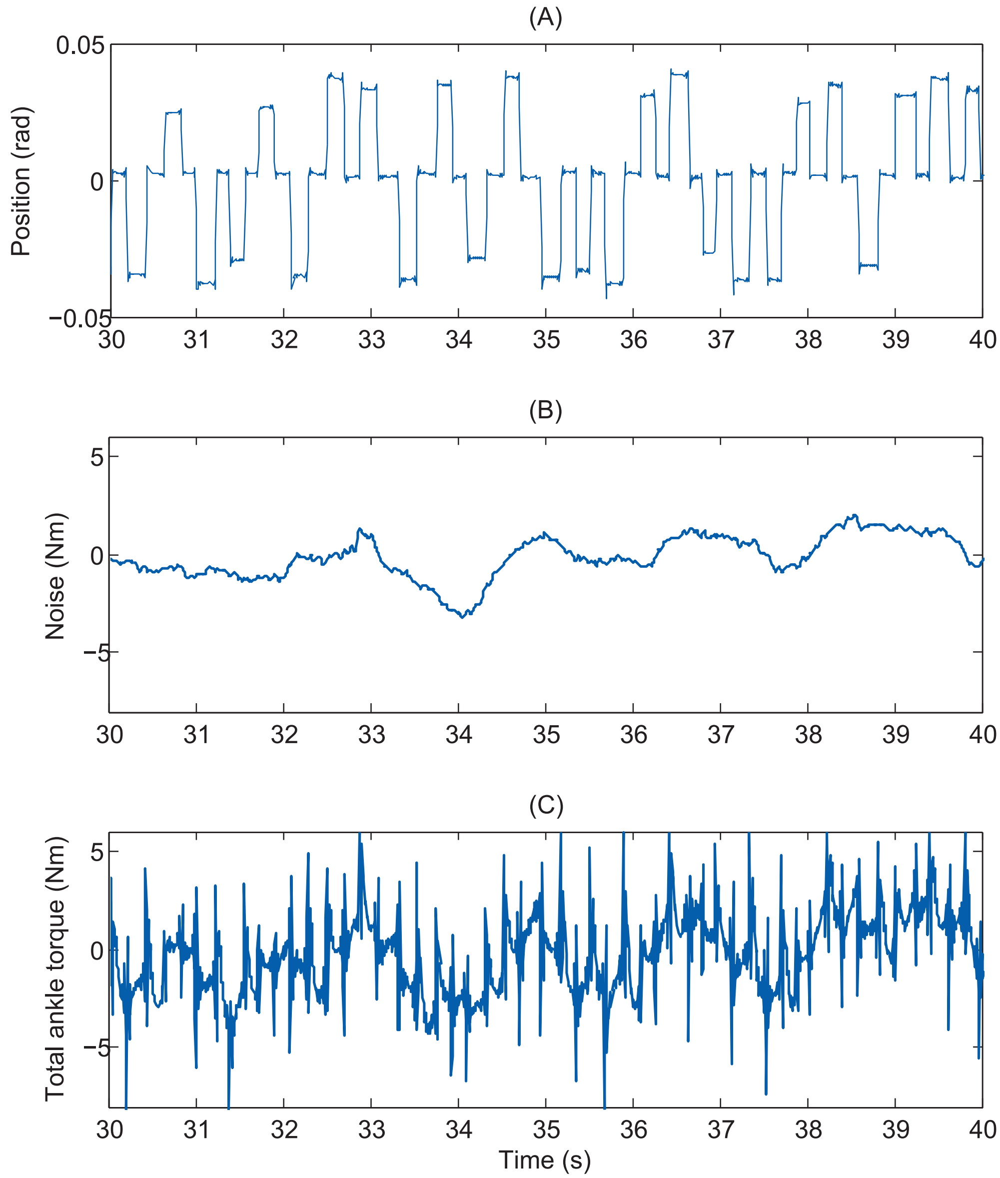

Figure 6–4: A 10 second segment of one realization of the simulated stiffness signals (SNR=10dB) (A) position input; (B) output noise; (C) total torque output (sum of intrinsic, reflex and voluntary torques and noise).

For use in simulations, each noise realization was scaled to generate the required *signal to noise ratio* (SNR) defined as:

$$\mathrm{SNR(dB)} = 10\log_{10}\frac{\sum_{k=0}^{N-1} tq^2(k)}{\sum_{k=1}^{N-1}(tq_v(k)+n(k))^2} \tag{6.29}$$

Identification

The performance of the SDSS was evaluated and compared to that of PC [37], and SS [122]. The basis functions used to describe the static nonlinearity of the reflex pathway were 12^{th}-order Tchebychev polynomial for all methods. Note that the SS method does not explicitly estimate the elements of the parallel-cascade model. Consequently SS results were not included when evaluating the accuracy with which the elements of the parallel-cascade model were estimated.

The gain of the reflex stiffness pathway can be distributed arbitrarily between its nonlinear and linear components since the intermediate signal $z(k)$ is not measured (Fig. 6–1). To ensure that the gain was distributed consistently, the gain of the linear element of the reflex pathway was set to 1 so that all the reflex gain was assigned to the nonlinear element. The linear element gain was estimated as the average of the gain in the pass-band region (0-1 Hz) of its frequency response.

Monte-Carlo studies

The algorithms' performance was evaluated in a series of Monte-Carlo simulations. For each series, 1000 trials were simulated with the same system parameters but with different realizations of the input and noise signals, selected randomly from the two input-noise libraries. Simulations were done at 1kHz and signals were decimated to 100 Hz for analysis. Fig. 6–4 shows 10s of the input, noise, and output+noise from a typical simulation trial.

Errors in estimates

SDSS and PC provide direct estimates of all parallel-cascade elements. Two types of errors were used to quantify the accuracy [276]:

$$\begin{cases} \text{bias error} & = \rho - E(\hat{\rho}) \\ \text{random error} & = E\left(\hat{\rho} - E(\hat{\rho})\right)^2 \end{cases} \tag{6.30}$$

where ρ is the true system and $\hat{\rho}$ is its estimate. The bias error provides a measure of how well the estimates retrieve the true value on average and the random error is a measure of the trial-to-trial variance of the estimates.

Index of the Probability of Superior Performance (IPSP)

The simulation gave access to the noise free intrinsic and reflex torques. So, the different methods could be compared in terms of how well their estimates predicted the noise free torques. This was measured in terms of %VAF, between the simulated and predicted intrinsic and reflex torques:

$$\begin{aligned} \%\text{VAF}_{\text{intrinsic}} &= 100\left(1 - \frac{var(\hat{tq}_I(k) - tq_I(k))}{var(tq_I(k))}\right) \\ \%\text{VAF}_{\text{reflex}} &= 100\left(1 - \frac{var(\hat{tq}_R(k) - tq_R(k))}{var(tq_R(k))}\right) \end{aligned}$$

The %VAF distributions were not Gaussian, so the significance of differences between methods was evaluated nonparametrically. For each Monte-Carlo trial, the difference between the %VAF of the SDSS and each of the other methods was computed. The percentage of times that this difference was positive was defined as the: *index of the probability of superior performance* (IPSP). Thus, an IPSP of 0 would indicate that the SDSS predictions were always worse than those of the other method; an IPSP of 0.5 would mean that predictions of the two methods performed best equally often; and an IPSP of 1 would mean that the SDSS predictions were always the best.

Decomposition Error

A %VAF less than 100 could arise from either over or underestimating the output of a pathway. To distinguish these, the difference between the true and predicted output *powers* for each pathway was examined. If a pathways is estimated correctly, this should be close to zero, values greater than zero would indicate underestimation of the pathhway and values less than zero would indicate overestimation.

6.5.2 Results

Accuracy/Precision

The first series of Monte-Carlo simulations examined the accuracy with which elements of the parallel-cascade model were estimated by the PC and SDSS methods. Noise was scaled to generate an SNR of 15dB.

Fig. 6–5 shows the estimates obtained in all Monte-Carlo trials using PC (left column) and SDSS (right column). The true values used in the simulation are shown in red. By inspection, it is evident that the SDSS estimates of all three elements are closer to the true values and are less variable than those of the PC estimates.

Fig. 6–6 presents the corresponding bias and random errors to permit a more detailed analysis. Fig. 6–6A shows that the bias error for the SDSS intrinsic pathway estimates was close to zero at all frequencies. In contrast, the bias error of PC was

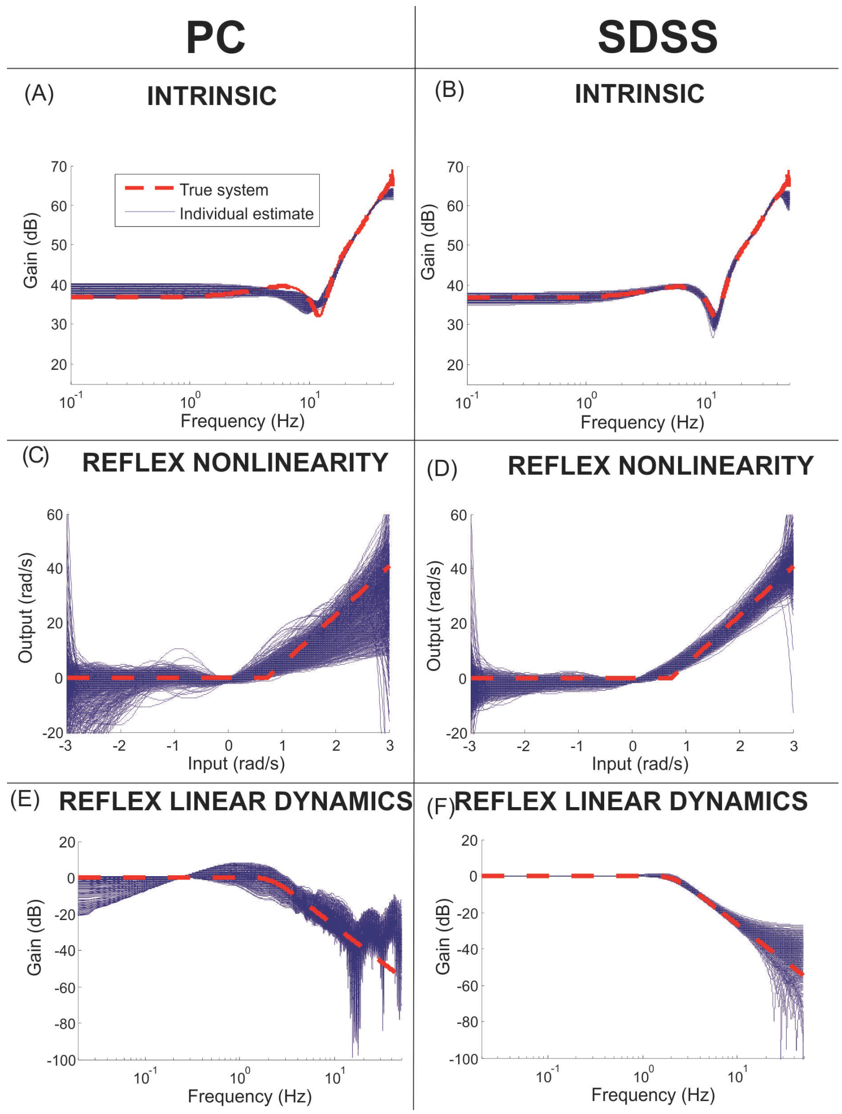

Figure 6–5: Estimates of the elements of the parallel-cascade model (blue) using the PC and SDSS methods from a Monte-Carlo simulation of 1000 trials with SNR=15dB superimposed on the true model (red). Left column: PC results; Right column: SDSS results. Estimate of the intrinsic stiffness using: (A) PC and (B) SDSS; reflex static nonlinear element using: (C) PC ;(D) SDSS; reflex linear element using: (E) PC; (F) SDSS.

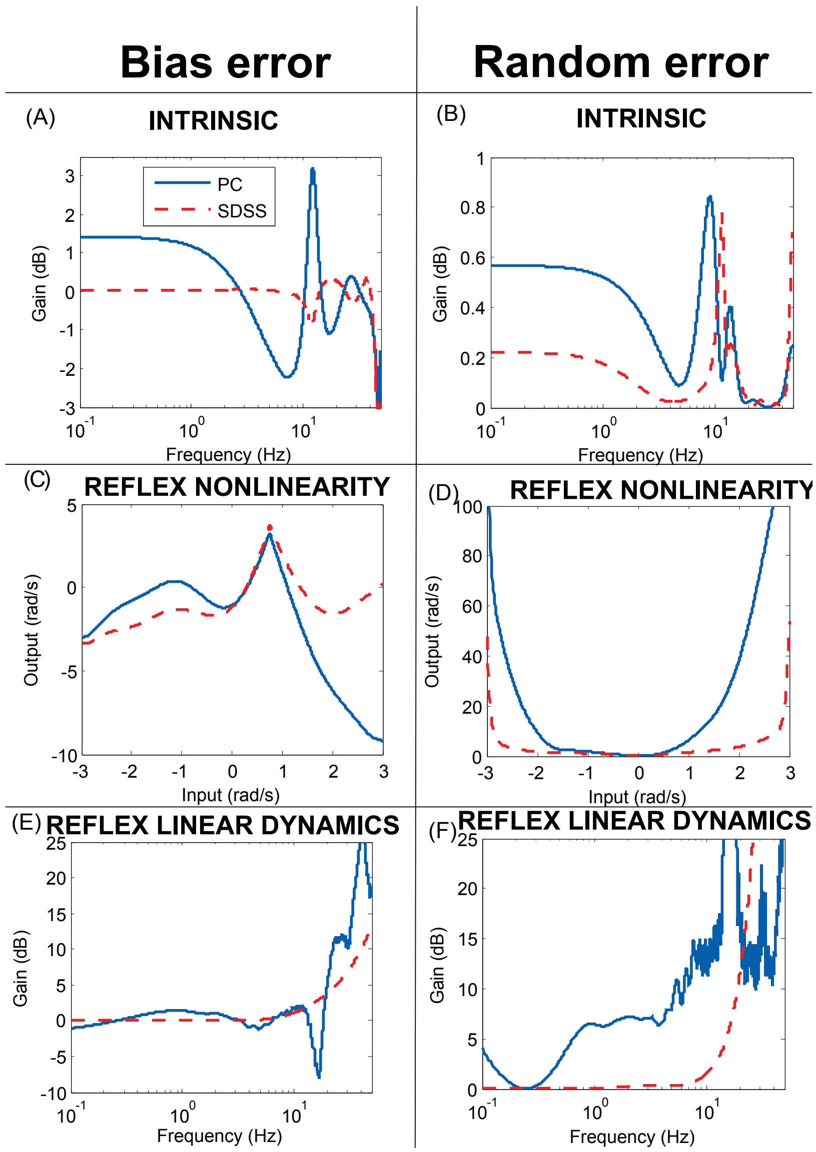

Figure 6–6: Bias and random errors in the estimates of the parallel-cascade elements using the PC (blue) and SDSS (dashed red) methods from a Monte-Carlo simulation of 1000 trials with SNR=15dB. Left column: bias error; Right column: random error. Error in the intrinsic estimates: (A) bias error and (B) random error; Error in the reflex nonlinear estimates: (C) bias error and (D) random error; Error in the reflex linear estimates: (E) bias error and (F) random error.

positive at low frequencies that indicates it overestimated the low frequency gain of the intrinsic pathway (elastic gain). The PC error peaked around 10 Hz (near the break frequency) that indicates that the pathway's break frequency was located incorrectly. Fig. 6–6B shows that the SDSS random error was also substantially lower than that of the PC method.

Fig. 6–6C,D show the estimation errors for the static nonlinearity. The bias errors of the methods were close for negative velocities where there was little reflex response. However, for positive velocities where the reflex response was larger, the PC estimates consistently underestimated the gain while the SDSS bias error was close to zero. The random errors of both estimates were near zero in the central region and increased near both ends. However, the SDSS random error stayed low over a much wider range of velocities than the PC estimates.

Fig. 6–6E,F demonstrate the estimation errors of the reflex linear element. The SDSS bias error was close to zero for frequencies lower than 10 Hz where the input had power and increased at larger frequencies. The PC bias error was also close to zero at low frequencies but always slightly larger than SDSS (Fig. 6–6E). The variability in the linear element estimates were significantly lower in SDSS estimates (Fig. 6–6F).

The large bias errors of the PC estimates suggests that the PC decomposed the intrinsic and reflex torques inaccurately. Fig. 6–7 confirms this by a box and whisker plot of the decomposition errors. Thus, the SDSS errors were distributed symmetrically about zero for both intrinsic and reflex pathways indicating that there was no consistent error. In contrast, the decomposition errors of the PC method were

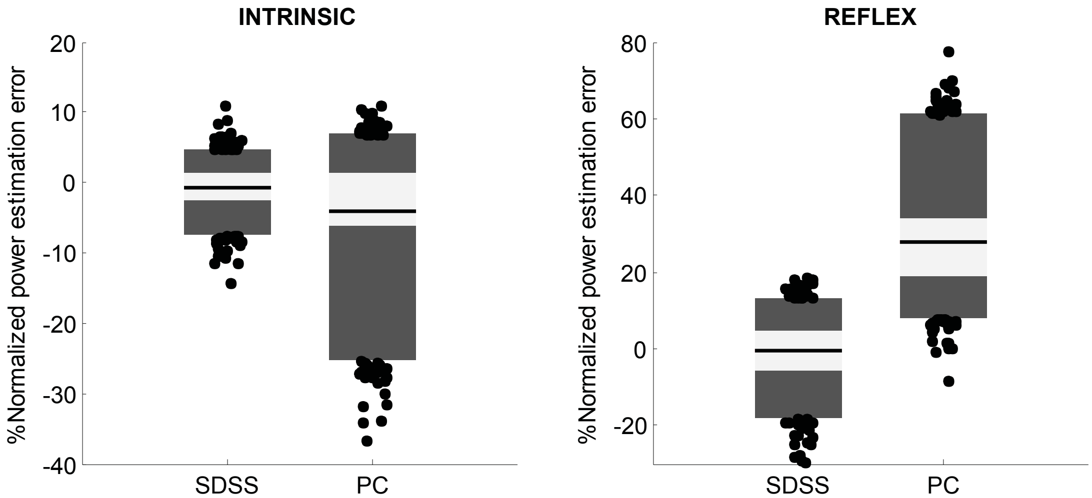

Figure 6–7: The decomposition error, difference between the true and predicted output powers for the (A) intrinsic; (B) reflex pathways. The black line shows the mean value; the light box shows the 25% and 75% percentiles, the dark box shows the 2.5% and 97.5% percentiles, and the filled circles show the residuals.

distributed asymmetrically; they were skewed to negative values for the intrinsic pathway and to positive values for the reflex pathway. Thus, the PC method consistently overestimated the intrinsic stiffness and underestimate the reflex stiffness.

Robustness

Fig. 6–8 summarizes the results of the Monte-Carlo simulation that examined the robustness of the three methods to noise at SNRs ranging from 0 to 30 dB.

Fig. 6–8A shows that for the intrinsic pathway, the SDSS estimates were the most accurate, they had the largest %VAF for all SNRs except 0 where the SS models were slightly better. IPSP values shown in Fig. 6–8C demonstrate that these differences were consistent since the SDSS accounted for the most variance with probability of 0.7 at the SNR of 5dB and close to 1 at higher SNRs.

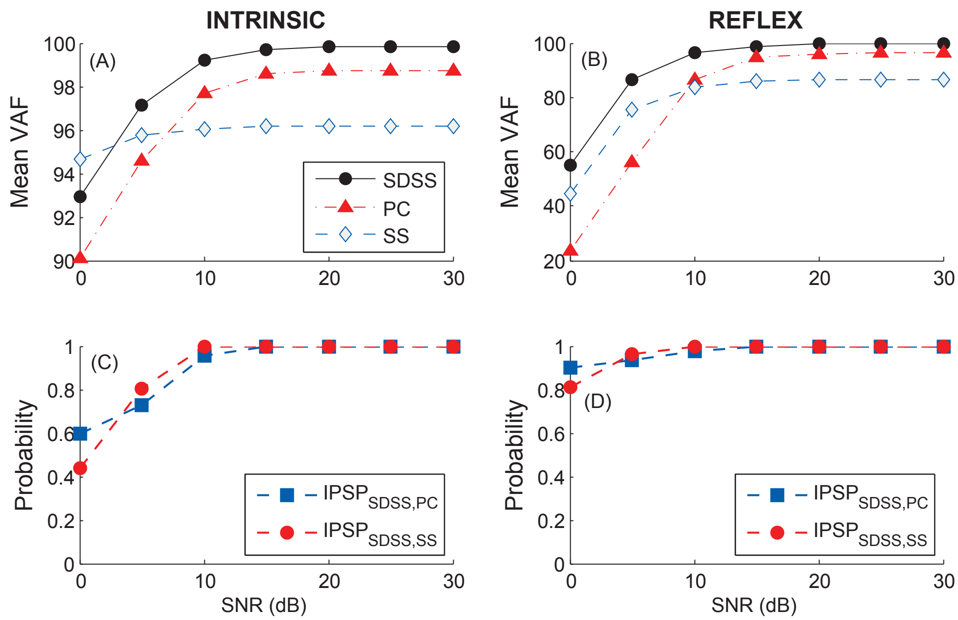

Figure 6–8: Performance of the SDSS, SS and PC as a function of SNR: (A) Mean value of $\%\text{VAF}_{\text{intrinsic}}$; (B) Mean value of $\%\text{VAF}_{\text{reflex}}$; (C) probability that the SDSS $\%\text{VAF}_{\text{intrinsic}}$ was greater than that of SS (blue) and PC (red) ; (F) probability that the SDSS $\%\text{VAF}_{\text{reflex}}$ was greater than of SS (blue) and PC(red).

Fig. 6–8B shows that for the reflex pathway, the SDSS estimates were always the most accurate having the highest %VAFs at all SNRs. The SDSS models were much better than the PC models at low SNRs. IPSP values in Fig. 6–8D confirms this; they were greater than 0.8 for all examined SNRs.

Relative contribution of intrinsic and reflex pathways

Fig. 6–9 summarizes the results of the Monte-Carlo simulation that evaluated the sensitivity of the methods to changes in the relative magnitudes of the intrinsic and reflex torques. Simulations were run using the nominal model but with reflex gains (5-75 $\frac{Nms}{rad}$) spanning the range reported for normal and spastic subjects [65, 135]. The noise level was adjusted to maintain a constant SNR of 5dB.

Fig. 6–9A shows the results for the intrinsic pathway identification. The mean %VAF for the SDSS was greater than or equal to those of the other methods at all reflex gains. IPSP values were large for low reflex gains and decreased as the reflex power increased (Fig. 6–9C). Thus, SDSS was the most accurate method for low reflex contributions while all three methods performed equally for larger reflex contribution.

Fig. 6–9B shows the results for the reflex pathway; SDSS had the largest mean %VAF. IPSP values were large and close to 1 (Fig. 6–9D) indicating that SDSS was significantly the most accurate method for the reflex pathway identification. All three methods performed poorly for the lowest reflex gain but SDSS degraded the least.

6.6 Experimental Studies

The practical application of SDSS was demonstrated by estimating the intrinsic and reflex stiffnesses at the ankle during tonic isometric contractions at three levels. These levels were selected to examine the performance of the intrinsic and reflex estimators at different total stiffnesses and relative contributions of the pathways.

6.6.1 Methods

Five subjects (three females) aged between {25-29} with no history of neuromuscular disorders were examined. Subjects gave informed consent to the experimental procedures that had been reviewed and approved by McGill University Institutional Review Board. The experimental methods were similar to those described in [271],

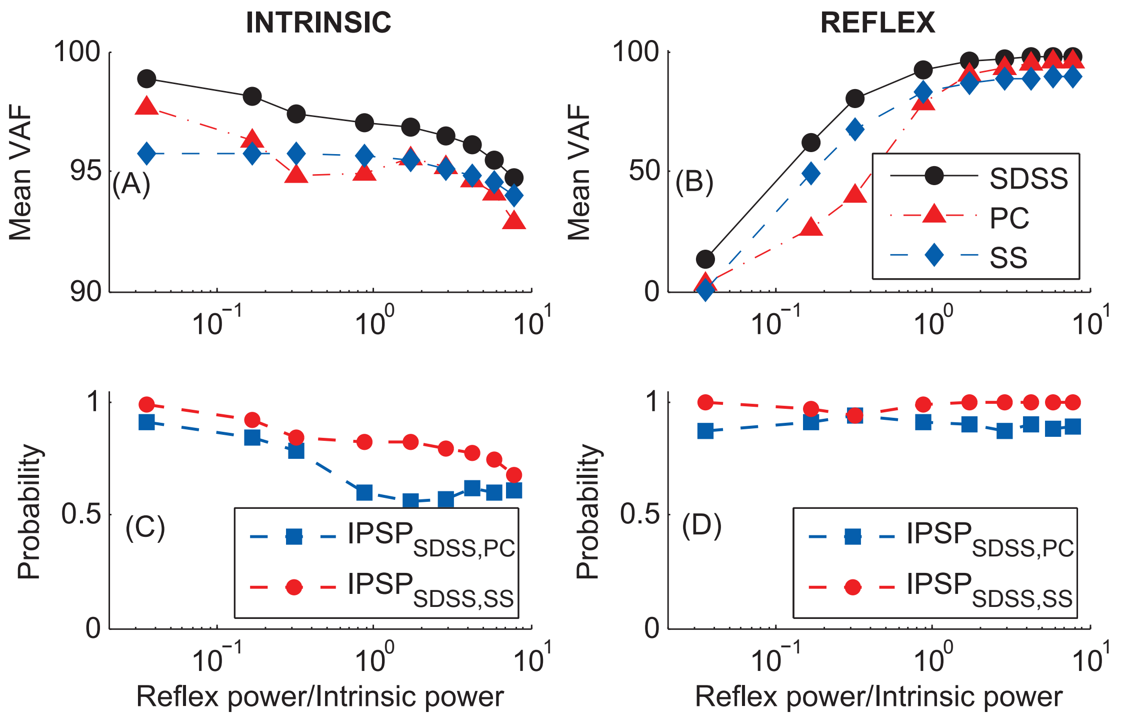

Figure 6–9: Performance of the SDSS, SS and PC methods as a function of the ratio of reflex to intrinsic torque power at SNR = 5dB: (A) Mean value of $\%\mathrm{VAF}_{\mathrm{intrinsic}}$; (B) Mean value of $\%\mathrm{VAF}_{\mathrm{reflex}}$; (C) probability that the SDSS $\%\mathrm{VAF}_{\mathrm{intrinsic}}$ was greater than that of SS (blue) and PC (red) ; (D) probability that the SDSS $\%\mathrm{VAF}_{\mathrm{reflex}}$ was greater than of SS (blue) and PC(red).

except that PRALDS input was used to generate position perturbations. The subject's left foot was attached to a hydraulic actuator which delivered position perturbations. By convention, neutral (zero) position was taken as the 90 degrees angle between the subject's foot and shank. Ankle dorsiflexion position and torques tending to dorsiflex the ankle were taken as positive. The ankle was flexed 0.225rad from the neutral position. Subjects were instructed to generate a constant muscle activation level with the aid of the visual feedback of their voluntary torque on an overhead monitor. The three levels were selected proportional to their Maximum Voluntary Contraction (MVC): 15% of plantarflexion MVC (PF trial), no muscle activation (REST trial), and 15% of dorsiflexion MVC (DF trial). For each trial, perturbations started, the subject was allowed to generate a stable contraction level, and then data were recorded for 60 seconds.

Since there was no access to the true intrinsic and reflex torques, we only assessed the performance of the SDSS and PC methods in terms of the $\%\mathrm{VAF}_{\mathrm{total}}$ between total measured and predicted torques.

6.6.2 Results

Fig. 6–10 shows a segment of a typical PF trial. Fig. 6–10A shows the recorded perturbations. Fig. 6–10B shows the measured total ankle torque (blue) along with that using the model identified by SDSS (red). It is evident that the two curves were very similar; indeed the identification %VAF was %87. Fig. 6–10C shows the predicted intrinsic torque and Fig. 6–10D shows the predicted reflex torque, illustrating how the two mechanisms contributed to the overall torque.

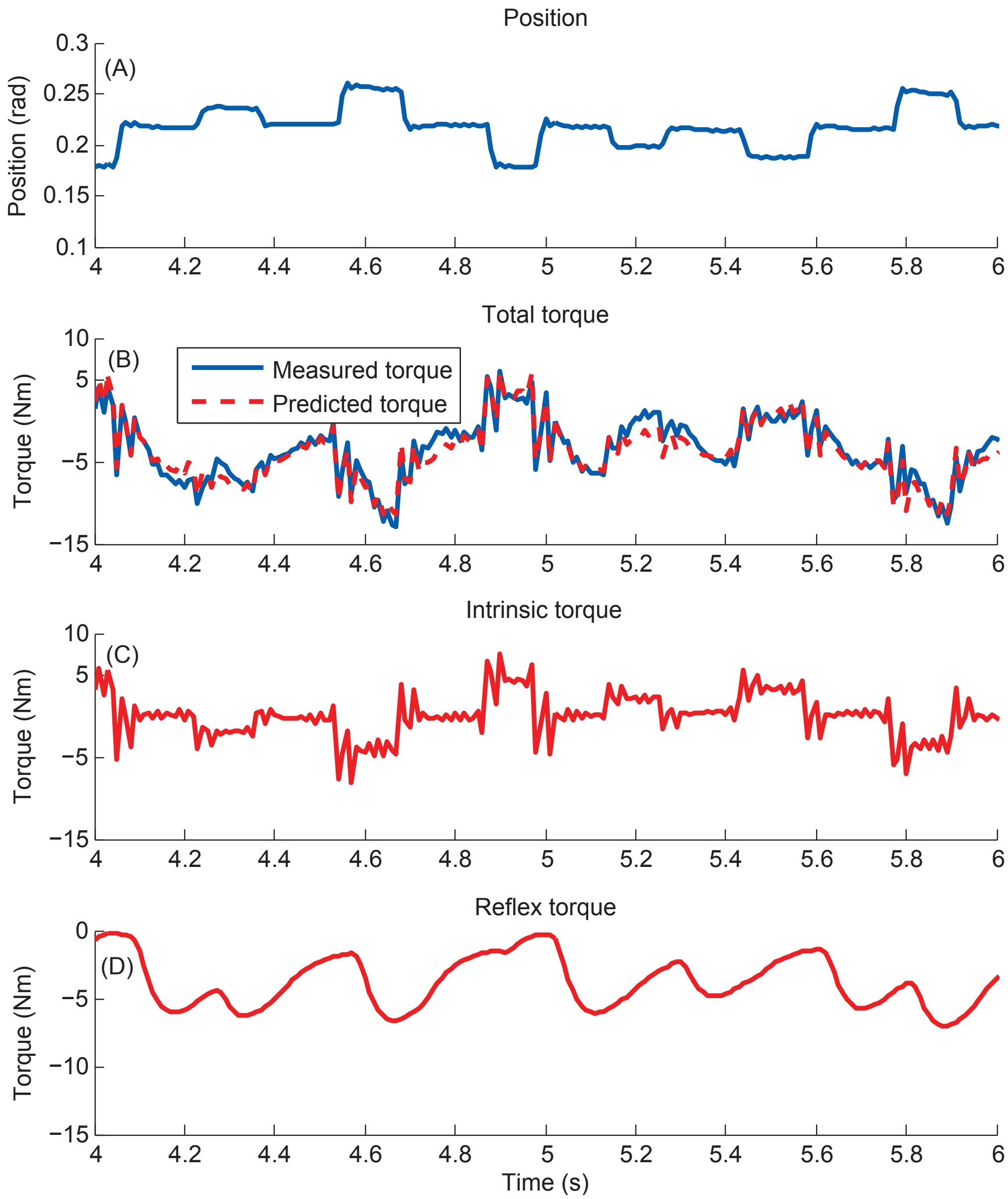

Figure 6–10: Experimental SDSS results for a typical subject during a PF trial (15% of plantarflexion MVC): (A) Measured position; (B) Measured torque along with the predicted total torque; (C) predicted intrinsic torque; (D) predicted reflex torque.

Fig. 6–11 shows the stiffness pathways for this subject using the SDSS and PC methods at the three contraction levels. The intrinsic stiffness estimates from the two methods exhibited similar characteristics. The gains of the frequency responses resembled a high-pass filter. The low-frequency gain (corresponding to the joint elasticity) was smaller in REST compared to PF and DF (Fig. 6–11B) as expected from previous studies [176]. However, there were important differences between the two sets of estimates. The low-frequency gains of the PC were larger than those of the SDSS (Fig. 6–11A-B).

The reflex pathway nonlinearities estimated with both methods were uni-directional rate sensitive and exhibited threshold or threshold-saturation behaviours (Fig. 6–11D). Thus, there was a response for positive velocities and little or no response for negative velocities. By visual inspection it is evident that there were differences in the threhold and slopes from case to case. Thus, the threshold was smaller in PF compared to REST or DF. However, the nonlinearities estimated with the two methods behaved somewhat differently (Fig. 6–11C). Thus, for SDSS the nonlinearity's threshold (determined by visual inspection) was lower in PF than for REST or DF and the nonlinearity saturated at high velocities. In contrast, in PC estimates there was no change in threshold nor was there any saturation.

The SDSS estimates of the reflex stiffness linear dynamics had similar low-pass characteristics at all activation levels (Fig. 6–11F). The PC estimates were also low-pass in nature but were much noisier. In addition, they changed with activation level, i.e. the filter break frequencies at DF and REST were different than those obtained from the SDSS (Fig. 6–11E).

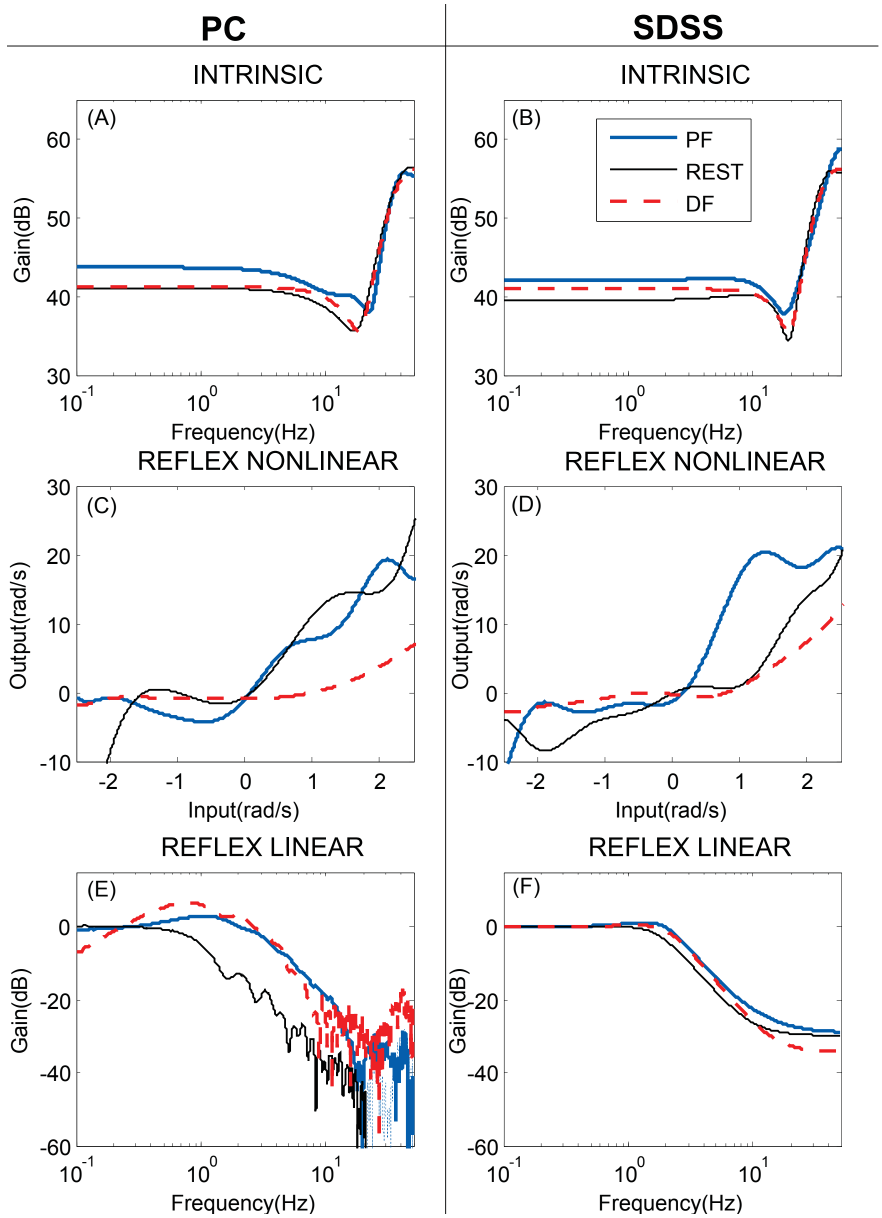

Figure 6–11: Typical stiffness pathways estimated using the PC (left) and SDSS (right) methods. Estimate of the: intrinsic stiffness models, using (A) PC and (B) SDSS, resemble high-pass filters; reflex static nonlinear element, using (C) PC and (D) SDSS, resemble a rectifier; reflex linear element, using (E) PC and (F) SDSS, resemble a low-pass filter.

The reflex pathway nonlinearities were parameterized by fitting a model consisting of a threshold and linear gain using trust-region-reflective method from MATLAB's optimization toolbox to the Tchebychev estimates. Fig. 6–12 shows the identification group results comparing the SDSS and PC methods. Both methods predicted the measured total torque equally well (Fig. 6–12A). Thus, the $\%\mathrm{VAF}_{\mathrm{total}}$ was $91.4\% \pm 2.5\%$ for the SDSS method and $91.2\% \pm 2.5\%$ for the PC method. The two algorithms, however, assigned the pathway gains differently. Thus, Fig. 6–12B shows that the intrinsic gain (elastic stiffness) resulted from the PC method was either larger or equal to that obtained from the SDSS method. The identified threholds were different (Fig. 6–12C). Finally, Fig. 6–12D shows that the gain of the reflex pathway (the slope of the nonlinearity) obtained from the PC method was always smaller or equal to that from the SDSS method.

6.7 Discussion

This paper develops a state-space representation for parallel-cascade model of ankle joint stiffness with parameters directly related to the underlying dynamics of the system. It presents a novel Structural Decomposition SubSpace (SDSS) method that decomposes the pathways and identifies all elements using a subspace based method. Extensive simulation and experimental studies show the SDSS decomposes the intrinsic and reflex torques accurately and estimates key parameters better than other methods.

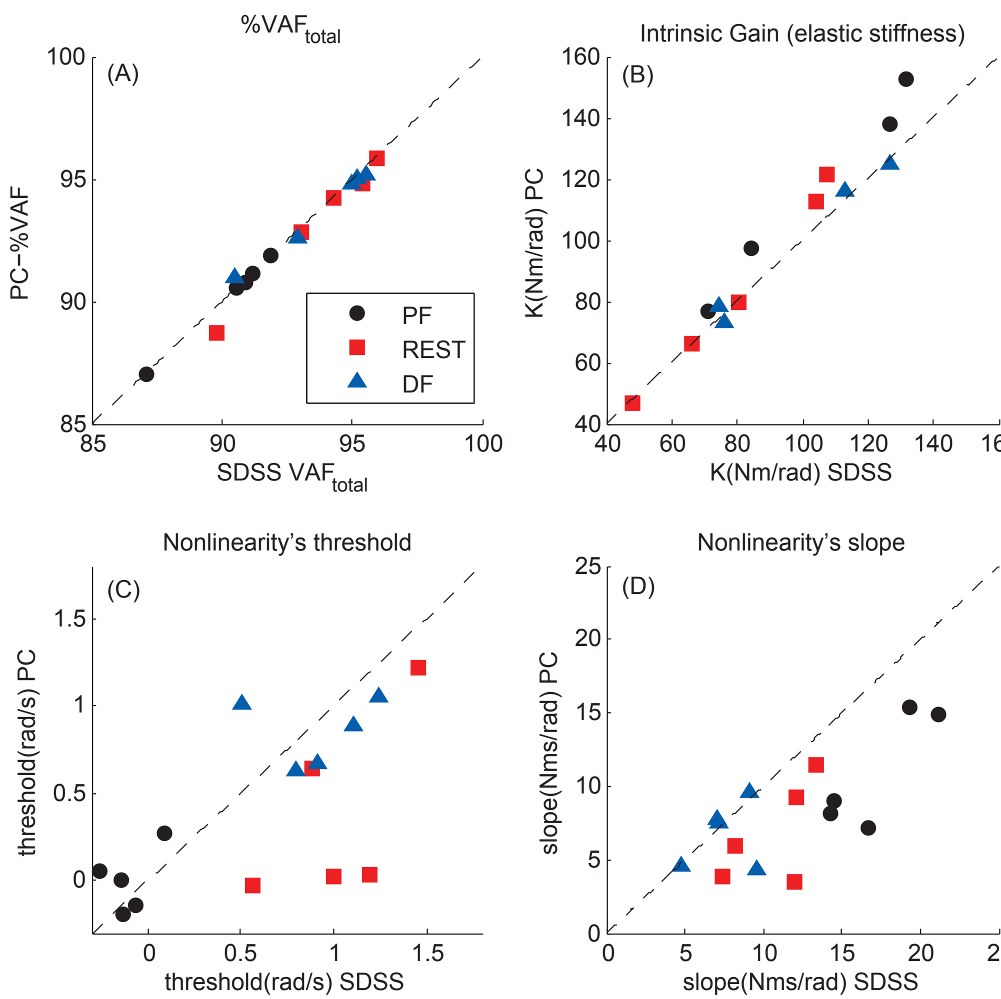

Figure 6–12: The distribution of pathway gains between SDSS and PC methods for all 5 subjects at all contraction levels: PF, REST, DF: (A) identification %VAF using SDSS vs. PC; (B) estimates of the intrinsic pathway gain using SDSS vs. PC; (C) estimates of the reflex pathway threshold using SDSS vs. PC; (D) estimates of the reflex pathway slope using SDSS vs. PC.

6.7.1 Algorithmic Issues

Subspace Identification

SDSS is a MOESP based subspace method [113] that is fast, and can deal with arbitrary colored output noise, as is the case for joint stiffness identification. It has the potential for closed-loop identification [120] which is necessary when the joint interacts with a compliant load [185, 122]. MOESP estimates the order of the reflex linear system before identifying state-space matrices. This reduces the *a priori* information required and is important for stiffness identification because previous experimental studies showed that the order of the reflex stiffness is variable [135]. Thus, while the order is usually two, normal subjects with a large muscle activation level as well as those with spasticity exhibit third-order characteristics.

SDSS estimates the parallel-cascade elements directly in contrast to the original subspace SS method which yielded a state-space model that required additional steps to extract the parallel-cascade elements. Thus, [122] used SLS optimization to separate the parameters of the static nonlinearity from the linear dynamics in the reflex path.

SDSS uses a short, two-sided IRF to model the intrinsic dynamics whereas the SS uses a linear mass-spring-damper model. Our approach has two advantages. First, the intrinsic model may be more complex than a pure viscoelastic-inertial structure due to the muscle tendon complex structure and/or fixation dynamics [206], [182]. Second, it avoids the need to differentiate position twice to estimate velocity and acceleration from the position record which is prone to numerical errors and noise amplification.

SDSS estimates the reflex elements iteratively using the *normalized alternative convex search* (NACS) approach whose convergence has recently established for any square integrable nonlinearity [273, 252, 262, 257, 256]. Fortunately, the convergence of the iteration does not depend on the choice of initial condition (step 7 of the algorithm). Thus, SDSS is guaranteed to converge, in contrast to PC which does not always converge.

Decomposition of Pathways

We used a novel approach to decompose the intrinsic and reflex pathways by projecting the measured torque onto the intrinsic and reflex spaces and their perpendicular complements. This is important because the intrinsic and reflex torques are not orthogonal in practice and cannot be easily decomposed. Ludvig et al. also decomposed the torque, but using a different approach [167]. They relied on a priori information and designed a special type of position perturbations that resulted in intrinsic and reflex torques that had near-zero correlations. In our work, we propose a general solution that is not limited to a specific input type. This approach can be further generalized for any system with parallel non-orthogonal pathways. Thus, each pathway can be estimated by performing proper projections. This has important applications for other biomedical systems that a single input simultaneously excites several pathways that sum to generate the output.

The decomposition works under the condition that the intrinsic and reflex regressors (Ψ_I, Ψ_R in (6.13)) and their union (Ψ in (6.12)) are full ranks. That is when the intrinsic and reflex spaces are not parallel to each other in Fig. 6–2. Fortunately, this can be easily achieved by designing a persistently exciting input like PRALDS or PRBS [116].

6.7.2 Simulation Methods

Identification methods are often developed and validated in simulation studies with ideal inputs and noises. However, their performance degrade considerably when applied to experimental data. For example, nonlinear actuator dynamics often cause the perturbations actually delivered to the joint to differ greatly from the ideally designed ones. Furthermore, in practice, noise is rarely white or Gaussian [247]. It is known that such non ideal behaviour will heavily affect identification accuracy. Thus, we accounted for these differences and designed simulation scenarios by mimicking real experiments using a realistic model and input and noise sequences observed experimentally. We believe that by doing so we ensured that our simulation results will be relevant to experimental conditions.

6.7.3 Simulation Results

Decomposition Accuracy (Bias Error)

The PC and SS methods had difficulty decomposing the pathways whereas the SDSS method always gave unbiased and accurate decompositions. SDSS decomposition was more accurate than SS because it considers more realistic dynamics for the intrinsic pathway. It was more accurate than PC because of the effectiveness of the orthogonal projections in extracting each pathway's contribution from an output contaminated with noise and contribution of the other pathway whereas PC iteration does not guarantee convergence of the decomposition. Thus, PC overestimated the intrinsic and underestimated the reflex pathway (Fig.6–7). This was because of overestimating the low frequency gain of the intrinsic pathway (Fig.6–6A) and underestimating the slope of the static nonlinearity (Fig.6–6C). Consequently, the PC method assigned the pathway gains inaccurately. Fig. 6–8(A-B) shows the estimates of both SS and PC methods were always biased even at the largest SNR level.

Precision (Random Error)

Our results demonstrated that SDSS was the most robust. Both output noise and the reflex torque appear as noise when estimating the intrinsic mechanics, and similarly both output noise and any unmodelled intrinsic torque appear as noise when estimating the reflex mechanics. Thus, we assessed the performance of the new estimators in two different ways: (*i*) by changing the output noise level in Fig. 6–8 and (*ii*) by changing the relative contribution of the pathways in Fig. 6–9.

The SDSS intrinsic and reflex estimators provided the most precise models. Statistical tests also revealed that SDSS was more robust than PC and SS at all conditions. SDSS was more robust than SS because its state-space structure for the reflex pathway had many fewer parameters. SDSS was more robust than PC because (*i*) the iterations used in PC are not guaranteed to converge and (*ii*) the SDSS considers a structure with many fewer parameters.

6.7.4 Experimental Results

SDSS successfully extracted stiffness models from experimental data and accurately predicted the measured torque. The experiments were performed at three different activation levels that resulted in a range of total stiffnesses and different ratio of intrinsic to reflex pathway contribution.

SDSS and PC methods predicted the total torque equally well; both estimates resulted in similar $\%\mathrm{VAF}_{\mathrm{total}}$ on average. However, they assigned the pathway gains differently (Fig. 6–12). So, the PC method's intrinsic gain estimates were consistently larger than those of SDSS. In contrast, the PC estimates of reflex stiffness gain (nonlinearity's slope) was smaller than those of SDSS. Our simulation studies demonstrated that the PC method overestimated intrinsic stiffness and underestimated reflex stiffness while SDSS had no bias error (Fig.6–7). We argue that SDSS results likely reflect the actual physiological behaviour.

Consequently, we used SDSS to estimate the parallel-cascade parameters for all subjects. Fig. 6–13 shows estimates changed consistently with activation level for all subjects: (A) The joint elasticity was smallest in REST and increased to PF and DF trials; (B) the threshold of the static nonlinearity was smallest in PF and increased to DF and REST trials; (C) the slope of static nonlinearity was largest in PF and decreased to DF and REST trials.

6.7.5 Conclusion

We presented the SDSS method for identification of the parallel-cascade model of ankle joint stiffness. We validated the method using extensive simulation and experimental studies and showed that the use of the new method is preferred because it estimates physiologically important parameters of the model which was not possible with the previous state-space method. Moreover, it is the most precise and accurate method compared to other available methods in conditions prevail during real experiments.

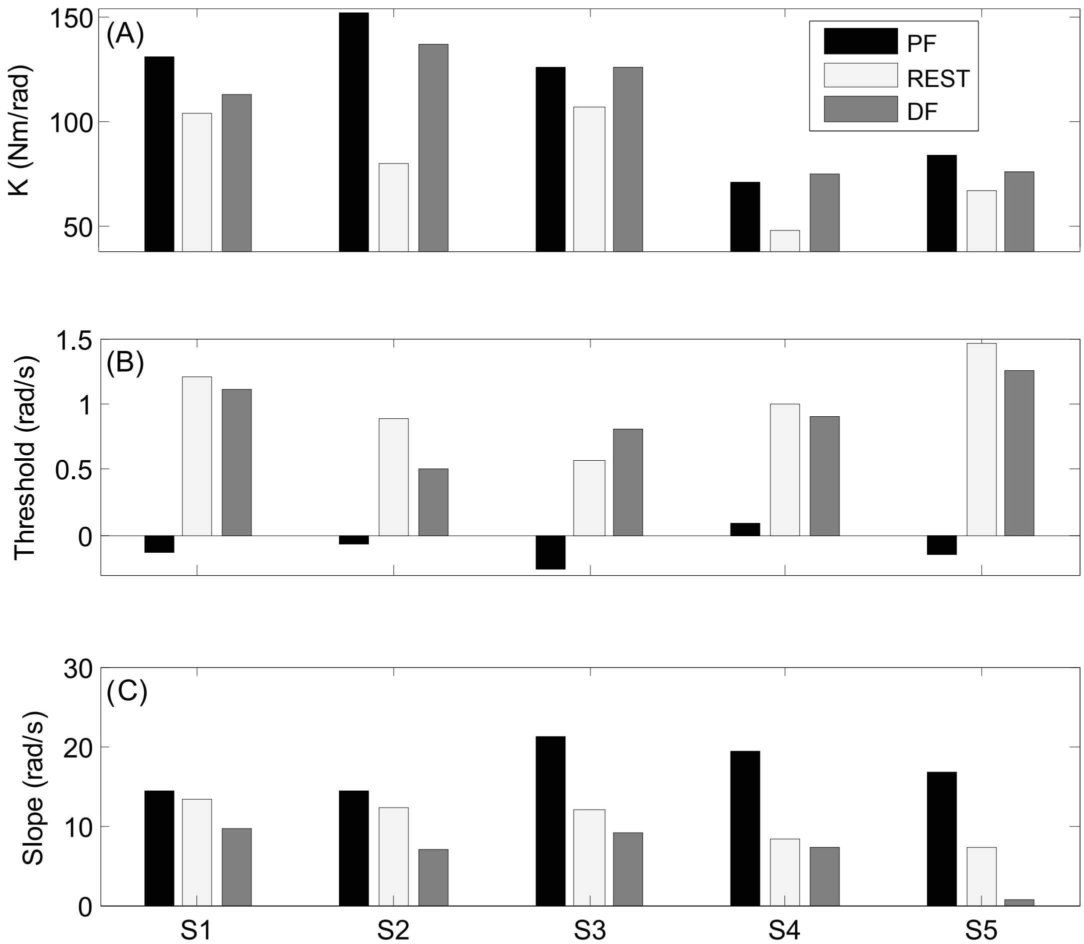

Figure 6–13: SDSS estimates of parallel-cascade parameters: (A) intrinsic elastic stiffnessess of PF (active ankle extensor muscles) and DF (active ankle flexor muscles) were larger than those of REST (no activation level) trials; (B) reflex nonlinearity's thresholds of PF trials were smaller than those of REST and DF trials; (C) reflex nonlinearity's slopes of PF trials were larger than those of REST and DF trials.

CHAPTER 7
Identification of Dynamic Joint Stiffness from Multiple Short Segments of Input-Output Data

In Chapter 6, I developed the SDSS method for identification of the parallel-cascade structure of joint stiffness. In Chapter 4, I presented the rationale and a method for identification of Hammerstein systems from multiple, stationary, short data segments. In this Chapter, I expand this idea on the SDSS method to identify the parallel-cascade structure from multiple, short, stationary segments of data. I show an application to identify stiffness at the ankle joint as a function of joint position during piecewise constant, imposed passive movement. This chapter is a journal paper that will be submitted to IEEE Transactions on Neural Systems and Rehabilitation Engineering.

Authors: Kian Jalaleddini, and Robert E. Kearney

Journal: IEEE Transactions on Neural Systems and Rehabilitation Engineering (to be submitted).

7.1 Abstract

This paper presents the *Short Segment Structural Decomposition SubSpace* (SS-SDSS) method to identify dynamic joint stiffness from short segments of stationary data can be acquired. The main application is when the data is non-stationary. Thus, our approach is to segment the non-stationary data into a number of short, stationary data segments and then identify a system from subsets of segments with the same properties. The method extends our previous state-space method by incorporating initial conditions in the system model and identifying them for each data segment. An extensive simulation study using realistic input and noise signals is presented that demonstrates the minimum number of segments and their lengths required for a successful identification. The application of the method is presented in measuring stiffness from experimental data during imposed movement of the ankle joint in normal human subjects. We demonstrate how stiffness changes as a function of the joint position during movement. We conclude that the SS-SDSS method is a valuable tool for measuring stiffness in functionally important tasks.

7.2 Introduction

Dynamic joint stiffness defines the dynamic relation between the position of a joint and the torque acting about it [37]. Joint stiffness plays a critical role in the control of posture and locomotion [10, 11, 12]. Thus, identifying mathematical models accurately describing these dynamics in functional tasks is significant. These mathematical models give insight on how the underlying neuromuscular systems function together to perform a task [19]. Moreover, they provide objective measures in diagnosis, assessment and treatment monitoring of the neuromuscular diseases that change the muscle tone. These models can also be used in the design of rehabilitation devices to match the stiffness of the lost or impaired joint to a normal one for the purpose of dexterous interaction with the environment [21, 23, 204, 25].

At the ankle, dynamic joint stiffness can be described with a *parallel-cascade* (PC) model. It consists of two parallel pathways (Fig. 7–1): (*i*) intrinsic stiffness modelling viscoelastic and inertial properties of the joint, active muscles and passive tissues; it has high-pass filter dynamics, (*ii*) reflex stiffness arising from changes in muscle activation due to stretch reflex mechanisms. This pathway has a block-oriented, nonlinear structure comprising a cascade of a differentiator, a delay operator, a static nonlinearity resembling a rectifier, followed by a linear system with low-pass dynamics [37].

The PC model has successfully described the relationship between the position and torque data at the ankle and a variety of other joints for stationary condition [37, 204, 202, 270, 75, 76, 134]. However, the assumption of stationarity is often violated during functionally important tasks when the joint operating point is not fixed. Examples include movements when the joint position and/or muscle activation level undergo large changes [186, 152, 193]; upright stance because of switching between different postural states [103]; large contractions resulting in muscle fatigue [104].

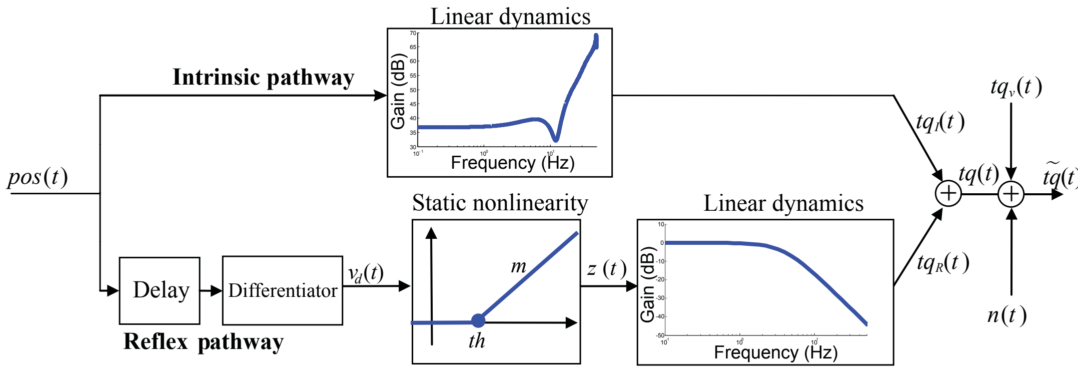

Figure 7–1: Parallel-cascade structure of the ankle joint stiffness. The input is the joint angular position and the output is the joint total torque which is the sum of the intrinsic, reflex and voluntary torques and measurement noise. The intrinsic pathway has a high-pass filter and the reflex pathway has a block oriented nonlinear model. Adapted from [6].

Marmarelis et al. proposed segmenting a non-stationary data record into short, stationary data segments and then identifying local, linear time-invariant models from subsets of segments with the same properties [277]. A similar approach to the identification of joint stiffness would have important applications. For instance, when stiffness dynamics vary slowly with time during quite stance, one could segment the data according to the postural state and then find local models describing the different strategies used for balance control. Segmentation would also be useful in estimating stiffness at high activation levels where it is difficult to maintain stationary contractions for a long period of time. Thus, subjects could perform multiple, short, large contractions without muscle fatigue and the data segmented to only include the intervals with large contractions. Consequently, it is of interest to have a method to identify stiffness from short, stationary data segments.

We recently developed the *Structural Decomposition SubSpace* (SDSS) method that uses a subspace technique to identify a state-space representation of the PC structure from a single stationary data record [6]. This paper presents an extension of the SDSS method to work with multiple short data segments. A part of this work has been presented at the Annual International Conference of the IEEE EMBS [278].

The rest of the paper is organized as follows: Section 7.3 gives reviews a state-space model of the PC structure, derives a data equation for multiple data segments, and presents the *Short Segment* SS-SDSS method for identification. Section 7.4 uses simulation studies to find the minimum number of segments and their lengths at a range of noise levels where the method successfully identifies the intrinsic and reflex pathways. Section 7.5 describes the successful application of the SS-SDSSS method to the identification of ankle stiffness during movements with piecewise constant trajectories that spanned the joint's range of motion. Section 7.6 provides a summary and a discussion.

7.3 Theory

Throughout the paper, vectors, matrices and scalars are shown by roman boldface uppercase, uppercase and lowercase letters respectively. The continuous time argument is t and the discrete time argument is k. A variable's superscript refers to the segment number, the tilde accented signal $\tilde{(\cdot)}$ indicates the noise-corrupted version of $(\cdot)$, and $\hat{(\cdot)}$ its estimate.

7.3.1 Modelling

Fig. 7–1 shows the PC model of ankle joint stiffness with the total torque as the sum of intrinsic, reflex and voluntary torques and measurement noise. The voluntary torque and measurement noise are assumed to be uncorrelated with the input signal. This model will be approximated with a discrete-time, state-space model.

Assume that data record comprises p stationary segments of joint angular position and total torque, where the i-th segment has N^i data points, $i \in \{1 \cdots p\}$:

$$\begin{aligned}\mathbf{POS}^i &= \begin{bmatrix} pos^i(0) & \cdots & pos^i(N^i-1) \end{bmatrix}^T \\ \tilde{\mathbf{TQ}}^i &= \begin{bmatrix} \tilde{tq}^i(0) & \cdots & \tilde{tq}^i(N^i-1) \end{bmatrix}^T\end{aligned} \tag{7.1}$$

We previously developed a state-space representation of stiffness for one segment [6]. The intrinsic pathway was modelled by a short, two-sided, *Impulse Response Function* (IRF) with weights $\mathbf{\Theta}_I = [h(-\Delta), \cdots, h(\Delta)]^T$ where Δ is the reflex delay. The reflex static nonlinearity was modelled by a Tchebychev basis function expansion of the delayed velocity with weights $\mathbf{\Lambda} = [\lambda_1, \cdots, \lambda_n]^T$ and the reflex linear dynamics by an l-th order state-space model with state-space matrices $\{A_R, B_R, C_R, D_R\}$. Consequently stiffness was modelled by a MISO, linear, state-space representation:

$$\begin{cases} \mathbf{X}^i(k+1) & = A_R\mathbf{X}^i(k) + B_T\mathbf{U}_T^i(k) \\ \tilde{tq}^i(k) & = C_R\mathbf{X}^i(k) + D_T\mathbf{U}_T^i(k) + e^i(k) \end{cases} \tag{7.2}$$

where the error is the sum of the voluntary torque and measurement noise $e^i(k) = tq_v^i(k) + n^i(k)$, and $\mathbf{U}_T^i(k)$ is the constructed input:

$$
\begin{aligned}
\mathbf{U}_T^i(k) &= \left[\mathbf{U}_R^i(k)\ \mathbf{U}_I^i(k)\right] \\
\mathbf{U}_I^i(k) &= \left[\begin{array}{ccc} pos^i(k-\Delta) & \cdots & pos^i(k+\Delta) \end{array}\right] \\
\mathbf{U}_R^i(k) &= \left[\begin{array}{ccc} g_1\left(v_d^i(k)\right) & \cdots & g_n\left(v_d^i(k)\right) \end{array}\right]
\end{aligned}
\tag{7.3}
$$

where $g_j(\cdot)$ is the j-th basis function of the expansion used to approximate the reflex nonlinear element.

From (7.2), it is evident that the total measured torque is a function of the input as well as the segment's *Initial Conditions* (IC):

$$
\begin{aligned}
\tilde{tq}^i(0) &= C_R\mathbf{X}^i(0) + D_T\mathbf{U}_T^i(0) + e^i(0) \\
\tilde{tq}^i(1) &= C_RA_R\mathbf{X}^i(0) + C_RB_T\mathbf{U}_T^i(0) + D_T\mathbf{U}_T^i(1) \\
&\quad + e^i(1) \\
&\vdots \\
\tilde{tq}^i(k) &= C_RA_R^k\mathbf{X}^i(0) + \sum_{r=0}^{k-1} C_RA_R^{k-1-r}B_T\mathbf{U}_T^i(r) \\
&\quad + D_T\mathbf{U}_T^i(k) + e^i(k)
\end{aligned}
\tag{7.4}
$$

Remark 3 *It is a common practice in the identification of biological systems to ignore the transient and consider the system in steady-state. However, when only short data segments are available, the contribution of the ICs ($\mathbf{X}^i(0)$) may become large and must be accounted for to avoid biased estimates of the system [279]. The* *contribution of the ICs is given by* $C_R A_R^k \mathbf{X}^i(0)$*. Since the system must be stable, all eigenvalues of* A_R *will lie inside the unit circle (*$eig(A_R) < 1$*) and the contribution from ICs will decay at a rate determined by the system time constants since* $\lim_{k\to\infty} A_R^k = 0$*. Thus, when the segment length* N^i *is short with respect to these time constants, the contribution from ICs will be important and must be considered in data equations as shown in (7.4).*

Rewrite (7.4) using Hankel matrices [1] :

$$\tilde{TQ}^{i}_{s,s,t^i} = \underbrace{\begin{bmatrix} C_R \\ C_R A_R \\ \vdots \\ C_R A_R^{s-1} \end{bmatrix}}_{\Gamma_s} \underbrace{\left[\mathbf{X}^i(s) \cdots \mathbf{X}^i(s+t^i-1) \right]}_{X^i_{s,t^i}}$$

$$+ \underbrace{\begin{bmatrix} D_\Omega & 0 & \cdots & 0 \\ CB_T & D_T & \cdots & 0 \\ \vdots & \vdots & \ddots & \vdots \\ C_R A_R^{s-2} B_T & C_R A_R^{s-3} B_T & \cdots & D_T \end{bmatrix}}_{H_s} U^i_{T\,s,s,t^i} \tag{7.6}$$

$$+ E^i{}_{s,s,t^i}$$

where, $U^i_{T\,s,s,t^i}$, $\tilde{TQ}^{i}_{s,s,t^i}$, $E^i{}_{s,s,t^i}$ are the Hankel matrices of the i^{th} segment of the input, noisy output and noise. Γ_s is the extended observability matrix. The size of the Hankel matrix, s, must be greater than the order of the linear dynamics. t^i spans the length of the segment:

$$t^i = N^i - 2s + 2 \tag{7.7}$$

1

Definition 2 *A Hankel matrix constructed from a discrete signal $o(k)$ has a constant block anti-diagonal shape:*

$$O_{i,j,k} = \begin{bmatrix} o(i) & \cdots & o(i+k-1) \\ \vdots & & \vdots \\ o(i+j-1) & \cdots & o(i+j+k-2) \end{bmatrix} \tag{7.5}$$

Expand the data equation (7.6) using extended Hankel matrices[2] to include all data segments.

$$\tilde{TQ}_{s,s,t^1,\cdots,t^p} = \Gamma_s \underbrace{\begin{bmatrix} X^1_{s,t^1} & \cdots & X^p_{s,t^p} \end{bmatrix}}_{X_{s,t^1,\cdots,t^p}} + H_s U_{T\,s,s,t^1,\cdots,t^p} + E_{s,s,t^1,\cdots,t^p} \tag{7.9}$$

Finally, concatenate the segments to give:

$$\begin{aligned} U_I &= [U_I^{1T}(0)\cdots U_I^{1T}(N^1-1)\cdots U_I^{pT}(0)\cdots U_I^{pT}(N^p-1)]^T \\ \mathbf{E} &= [e^1(0)\cdots e^1(N^1-1)\cdots e^p(0)\cdots e^p(N^p-1)] \\ \tilde{\mathbf{TQ}} &= [\tilde{tq}^1(0)\cdots \tilde{tq}^1(N^1-1)\cdots \tilde{tq}^p(0)\cdots \tilde{tq}^p(N^p-1)]^T \end{aligned} \tag{7.10}$$

which will be used later in the data equations.

7.3.2 Identification Algorithm

The objective is to estimate the intrinsic IRF ($\mathbf{\Theta}_I$), the coefficients of the static nonlinearity ($\mathbf{\Lambda}$), the state-space matrices A_R, B_R, C_R, D_R of the linear element, and the ICs $\{\mathbf{X}^1(0), \cdots, \mathbf{X}^p(0)\}$ from the recorded position and torque.

2

Definition 3 *The extended Hankel matrix for p Hankel matrices of signal $o(k)$:*

$$O_{i,j,t^1,\cdots,t^p} = \begin{bmatrix} O_{i,j,t^1} & \cdots & O_{i,j,t^p} \end{bmatrix} \tag{7.8}$$

Reflex pathway dynamics

Extend the *Multivariable Output Error State-sPace* MOESP algorithm of [113] with the past input as an *instrumental variable* (IV) to estimate the order of the reflex linear element and its state-space matrices A_R and C_R. To this end, form the LQ decomposition:

$$\begin{bmatrix} U_{T s,s,t^1,\cdots,t^p} \\ U_{T 0,s,t^1,\cdots,t^p} \\ \tilde{Y}_{s,s,t^1,\cdots,t^p} \end{bmatrix} = \begin{bmatrix} L_{11} & 0 & 0 \\ L_21 & L_{22} & 0 \\ L_{31} & L_{32} & L_{33} \end{bmatrix} \begin{bmatrix} Q_1 \\ Q_2 \\ Q_3 \end{bmatrix} \tag{7.11}$$

The matrix $U_{T 0,0,t^1,\cdots,t^p}$ is the IV. It is the past input and so not correlated with the noise but is correlated with the rest of the data equation (7.9). Therefore, it is a suitable IV in the presence of an arbitrarily colored noise. Next, compute the singular value decomposition of L_{32}:

$$L_{32} = U\Sigma V^T \tag{7.12}$$

Inspect the singular values, the diagonal entries of Σ and separate them into two subsets, one containing "large" singular values that can be attributed to the system dynamics and a second subset of "small" singular values due to noise. The number of "large" singular values is equal the order of the linear element of the reflex pathway. Consequently, the first l columns of U are then an estimate of the extended observability matrix $\hat{\Gamma}_l$. The first row of $\hat{\Gamma}_l$ gives an estimate of C_R while A_R can be estimated from:

$$\hat{A}_R = \hat{\Gamma}_{l1}^{\dagger}\hat{\Gamma}_{l2} \tag{7.13}$$

where $\hat{\Gamma}_{l1}$ as the upper $(l-1)$ rows of $\hat{\Gamma}_l$, and $\hat{\Gamma}_{l2}$ as the lower $(l-1)$ rows of $\hat{\Gamma}_l$ and $(\cdot)\dagger$ is the pseudo-inverse operator.

These estimators can be demonstrated to be unbiased by extending Theorem 9.3 of [102] to the case of extended Hankel matrices.

Decomposition

The next step is to decompose the measured torque into its intrinsic and reflex components. To this end, Form the data equation [6]:

$$\mathbf{T\tilde{Q}} = \Phi_I \mathbf{\Theta_I} + \Phi_R \mathbf{\Theta_R} + \mathbf{E} \tag{7.14}$$

where Φ_I is the regressor for the intrinsic parameter set:

$$\Phi_I = U_I \tag{7.15}$$

and $\mathbf{\Theta_I}$ contains the unknown intrinsic IRF weights:

$$\mathbf{\Theta}_I = \begin{bmatrix} h(-\Delta) & \cdots & h(0) & \cdots & h(\Delta) \end{bmatrix}^T \tag{7.16}$$

Φ_R is the regressor for the reflex parameter set:

$$\Phi_R = [\Xi_1 \ \cdots \ \Xi_p \ \Psi] \tag{7.17}$$

that is constructed from the input and the estimates $\hat{A}_R$ and $\hat{C}_R$:

$$\Xi_1 = \begin{bmatrix} \hat{C}_R \\ \vdots \\ \hat{C}_R \hat{A}_R^{t^1-1} \\ 0 \\ \vdots \\ 0 \end{bmatrix}, \;\cdots\;, \Xi_p = \begin{bmatrix} 0 \\ \vdots \\ 0 \\ \hat{C}_R \\ \vdots \\ \hat{C}_R \hat{A}_R^{t^p-1} \end{bmatrix} \tag{7.18}$$

$$\Psi = \begin{bmatrix} 0 \\ \mathbf{U}_R^{1\,T}(0) \otimes \hat{C}_R \\ \vdots \\ \sum_{\tau=0}^{N^1-2} \mathbf{U}_R^{1\,T}(\tau) \otimes \hat{C}_R \hat{A}_R^{N^1-2-\tau} \\ \vdots \\ 0 \\ \mathbf{U}_R^{p\,T}(0) \otimes \hat{C}_R \\ \vdots \\ \sum_{\tau=0}^{N^p-2} \mathbf{U}_R^{p\,T}(\tau) \otimes \hat{C}_R \hat{A}_R^{N^p-2-\tau} \end{bmatrix} \tag{7.19}$$

$\mathbf{\Theta_R}$ contains the unknown parameters of the reflex pathway including: (i) the ICs; (ii) the basis expansion coefficients of the reflex nonlinearity $(\{\lambda_1 \;\cdots\; \lambda_n\}$; (iii) the state-space matrices of the reflex linear dynamic elements ($\{b_1 \ \cdots \ b_l \ d\}$):

$$\begin{aligned}\mathbf{\Theta_R} =[\ & \mathbf{X}^1(0) \quad \cdots \quad \mathbf{X}^p(0) \quad b_1\lambda_1 \quad \cdots \quad b_l\lambda_1 \quad \cdots \quad b_1\lambda_n \\ & \cdots \quad b_l\lambda_n \quad d\lambda_1 \quad \cdots \quad d\lambda_n\ ]^T\end{aligned} \tag{7.20}$$

Now, decompose the intrinsic and reflex torques from the total torque using the decomposition procedure described in [6], based on the orthogonal projection on the column space of the intrinsic and reflex pathways and their perpendicular complements. To this end, define the orthogonal projection operators:

$$\begin{cases} P_I & = \Psi_I \Psi_I^\dagger \\ P_R & = \Psi_R \Psi_R^\dagger \end{cases}$$

Compute the least squares estimate of the intrinsic parameters:

$$\hat{\mathbf{\Theta}}_I = ((I - P_I P_R)\Psi_I)^\dagger \, P_I (I - P_R)\tilde{\mathbf{TQ}} \tag{7.21}$$

and use it to decompose the intrinsic and reflex torques:

$$\begin{aligned}\hat{\mathbf{TQ}}_I &= \Phi_I \hat{\mathbf{\Theta}}_I \\ \hat{\mathbf{TQ}}_R &= \tilde{\mathbf{TQ}} - \hat{\mathbf{TQ}}_I\end{aligned} \tag{7.22}$$

Estimation of the remaining parameters

It remains to estimate the ICs, the coefficients of the reflex nonlinearity, and B_R and D_R state-space matrices of the reflex linear dynamics using:

$$\hat{\mathbf{T}}\mathbf{Q}_R = \Phi_R \mathbf{\Theta_R} \tag{7.23}$$

This problem is not linear in the parameters $\mathbf{\Lambda}$, $\{b_1, \ \cdots, \ b_m, \ d\}$ and ICs $\{\mathbf{X}^1(0), \ \cdots, \ \mathbf{X}^p(0)\}$. Therefore, estimate them using the iterative algorithm we described in [278] which can be summarized as follows. First, separate the parameters into two sets:

$$\begin{aligned} \mathbf{\Theta}_A &= \mathbf{\Lambda} \\ \mathbf{\Theta}_B &= [\zeta^1 \ \cdots \ \zeta^p \ b_1 \ \cdots \ b_l \ d]^T \end{aligned} \tag{7.24}$$

where ζ^i is a scaled version of the initial condition $\zeta^i = \frac{\mathbf{X}^i(0)}{\lambda_1}$. Now, if the set $\mathbf{\Theta}_A$ is fixed, the output is a linear function of $\mathbf{\Theta}_B$. Conversely, if $\mathbf{\Theta}_B$ is fixed, the output is a linear function of $\mathbf{\Theta}_A$. Thus, (7.23) can be solved by iteratively solving two linear least-squares problems. These two problems can be stated as follows for the iteration index f.

Problem I: If the parameter set $\mathbf{\Theta}_{A,f-1}$ is known, then the output depends linearly on $\mathbf{\Theta}_{B,f}$:

$$\hat{\mathbf{T}}\mathbf{Q}_R = \Phi_R \Phi_{A,f-1} \mathbf{\Theta}_{B,f} \tag{7.25}$$

where:

$$\Phi_{A,f} = \begin{bmatrix}
\lambda_{1,f} & & 0 & 0 & \cdots & 0 & 0 \\
\vdots & \ddots & \vdots & \vdots & \ddots & \vdots & \vdots \\
0 & & \lambda_{1,f} & 0 & \cdots & 0 & 0 \\
0 & \cdots & 0 & \lambda_{1,f} & \cdots & 0 & 0 \\
\vdots & \ddots & \vdots & \vdots & \ddots & 0 & 0 \\
0 & \cdots & 0 & 0 & \cdots & \lambda_{1,f} & 0 \\
 & \vdots & & & \vdots & & \vdots \\
0 & \cdots & 0 & \lambda_{n,f} & \cdots & 0 & 0 \\
\vdots & \ddots & \vdots & \vdots & \ddots & 0 & 0 \\
0 & \cdots & 0 & 0 & \cdots & \lambda_{n,f} & 0 \\
0 & & & \cdots & & 0 & \lambda_{1,f} \\
 & & & & & & \vdots \\
0 & & & \cdots & & 0 & \lambda_{n,f}
\end{bmatrix} \tag{7.26}$$

which leads to the linear least-squares estimate:

$$\hat{\mathbf{\Theta}}_{B,f} = (\Phi_R \Phi_{A,f-1})^{\dagger} \, \hat{\mathbf{T}}\mathbf{Q}_R \tag{7.27}$$

Problem II: If the parameter set $\mathbf{\Theta}_{B,f-1}$ is known, the output is linearly dependent on $\mathbf{\Theta}_{A,f}$:

$$\hat{\mathbf{T}}\mathbf{Q}_R = \Phi_R \Phi_{B,f-1} \mathbf{\Theta}_{A,f} \tag{7.28}$$

where:

$$\Phi_{B,f} = \begin{bmatrix} \zeta_f^1 & \cdots & 0 \\ \vdots & \vdots & \vdots \\ \zeta_f^p & \cdots & 0 \\ b_{1,f} & \cdots & 0 \\ \vdots & \vdots & \vdots \\ b_{l,f} & \cdots & 0 \\ \vdots & \vdots & \vdots \\ 0 & \cdots & b_{1,f} \\ \vdots & \vdots & \vdots \\ 0 & \cdots & b_{l,f} \\ d_f & \cdots & 0 \\ & \ddots & \\ 0 & \cdots & d_f \end{bmatrix} \tag{7.29}$$

leading to the linear least-squares estimate:

$$\hat{\mathbf{\Theta}}_{A,f} = (\Phi\Phi_{B,f-1})^{\dagger}\, \hat{\mathbf{T}}\mathbf{Q}_R \tag{7.30}$$

Algorithm

The following routine summarizes the steps of the SS-SDSS identification algorithm.

1. Record p segments of the position input and torque output.
2. Construct the extended Hankel matrices of the input $U_{T\,s,s,t^1,\cdots,t^p}$, the IV $U_{T\,0,s,t^1,\cdots,t^p}$, and output $\tilde{TQ}_{s,s,t^1,\cdots,t^p}$ using (7.8).

3. Perform the LQ decomposition of (7.11).
4. Perform the singular value decomposition on L_{32} using (7.12).
5. Separate the singular values of Σ into two subsets of "large" and "small" values.
6. Set the order of the linear system in the reflex pathway, l, to the number of "large" singular values. Form $\hat{\Gamma}_l$ as the first l columns of U.
7. Estimate $\hat{C}_R$ as the first row of $\hat{\Gamma}_l$.
8. Estimate $\hat{A}_R$ from (7.13).
9. Form the regressors Φ_I and Φ_R using the constructed input, $\hat{A}_R$ and $\hat{C}_R$.
4. Choose an arbitrary non-zero $\mathbf{\Theta}_{A,0}$ to start the iteration and set the iteration index $f = 1$.
5. Construct the matrix $\Phi_{A,f-1}$ using (7.26). Solve (7.27) to estimate $\mathbf{\Theta}_{B,f}$.
6. Construct the matrix $\Phi_{A,f-1}$ using (7.29). Solve (7.30) to estimate $\mathbf{\Theta}_{A,f}$.
7. Let q be the sign of the first non-zero element of $\mathbf{\Theta}_{A,f}$, i.e., $q \triangleq \operatorname{sgn}(\lambda_{1,f})$ and perform the normalization:

$$\begin{aligned}\mathbf{\Theta}_{A,f} &\triangleq q\frac{\mathbf{\Theta}_{A,f}}{\|\mathbf{\Theta}_{A,f}\|}\\ \mathbf{\Theta}_{B,f} &\triangleq q\mathbf{\Theta}_{B,f}\,\|\mathbf{\Theta}_{B,f}\|\end{aligned}\tag{7.31}$$

8. Evaluate the *sum of squared errors* (SSE) between the predicted and recorded outputs. If the relative improvement in SSE is greater than a threshold, replace f by $f+1$ and go to step 2. Otherwise, terminate.

If the reflex static nonlinearity is square integrable, the normalization (7.31) ensures the convergence to the global minimum [252, 257, 262, 256].

Algorithm limits

It follows from (7.7) that the length of each segment must be greater than:

$$\min\left(N^i\right) = 2s - 1 \tag{7.32}$$

Furthermore, at least $2sp - p + 2ns + 3s$ total number of samples are required due to numerical reasons of SVD computation.

7.4 Simulation Studies

Simulation scenarios mimic important experimental conditions to evaluate the performance of the SS-SDSS method and assess the reliability of the estimates. The specific objective is to find minimum data requirements in a range of experimental conditions where the method successfully identifies stiffness.

7.4.1 Methods

Models

The PC model of stiffness shown in Fig. 7–1 was simulated using MATLAB. The simulation parameters were based on those reported in the literature. Thus, the intrinsic pathway model was modelled with a discrete-time IRF, estimated from experimental data reported in [6], with the high-pass dynamics shown in Fig. 7–2. For the reflex pathway, the delay was set to 40ms [65], the static nonlinearity was a half-wave rectifier (as in Fig. 7–1) with a threshold at 0 rad/s [65], and the linear element was the low-pass filter [6]:

$$\frac{184.96}{s^2 + 16.8s + 184.96} \tag{7.33}$$

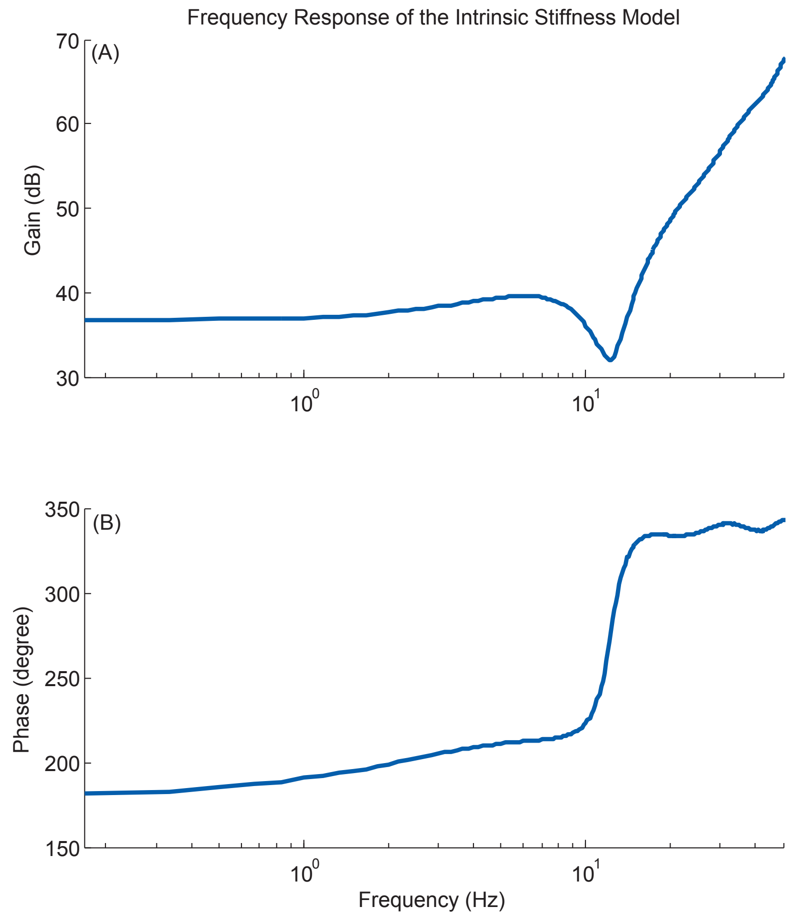

Figure 7–2: The frequency response function of the intrinsic stiffness model used in simulation studies: (A) gain; (B) phase.

Simulations were done at 1kHz and the resulting signals were decimated to 100 Hz for analysis purposes.

Input

The characteristics of the input signal (e.g. frequency content and amplitude distribution) strongly affect the identification performance. Consequently, we built a library of realistic signals by recording the position records generated when different realizations of a *Pseudo Random Arbitrary Level Distributed Sequence* (PRALDS) were applied to our actuator while subjects maintained a constant muscle contraction level. The PRALDS sequence switched between random amplitudes with maximum of 0.04rad at time intervals drawn from a uniform random variable ranging from 100 to 200ms. The input library contained 210 realizations, each 60s long.

Noise

The characteristics of the noise will also influence the identification accuracy. The noise associated with ankle torque in stiffness identification experiments is complex being neither white nor Gaussian. Rather, it comprises (*i*) a white Gaussian component due to electronics and signal conditioning circuitries and (*ii*) a low-pass non-Gaussian component due to variations in the voluntary drive [247]. Consequently, to simulate the noise accurately, we built a library of noise signals by recording ankle torque while subjects attempted to maintain a constant muscle contraction with no position perturbation. The noise library contained 210 realizations, each 60s long.

Monte-Carlo Series

Monte-Carlo (MC) experiments evaluated the performance of the algorithm by finding the minimum number of segments required for a *successful* identification. Each MC series simulated 200 trials each 60s long with different realizations of the input and noise signals selected randomly from the input-noise libraries.

We evaluated the performance of the algorithm in MC series which varied three factors that occur in real experiments and affect the identification accuracy. The first was the relative magnitude of the noise power to the total torque power defined as the *Signal to Noise Ratio* (SNR):

$$\text{SNR}_{\text{dB}} = 10log\frac{\text{power}(tq(k))}{\text{power}(tq_v(k) + n(k))} \tag{7.34}$$

MC series were carried out at SNR levels of 10, 15 and 20dB, values comparable to those observed in real experiments.

The second factor was the relative contribution of the intrinsic and reflex pathways which was expected to influence the decomposition algorithm. This factor was quantified in terms of the ratio of the power in the two pathways:

$$\text{RtI} = \frac{\text{power}(tq_R(k))}{\text{power}(tq_I(k))} \tag{7.35}$$

MC series were run at RtI levels of $\frac{1}{3}$, 1 and 3. This was achieved by changing the slope of the nonlinearity from 12.25 to 17.5 and to 24 rad/s respectively; levels are within the range observed from normal subjects [65].

The third factor was the segment length. For each combination of SNR and RtI levels, the data of each simulated MC record was divided into a number of segments with lengths drawn from a uniform random distribution. MC series were run with the minimum of this distribution varying systematically from the set $\{0.1, 0.2, \cdots, 1, 2, \cdots, 10\}$ while its maximum was always 0.1s larger than its minimum.

Accuracy

The accuracy of each estimate was assessed by evaluating how well it predicted the response to a trial with a novel input realization. The validation %*Variance*

Accounted For (VAF) was used as a measure of the accuracy of the estimates:

$$\%\text{VAF} = 100\left(1 - \frac{var(\hat{y}(k) - y(k))}{var(y(k))}\right) \tag{7.36}$$

where $y(k)$ is the noise-free output of the true model to a new input and $\hat{y}(k)$ is the model estimate. Thus, a %VAF of 100% means the model was perfect and accounted for all the output variance.

The identification was deemed to be *successful* if the validation VAF was larger than 95% in more than 95% of the MC trials. This measure was evaluated for both the intrinisc and reflex pathways:

$$\%\text{VAF}_{\text{intrinsic}} = 100\left(1 - \frac{var(\hat{tq}_I(k) - tq_I(k))}{var(tq_I(k))}\right)$$
$$\%\text{VAF}_{\text{reflex}} = 100\left(1 - \frac{var(\hat{tq}_R(k) - tq_R(k))}{var(tq_R(k))}\right)$$

7.4.2 Results

Fig. 7–3 shows a segment from a typical Monte-Carlo simulation trial where the identification was successful. It is clear that there is a great consistency between all simulated and predicted torques. Thus, both intrinsic and reflex torques were predicted accurately and the residuals were small, demonstrating that the pathways were decomposed and identified correctly. Furthermore, the reflex torque at the onset of each segment was accurate, indicating that the initial conditions were estimated well.

The success curves for the identification of the intrinsic pathway as functions of segment length are shown for different values of the SNR (Fig. 7–4(B)) and RtI

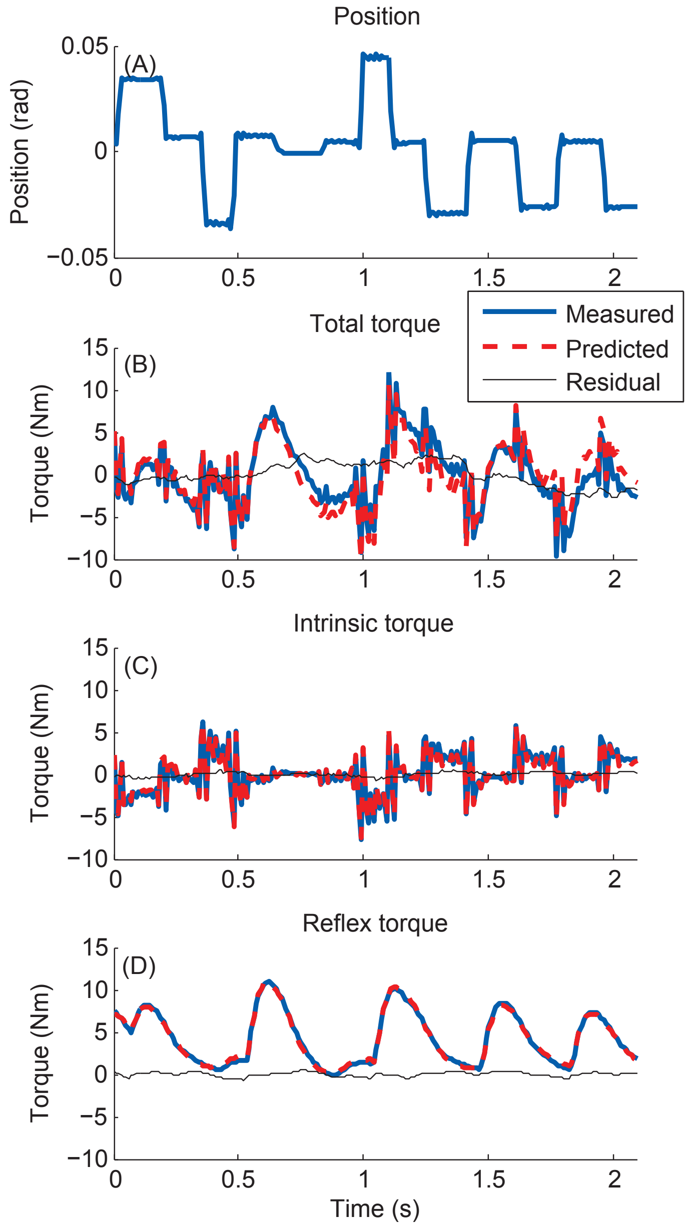

Figure 7–3: A segment from a typical Monte-Carlo trial where stiffness was estimated from 20 segments with mean length of 2s and SNR of 10dB. (A,B) segment position; (C,D) the total measured, predicted torque and residuals; (E,F) the true intrinsic torque, predicted one and residuals; (G,H) the true reflex torque, predicted one and residuals.

(Fig. 7–4(B)). There are three main observations: (*i*) the curves resemble rectangular hyperbolas with the coordinate axes as their asymptotes; that is the smaller the segment length, the more segments were required for a successful identification; (*ii*) the total number of samples required for a successful identification (mean segment length $\times$ number of segments) increased as the SNR level decreased; (*iii*) the number of samples required for a successful identification decreased as the RtI level decreased.

The success curves for the identification of the reflex pathway as functions segment lengths are shown for different values of the SNR (Fig. 7–4(C)) and RtI (Fig. 7–4(D)). The curves are generally similar to those of the intrinsic pathways but two main differences are apparent. First, the number of samples required for a successful identification was always greater than that for the intrinsic pathway. Second, the number of samples required for a successful identification increased as the RtI level decreased whereas it increased for the intrinsic pathway.

7.5 Experimental Studies

The practical utility of the SS-SDSS method was examined by applying it to data from experiments on normal human ankle joints at rest which were moved passively through their range of motions in a piecewise constant manner.

7.5.1 Methods

We recruited five healthy subject who gave informed consent to the experimental procedures, which had been reviewed and approved by McGill University Institutional Review Board. The experimental apparatus was similar to that described in [135]. The subject's left foot was attached to a hydraulic actuator using a custom made low-inertia boot. The actuator was operated in position-servo mode

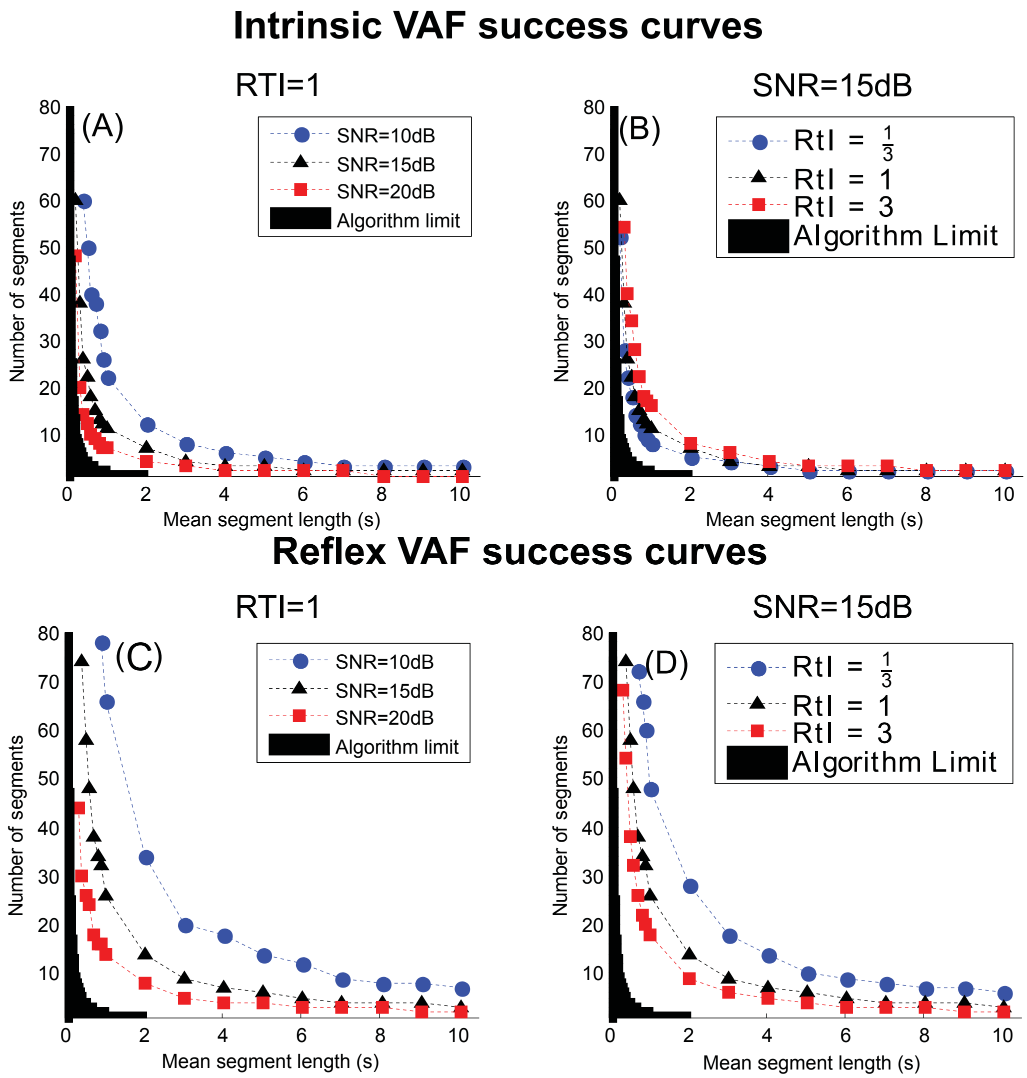

Figure 7–4: Success curves for the intrinsic and reflex pathway identification. The minimum number of segments required as a function of mean segment length for successful identification: (A,B) success curve for the identification of intrinsic pathway: (A) changes with SNR level when RtI=1 ; (B) changes with RtI level when SNR=15dB; (C,D) success curve for the identification of reflex pathway: (C) changes with SNR level when RtI=1 ; (D) changes with RtI level when SNR=15dB. The black area shows the algorithm limits where the algorithm fails.

to control the angular position of the ankle. The neutral position (90 degrees angle between shank and foot) was taken as 0rad, plantarflexing displacements were taken as negative and dorsiflexing displacements as positive. Subjects were instructed to remain relaxed and not to resist to position perturbations.

The angular position command sent to the actuator was the sum of a slow and large displacement superimposed with small perturbations. The large displacement trajectory was a piecewise constant signal that spanned the subject's range of motion. It was generated by switching randomly between levels selected from the set $\{-0.4, -0.3, \cdots, 0, 0.05, \cdots, 0.3\}rad$ as permitted by the subject's range of motion at time intervals drawn from a uniform random variable ranging from 4 to 7s. The resultant trajectory was then low-pass filtered for the sake of subject's comfort with a second-order Butterworth filter with a cut-off frequency of 2.5Hz to avoid sharp transitions in the ankle displacements.

The large displacement was not suitable for identification because it had little frequency content. Consequently, PRALDS perturbations were added to the actuator input [6]. The switching rate of PRALDS was a uniform random variable with minimum and maximum of 250 and 350ms and its peak amplitude was 0.04rad. Fig. 7–5 shows a typical recorded position trajectory.

10 trials of 120s were recorded, separated by one minute rest time. Position, torque and EMGs were sampled at 1kHz and then decimated to 100Hz for the analysis. EMG signals from triceps surae and tibialis anterior muscles were examined to confirm that subjects remained relaxed with no background voluntary activity.

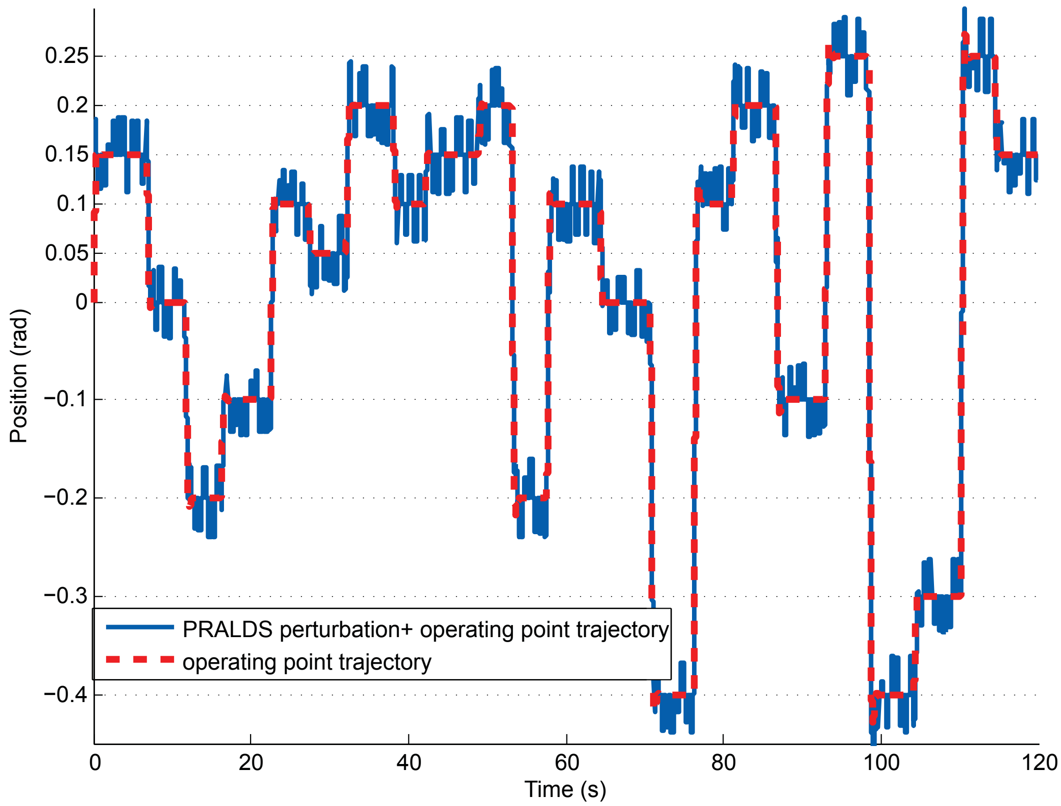

Figure 7–5: Position record from a typical experimental trial. The joint angular position was the sum of a large, piecewise constant displacement (red) and PRALDS perturbations. The large displacement trajectory was scaled to span the subject's range of motion and result in non-stationary data. The PRALDS perturbation was used to stimulate the system for identification purposes.

Multiple stationary data segments were assembled for each position level. This was achieved by segmenting the 10 trials according to the position large displacement trajectory. The first 1.5s of each segment was removed to avoid transients associated with the change in mean position. This yielded an average of 22 segments for each level with minimum and maximum of 18 and 27. The average segment length was $3.92 \pm 1.41s$.

One subject performed an extra trial in the absence of large displacements when only PRALDS perturbations were applied to the ankle. Similar to the previous experiments, the subject was instructed to remain relaxed and position an torque were recorded for 60s. This trial is referred to as the stationary trial and is used to assess the performance of the SS-SDSS method against the SDSS method.

7.5.2 Results

Stationary Trial

Since the data were stationary, the SDSS method identified stiffness as the first line method. 120 segments, each 0.5s, were then selected randomly from the stationary data and used by the SS-SDSS method to identify stiffness. The segmentation and identification process was repeated 100 times. Fig. 7–6 compares the estimates using the two methods and shows that the SS-SDSS estimates were very close to the SDSS estimates. Consequently, the SS and SDSS methods had similar performances at quasi static conditions.

Typical Subject Results

Fig. 7–7 shows a section of an input-output record for a typical trial. The output torque characteristics changed considerably with the position operating point; at a

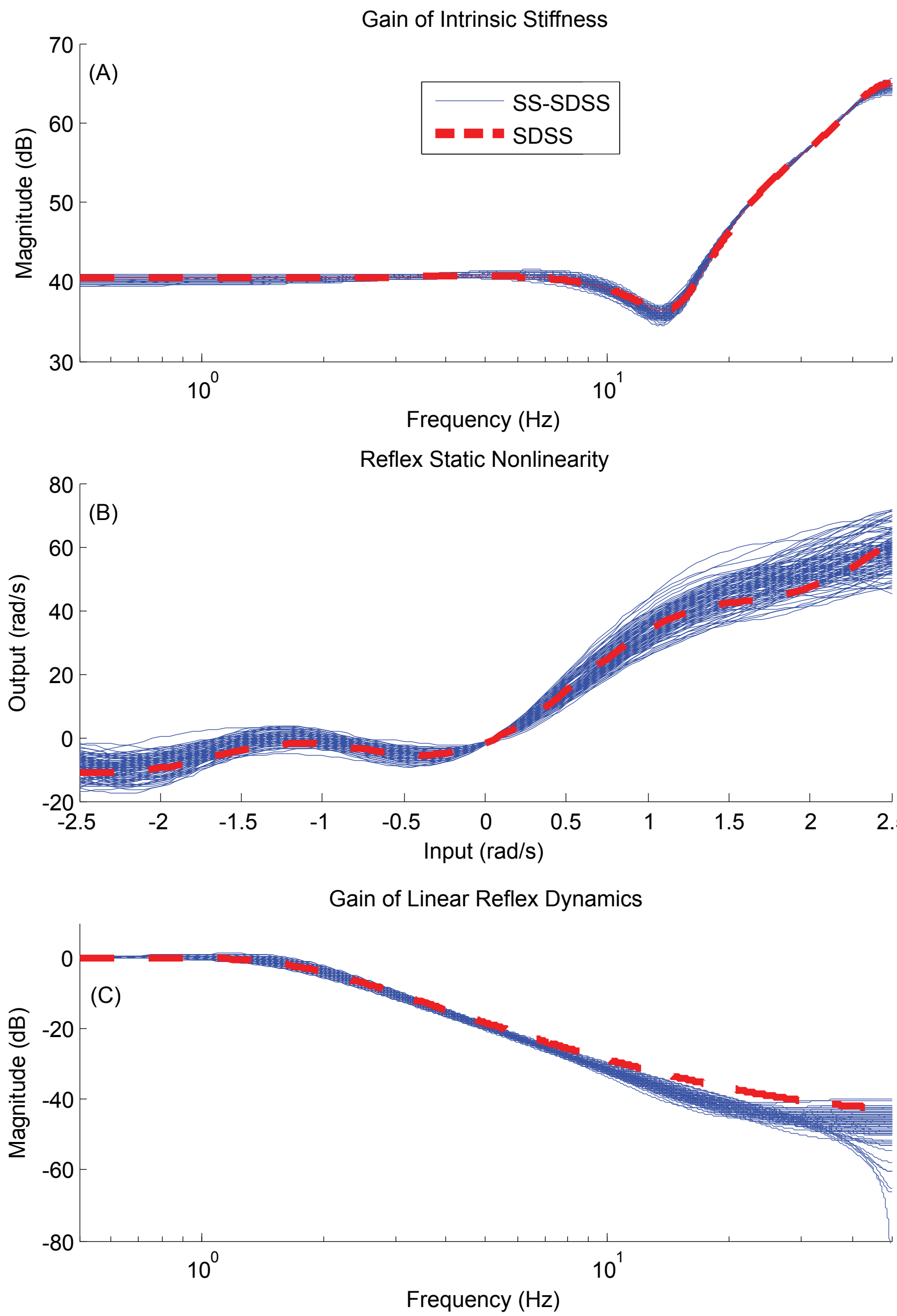

Figure 7–6: Identified models from SDSS and SS-SDSS methods during a quasi static condition when the ankle was flexed at 0.3rad: (A) intrinsic stiffness; (B) reflex static nonlinearity; (C) linear reflex dynamics.

dorsiflexed position (+0.25), reflex activity was present and large; while at a more plantarfelxed position (-0.4rad), reflex activity was altogether absent.

The models estimated predicted the torque very accurately for all 10 positions and the residuals were small. The average identification VAF was high ($90.2\% \pm 2.5\%$). Fig. 7–8 shows a typical segment recorded together with the predicted torque. There is great consistency between the measured and predicted torque and the residuals are relatively small compared to the measured torque. Thus, the model accurately predicted the torque. The torque at the first 300ms is due to the IC and it is estimated consistently. Consequently, the the model accurately estiamted the IC.

Fig. 7–9 illustrates the stiffness estimates for this subject. The frequency response of the intrinsic was high-pass nature and changed significantly with joint position. The low frequency gain and break frequency were minimal at -0.2rad and increased as the ankle was moved to more dorsiflexed or plantarflexed positions (Fig. 7–9A).

The reflex pathway also changed considerably with the joint position. There was no reflex response at positions more plantarflexed than 0 rad. That is the order of the reflex linear element was estimated to be zero. At dorsiflexed positions, the threshold and slope of the nonlinearity changed with position; the threshold decreased and slope increased as the ankle was moved to more dorsiflexed positions (Fig. 7–9B). The linear element of the reflex pathway was always low-pass in nature (Fig. 7–9C).

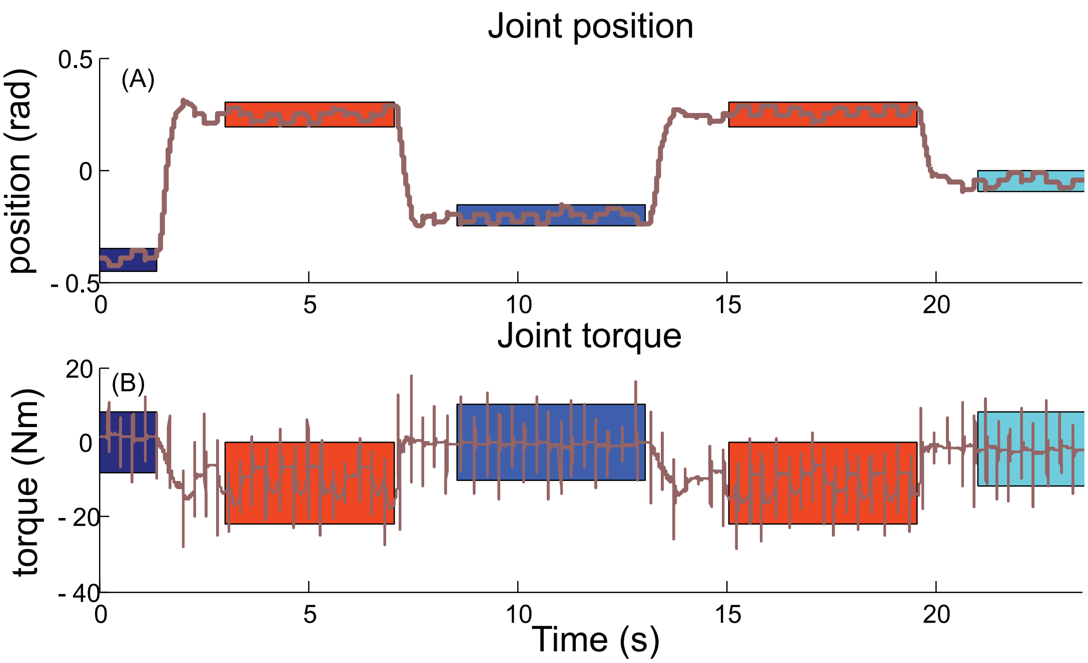

Figure 7–7: Typical position and torque data recorded from a normal subject. Segments used for identification are highlighted in different colors. Each color represents segments with the same properties: (A) joint angular position; (B) joint torque.

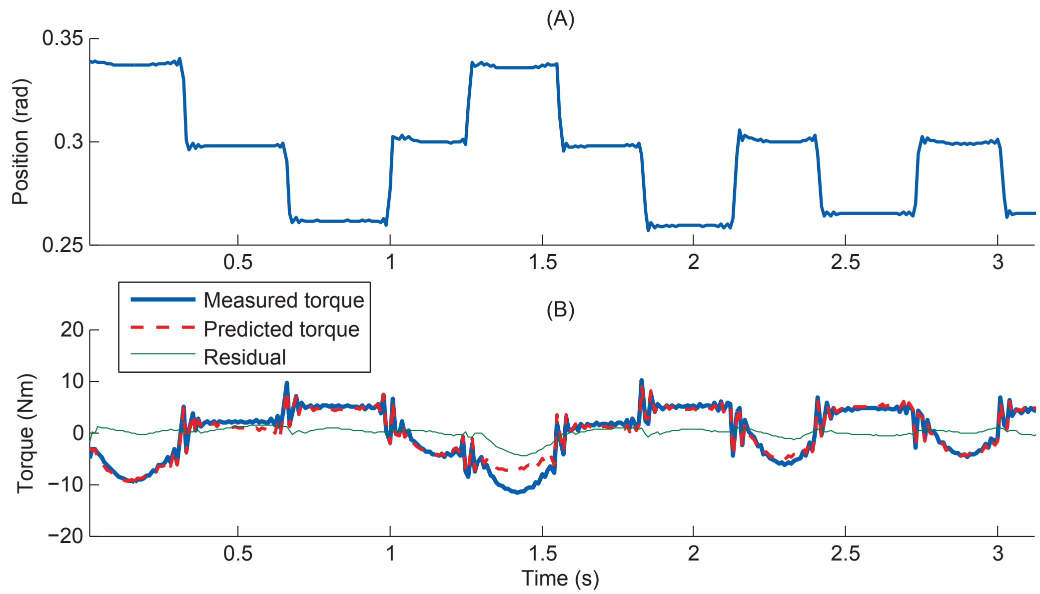

Figure 7–8: A typical recorded position-torque segment together with the predicted torque using the model when the ankle position is at 0.3 rad. The residuals are small compared to the measured torque at all time. Thus, the model predicted the torque and the IC accurately.

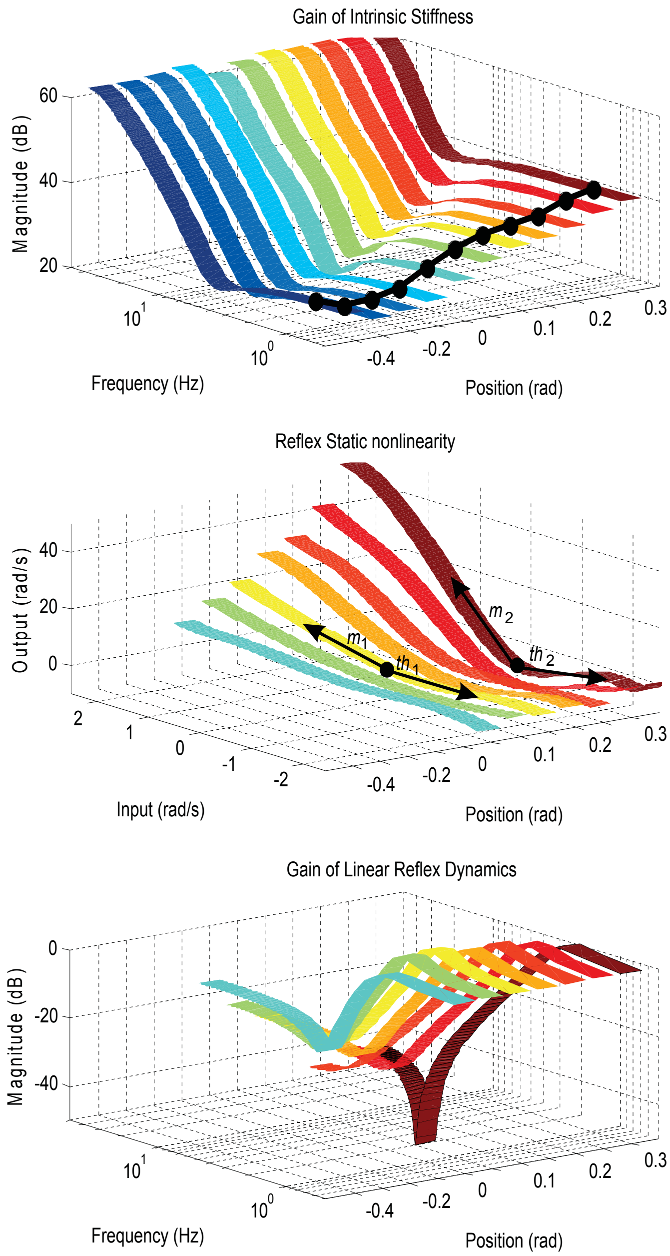

Figure 7–9: Parallel-Cascade models identified as a function of position: (A) gain portion of the intrinsic stiffness frequency response, black curve illustrates the low frequency gain (the elastic parameter); (B) estimates of the reflex static nonlinearity resemble half-wave rectifiers with varying thresholds (th_1 vs th_2) and slopes (m_1 vs m_2) models; (C) gain portion of the frequency responses of the reflex linear element.

Group Results

To estimate the stiffness parameters, the elastic parameter was estimated as the DC gain of the frequency response function of the intrinsic pathway. A half-wave rectifier model consisting of a threshold and slope was fitted to the identified Tchebychev polynomials using MATLABs optimization toolbox with the trust-region-reflective method.

Fig. 7–10 shows the stiffness parameters estimated for all five subjects. The elastic parameter was minimum midway through plantarflextion around -0.2 rad and increased significantly toward dorsiflexed positions (Fig. 7–10A). The reflex threshold (th in Fig. 7–1) decreased toward dorsiflexed positions. The reflex slope (m in Fig. 7–1) increased toward dorsiflexed positions which together with threshold modulation resulted in a larger reflex response when the ankle was dorsiflexed. We did not find a strong and consistent dependency of damping and natural frequency of the linear reflex dynamics with position.

7.6 Discussion

7.6.1 Summary

This paper presented the SS-SDSS method for identification of the ankle joint stiffness parallel-cascade structure from short stationary data segments. It fits an impulse response function to the intrinsic stiffness pathway, a polynomial to the static nonlinearity of the reflex pathway, and a state-space model to the linear dynamics of the reflex pathway. The method also estimates the initial conditions that contribute to the output of each segment. Simulation studies evaluate the performance of the

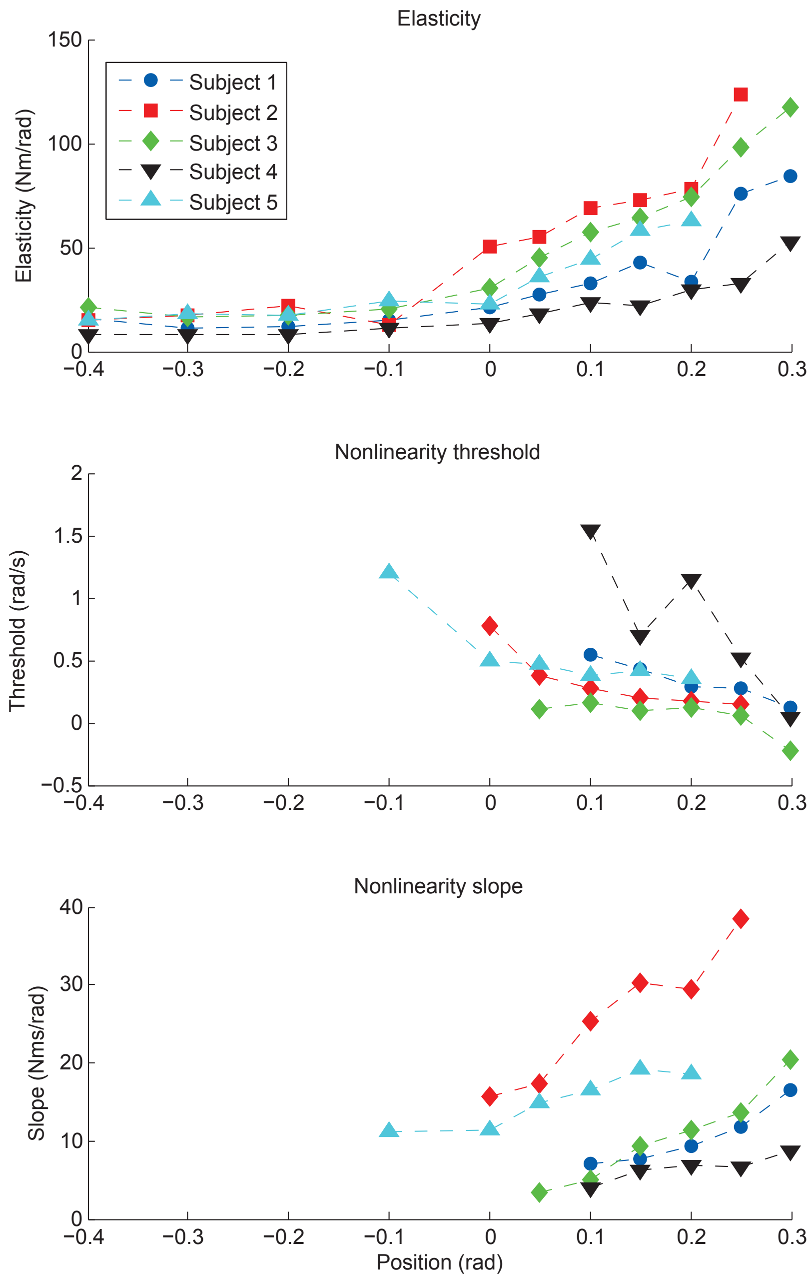

Figure 7–10: Identified stiffness parameters from all subjects : (A) the elastic parameter; (B) reflex nonlinearity threshold; (C) reflex nonlinearity slope.

method and find the total number of data samples required for a successful identification at different experimental conditions. Experimental studies show a successful application of the method in identification of the ankle joint stiffness during passive imposed movements. They demonstrate that the reflex response is controlled by changes in both threshold and gain of the pathway.

7.6.2 Algorithm Features

The SS-SDSS method is a MOESP-based subspace method and therefore inherits many of its appealing features. First, while MOESP requires little *a priori* information, it is a parametric method, and so yields models with few parameters. This is because MOESP estimates the order of the reflex linear system as part of the identification procedure; only an upper-bound on the system order needs to be specified. This is important because the reflex linear element may have more complex dynamics especially in pathological subjects [135]. Second, it can handle arbitrary colored output noise which is important because the color of the voluntary torque (considered as the output noise) is not generally known to the modeller. Third, it has been extended for identification from closed-loop data [120]. This is of particular interest when the joint is interacting with a compliant load [74, 185].

SS-SDSS also inherits the appealing features of the SDSS method. First, it decomposes the measured torque into the intrinsic and reflex torques using an orthogonal projection technique that is robust to the noise and has no convergence issues since it is not iterative [6]. Second, it provides more relevant physiological information by estimating all elements of the parallel-cascade model from the state-space model. Third, it is guaranteed to converge because it uses the normalized alternative convex search to estimate the parameters of the reflex path and the initial conditions [256, 257]. These features of the SS-SDSS method makes it an excellent tool for identification of stiffness in functionally important tasks.

The method is comparable to some other works in the literature applicable for identification of the joint biomechanics from short data segments. Ludvig and Perreault developed a nonparametric method for the identification of linear systems [190]. Their method, however, did not account for the initial conditions, making it applicable to systems with very short memories, e.g. only the intrinsic pathway. Thus, it can be expected to give biased results in the presence of the reflex activity when used with short data segments. Others considered accounting for initial conditions. Thus, Zhao and Kearney proposed a subspace approach for the identification of a general MIMO linear system encompassing the PC model [267]. However, this method required all data segments to have the same length which is difficult to achieve due to the highly unpredictable nature of the system in real experiments. Moreover, their model parameters were not directly related to the original stiffness parameters. Kukreja et al. identified a Hammerstein structure (applicable to the reflex stiffness path) from short segments of data using a transfer-function identification technique [265]. They considered and estimated initial conditions but their method deteriorated rapidly when the noise was not white, as is the case in stiffness identification [280].

7.6.3 Simulation Results

We verified the effectiveness of the SS-SDSS method in extensive simulation studies mimicking realistic experimental conditions that can affect the algorithm performance. Thus, we used Monte-Carlo simulations to give the statistics of the estimates. The input was the joint angular position recorded from our hydraulic actuator when position perturbations were delivered to subjects. Thereby, accounting for the nonlinear filtering of the actuator and load. The noise was the torque when no position perturbations were delivered to the ankle. This accounted for non-Gaussian and non-white characteristics of the noise.

Simulations were carried out over the range of parameter values observed in real experiments. Thus, we explored different levels of the noise power and different relative contributions of the intrinsic and reflex pathways. The method's performance is also dependent on the available data, i.e. number of data segments and their lengths. So, we examined different combinations of these up to the algorithm's limit.

There are two important observations from the simulation studies. First, successful identification of the reflex pathway is more difficult than the intrinsic pathway. This is mainly because of the more complex structure of the reflex pathway, i.e. Hammerstein vs linear. Second, there is a trade off between the number of segments and the mean segment length, that is the smaller the mean segment length, the more segments are required. This is important in the design of experiments since it provides guidelines to the modeller on how long the experiment must last prior to performing the experiment for reliable measurements.

7.6.4 Experimental Results

We demonstrated that the SS-SDSS method successfully identified stiffness during an imposed, passive movement of the ankle in a piecewise constant manner. We chose this paradigm because the changes of stiffness with joint position are well documented for stationary conditions [135]. Furthermore, extracting stationary segments was straightforward from this quasi-stationary task. Thus, the method accurately predicted the output and identified stiffness models and initial conditions at different segment lengths.

The stiffness model estimated from short segments were similar in shape and changed with position in a manner consistent with previous reports under stationary conditions. Thus, the intrinsic pathway had high-pass dynamics (Fig. 7–9(A)) whose low-frequency gain, corresponding to the joint elastic parameter, was minimal around -0.2 rad and increased gradually with plantarflexion and rapidly with dorsiflexion. This pattern is consistent with that reported in [175] from operating point studies which identified the elastic gain as a function of the ankle joint position but in the absence of reflex activity.

The reflex pathway was identified with a Hammerstein structure. The nonlinearities resembled a rectifier and the linear elements had low-pass filter dynamics (Fig. 7–9(B,C)) which are again consistent with the literature [37]. We provide experimental evidence for the first time that both the threshold of the nonlinearity and its slope (gain of the pathway) modulate with the joint position (Fig. 7–10(B,C)). Thus, the reflex pathway contribution was small when the joint was plantarflexed and increased toward more dorsiflexed positions. This resulted from changes in both the gain and threshold of the pathway.

We validated the identified models at each position level. Thus, the identified model when all data segments were used was taken as the nominal model. Next,

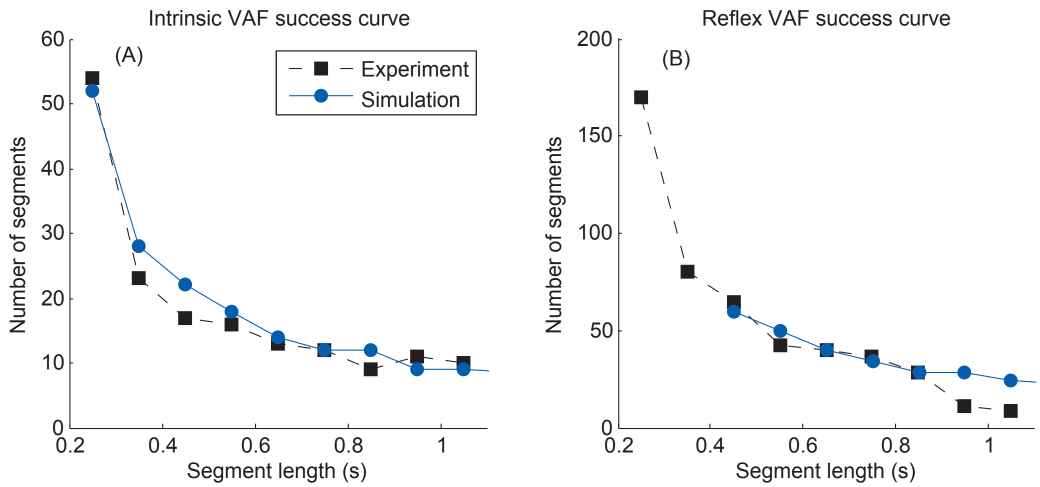

Figure 7–11: Success curves for the (A) intrinsic and (B) reflex pathway identification obtained from experimental data matched with simulation results. The effective experimental SNR level was 13.41dB and the matched simulation SNR level was 15dB. The experimental RtI level was 0.34 and the matched simulation level was $\frac{1}{3}$.

we re-segmented the data to equal-length segments with length selected from the set $\{0.25, 0.35, \cdots, 1.05\}$s. We re-identified the system at each segment length and found the required number of segments such that the validation VAF was greater than 95%. Fig. 7–11 shows the success curves when the ankle position was 0.25rad. We selected this level because the effective SNR calculated from the residuals power was 13.41dB and the RtI level was 0.34. Thus, we could easily match it to the success curves from the simulation study performed at the SNR of 15dB and RtI of $\frac{1}{3}$. It is clear that these two curves matched each other closely for both pathways. Consequently, our simulation studies were valid and accurately predicted conditions for a successful identification from experimental data.

7.6.5 Other Applications

The SS-SDSS method would be a powerful tool to characterize joint stiffness in tasks where either only short segments of data can be recorded (e.g. high contraction levels) or when the underlying dynamics are slow time-varying (e.g. quite stance). In future, it will be of interest to explore the utility of the algorithm at different experimental conditions.

An important clinical application of the method would be in quantifying severity of spasticity. The Ashworth test assesses the patients with lesion in their central nervous system, cerebral palsy, multiple sclerosis, spinal cord injury, stroke, etc [23, 281]. This test examines the resistance of the joint to passive movements in its range of motion. A trained physician applies the movement and scores the resistance based on their feeling of the resistance. Our new method could be be a useful adjunct to quantify spasticity in the joint range of motion to provide a more objective assessment [282, 156].

The method has applications to other systems showing time-varying or switching behaviour. For instance, the *Vestibulo Ocular Reflex* (VOR) circuit can be modeled with a Hammerstein structure; however, due to the switching nature of this type of eye movement, the VOR data consists of both slow and fast intervals sequentially. This results in variable length short segments of data in each mode with variable initial conditions. The Hammerstein part of the SS-SDSS method can be a useful tool for identification of such systems [265, 279].

CHAPTER 8
Discussion and Conclusion

This chapter starts by providing a general discussion and a summary of the chapters. I then list the original contributions of this thesis and presents areas of future research that can be addressed using the tools developed in this thesis. Finally, it provides recommendations and suggestions for improvement of the developed tools.

8.1 Discussion

This thesis developed a number of analytical tools for accurate measurement of stiffness during postural and imposed movement tasks. It provided rigorous testing of these tools in extensive simulation and experimental analysis and showed that they outperformed other available tools. Moreover, they unmasked important properties of the neuromuscular system and provided guidelines for future experimental designs.

Dynamic joint stiffness at the ankle can be modelled by a parallel-cascade structure with intrinsic and reflex pathways. Intrinsic stiffness has a quasi linear model and reflex stiffness has a BONL structure that is the cascade of a differentiator followed by a Hammerstein system. Any method for identification of the parallel-cascade structure must incorporate identification of Hammerstein structures. Consequently, this thesis provided tools for identification of Hammerstein structures applicable to stiffness identification as well as other biomedical systems with Hammerstein structure; it also provides tools for identification of the parallel-cascade structure specific for joint stiffness identification.

The decomposition of the torque into its intrinsic and reflex components is significant not only for modelling purposes but also for its application to the diagnosis and treatment monitoring of neuromuscular diseases. The difficulty is that intrinsic and reflex torques change together and are not individually available for measurement; only a noisy version of their sum can be measured. Consequently, decomposition of the torque is a challenging task and was an open problem which required further attention. This thesis solved this problem by providing an efficient analytical framework for decomposition of the output of systems with parallel pathways with little a priori information about their pathways.

The next step following decomposition is to estimate the intrinsic and reflex stiffnesses. This is challenging because they are complex and highly nonlinear. I addressed this problem by developing a linear state-space model of stiffness whose parameters were directly related to those of the parallel-cascade structure. The main significance was the ease of building continuous time models of the parallel-cascade elements from the linear state-space model. This was necessary to acquire any physiological interpretation. Consequently, I showed how the physiologically meaningful parameters such as the elastic and viscous parameter of the intrinsic pathway and the threshold and gain of the reflex pathway are modulated as functions of joint position or activation direction.

In a number of functionally important tasks data is either non stationary or stationary for a short period of time. I proposed to segment the measured nonstationary data into multiple, short, stationary segments. I showed that stiffness can be regarded as quasi time-invariant for data segments with the same properties, Consequently, I extended the Hammerstein and parallel-cascade methods to identify local time-invariant stiffness models from multiple, short data segments having the same properties. The main challenge was the issue of initial conditions that became important at the onset of each segment. Thus, the new methods estimated initial conditions as part of the identification algorithm. The main significance was developing a tool to explore and measure stiffness in numerous functional tasks such as upright stance, movement, etc, when the time-varying nature is slow.

This thesis pays extra attention to the static nonlinearity of the reflex pathway. Changes in the static nonlinearity had *not* been previously studied because: (*i*) the binary type signal used for excitation did not evenly excite the input range of the nonlinearity; (*ii*) lack of an accurate identification method to separate changes in the static nonlinearity from those in the linear element. This thesis uses a more effective input signal to more evenly excite the input range of the static nonlinearity. Moreover, development of accurate identification methods was the main focus of this thesis. I demonstrated that the new methods accurately tracked changes in the static nonlinearity from changes in the linear element of the reflex stiffness Hammerstein model in extensive simulation studies. Consequently, the new tools are significant and provide an accurate estimate of the static nonlinearity.

Some previous works assumed that modulation of reflex response is entirely a threshold mechanism [283]. Others hypothesized that it is entirely a gain mechanism [10, 65]. My experimental results demonstrated that both the threshold and gain change, in opposite directions, as functions of activation direction and joint position.

It is important to understand what physiological mechanisms potentially regulate the threshold and gain. Modulation of reflex gain can occur in the sensory organ (muscle spindle) and/or in the motorneuron pool. Activation of intrafusal muscle fibers in response to gamma static drive increases the baseline of the afferent firing rate [58]. This will change the threshold by bringing motor units closer to their threshold, facilitating their recruitments. Activation of intrafusal muscle fibers in response to gamma dynamic drive increases the sensitivity of the afferent [58]. This will change the gain of the reflex response. According to the alpha-gamma coactivation hypothesis, static and dynamic gamma motor neurons are synchronized with alpha motor neurons [284]. Consequently, this can be one important mechanism changing the threshold and gain of the response as a function of activation direction. Thus, when the ankle plantarflexor muscles are active, gamma motor neurons are coactivated. Hence, threshold decreases and gain increases. In contrary, when the ankle plantarflexor muscles are silent, gamma motor neurons are also silent. Hence, threshold increases and gain decreases.

Modulation can also occur in the motorneuron pool. Neurons carrying descending commands synapse with alpha motor neurons. Muscle spindle afferents also make synapses with alpha motor neurons. Activation of the ankle plantarflexor muscles will lower the threshold by facilitating the recruitment of larger motor units. Recruitment of larger motor units will increase the gain since larger motor units include more motor fibres. Nevertheless, other mechanisms such as the role of presynaptic inhibition and golgi-tendon organs cannot be ruled out.

In the following section, I will provide a more detailed summary of the findings of each chapter.

8.1.1 Summary

I started by developing the NSS method for identification of Hammerstein structures. It yielded independent estimates of the nonlinear and linear elements of a Hammerstein structure to facilitate any physiological interpretation. Contrary to other Hammerstein methods, the convergence of the new method was guaranteed. The number of parameters in the NSS state-space formulation was minimal compared to the original state-space formulation. Furthermore, any parameter was directly related to the static nonlinearity or the linear element; this increased its robustness. It estimated the order of the linear system prior to the parameter identification and thus, required little a priori information compared to other parametric methods. I explored the validity of the method using simulation studies on a Hammerstein model of the reflex stiffness. Thus, it was more robust to noise when tested against other available methods. It was more accurate and had lower variance in the estimates. Furthermore, it successfully distinguished changes in the static nonlinearity from the linear element. I showed an application to experimental data in identifying the reflex EMG response. Thus, it successfully identified the system in an isometric task at two voluntary contraction directions: PF when the ankle plantarflexor muscles were active; DF when ankle dorsiflexor muscles were active. The results showed that both the threshold of the static nonlinearity and the gain of the linear element modulated with contraction direction. Thus, at the PF contraction, the threshold was small and gain was large whereas at the DF contraction, the threshold was large and gain was small.

Next, I extended the NSS method for identification from short segments of data. I showed that initial conditions contribute significantly when only short segments of data are available. Thus, they were accounted for in the data equations and identified as part of the identification routine. The new method successfully identified the reflex EMG response in a stance experiment. I segmented the data based on the postural state acquired from the subject sway. The results showed that the reflex EMG response was larger during forward lean postural state than backward lean.

I developed the SDSS method for identification of the parallel-cascade model of stiffness. This method works by identifying an IRF model of the intrinsic pathway, a basis expansion of the reflex nonlinearity and a state-space model of the reflex linear dynamics. The SDSS method works by decomposing the total measured torque to the intrinsic and reflex torques using orthogonal projections to the intrinsic and reflex spaces and their perpendicular complements. Since the decomposition is not iterative, it did not have convergence problem. The SDSS method then fits an IRF to the estimated intrinsic torque, and uses the NSS method to identify the reflex Hammerstein structure. I showed that the SDSS method is more precise and accurate compared to other available parallel-cascade identification methods using both simulation and experimental studies. I demonstrated how the stiffness parameters of health subjects are modulated during isometric conditions as a function of muscle activation level. Thus, the elastic parameter was minimal at rest and increased with activation level. The reflex threshold was small and the reflex gain was large when the ankle plantarflexor muscles were active. The reflex threshold was small and the reflex gain was large when the ankle plantarflexor muscles were active.

I also extended the SDSS method to work for multiple, short segments of input-output data. This was achieved by incorporating the contribution of initial conditions in the system response. I performed an extensive simulation study and found the number of data samples required for a successful identification. Simulations swept a range of parameters that could be observed in real experiments. So, I explored different levels of the noise power and relative contribution of the intrinsic and reflex pathways. I applied the method to experimental data where the ankle joint was passively moved in the subject's range of motion. I showed that the method provided estimates that accurately predicted the torque. I also extracted the stiffness parameters and showed they were modulated during the course of movement. Thus, the elastic parameter was minimal mid range through the range of motion in the plantarflexion direction. It increased with plantarflexion and dorsiflexion of the joint. Moreover, the reflex threshold decreased and the reflex gain increased as the joint was moved from a plantarflexed toward a dorsiflexed position.

8.2 Original Contributions

Hammerstein Structures:

1. I developed the NSS method, the first subspace method for identification of Hammerstein structure that provides estimates of the individual elements of the structure with guaranteed convergence. This facilitates providing physiological interpretations. The previous subspace approach identified a state-space model

but did not provide individual models of the static nonlinearity and the linear dynamics.

2. I demonstrated that the NSS method accurately tracks changes in the threshold and saturation of the nonlinearity from changes in the gain of the linear element in a Hammerstein model of the reflex stiffness. The previous subspace method was unable to distinguish changes in the threshold/saturation of the nonlinearity from changes in the gain of the linear element. I demonstrated that the NSS method is more precise and accurate than a number of Hammersein identification methods that are frequently used in practice.

Parallel-Cascade Models:

3. I developed the SDSS method, the first subspace method that decomposes the torque with no convergence problem and provides estimates of all individual elements of the parallel-cascade model. Previous methods suffered from convergence issues and/or did not provide estimates of the individual elements.
4. I demonstrated that the SDSS method is more robust, accurate and precise than previous methods.
5. I developed the SS-SDSS method, the first method that identifies stiffness from multiple arbitrary-length short data segments by incorporating the effect of initial conditions. Previous methods did not consider initial conditions and suffered from biases in the estimates of the parameters in the presence of reflex response. I found experimental conditions that the SS-SDSS method

successfully identifies stiffness. This provides guidelines for the design of new experiments for reliable measurements.

6. I demonstrated that both the threshold and gain parameters of the reflex stiffness are modulated as a function of the ankle joint position and contraction direction. Previous experimental studies assumed a fixed threshold at zero which my results demonstrate to be inaccurate.

8.2.1 Future Work

Future Experimental Studies

The experimental studies in this thesis were designed to explore the validity of the identification methods. However, they unveiled interesting characteristics of the neuromuscular system. The contribution of experimental findings is secondary to the development of system identification tools. Nevertheless, they can be used as proof of principles for the design of future experiments. One immediate hypothesis to study is the threshold-gain co-variation as a function of the joint position/torque. This would extend our understanding of how the neuromuscular system regulates the reflex mechanisms.

Variance of the Estimates

The MOESP subspace method does not provide explicit estimates of the variance or confidence intervals of the state-space model parameters. Techniques such as Monte-Carlo testing, bootstrapping and cross validating have proven to be useful alternatives to give statistics of the estimates [285]. In this thesis, I have heavily performed Monte-Carlo testings in simulation studies to give the confidence intervals of parameters in a range of experimental conditions. This gives an indirect estimate of the expected confidence intervals in real experiments. I have also performed a number of cross validation studies on experimental data to validate changes in the threshold of the reflex static nonlinearity.

In order to acquire the confidence intervals of the estimates from experimental data, I propose to use a bootstrap technique. Thus, a smaller segment of the available data is selected and the stiffness parameters are identified. This process is then repeated by randomly selecting the segment many times and performing the identification. This gives a range for the parameters which can be used to extract the statistics of the parameters, e.g. mean, variance, confidence interval, etc.

Diagnosis, Assessment and Treatment

The developed methods are significant in understanding the pathophysiology as well as assessment, diagnosis, treatment prescription and monitoring of neuromuscular pathologies that change the muscle tone. In this section, I demonstrate this potential application of the developed methods on an SCI subject. I show some preliminary results, however, further analysis and exploring this aspect of the application is subject of future works.

SCI results from a change in the spinal cord's normal motor, sensory, or autonomic function. SCI patients often lose limbs strength and dexterity, bowel and bladder control, sexual function, etc [286]. Common causes of SCI damage are trauma (e.g. car accident, fall) or disease (e.g. transverse myelitis). In Canada, there are more than 86000 SCI patients and it is estimated that there are more than 4300 new SCI cases each year. The estimated annual cost of traumatic injuries alone is 3.6 billion Dollars [287].

One of the common syndrome in SCI patients is spasticity which is defined as the increased velocity-dependent resistance of muscles to stretching [288]. Spasticity is due to the loss of motor neuron inhibition and is accompanied by hypertonia, clonus, spasm and lack or impaired voluntary movement [289].

Ashworth and Fugl-Meyer scales are the widely used clinical tests to assess spasticity and to quantify the recovery of patients benefiting from a treatment or training [290, 291]. It has been reported that such clinical tests are subjective and fail to demonstrate the origin of stiffness associated with spasticity. Furthermore, they provide limited reproducibility and resolution [156, 200, 21, 292, 293, 139].

Accurate assessment of increased stiffness and identification of its origins and components is important to prescribe the correct treatment. For example, injection of botulinum toxin-A is often the first-line treatment for spasticity [136]. However, Aluhsaini et al showed that this treatment did not help children with cerebral palsy when the origin of the stiffness was intrinsic [23]. Rather, other methods such as orthopedic surgery could be used to loosen the tight muscles and to release the stiff joints [137]; orthotic management such as the use of ankle-foot-orthoses is also found to be useful [138].

I used the SDSS method to identify stiffness for an SCI subject. It is interesting to note that as recommended by the SDSS order selection, I selected a third-order system for the reflex pathway linear system, see Figure 8–1. The third-order model for the reflex system has been already suggested for spastic patients based on the hypothesis that it reflects clonus-like reflex activations that comprises several distinct bursts of activity [294].

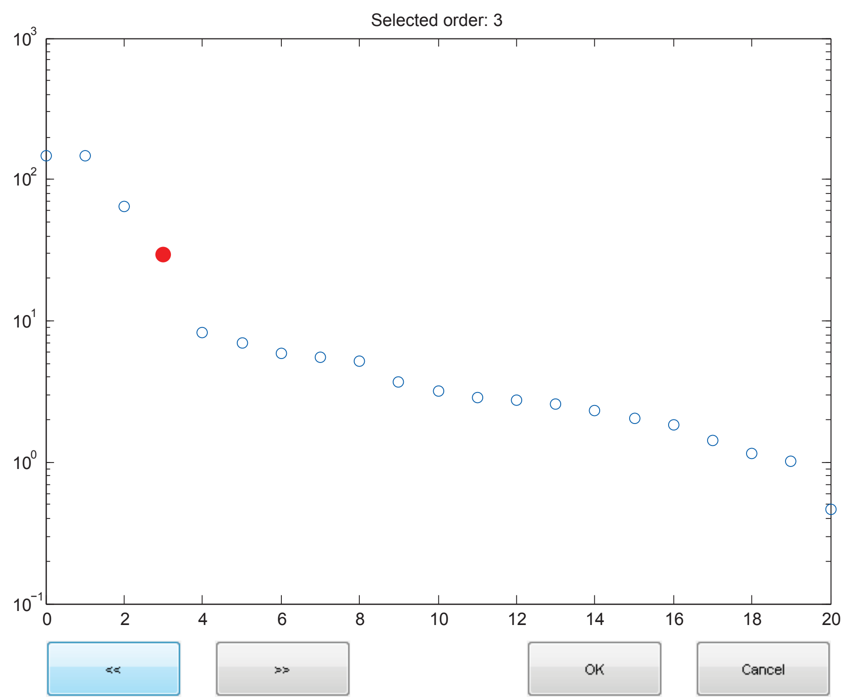

Figure 8–1: SDSS order selection selected a third order system for the reflex pathway linear dynamics.

The SDSS method successfully identified stiffness with identification %VAF of 92.2%. Figure 8–2 shows a 6s segment of the input and output data along with the predicted responses. There are two main observations: (1) the reflex contribution is much larger compared to that of a normal subject at rest; the intrinsic torque VAF is only 10.7% while the reflex torque VAF is 85.8%. (2) the reflex response to a single perturbation shows multiple bursts of reflex responses (clonus-like response). These activation bursts coincides with EMG activity.

Figure 8–3 demonstrates the identified stiffness model. The intrinsic stiffness model shows high-pass dynamics similar to those observed in normal subjects. However, the slope of the static nonlinearity (the gain of the reflex pathway) is significantly larger than those observed in normal subjects. The linear element of the reflex stiffness pathway shows a resonance at 5Hz to capture the clonus-like responses.

Some studies hypothesized that spasticity results purely from a decrease in the reflex threshold [295, 296] or purely because of increase in the gain [297, 298]. I have shown that SDSS is a powerful tool to distinguish changes in the threshold from the gain of the reflex pathway. Consequently, SDSS can be used to document changes in the threshold and gain in spastic patients.

It will be of interest to use the SDSS method to study spasticity in other pathologies such as Multiple Sclerosis, Cerebral Palsy, Stroke, etc. It will also remain of interest to use the SS-SDSS method to quantify stiffness during joint imposed movements similar to those exerted in the Ashworth test to provide a more objective assessment of spasticity.

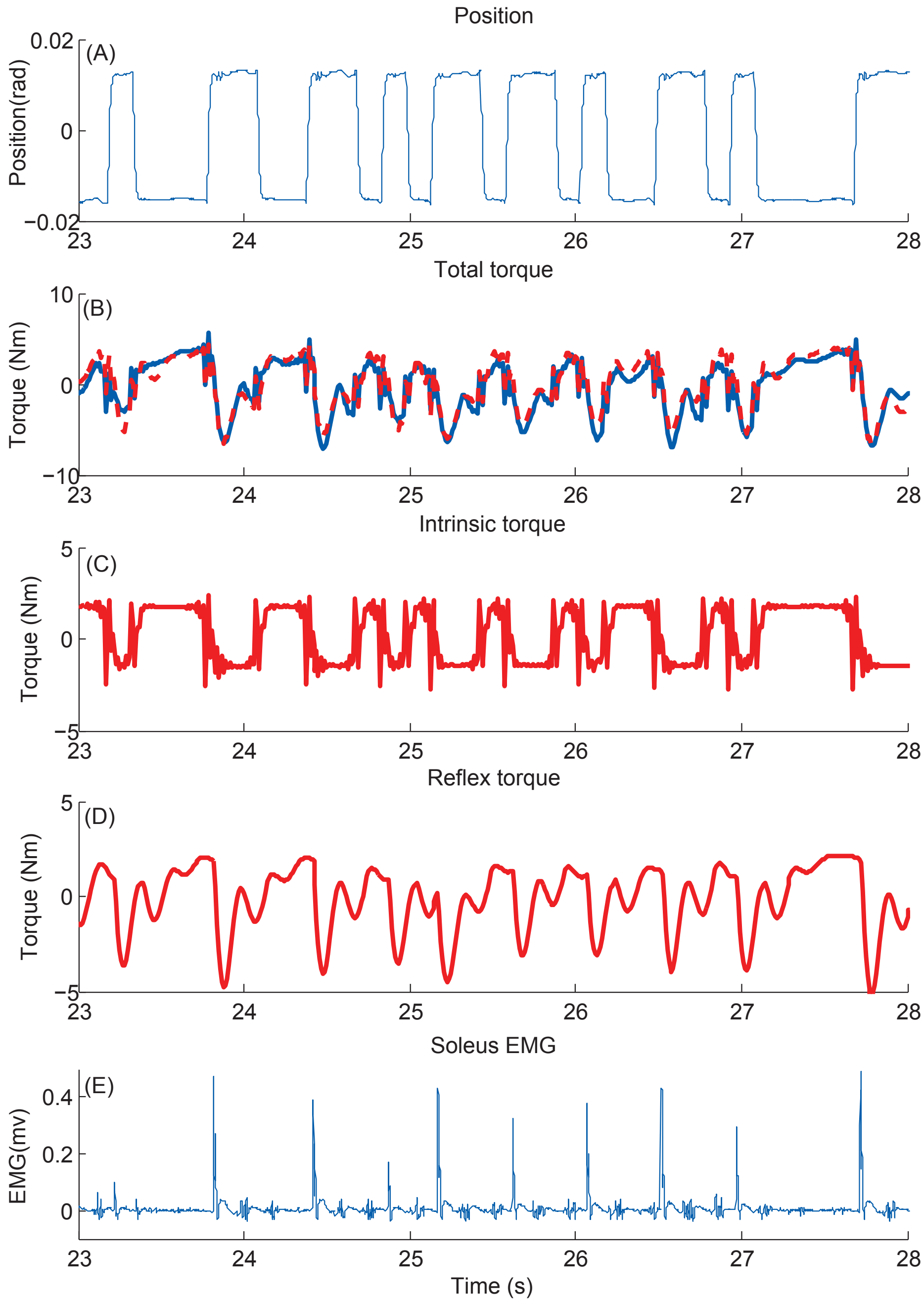

Figure 8–2: A segment of input-output data from a spastic subject: (A) measured position; (B) measured torque along with the predicted one; (C) predicted intrinsic torque; (D) predicted reflex torque; (E) measured Soleus EMG signal.

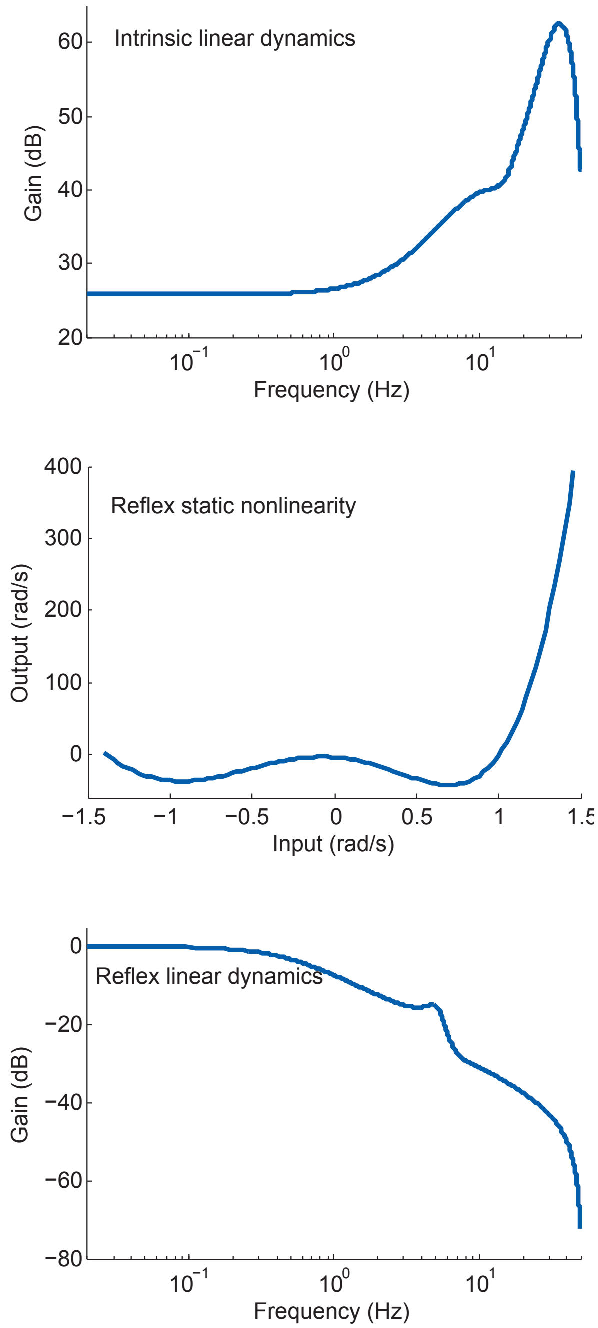

Figure 8–3: Identified spastic stiffness model showing the gain of the frequency response of the intrinsic stiffness, the reflex pathway static nonlinearity and the gain of the frequency response of the reflex linear element.

Closed-Loop Identification

When a joint interacts with a compliant load, the generated torques in response to position perturbations and voluntary mechanisms change the joint position via a feedback representing dynamics of the load. This has significant practical applications such as during upright stance where the body is considered as an inertial load with that the ankle is interacting. Consequently, in such conditions, the position and torque signals are recorded from a closed-loop system.

Subjects modulate their muscle activation according to the requirement of a task. For example, during walking, the Triceps Surae muscles are activated during the stance phase of the gait cycle and the Tibialis anterior muscle becomes activated during the swing phase [186]. The degree of the activation and coactivation of muscles changes the voluntary torques. This thesis studied stiffness when the activation was held constant throughout the experiment. Thus, this constant was removed prior to the identification. However, when the activation is varying, one needs to decompose the total torque to the intrinsic, reflex and voluntary torques. One way to perform the decomposition is to estimate the voluntary torque from the background EMG signals. This relationship has been modelled as a Hammerstein model in a closed-loop system. The feedback loop has been attributed to the inherent force feedback mechanisms of the Golgi tendon organs [299]. Consequently, identification of Hammerstein system from closed-loop data is also important in studying stiffness in a more function task.

The main difficulty in identification of closed-loop system is that the output noise (voluntary torque and measurement noise) enters the input signal via the feedback. The input and noise become correlated which is in contrast with the first assumption of many cross-correlation based methods such as the HK, SLS or PC methods. [181]. Consequently, closed-loop identification of stiffness is a challenging problem.

The MOESP method has been modified to consistently identify systems from data recorded in closed-loop. This can be achieved by using proper instrumental variables such as the past input and output signals together [120] or the reference input signal that is not correlated with the noise but is correlated with the system states [116]. This version is called the *Errors In Variables* (EIV-MOESP) method. Zhao et al successfully applied this method to identify stiffness in closed-loop and showed that it outperformed the PC method [300, 122].

It will be of interest to extend the methods of this thesis to the closed-loop condition. This can be achieved by considering the reference input and the past input and output signals as instrumental variables to estimate the A and C matrices. The reference input can also be used as an instrumental variable in the iterative least-squares solutions of the parameters of the static nonlinearity and the B and D state-space matrices.

Identification of the Reflex Static Nonlinearity

I demonstrated that the threshold and slope of the reflex static nonlinearity are modulated as functions of the joint position and activation direction. Consequently, it is important to accurately identify these parameters in order to understand how the neuromuscular system regulates the reflex mechanism. One option is to use splines to extract these parameters. I show an extension of the NSS method to use splines in Appendix A.2. The main difficulty is that the output is a nonlinear function of the spline knot sequence that is difficult to solve.

In future, it will be of interest to extend the method to use splines with optimized knot location computed analytically or numerically. One way to solve this problem is to separate the unknown parameters into two sets, one that is the knot sequence and one that consists of the coefficients of the splines together with the state-space matrices of the linear element. Thus, a separable least squares technique can be developed to solve the problem. It is also of interest apply the decomposition routine and extend this Hammerstein method to the parallel-cascade model.

Time-Varying Identification

I have developed a number of methods to identify stiffness during time-invariant or quasi time-invariant conditions. However, during movement, changes in the joint position and muscle activation are large and stiffness dynamics exhibit time-varying behaviours. Consequently, it will be of interest to extend the developed methods to identify time-varying stiffness models.

One way to characterize the time-varying properties of stiffness is to relate the time-varying changes in the parameters as a function of a scheduling variable which can be the joint position, muscle activation or even time. Sobhani et al. extended the NSS method to identify LPV Hammerstein models with a time-varying LPV static nonlinearity and a time-invariant state-space model [301]. This method successfully identified the reflex EMG response of the ankle plantarflexors during movement [302]. Sobhani et al. also extended the SDSS method to identify the parallel-cascade system with a time-varying LPV IRF model of the intrinsic pathway and a time-varying LPV reflex static nonlinearity a and time-invariant reflex linear dynamics. They showed a successful application in measuring stiffness during movement [206]. In the future, it is of interest to apply these methods to identify stiffness in an activation varying task.

The main difficulty of these LPV extensions is that the reflex linear element was assumed to be time-invariant. However, there is evidence that these dynamics change with the joint operating point [65]. Consequently, it remains of interest to extend the LPV methods for time-varying LPV reflex dynamics. This problem can be addressed by expanding the state-space matrices of the reflex linear dynamics as a function of the scheduling variable. The coefficients of these expansion can be identified using two approaches: (i) formulating the problem of estimating the expansion coefficients as a nonlinear optimization search and using the identified time-invariant model to initialize the search [303]. (i) identifying the expansion coefficients using the Kernel methods that have been developed for open-loop and closed-loop systems [304, 305].

APPENDIX A
Appendix

A.1 Documentations and Implementations

The algorithms developed in each chapter of this thesis are implemented in the *NonLinear IDentification* (NLID) toolbox, an object oriented toolbox developed in our laboratory.

Segmented Data

I created the segdat object which is a subset of the nldat object to support segmented data. Consequently, it has all parameters of the nldat object with some new parameters to show the start and end of the segments.

Construction:

dataSEGDAT = segdat(data,'onsetPointer',onsetPointer,'segLength',segLength);

where onsetPointer is a vector with elements showing the first sample of each data segment and segLength is a vector with elements showing the length of each data segment in samples.

Methods:

The segdat object inherits all methods of the nldat objects. Some methods such as ddt, decimate, cat, nldat, vaf are updated to support the new feature.

State-Space Model

I created the ssm object for discrete time state-space models.

Construction:

systemSSM = ssm('A',A,'B',B,'C',C,'D',D,'domainIncr',ts,'nDelayInput',Δ);

where A, B, C, D are the state-space matrices, ts is the sampling time and Δ is the input delay.

Identification:

systemSSM = nlident(systemSSM,z,'idMethod',idMethod,'orderSelect',orderSelect ,'hankleSize',hankleSize,'displayFlag',displayFlag);

or

systemSSM = ssm(z,'idMethod',idMethod,'orderSelect',orderSelect ,'hankleSize',hankleSize,'displayFlag',displayFlag);

where z contains the input and output signals as nldat or segdat objects. The idMethod can be set to PI to use the past input or PO to use the past output as the instrumental variable of the MOESP subspace method. orderSelect can be set to 'manual' for the user to select the order of the system by inspecting singular values or 'largest-gap' for the method to automatically select the system order based on the largest gap between large and small singular values. hankelSize is an integer number that defines the size of the hankel matrix and must be set by the user to be larger than the system order. If displayFlag is set to 1, the algorithm plots the predicted output superimposed with the measured output after the identification.

Methods:

systemSSM = nlident(systemSSM,z) identifies the ssm object parameters from input and output signals.

output = nlsim(systemSSM,input) simulates the ssm object to the input signal that can be an nldat or segdat object.

plot(systemSSM) plots the IRF representation of the ssm object.

systemFRESP = fresp(system) converts the ssm object to an NLID frequency response object.

systemIRF = irf(system) converts the ssm object to an NLID impulse response object.

set(system) sets the parameters of the ssm object.

Hammerstein Model

I updated the nlbl object to support state-space models.

Construction:

systemHammerstein = nlbl('elements',systemPOLYNOM,systemSSM);

where systemPOLYNOM is a polynom (polynomial) object that represents the static nonlinearity and systemSSM is an ssm object.

Identification:

systemHammerstein = nlident(systemHammerstein,z,'idMethod','subspace'
,'maxOrderNLE',maxOrderNLE,'threshNSE',threshNSE,'hankleSize',hankleSize
,'orderSelect',orderSelect,'nDelayInput',nDelayInput);

or

systemHammerstein = nlbl(z,'idMethod','subspace','maxOrderNLE',maxOrderNLE
,'threshNSE',threshNSE,'hankleSize',hankleSize,'orderSelect',orderSelect
,'nDelayInput',nDelayInput);

where z contains the input and output signals as nldat or segdat objects. maxOrderNLE is the maximum order of the Tchebychev polynomial, threshNSE is the threshold for termination of the iterative Hammerstein method and the rest of the parameters are similar to those explained for the ssm object. It uses the NSS (for nldat objects) and SS-NSS (for segdat objects) method developed in Chapter 4 and 5 for identification.

Methods:

The following Hammerstein methods are modified to support the new state-space model.

systemSSM = nlident(systemSSM,z,'idMethod','subspace') identifies a Hammerstein structure using the MOESP subspace method.

output = nlsim(systemSSM,input) simulates the Hammerstein model to the input signal that can be an nldat or segdat object.

plot(systemSSM) plots the Hammerstein model with the IRF representation of the ssm object.

Parallel-Cascade Identification

The following function estimates the parallel-cascade model from position and torque data. It is based on the methods developed in Chapter 6 and 7.

Syntax:

[intrinsicModel, reflexModel, tqI, tqR, tqT] = SDSS_stiffnessID (z)

where z is input-output data as nldat or segdat objects.

intrinsicModel is the IRF model of the intrinsic pathway.

reflexModel is the Hammerstein model of the reflex pathway with a Tchebychev polynomial identified for the static nonlinearity and a state-space model for the linear dynamics.

[tqI, tqR, tqT] are the predicted intrinsic, reflex and total torques.

The following options are available when calling this routine.

'decimation_ratio': The ratio that the input-output are decimated with. The default is 10.

'order': is the maximum order of reflex static nonlinearity. The default is 12.

'hankel_size': is the size of Hankel matrix and must be larger than the order of the reflex linear dynamics. The default is 20.

'delay': is the delay of the reflex stiffness pathway in seconds. The default is 0.04.

'orderdetection': The order selection method used for the subspace method. It can be 'manual' or 'largest-gap. The default is 'manual'

A.2 Subspace Identification of Hammerstein Systems Using B-Splines

I showed that the threshold and slope of the reflex static nonlinearity are modulated as a function of the activation direction in Chapter 4 and 6, and as a function of joint position in Chapter 7. Consequently, it is important that the identification method accurately identifies the threshold and slope of the nonlinearity. In this chapter, I develop this idea by using B-Splines as a basis to expand the reflex static nonlinearity. This chapter is a conference paper that was published in Proceedings of 34th Annual International Conference of the IEEE Engineering in Medicine and Biology Society.

Proceedings: 34th Annual International Conference of the IEEE Engineering in Medicine and Biology Society, pp. 3316-3319, 2012.

A.2.1 Abstract

This paper presents an algorithm for the identification of Hammerstein cascades with hard nonlinearities. The nonlinearity of the cascade is described using a B-spline basis with fixed knot locations; the linear dynamics are described using a state-space model. The algorithm automatically estimates both the order of the linear system and the number and locations of the knots used to characterize the nonlinearity. Therefore, it significantly reduces the *a priori* knowledge about the underlying system required for identification. A simulation study on a model of reflex stiffness shows that the new method estimates the nonlinearity accurately in the presence of output noise.

A.2.2 Introduction

The Hammerstein structure consists of a zero memory static nonlinearity followed by a linear dynamic system as illustrated in Fig. 1 [249], [96]. Biological examples include the reflex stiffness of the human ankle joint and the mechanical behavior of lung tissue [37], [81]. Therefore, the accurate identification of Hammerstein systems is an important problem.

Subspace methods are a well-developed set of tools for the identification of linear systems. They represent a linear system by a state-space model that can be estimated with no *a priori* knowledge about the system order [113], [123].

Recently, we developed a subspace algorithm for the identification of Hammerstein cascades that uses the framework proposed in [252] to estimate the parameters corresponding to the nonlinearity separately from those of the linear state-space model. The algorithm models the nonlinearity with an orthogonal Tchebychev polynomial, and separates the parameters into two sets: one corresponding to the static nonlinearity and the second to the state-space model. The output is a linear function of each parameter set provided the other set is held constant. Consequently, an iterative least-squares procedure can be used to find the optimum nonlinear and linear component parameters [258].

We assessed the performance of this algorithm using a small signal model of ankle stretch reflex stiffness where we modeled the nonlinearity with a half-wave rectifier (threshold) and the linear component with a second-order low-pass filter. We demonstrated that the algorithm could distinguish changes in threshold from those in the linear component gain [306].

A more general model for the reflex stiffness of one muscle would include both threshold and saturation behaviors [229]. Moreover, joints are controlled by multiple muscles which can be expected to have different thresholds and saturations. This could lead to nonlinearities with sharp changes in slopes. The presence/absence of these corner points could be significant in interpreting the underlying physiology

[221]. Pilot experimental results from our laboratory confirm that the reflex nonlinearity is more complex than a simple half-wave rectifier [306].

Such hard nonlinearities are difficult to model using finite-order polynomials due to problems with oscillations and instability. Consequently, it is difficult to accurately estimate the corner points when using a Tchebychev expansion to describe the nonlinearity. One solution to this problem is to represent the nonlinearities using splines as in [250].

The contribution of this paper is twofold. First, we develop a subspace identification method for Hammerstein cascades using splines. Splines have been used for Hammerstein identification previously, but the linear component was described in terms of its *impulse response function* (IRF) [250]. Replacing the IRF with a state-space model can reduce the number of unknown parameters dramatically - especially for systems with large memory. Therefore, state-space identification should be more robust in presence of noise.

Second, in our spline formulation, we show how to choose number of knots and their locations to describe the static nonlinearity parsimoniously. This is significant since the proper choice of the nonlinearity is not well understood and is usually based on trial and error.

The paper is organized as follows. Section II reviews the B-spline basis functions, formulates the problem and describes the algorithm. Section III presents the results of a simulation study that evaluates the performance of the new algorithm and compares it to our previous method. Section IV provides a summary and some concluding remarks.

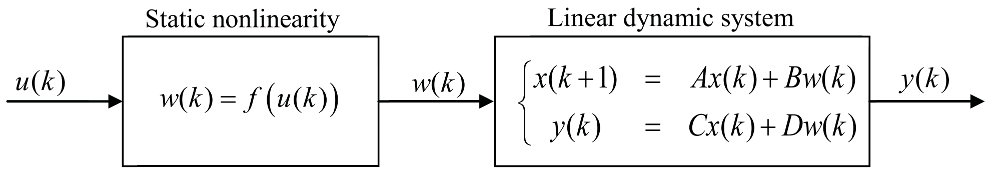

Figure A–1: Hammerstein model as a cascade of nonlinear-linear block.

A.2.3 Theory

B-Spline

A k-th order B-spline is defined by a set of knot points where the output between each pair of knots is given by a $(k-1)$-th order polynomial. The first $(k-2)$ derivatives of the spline are continuous at the knot locations [307]. If the knot sequence $\Lambda = \{\lambda_1,\ \lambda_2,\ \cdots, \lambda_{n+k}\}^T$ is as follows:

$$\begin{aligned} \lambda_1 = \cdots = \lambda_k = L_1 < \lambda_{k+1} \leqslant \cdots \leqslant \lambda_n < \\ < L_2 = \lambda_{n+1} = \cdots = \lambda_{n+k} \end{aligned} \tag{A.1}$$

where L_1 and L_2 are the minimum and maximum of the nonlinearity's input. Then, the spline's output w is defined as:

$$w = \sum_{j=1}^{n} S_j^{\{k\}}(u)\alpha_j \tag{A.2}$$

where α is the set of coefficients of the B-spline $\alpha = [\alpha_1, \cdots, \alpha_n]^T$ and $S_j^{\{k\}}$ is the sequence of normalized B-splines of order k with respect to the knot sequence Λ and is derived from the following recursive equation:

$$S_j^{\{1\}}(u) = \begin{cases} 1 & \text{if } \lambda_j \leqslant u < \lambda_{j+1} \\ \\ 0 & \text{otherwise} \end{cases} \tag{A.3a}$$

$$S_j^{\{k\}}(u) = p_j^{\{k\}}(u) S_j^{\{k-1\}}(u) + \left(1 - p_{j+1}^{\{k\}}(u)\right) S_{j+1}^{\{k-1\}}(u) \tag{A.3b}$$

$$p_j^{\{k\}}(u) = \begin{cases} \frac{u-\lambda_j}{\lambda_{j+k-1}-\lambda_j} & \text{if } \lambda_j < \lambda_{j+k-1} \\ \\ 0 & \text{otherwise} \end{cases} \tag{A.3c}$$

Now, the output of the nonlinearity based on this approximation is:

$$W = \boldsymbol{S}\alpha \tag{A.4}$$

where, W is the sampled vector of the output of the nonlinearity $W = [w(1), \cdots, w(N)]^T$ and $\boldsymbol{S}$ is the observation matrix defined as follows:

$$\boldsymbol{S} = \begin{bmatrix} S_1^{\{k\}}(u(1)) & \cdots & S_n^{\{k\}}(u(1)) \\ S_1^{\{k\}}(u(2)) & \cdots & S_n^{\{k\}}(u(2)) \\ \vdots & & \vdots \\ S_1^{\{k\}}(u(N)) & \cdots & S_n^{\{k\}}(u(N)) \end{bmatrix} \tag{A.5}$$

Hammerstein Formulation

Consider the *single input single output* SISO Hammerstein system shown in Fig. 1. Assume that the order of the linear system is m and the elements of the B and D state-space matrices are $B = [b_1, \cdots, b_m]^T$ and $D = [d]$. Transform this SISO nonlinear cascade to a *multi input single output* MISO linear system whose n inputs are the outputs of the constructed spline basis functions, i.e., $U(k) =$

$\left[S_1^{\{k\}}(u(k),\Lambda) \ \cdots \ S_n^{\{k\}}(u(k),\Lambda)\right]^T$. The resulting MISO state-space model is:

$$\begin{cases} x(k+1) & = Ax(k) + B_\alpha U(k) \\ y(k) & = Cx(k) + D_\alpha U(k) \end{cases} \tag{A.6}$$

where, $x(k)$ is the state vector while, A and C are the linear system state-space matrices. The elements of B_α and D_α are given by:

$$B_\alpha = \begin{bmatrix} b_1\alpha_1 & \cdots & b_1\alpha_n \\ \vdots & \ddots & \vdots \\ b_m\alpha_1 & \cdots & b_m\alpha_n \end{bmatrix} \tag{A.7}$$

$$D_\alpha = \begin{bmatrix} d\alpha_1 & \cdots & d\alpha_n \end{bmatrix} \tag{A.8}$$

The measured output $\tilde{y}(k)$ is contaminated with noise:

$$\tilde{y}(k) = y(k) + n(k) \tag{A.9}$$

If the state-space matrices A and C are known, the output of the Hammerstein system is given by [258], [116]:

$$\begin{aligned} \tilde{y}(k) = & \left[\sum_{\tau=0}^{k-1} U^T(\tau) \otimes CA^{k-1-\tau}\right] \text{vec}(B_\alpha) + U^T(k)\text{vec}(D_\alpha) \\ & + n(k) \end{aligned} \tag{A.10}$$

where $\otimes$ is the Kronecker product. Rewriting (A.10) in a matrix format gives:

$$\begin{aligned} \tilde{Y} = & \Psi \left[\alpha_1 b_1 \ \cdots \ \alpha_1 b_m \ \cdots \ \alpha_n b_1 \ \cdots \ \alpha_n b_m \ \alpha_1 d \ \cdots \ \alpha_n d\right]^T \\ & + N \end{aligned} \tag{A.11}$$

where Ψ is the observation matrix defined using the input signal as well as A and C according to (A.10). This relation shows that the unknown parameters comprise two sets: α which contains the coefficients of the spline, and $\theta_{bd} = [b_1, \cdots, b_m, d]^T$ which contains the state-space elements.

Identification Algorithm

Step 1: Assume the knot sequence Λ, $\lambda_1 = \cdots = \lambda_k = \min(u(k))$ and $\lambda_{n+1} = \cdots = \lambda_{n+k} = \max(u(k))$ where $\lambda_{k+1}, \cdots, \lambda_n$ are equally spaced across the input signal range with the resolution of $\frac{\max(u(k)) - \min(u(k))}{n-k}$.

Step 2: Construct the B-spline basis expansion (A.5) of the input signal using the knot sequence Λ.

Step 3: Use the MOESP algorithm, described in [113], to estimate the A and C matrices of the linear state-space model of (A.6) using the constructed input signal (U(k)) and noisy output (A.9).

Step 3: Initialize the coefficients set $\alpha = [1, \cdots, 1]^T_{n\times 1}$.

Step 4: Construct the matrix Ψ_α:

$$\Psi_\alpha = \Psi \begin{bmatrix} 0 & \cdots & \cdots & \cdots & \cdots & \cdots & 0 & \hat{\alpha}_1 & \cdots & \hat{\alpha}_n \\ 0 & \cdots & \hat{\alpha}_1 & \cdots & 0 & \cdots & \hat{\alpha}_n & 0 & \cdots & 0 \\ \vdots & \iddots & \vdots & & \vdots & \iddots & \vdots & \vdots & & \vdots \\ \hat{\alpha}_1 & \cdots & 0 & \cdots & \hat{\alpha}_n & \cdots & 0 & 0 & \cdots & 0 \end{bmatrix}^T \tag{A.12}$$

Estimate θ_{bd} by solving the least-squares problem: $Y = \Psi_\alpha \theta_{bd}$

Step 5: Construct the matrix Ψ_{bd}:

$$\Psi_{bd} = \Psi \begin{bmatrix} b_1 & 0 & \cdots & 0 \\ \vdots & \vdots & \ddots & \vdots \\ b_m & 0 & \cdots & 0 \\ 0 & b_1 & \cdots & 0 \\ \vdots & \vdots & \ddots & \vdots \\ 0 & b_m & \cdots & 0 \\ \vdots & \vdots & \vdots & \vdots \\ 0 & 0 & \cdots & b_1 \\ \vdots & \vdots & \ddots & \vdots \\ 0 & 0 & \cdots & b_m \\ d & \cdots & \cdots & 0 \\ \vdots & \ddots & & \vdots \\ \vdots & & \ddots & \vdots \\ 0 & \cdots & \cdots & d \end{bmatrix} \tag{A.13}$$

Estimate α by solving the least-squares problem: $Y = \Psi_{bd}\alpha$.

Step 6: Compute the *sum of squared errors* SSE for the model and compare it to that from the previous iteration. Go to step 7 if there is not a significant decrease. Otherwise, go to Step 4.

Step 7: Sort the knot points as follows. Recall that in a k^{th} order spline, the $(k-1)^{\text{th}}$ derivative is discontinuous at the knot locations. If the $(k-1)^{\text{th}}$ derivative is discontinuous at a knot location, that knot is active and contributes to the characterization of the static nonlinearity. If the $(k-1)^{\text{th}}$ derivative is continuous, that knot does not actively contribute in characterization of the static nonlinearity [308]. In the presence of output noise, however, the spline coefficient estimation is not perfect and small discontinuities in the $(k-1)^{\text{th}}$ derivative may be observed at inactive knots. Consequently, we sort the knots according to the amount of discontinuity in the $(k-1)^{\text{th}}$ derivative which can be simply measured from the $(k-2)^{\text{th}}$ derivative at knot locations.

Step 8 Iteratively, identify the system by adding knots according to the order of the sorted sequence of Step 7. Calculate the *mean squared error* (MSE) at each identification. Stop adding knots when no significant improvement in MSE is observed.

A.2.4 Simulation Results

We assessed the performance of the algorithm using a small signal model of ankle stretch reflex stiffness. The input to this system is the angular velocity of the ankle joint and the output is the reflex torque. This system was modeled as a Hammerstein system consisting of a half wave rectifier followed by a second-order low pass filter [37], [65].

More recent work has demonstrated that in the human ankle, the threshold is not fixed at zero [249] but changes with the background torque level [306]. Moreover, there is also experimental evidence for a saturation nonlinearity. Furthermore, several muscles, presumably with different thresholds, interact to generate the overall reflex response. Therefore, we considered a more general nonlinearity model consisting of a threshold, an intermediate change of slope, and a saturation as shown in Fig. 2. This type of nonlinearity models three experimental phenomena: (a) the strong

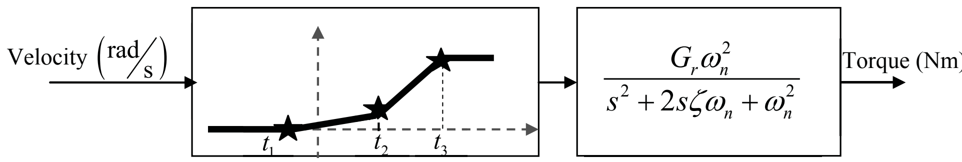

Figure A–2: Hammerstein model of reflex stiffness.

unidirectional rate sensitivity (t_1), (b) activation of a set of new muscle fibers (t_2) and (c) the saturation of the response at high velocities (t_3). Consequently, the nonlinearity has three corner points which were set to $t_1 = -0.4,\ t_2 = 0,\ t_3 = 0.4$. We modeled the linear system as a second-order low-pass filter:

$$G(s) = \frac{G_r\omega_n^2}{s^2 + 2s\zeta\omega_n + \omega_n^2} \tag{A.14}$$

The parameters of the linear element were chosen to be similar to those found experimentally ($G_r = 1,\ \omega_n = 55,\ \zeta = 2.2$) [65].

The input angular joint velocity signal was a uniform random number between -3 and 3 rad/s. We simulated the input and output signals at 1000 Hz for 60s. A realization of white Gaussian noise was added to the output to generate a *signal to noise ratio* (SNR) of 10 dB.

We identified that system from the simulated data using an initial spline of order 2 with 34 knots equally spaced in the range of input.

Fig. 3(A) shows the derivative of the nonlinearity estimated with 34 knots after step 6 of the algorithm. It is evident that the derivative is discontinuous at some knot locations but not others. To separate knots whose discontinuities were not significant from those with significant discontinuities, we sorted the knots by the value of their second derivatives as shown in Fig. 3(B). Fig. 3(C) shows that after selection of the first five knots, the MSE between the predicted output of the Hammerstein cascade and clean output converged to a small number. This indicates that only the first five knots were important and adding more knots would not significantly improve the identification. Consequently, we consider only the first five important knots as active ones.

We identified the system once again using only the active knots and also compared the result with our previous algorithm in [258] which used an 8-th order Tchebychev polynomial with a subspace identification approach. Fig. 4(A) shows the results. It is evident that the spline was more accurate despite having fewer parameters than the polynomial. Moreover, the transition points, which were not easily identified in the Tchebychev polynomial, were clearly evident with splines. The *variance accounted for* (VAF) of the estimated output compared to the clean output using spline was higher than Tchebychev: 99.97% for B-spline and 97.62% for Tchebychev. Fig. 4(B) shows that the frequency response of the identified linear dynamic using B-spline and Tchebychev matched the true system accurately.

A.2.5 Discussion

An identification algorithm was developed for Hammerstein cascade systems. The algorithm uses a subspace approach and is useful for systems with hard nonlinearities. It models the nonlinear element with a B-spline and the linear element with a state-space model. It then transforms a SISO Hammerstein system to a MISO linear system.

Simulation results of a model of ankle reflex stiffness show that the new method provided more accurate estimates of the nonlinearity than our previous subspace

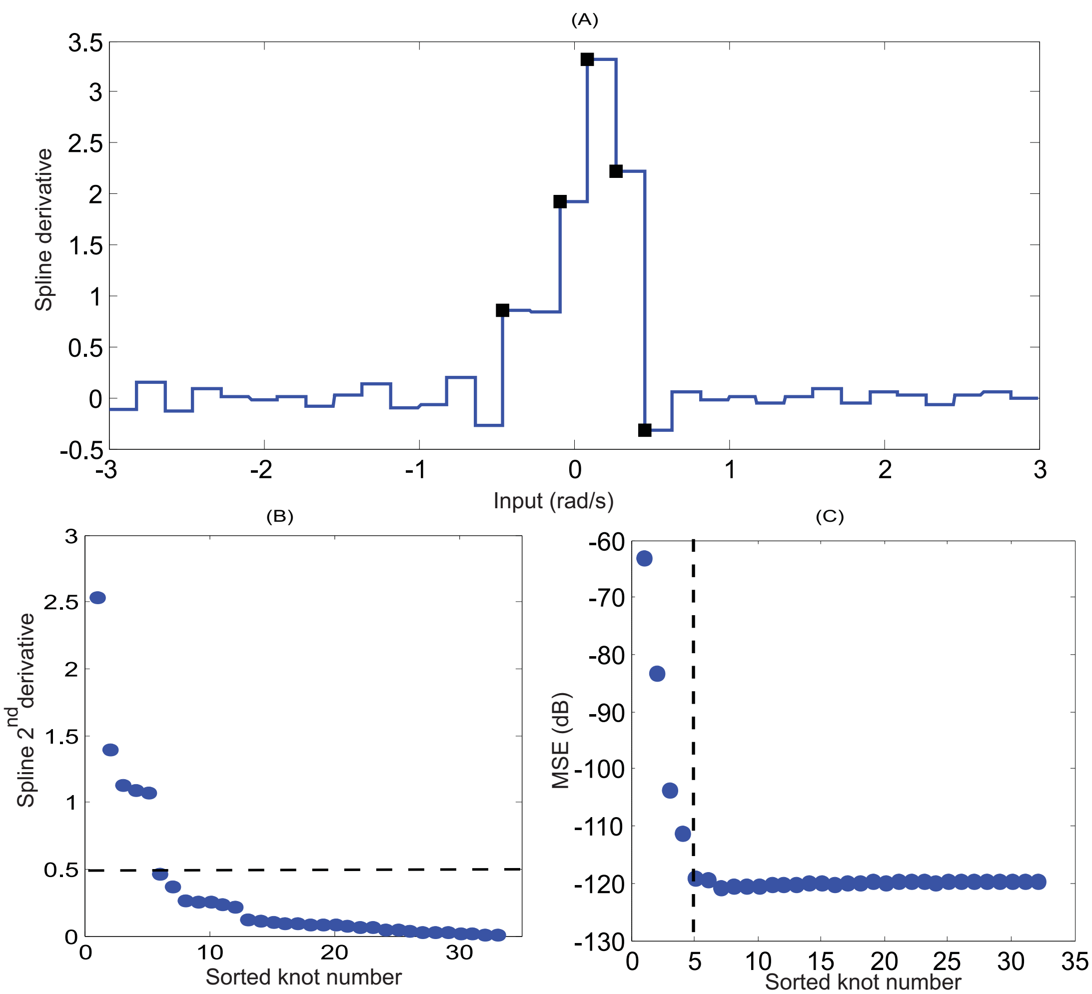

Figure A–3: Selection of active knots: (A) first derivative of the estimated spline; (B) sorted knots according to the second derivative of the spline; (C) MSE according to the sorted knot sequence.

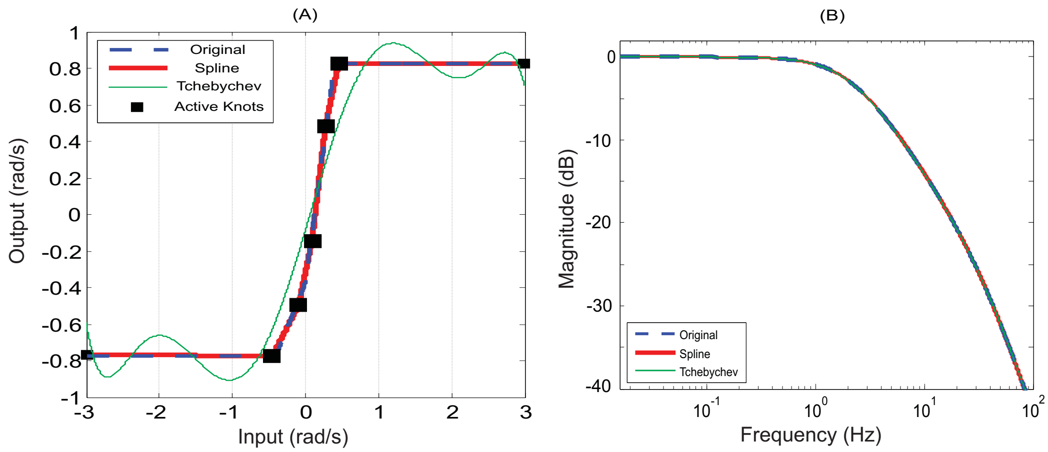

Figure A–4: Identified Hammerstein system: (A) Static nonlinearity, spline using only active knots superimposed on the 8-th order Tchebychev approximation; (B) Identified linear system frequency response.

method and could successfully detect sharp corner points. This improvement should make possible a better understanding of the underlying physiological information.

The new method requires minimal *a priori* information. The method uses the MOESP subspace algorithm to estimate the A and C state-space matrices. Prior to the identification of these matrices, MOESP estimates the order of the linear system. Second, the method determines the minimal number of knots and their locations required to represent the static nonlinearity.

Another advantage of the method is that it does not require the use of Gaussian inputs. It uses an over-parameterized MISO model and so does not rely on Busgang's theorem and therefore does not require a Gaussian distribution for the input signal. This is useful for experiments where Gaussian inputs cannot be used or generated, such as studies of reflex stiffness where a PRBS input signal is often used for identification. It is also advantageous to use uniformly distributed inputs in Hammerstein identification, since the input can equally excite all regions in the nonlinearity [309].

The knot locations used for the parsimonious model were a subset of those used for the initial segmentation. Consequently, the estimation of corner point locations in the hard nonlinearity is limited to the resolution of segmentation, i.e., location of knots. For instance, in the simulation study, the input range was between -3 to 3 rad/s and we used 34 knots. Therefore, the resolution of corner point estimation is ± 0.09 rad/s. One way to increase the estimation accuracy of the corner points would be to use methods that consider variable knot location. However, for variable knot locations, the problem is highly nonlinear [92], [250]. Therefore, nonlinear optimization techniques need to be used to find the optimum knot location. It is known that if the initial condition of a nonlinear optimization problem is set properly, the likelihood of convergence to global minimum is increased. The new method can be a good candidate to find the initial condition for the optimization search, i.e., we can use active knots as initial condition of the optimization search to finely tune their optimal location.

References

[1] E. Kandel, J. Schwartz, T. Jessell, S. Siegelbaum, and A. Hudspeth, *Principles of Neural Science*. McGraw-Hill, 2013.

[2] A. Mannard and R. B. Stein, "Determination of the frequency response of isometric soleus muscle in the cat using random nerve stimulation," *The Journal of Physiology*, vol. 229, no. 2, pp. 275–296, 1973.

[3] E. P. Widmaier, H. Raff, and K. T. Strang, *Vander's human physiology : the mechanisms of body function*. McGraw-Hill, 2006.

[4] K. L. Moore, A. F. Dalley, and A. M. R. Agur, *Clinically Oriented Anatomy*. Lippincott Williams & Wilkins, 2014.

[5] F. H. Netter, *Atlas of Human Anatomy*. Elsevier, 2011.

[6] K. Jalaleddini, E. Sobhani Tehrani, and R. E. Kearney, "A subspace approach to the structural decomposition and identification of ankle joint dynamic stiffness," *submitted to IEEE Transactions on Biomedical Engineering*, 2015.

[7] "Occupational therapy practice, framework: Domain & process," *The American Journal of Occupational Therapy*, vol. 62, no. 6, pp. 625–688, 2008.

[8] E. Goldstein, *Sensation and perception*. Cengage Learning, 2013.

[9] N. Hogan, "Impedance control: An approach to manipulation," in *American Control Conference, 1984*, June 1984, pp. 304–313.

[10] T. Nichols and J. C. Houk, "Improvement in linearity and regulation of stiffness that results from actions of stretch reflex," *Journal of Neurophysiology*, vol. 39, no. 1, pp. 119–142, 1976.

[11] M. Casadio, P. G. Morasso, and V. Sanguineti, "Direct measurement of ankle stiffness during quiet standing: implications for control modelling and clinical application," *Gait & Posture*, vol. 21, no. 4, pp. 410–424, 2005.

[12] Y.-S. Chen and S. Zhou, "Soleus h-reflex and its relation to static postural control," *Gait & Posture*, vol. 33, no. 2, pp. 169–178, 2011.

[13] N. Hogan, "The mechanics of multi-joint posture and movement control," *Biological Cybernetics*, vol. 52, no. 5, pp. 315–331, 1985.

[14] R. D. Trumbower, M. A. Krutky, B.-S. Yang, and E. J. Perreault, "Use of self-selected postures to regulate multi-joint stiffness during unconstrained tasks," *PLoS ONE*, vol. 4, no. 5, p. e5411, 05 2009.

[15] E. Perreault, R. Kirsch, and P. Crago, "Effects of voluntary force generation on the elastic components of endpoint stiffness," *Experimental Brain Research*, vol. 141, no. 3, pp. 312–323, 2001.

[16] F. A. Mussa-Ivaldi, N. Hogan, and E. Bizzi, "Neural, mechanical, and geometric factors subserving arm posture in humans," *The Journal of neuroscience*, vol. 5, no. 10, pp. 2732–2743, 1985.

[17] J. Chen, S. Siegler, and C. D. Schneck, "The three-dimensional kinematics and flexibility characteristics of the human ankle and subtalar jointpart ii: flexibility characteristics," *Journal of biomechanical engineering*, vol. 110, no. 4, pp. 374–385, 1988.

[18] S. Siegler, J. Chen, and C. Schneck, "The three-dimensional kinematics and flexibility characteristics of the human ankle and subtalar jointspart i: Kinematics," *Journal of biomechanical engineering*, vol. 110, no. 4, pp. 364–373, 1988.

[19] R. E. Kearney and I. W. Hunter, "System identification of human joint dynamics," *Critical Reviews in Biomedical Engineering*, vol. 18, pp. 55–87, 1990.

[20] E. Toft, T. Sinkjaer, S. Andreassen, and K. Larsen, "Mechanical and electromyographic responses to stretch of the human ankle extensors," *Journal of Neurophysiology*, vol. 65, no. 6, pp. 1402–1410, 1991.

[21] L. Bar-On, K. Desloovere, G. Molenaers, J. Harlaar, T. Kindt, and E. Aertbelien, "Identification of the neural component of torque during manually-applied spasticity assessments in children with cerebral palsy," *Gait & Posture*, vol. 40, no. 3, pp. 346 – 351, 2014.

[22] M. P. Amato and G. Ponziani, "Quantification of impairment in ms: discussion of the scales in use," *Multiple sclerosis*, vol. 5, no. 4, pp. 216–219, 1999.

[23] A. A. A. Alhusaini, J. Crosbie, R. B. Shepherd, C. M. Dean, and A. Scheinberg, "No change in calf muscle passive stiffness after botulinum toxin injection in children with cerebral palsy," *Developmental Medicine & Child Neurology*, vol. 53, no. 6, pp. 553–558, 2011.

[24] M. Mirbagheri, X. Niu, and D. Varoqui, "Prediction of stroke motor recovery using reflex stiffness measures at one month," *Neural Systems and Rehabilitation Engineering, IEEE Transactions on*, vol. 20, no. 6, pp. 762–770, Nov 2012.

[25] J. Palazzolo, M. Ferraro, H. Krebs, D. Lynch, B. Volpe, and N. Hogan, "Stochastic estimation of arm mechanical impedance during robotic stroke rehabilitation," *Neural Systems and Rehabilitation Engineering, IEEE Transactions on*, vol. 15, no. 1, pp. 94–103, 2007.

[26] J. Veneman, R. Kruidhof, E. Hekman, R. Ekkelenkamp, E. van Asseldonk, and H. van der Kooij, "Design and evaluation of the lopes exoskeleton robot for interactive gait rehabilitation," *Neural Systems and Rehabilitation Engineering, IEEE Transactions on*, vol. 15, no. 3, pp. 379–386, 2007.

[27] H. Kazerooni, "The human power amplifier technology at the university of california, berkeley," *Robotics and Autonomous Systems*, vol. 19, no. 2, pp. 179 – 187, 1996.

[28] R. Ham, T. Sugar, B. Vanderborght, K. Hollander, and D. Lefeber, "Compliant actuator designs," *Robotics Automation Magazine, IEEE*, vol. 16, no. 3, pp. 81–94, September 2009.

[29] I. Sardellitti, G. Palli, N. Tsagarakis, and D. Caldwell, "Antagonistically actuated compliant joint: Torque and stiffness control," in *Intelligent Robots and Systems (IROS), 2010 IEEE/RSJ International Conference on*, Oct 2010, pp. 1909–1914.

[30] S. Migliore, E. Brown, and S. DeWeerth, "Biologically inspired joint stiffness control," in *Robotics and Automation, 2005. ICRA 2005. Proceedings of the 2005 IEEE International Conference on*, April 2005, pp. 4508–4513.

[31] S. Wolf and G. Hirzinger, "A new variable stiffness design: Matching requirements of the next robot generation," in *Robotics and Automation, 2008. ICRA 2008. IEEE International Conference on*, May 2008, pp. 1741–1746.

[32] E. Kato, H. Kanehisa, T. Fukunaga, and Y. Kawakami, "Changes in ankle joint stiffness due to stretching: The role of tendon elongation of the gastrocnemius muscle," *European Journal of Sport Science*, vol. 10, no. 2, pp. 111–119, 2010.

[33] L. Ljung, "Perspectives on system identification," *Annual Reviews in Control*, vol. 34, no. 1, pp. 1 – 12, 2010.

[34] F. E. Zajac, "Muscle and tendon: properties, models, scaling, and application to biomechanics and motor control." *Critical reviews in biomedical engineering*, vol. 17, no. 4, pp. 359–411, 1988.

[35] A. M. L. and D. D. T., "The influence of muscle model complexity in musculoskeletal motion modeling," *Journal of Biomechanical Engineering*, vol. 107, no. 2, pp. 403–420, 1985.

[36] J. Winters and L. Stark, "Muscle models: What is gained and what is lost by varying model complexity," *Biological Cybernetics*, vol. 55, no. 6, pp. 403–420, 1987.

[37] R. E. Kearney, R. B. Stein, and L. Parameswaran, "Identification of intrinsic and reflex contributions to human ankle stiffness dynamics," *IEEE Transactions on Biomedical Engineering*, vol. 44, no. 6, pp. 493–504, 1997.

[38] F. J. Valero-Cuevas, "A mathematical approach to the mechanical capabilities of limbs and fingers," in *Progress in Motor Control*. Springer, 2009, pp. 619–633.

[39] A. Huxley, "Cross-bridge action: present views, prospects, and unknowns." *Journal of Biomechanics*, vol. 33, no. 10, pp. 1189 – 1195, 2000.

[40] H. L. Sweeney and A. Houdusse, "Structural and functional insights into the myosin motor mechanism," *Annual Review of Biophysics*, vol. 39, no. 1, pp. 539–557, 2010.

[41] G. Offer and K. Ranatunga, "A cross-bridge cycle with two tension-generating steps simulates skeletal muscle mechanics," *Biophysical Journal*, vol. 105, no. 4, pp. 928 – 940, 2013.

[42] R. J. Monti, R. R. Roy, and V. R. Edgerton, "Role of motor unit structure in defining function," *Muscle & Nerve*, vol. 24, no. 7, pp. 848–866, 2001.

[43] S. J. Goldberg and M. S. Shall, *Peripheral and Spinal Mechanisms in the Neural Control of Movement*. Elsevier, 1999, ch. Motor units of extraocular muscles: recent findings, pp. 221–232.

[44] R. M. Enoka and A. J. Fuglevand, “Motor unit physiology: Some unresolved issues,” *Muscle & Nerve*, vol. 24, no. 1, pp. 4–17, 2001.

[45] M. Cannell and D. Allen, “Model of calcium movements during activation in the sarcomere of frog skeletal muscle,” *Biophysical Journal*, vol. 45, no. 5, pp. 913–925, 1984.

[46] A. Nikooyan, H. Veeger, P. Westerhoff, B. Bolsterlee, F. Graichen, G. Bergmann, and F. van der Helm, “An emg-driven musculoskeletal model of the shoulder,” *Human Movement Science*, vol. 31, no. 2, pp. 429 – 447, 2012.

[47] E. Henneman, G. Somjen, and D. O. Carpenter, “Functional significance of cell size in spinal motoneurons,” *Journal of Neurophysiology*, vol. 28, no. 3, pp. 560–580, 1965.

[48] M. E. Llewellyn, K. R. Thompson, K. Deisseroth, and S. L. Delp, “Orderly recruitment of motor units under optical control in vivo,” *Nature medicine*, vol. 16, no. 10, pp. 1161–1165, 2010.

[49] R. Person and L. Kudina, “Discharge frequency and discharge pattern of human motor units during voluntary contraction of muscle,” *Electroencephalography and Clinical Neurophysiology*, vol. 32, no. 5, pp. 471 – 483, 1972.

[50] S. Andreassen and L. Arendt-Nielsen, “Muscle fibre conduction velocity in motor units of the human anterior tibial muscle: a new size principle parameter,” *The Journal of physiology*, vol. 391, no. 1, pp. 561–571, 1987.

[51] H. Milner-Brown, R. Stein, and R. Yemm, “The orderly recruitment of human motor units during voluntary isometric contractions,” *The Journal of physiology*, vol. 230, no. 2, p. 359, 1973.

[52] T. Oya, S. Riek, and A. G. Cresswell, “Recruitment and rate coding organisation for soleus motor units across entire range of voluntary isometric plantar flexions,” *The Journal of physiology*, vol. 587, no. 19, pp. 4737–4748, 2009.

[53] P. B. C. Matthews, “The response of deeferented muscle spindle receptors to stretching at different velocities,” *Journal of Physiology London*, vol. 168, pp. 660–678, 1963.

[54] P. B. C. Matthews and R. B. Stein, "The sensitivity of muscle spindle afferents to small sinusoidal changes of length," *The Journal of Physiology*, vol. 200, pp. 723–743, 1969.

[55] D. Barker, *The Morphology of Muscle Receptors*, ser. Handbook of Sensory Physiology. Springer Berlin Heidelberg, 1974, vol. 3 / 2, pp. 1–190.

[56] P. B. C. Matthews, "Evolving views on the internal operation and functional role of the muscle spindle," *Journal of Physiology*, pp. 1–30, 1981.

[57] A. Crowe and P. B. C. Matthews, "The effects of stimulation of static and dynamic fusimotor fibers on the response to stretching of the primary endings of muscle spindle," *Journal of Physiology London*, vol. 174, pp. 109–131, 1964.

[58] M. P. Mileusnic, I. E. Brown, N. Lan, and G. E. Loeb, "Mathematical models of proprioceptors. i. control and transduction in the muscle spindle," *Journal of neurophysiology*, vol. 96, no. 4, pp. 1772–1788, 2006.

[59] A. Schaafsma, E. Otten, and J. D. V. Willigen, "A muscle spindle model for primary afferent firing based on a simulation of intrafusal mechanical events," *Journal of Neurophysiology*, vol. 65, no. 6, 1991.

[60] D. Angers and G. Y. Delisle, "Study of the action of static and dynamic fusimotor fibers with a mechanical model of the mammalian muscle spindle," *IEEE Transactions on Biomedical Engineering*, vol. 18, no. 3, pp. 175–180, 1971.

[61] R. Banks, "The motor innervation of mammalian muscle spindles," *Progress in neurobiology*, vol. 43, no. 4, pp. 323–362, 1994.

[62] I. A. Boyd, "The structure and innervation of the nuclear bag muscle fibre system and the nuclear chain muscle fibre system in mammalian muscle spindles," *Philosophical Transactions of the Royal Society of London. Series B, Biological Sciences*, vol. 245, no. 720, pp. pp. 81–87+818+89–136, 1962.

[63] J. C. Houk, W. Z. Rymer, and P. E. Crago, "Dependence of dynamic response of spindle receptors on muscle length and velocity," *The Journal of Neurophysiology*, vol. 46, no. 1, pp. 143–166, 1981.

[64] G. Loeb and J. Duysens, "Activity patterns in individual hindlimb primary and secondary muscle spindle afferents during normal movements in unrestrained cats," *Journal of neurophysiology*, vol. 42, no. 2, pp. 420–440, 1979.

[65] M. M. Mirbagheri, H. Barbeau, and R. E. Kearney, "Intrinsic and reflex contributions to human ankle stiffness: variation with activation level and position," *Experimental Brain Research*, vol. 135, no. 4, pp. 423–436, 2000.

[66] M. Dimitriou and B. B. Edin, "Human muscle spindles act as forward sensory models," *Current Biology*, vol. 20, no. 19, pp. 1763 – 1767, 2010.

[67] D. G. Kamper, H. C. Fischer, M. O. Conrad, J. D. Towles, W. Z. Rymer, and K. M. Triandafilou, "Finger-thumb coupling contributes to exaggerated thumb flexion in stroke survivors," *Journal of Neurophysiology*, vol. 111, no. 12, pp. 2665–2674, 2014.

[68] D. C. Boone and S. P. Azen, "Normal range of motion of joints in male subjects," *The Journal of Bone & Joint Surgery*, vol. 61, no. 5, pp. 756–759, 1979.

[69] A. Roaas and G. B. J. Andersson, "Normal range of motion of the hip, knee and ankle joints in male subjects, 30-40 years of age," *Acta Orthopaedica*, vol. 53, no. 2, pp. 205–208, 1982.

[70] J. T. Cramer, T. W. Beck, T. J. Housh, L. L. Massey, S. M. Marek, S. Danglemeier, S. Purkayastha, J. Y. Culbertson, K. A. Fitz, and A. D. Egan, "Acute effects of static stretching on characteristics of the isokinetic angle-torque relationship, surface electromyography, and mechanomyography," *Journal of Sports Sciences*, vol. 25, no. 6, pp. 687–698, 2007.

[71] E. Kato, H. Kanehisa, T. Fukunaga, and Y. Kawakami, "Changes in ankle joint stiffness due to stretching: The role of tendon elongation of the gastrocnemius muscle," *European Journal of Sport Science*, vol. 10, no. 2, pp. 111–119, 2010.

[72] D. Westwick and R. Kearney, *Identification of nonlinear physiological systems.* Wiley-IEEE, 2003, pp. 39–56.

[73] C. M. Niu, S. K. Nandyala, and T. D. Sanger, "Emulated muscle spindle and spiking afferents validates vlsi neuromorphic hardware as a testbed for sensorimotor function and disease," *Frontiers in Computational Neuroscience*, vol. 8, no. 141, 2014.

[74] E. de Vlugt, A. C. Schouten, and F. C. van der Helm, "Closed-loop multivariable system identification for the characterization of the dynamic arm compliance using continuous force disturbances: a model study," *Journal of Neuroscience Methods*, vol. 122, no. 2, pp. 123 – 140, 2003.

[75] K. M. Moorhouse and K. P. Granata, "Trunk stiffness and dynamics during active extension exertions," *Journal of Biomechanics*, vol. 38, no. 10, pp. 2000 – 2007, 2005.

[76] C. Sprague, "System identification of wrist stiffness in parkinson's disease patients," Master's thesis, University of Pittsburgh, 2008.

[77] P. Hunter, A. McCulloch, and H. ter Keurs, "Modelling the mechanical properties of cardiac muscle," *Progress in Biophysics and Molecular Biology*, vol. 69, pp. 289 – 331, 1998.

[78] J. Zhang, R. Kearney, G. Kiruluta, M. Elhilali, and I. Hunter, "System identification of bladder hydrodynamics," in *Engineering in Medicine and Biology Society, 1994. Engineering Advances: New Opportunities for Biomedical Engineers. Proceedings of the 16th Annual International Conference of the IEEE*, 1994, pp. 1023–1024 vol.2.

[79] J. J. Eggermont, "Wiener and volterra analyses applied to the auditory system," *Hearing Research*, vol. 66, no. 2, pp. 177 – 201, 1993.

[80] D. T. Westwick and R. E. Kearney, "Nonparametric identification of nonlinear biomedical systems, part i: Theory," *Critical reviews in biomedical engineering*, vol. 26, no. 3, pp. 153 – 226, 1998.

[81] G. N. Maksym, R. E. Kearney, and J. H. T. Bates, "Nonparametric block-structured modeling of lung tissue strip mechanics," *Annals of Biomedical Engineering*, vol. 26, pp. 242–252, 1998.

[82] S. Sadeghi, L. Minor, and K. Cullen, "Dynamics of the horizontal vestibuloocular reflex after unilateral labyrinthectomy: response to high frequency, high acceleration, and high velocity rotations," *Experimental Brain Research*, vol. 175, no. 3, pp. 471–484, 2006.

[83] I. Hunter and R. Kearney, "Two-sided linear filter identification," *Medical and Biological Engineering and Computing*, vol. 21, no. 2, pp. 203–209, 1983.

[84] C. Runge, "Über empirische funktionen und die interpolation zwischen äquidistanten ordinaten," *Zeitschrift für Mathematik und Physik*, vol. 46, no. 224-243, p. 20, 1901.

[85] F. Giri and E. W. Bai, *Block-Oriented Nonlinear System Identification*. Springer, 2010.

[86] A. Hammerstein, "Nichtlineare integralgleichungen nebst anwendungen," *Acta Mathematica*, vol. 54, no. 1, pp. 117–176, 1930.

[87] W. Chan and H. L. Galiana, "A nonlinear model of the neural integrator improves detection of deficits in the human VOR," *IEEE Transactions on Biomedical Engineering*, vol. 57, pp. 1012–1023, 2010.

[88] W. Huebner, G. Saidel, and R. Leigh, "Nonlinear parameter estimation applied to a model of smooth pursuit eye movements," *Biological Cybernetics*, vol. 62, no. 4, pp. 265–273, 1990.

[89] R. Emerson, M. Korenberg, and M. Citron, "Identification of complex-cell intensive nonlinearities in a cascade model of cat visual cortex," *Biological Cybernetics*, vol. 66, no. 4, pp. 291–300, 1992.

[90] E. Eskinat, S. H. Johnson, and W. L. Luyben, "Use of hammerstein models in identification of nonlinear systems," *AIChE Journal*, vol. 37, no. 2, pp. 255–268, 1991.

[91] K. Hunt, M. Munih, N. Donaldson, and F. Barr, "Investigation of the hammerstein hypothesis in the modeling of electrically stimulated muscle," *Biomedical Engineering, IEEE Transactions on*, vol. 45, no. 8, pp. 998–1009, Aug 1998.

[92] D. T. Westwick, S. L. Kukreja, and M. J. Brenner, "Identification of highly resonant Hammerstein systems with hard nonlinearities," in *Proceedings of ICNPAA-2006: Mathematical Problems in Engineering and Aerospace Sciences*, 2007, pp. 813–820.

[93] N. Wiener, *Nonlinear problems in random theory.* Wiley, 1966.

[94] P. Z. Marmarelis and K.-I. Naka, "White-noise analysis of a neuron chain: An application of the wiener theory," *Science*, vol. 175, pp. 1276–1278, 1972.

[95] B. N. Segal and J. S. Outerbridge, "Vestibular (semicircular canal) primary neurons in bullfrog: nonlinearity of individual and population response to rotation," *Journal of Neurophysiology*, vol. 47, no. 4, pp. 545–562, 1982.

[96] I. W. Hunter and M. J. Korenberg, "The identification of nonlinear biological systems: Wiener and Hammerstein cascade models," *Biological Cybernetics*, vol. 55, no. 2-3, pp. 135–144, 1986.

[97] A. D. Kalafatis, L. Wang, and W. R. Cluett, "Identification of time-varying ph processes using sinusoidal signals," *Automatica*, vol. 41, no. 4, pp. 685 – 691, 2005.

[98] G. Palm, "On representation and approximation of nonlinear systems," *Biological Cybernetics*, vol. 34, no. 1, pp. 49–52, 1979.

[99] M. J. Korenberg, "Parallel cascade identification and kernel estimation for nonlinear systems," *Annals of Biomedical Engineering*, vol. 19, no. 4, pp. 429–455, 1991.

[100] D. Westwick and R. Kearney, "An object-oriented toolbox for linear and nonlinear system identification," in *Proceedings of IEEE Engineering in Medicine and Biology Society*, 2004, pp. 514–517.

[101] L. Ljung, Ed., *System Identification (2Nd Ed.): Theory for the User*. Prentice Hall PTR, 1999.

[102] M. Verhaegen and V. Verdult, *Filtering and System Identification, A Least Squares Approach*. Cambridge University Press, 2007, pp. 292–339.

[103] C. Lang and R. Kearney, "Modulation of ankle stiffness during postural sway," in *Engineering in Medicine and Biology Society (EMBC), 2014 36th Annual International Conference of the IEEE*, 2014, pp. 4062–4065.

[104] L.-Q. Zhang and W. Z. Rymer, "Reflex and intrinsic changes induced by fatigue of human elbow extensor muscles," *Journal of Neurophysiology*, vol. 86, no. 3, pp. 1086–1094, 2001.

[105] R. F. Kirsch and W. Z. Rymer, "Neural compensation for fatigue-induced changes in muscle stiffness during perturbations of elbow angle in human," *Journal of Neurophysiology*, vol. 68, no. 2, pp. 449–470, 1992.

[106] M. J. Levin, "Optimum estimation of impulse response in the presence of noise," *Circuit Theory, IRE Transactions on*, vol. 7, no. 1, pp. 50–56, Mar 1960.

[107] L. Rabiner, R. Crochiere, and J. Allen, "Fir system modeling and identification in the presence of noise and with band-limited inputs," *Acoustics, Speech and Signal Processing, IEEE Transactions on*, vol. 26, no. 4, pp. 319–333, Aug 1978.

[108] D. Westwick and R. Kearney, "Identification of physiological systems: a robust method for non-parametric impulse response estimation," *Medical and Biological Engineering and Computing*, vol. 35, no. 2, pp. 83–90, 1997.

[109] E. A. Pohlmeyer, S. A. Solla, E. J. Perreault, and L. E. Miller, "Prediction of upper limb muscle activity from motor cortical discharge during reaching," *Journal of Neural Engineering*, vol. 4, no. 4, p. 369, 2007.

[110] C.-Y. Dong, T.-W. Yoon, D. Bates, and K.-H. Cho, "Identification of feedback loops embedded in cellular circuits by investigating non-causal impulse response components," *Journal of Mathematical Biology*, vol. 60, no. 2, pp. 285–312, 2010.

[111] S. J. Qin, "An overview of subspace identification," *Computers & Chemical Engineering*, vol. 30, no. 1012, pp. 1502 – 1513, 2006.

[112] W. Larimore, "Canonical variate analysis in identification, filtering, and adaptive control," in *Decision and Control, 1990., Proceedings of the 29th IEEE Conference on*, Dec 1990, pp. 596–604 vol.2.

[113] M. Verhaegen and P. Dewilde, "Subspace model identification part 1. the output error state space model identification class of algorithm," *International Journal of Control*, vol. 56, no. 5, pp. 1187–1210, 1992.

[114] P. V. Overschee and B. D. Moor, "N4sid: Subspace algorithms for the identification of combined deterministic-stochastic systems," *Automatica*, vol. 30, no. 1, pp. 75 – 93, 1994.

[115] ——, "A unifying theorem for three subspace system identification algorithms," *Automatica*, vol. 31, no. 12, pp. 1853 – 1864, 1995.

[116] L. R. J. Haverkamp, "State space identification: Theory and practice," Ph.D. dissertation, Delft University of Technology, 2001.

[117] B. Haverkamp, C. T. Chou, and M. Verhaegen, "SMI toolbox : A Matlab toolbox for state space model identification," *Journal A*, vol. 38, no. 3, pp. 34–37, 1997.

[118] M. Verhaegen and D. Westwick, "Identifying MIMO Hammerstein systems in the context of subspace model identification methods," *International Journal of Control*, vol. 63, no. 2, pp. 331–349, 1996.

[119] D. Westwick and M. Verhaegen, "Identifying mimo wiener systems using subspace model identification methods," *Signal Processing.*, vol. 52, no. 2, pp. 235–258, 1996.

[120] C. T. Chou and M. Verhaegen, "Subspace algorithm for the identification of multivariable dynamic errors-in-variables models," *Automatica*, vol. 33, no. 10, pp. 1857–1869, 1997.

[121] S. Kukreja, B. Haverkamp, D. Westwick, R. Kearney, H. Galiana, and M. Verhaegen, "Subspace identification method for ankle mechanics," in *Engineering in Medicine and Biology Society, 1995., IEEE 17th Annual Conference*, vol. 2, Sep 1995, pp. 1413–1414 vol.2.

[122] Y. Zhao, D. T. Westwick, and R. E. Kearney, "Subspace methods for identification of human ankle joint stiffness," *IEEE Transactions on Biomedical Engineering*, vol. 58, pp. 3039–3048, 2011.

[123] M. Verhaegen and P. Dewilde, "Subspace model identification part 2. analysis of the elementary output-error state space model identification algorithm," *International Journal of Control*, vol. 56, no. 5, pp. 1211–1241, 1992.

[124] A. G. Feldman, "Functional tuning of nervous system with control of movement or maintenance of a steady posture. 2. controllable parameters of muscles," *BIOPHYSICS-USSR*, vol. 11, no. 3, p. 565, 1966.

[125] J. E. Colgate and N. Hogan, "Robust control of dynamically interacting systems," *International Journal of Control*, vol. 48, no. 1, pp. 65–88, 1988.

[126] M. L. Latash and V. M. Zatsiorsky, "Joint stiffness: Myth or reality?" *Human Movement Science*, vol. 12, no. 6, pp. 653 – 692, 1993.

[127] L. E. Kinsler, A. R. Frey, A. B. Coppens, and J. V. Sanders, *Fundamentals of acoustics.* Wiley-VCH, 1999.

[128] P. L. Gatti, *Applied Structural and Mechanical Vibrations: Theory and Methods.* CRC Press, 2014.

[129] W. MacKay, D. Crammond, H. Kwan, and J. Murphy, "Measurements of human forearm viscoelasticity," *Journal of Biomechanics*, vol. 19, no. 3, pp. 231 – 238, 1986.

[130] D. Formica, S. K. Charles, L. Zollo, E. Guglielmelli, N. Hogan, and H. I. Krebs, "The passive stiffness of the wrist and forearm," *Journal of Neurophysiology*, vol. 108, no. 4, pp. 1158–1166, 2012.

[131] J. Nielsen, T. SinkjAer, E. Toft, and Y. Kagamihara, "Segmental reflexes and ankle joint stiffness during co-contraction of antagonistic ankle muscles in man," *Experimental Brain Research*, vol. 102, no. 2, pp. 350–358, 1994.

[132] W. Mugge, D. Abbink, A. Schouten, J. Dewald, and F. van der Helm, "A rigorous model of reflex function indicates that position and force feedback are flexibly tuned to position and force tasks," *Experimental Brain Research*, vol. 200, no. 3-4, pp. 325–340, 2010.

[133] A. Schouten, E. de Vlugt, J. van Hilten, and F. van der Helm, "Quantifying proprioceptive reflexes during position control of the human arm," *IEEE Transactions on Biomedical Engineering*, vol. 55, no. 1, pp. 311–321, 2008.

[134] F. C. van der Helm, A. C. Schouten, E. de Vlugt, and G. G. Brouwn, "Identification of intrinsic and reflexive components of human arm dynamics during postural control," *Journal of Neuroscience Methods*, vol. 119, no. 1, pp. 1 – 14, 2002.

[135] M. Mirbagheri, H. Barbeau, M. Ladouceur, and R. Kearney, "Intrinsic and reflex stiffness in normal and spastic, spinal cord injured subjects," *Experimental Brain Research*, vol. 141, no. 4, pp. 446–459, 2001.

[136] A. B. Ward, "Spasticity treatment with botulinum toxins," *Journal of Neural Transmission*, vol. 115, no. 4, pp. 607–616, 2008.

[137] E. A. Mitsiokapa, A. F. Mavrogenis, H. Skouteli, S. G. Vrettos, G. Tzanos, A. D. Kanellopoulos, D. S. Korres, and P. J. Papagelopoulos, "Selective percutaneous myofascial lengthening of the lower extremities in children with spastic cerebral palsy," *Clinics in Podiatric Medicine and Surgery*, vol. 27, no. 2, pp. 335 – 343, 2010.

[138] B. Balaban, E. Yasar, U. Dal, K. Yazicioglu, H. Mohur, and T. A. Kalyon, "The effect of hinged ankle-foot orthosis on gait and energy expenditure in spastic hemiplegic cerebral palsy," *Disability and Rehabilitation*, vol. 29, no. 2, pp. 139–144, 2007.

[139] M. Mirbagheri, X. Niu, and D. Varoqui, "Prediction of stroke motor recovery using reflex stiffness measures at one month," *Neural Systems and Rehabilitation Engineering, IEEE Transactions on*, vol. 20, no. 6, pp. 762–770, 2012.

[140] T. Sinkjaer, E. Toft, S. Andreassen, and B. C. Hornemann, "Muscle stiffness in human ankle dorsiflexors: intrinsic and reflex components," *Journal of Neurophysiology*, vol. 60, no. 3, pp. 1110–1121, 1988.

[141] N. Mrachacz-Kersting and T. Sinkjaer, "Reflex and non-reflex torque responses to stretch of the human knee extensors," *Experimental Brain Research*, vol. 151, no. 1, pp. 72–81, 2003.

[142] J. Allum, K.-H. Mauritz, and V. H., "The mechanical effectiveness of short latency reflexes in human triceps surae muscles revealed by ischaemia and vibration," *Experimental Brain Research*, vol. 48, no. 1, pp. 153–156, 1982.

[143] S. J. Fellows, F. Dmges, R. Tpper, A. F. Thilmann, and J. Noth, "Changes in the short- and long-latency stretch reflex components of the triceps surae muscle during ischaemia in man." *The Journal of Physiology*, vol. 472, no. 1, pp. 737–748, 1993.

[144] T. Sinkjr and R. Hayashi, "Regulation of wrist stiffness by the stretch reflex," *Journal of Biomechanics*, vol. 22, no. 11-12, pp. 1133 – 1140, 1989.

[145] A. Berardelli, M. Hallett, C. Kaufman, E. Fine, W. Berenberg, and S. Simon, "Stretch reflexes of triceps surae in normal man." *Journal of Neurology, Neurosurgery & Psychiatry*, vol. 45, no. 6, pp. 513–525, 1982.

[146] G. C. Agarwal and G. L. Gottlieb, "Effect of virration on the ankle stretch reflex in man," *Electroencephalography and Clinical Neurophysiology*, vol. 49, no. 1-2, pp. 81 – 92, 1980.

[147] J. Hoffer and S. Andreassen, "Regulation of soleus muscle stiffness in premammillary cats: intrinsic and reflex components," *Journal of neurophysiology*, vol. 45, no. 2, pp. 267–285, February 1981.

[148] S. Grillner and M. Udo, "Motor unit activity and stiffness of the contracting muscle fibres in the tonic stretch reflex," *Acta Physiologica Scandinavica*, vol. 81, no. 3, pp. 422–424, 1971.

[149] R. Kirsch, D. Boskov, and W. Rymer, "Muscle stiffness during transient and continuous movements of cat muscle: perturbation characteristics and physiological relevance," *Biomedical Engineering, IEEE Transactions on*, vol. 41, no. 8, pp. 758–770, Aug 1994.

[150] E. Bizzi, N. Accornero, W. Chapple, and N. Hogan, "Posture control and trajectory formation during arm movement," *The Journal of Neuroscience*, vol. 4, no. 11, pp. 2738–2744, 1984.

[151] G. M. Goodwin, D. Hoffman, and E. S. Luschei, "The strength of the reflex response to sinusoidal stretch of monkey jaw closing muscles during voluntary contraction." *The Journal of Physiology*, vol. 279, no. 1, pp. 81–111, 1978.

[152] R. F. Kirsch and R. E. Kearney, "Identification of time-varying stiffness dynamics of the human ankle joint during an imposed movement," *Experimental Brain Research*, vol. 114, no. 1, pp. 71–85, 1997.

[153] R. R. Carter, P. E. Crago, and M. W. Keith, "Stiffness regulation by reflex action in the normal human hand," *Journal of Neurophysiology*, vol. 64, no. 1, pp. 105–118, 1990.

[154] E. Perreault, P. Crago, and R. Kirsch, "Estimation of intrinsic and reflex contributions to muscle dynamics: a modeling study," *IEEE Transactions on Biomedical Engineering*, vol. 47, no. 11, pp. 1413 –1421, 2000.

[155] P. Forbes, R. Happee, F. C. van der Helm, and A. Schouten, "Emg feedback tasks reduce reflexive stiffness during force and position perturbations," *Experimental Brain Research*, vol. 213, no. 1, pp. 49–61, 2011.

[156] E. de Vlugt, J. de Groot, K. Schenkeveld, J. Arendzen, F. van der Helm, and C. Meskers, "The relation between neuromechanical parameters and ashworth score in stroke patients," *Journal of NeuroEngineering and Rehabilitation*, vol. 7, no. 1, 2010.

[157] R. E. Kearney and C. W. Y. Chan, "Contrasts between the reflex responses of tibialis anterior and triceps surae to sudden ankle rotation in normal human subjects," *Electroencephalography and Clinical Neurophysiology*, vol. 54, pp. 301–310, 1982.

[158] R. E. Kearney and I. W. Hunter, “System identification of human triceps surae stretch reflex dynamics,” *Experimental Brain Research*, vol. 51, pp. 117–127, 1983.

[159] R. Kearney and I. Hunter, “System identification of human stretch reflex dynamics: Tibialis anterior,” *Experimental Brain Research*, vol. 56, no. 1, pp. 40–49, 1984.

[160] P. van Drunen, E. Maaswinkel, F. van der Helm, J. van Dien, and R. Happee, “Identifying intrinsic and reflexive contributions to low-back stabilization,” *Journal of Biomechanics*, vol. 46, no. 8, pp. 1440 – 1446, 2013.

[161] J. Perry and G. A. Bekey, “Emg-force relationships in skeletal muscle,” *Crit Rev Biomed Eng*, vol. 7, no. 1, pp. 1–22, 1981.

[162] J. Coggshall and G. Bekey, “Emg-force dynamics in human skeletal muscle,” *Medical and biological engineering*, vol. 8, no. 3, pp. 265–270, 1970.

[163] J. Mercer, N. Bezodis, D. DeLion, T. Zachry, and M. Rubley, “EMG sensor location: Does it influence the ability to detect differences in muscle contraction conditions?” *Journal of Electromyography and Kinesiology*, vol. 16, no. 2, pp. 198 – 204, 2006.

[164] H. J. Hermens, B. Freriks, C. Disselhorst-Klug, and G. Rau, “Development of recommendations for {SEMG} sensors and sensor placement procedures,” *Journal of Electromyography and Kinesiology*, vol. 10, no. 5, pp. 361 – 374, 2000.

[165] T. J. Koh and M. D. Grabiner, “Evaluation of methods to minimize cross talk in surface electromyography,” *Journal of Biomechanics*, vol. 26, Supplement 1, no. 0, pp. 151 – 157, 1993.

[166] W. Yao, R. J. Fuglevand, and R. M. Enoka, “Motor-unit synchronization increases emg amplitude and decreases force steadiness of simulated contractions,” *Journal of Neurophysiology*, vol. 83, no. 1, pp. 441–452, 2000.

[167] D. Ludvig and R. E. Kearney, “Real-time estimation of intrinsic and reflex stiffness,” *IEEE Transactions on Biomedical Engineering*, vol. 54, no. 10, pp. 1875–1884, 2007.

[168] Y. Zhao, “Identification of ankle joint stiffness using subspace methods,” Ph.D. dissertation, McGill University, 2009.

[169] H. C. Kwan, J. T. Murphy, and M. W. Repeck, “Control of stiffness by the medium latency electromyographic response to limb perturbation,” *Canadian Journal of Physiology and Pharmacology*, vol. 57, no. 3, pp. 277–285, 1979.

[170] P. Blanpied and G. L. Smidt, “Human plantarflexor stiffness to multiple single-stretch trials,” *Journal of biomechanics*, vol. 25, no. 1, pp. 29–39, 1992.

[171] S. De Serres and T. Milner, “Wrist muscle activation patterns and stiffness associated with stable and unstable mechanical loads,” *Experimental Brain Research*, vol. 86, no. 2, pp. 451–458, 1991.

[172] “The influence of track compliance on running,” *Journal of Biomechanics*, vol. 12, no. 12, pp. 893 – 904, 1979.

[173] P. Dyhre-Poulsen, E. B. Simonsen, and M. Voigt, “Dynamic control of muscle stiffness and h reflex modulation during hopping and jumping in man,” *The Journal of Physiology*, vol. 437, no. 1, pp. 287–304, 1991.

[174] P. Weiss, R. Kearney, and I. Hunter, “Position dependence of ankle joint dynamics-ii. active mechanics,” *Journal of Biomechanics*, vol. 19, no. 9, pp. 737 – 751, 1986.

[175] ——, “Position dependence of ankle joint dynamics-i. passive mechanics,” *Journal of Biomechanics*, vol. 19, no. 9, pp. 727 – 735, 1986.

[176] P. L. Weiss, I. W. Hunter, and R. E. Kearney, “Human ankle joint stiffness over the full range of muscle activation levels,” *Journal of Biomechanics*, vol. 21, no. 7, pp. 539–544, 1988.

[177] W. A. MacKay, “Resonance properties of the human elbow,” *Canadian Journal of Physiology and Pharmacology*, vol. 62, no. 7, pp. 802–808, 1984.

[178] G. C. Joyce, P. M. H. Rack, and H. F. Ross, “The forces generated at the human elbow joint in response to imposed sinusoidal movements of the forearm,” *The Journal of Physiology*, vol. 240, no. 2, pp. 351–374, 1974.

[179] G. L. Gottlieb and G. C. Agarwal, “Dependence of human ankle compliance on joint angle,” *Journal of Biomechanics*, vol. 11, no. 4, pp. 177 – 181, 1978.

[180] S.-P. Ma and G. I. Zahalak, “The mechanical response of the active human triceps brachii muscle to very rapid stretch and shortening,” *Journal of Biomechanics*, vol. 18, no. 8, pp. 585 – 598, 1985.

[181] D. Ludvig and R. Kearney, "Estimation of joint stiffness with a compliant load," in *Engineering in Medicine and Biology Society, 2009. EMBC 2009. Annual International Conference of the IEEE*, Sept 2009, pp. 2967–2970.

[182] H. Lee, H. Krebs, and N. Hogan, "Multivariable dynamic ankle mechanical impedance with relaxed muscles," *Neural Systems and Rehabilitation Engineering, IEEE Transactions on*, vol. PP, no. 99, pp. 1–1, 2014.

[183] E. de Vlugt, A. C. Schouten, and F. C. van der Helm, "Quantification of intrinsic and reflexive properties during multijoint arm posture," *Journal of Neuroscience Methods*, vol. 155, no. 2, pp. 328 – 349, 2006.

[184] E. de Vlugt, A. C. Schouten, and F. C. T. van der Helm, "Adaptation of reflexive feedback during arm posture to different environments," *Biological Cybernetics*, vol. 87, no. 1, pp. 10–26, 2002.

[185] D. Westwick and E. J. Perreault, "Closed-loop identification: Application to the estimation of limb impedance in a compliant environment," *IEEE Transactions on Biomedical Engineering*, vol. 58, no. 3, pp. 521–530, 2011.

[186] H. Lee and N. Hogan, "Time-varying ankle mechanical impedance during human locomotion," *IEEE Transactions on Neural Systems and Rehabilitation Engineering*, vol. PP, no. 99, pp. 1–1, 2014.

[187] M. Lortie and R. Kearney, "Identification of physiological systems: Estimation of linear time varying dynamics with non-white inputs and noisy outputs," *Medical and Biological Engineering and Computing*, vol. 39, no. 3, pp. 381–390, 2001.

[188] F. Lacquaniti, N. A. Borghese, and M. Carrozzo, "Transient reversal of the stretch reflex in human arm muscles," *Journal of Neurophysiology*, vol. 66, no. 3, pp. 939–954, 1991.

[189] Y. Xu and J. Hollerbach, "A robust ensemble data method for identification of human joint mechanical properties during movement," *Biomedical Engineering, IEEE Transactions on*, vol. 46, no. 4, pp. 409–419, 1999.

[190] D. Ludvig and E. Perreault, "System identification of physiological systems using short data segments," *Biomedical Engineering, IEEE Transactions on*, vol. 59, no. 12, pp. 3541–3549, Dec 2012.

[191] ——, “Task-relevant adaptation of musculoskeletal impedance during posture and movement,” in *American Control Conference (ACC), 2014*, June 2014, pp. 4784–4789.

[192] D. Ludvig, S. Antos, and E. Perreault, “Joint impedance decreases during movement initiation,” in *Engineering in Medicine and Biology Society (EMBC), 2012 Annual International Conference of the IEEE*, 2012, pp. 3304–3307.

[193] D. Ludvig, T. Visser, H. Giesbrecht, and R. Kearney, “Identification of time-varying intrinsic and reflex joint stiffness,” *IEEE Transactions on Biomedical Engineering*, vol. 58, no. 6, pp. 1715–1723, June 2011.

[194] S. van Eesbeek, F. Van der Helm, M. Verhaegen, and E. de Vlugt, “LPV subspace identification of time-variant joint impedance,” in *Neural Engineering (NER), 2013 6th International IEEE/EMBS Conference on*, 2013, pp. 343–346.

[195] E. Sobhani Tehrani, K. Jalaleddini, and R. Kearney, “Linear parameter varying identification of ankle joint intrinsic stiffness during imposed walking movements,” in *Engineering in Medicine and Biology Society (EMBC), 2013 35th Annual International Conference of the IEEE*, July 2013, pp. 4923–4927.

[196] E. de Vlugt, S. van Eesbeek, P. Baines, J. Hilte, C. G. Meskers, and J. H. de Groot, “Short range stiffness elastic limit depends on joint velocity,” *Journal of Biomechanics*, vol. 44, no. 11, pp. 2106 – 2112, 2011.

[197] S. van Eesbeek, J. H. de Groot, F. C. van der Helm, and E. de Vlugt, “In vivo estimation of the short-range stiffness of cross-bridges from joint rotation,” *Journal of Biomechanics*, vol. 43, no. 13, pp. 2539 – 2547, 2010.

[198] L. Galiana, J. Fung, and R. Kearney, “Identification of intrinsic and reflex ankle stiffness components in stroke patients,” *Experimental Brain Research*, vol. 165, no. 4, pp. 422–434, 2005.

[199] D. Ludvig, I. Cathers, and R. E. Kearney, “Voluntary modulation of human stretch reflexes,” *Experimental Brain Research*, vol. 183, no. 2, pp. 201–213, 2007.

[200] L. Alibiglou, W. Rymer, R. Harvey, and M. Mirbagheri, "The relation between ashworth scores and neuromechanical measurements of spasticity following stroke," *Journal of NeuroEngineering and Rehabilitation*, vol. 5, no. 1, 2008.

[201] M. M. Mirbagheri, C. Tsao, and W. Z. Rymer, "Natural history of neuromuscular properties after stroke: a longitudinal study," *Journal of Neurology, Neurosurgery & Psychiatry*, vol. 80, no. 11, pp. 1212–1217, 2009.

[202] K. M. Moorhouse and K. P. Granata, "Role of reflex dynamics in spinal stability: Intrinsic muscle stiffness alone is insufficient for stability," *Journal of Biomechanics*, vol. 40, no. 5, pp. 1058 – 1065, 2007.

[203] R. Xia, M. Radovic, A. Threlkeld, and Z.-H. Mao, "System identification and modeling approach to characterizing rigidity in parkinson's disease: Neural and non-neural contributions," in *Bioinformatics and Biomedical Engineering (iCBBE), 2010 4th International Conference on*, 2010, pp. 1–4.

[204] C. Larivirea, D. Ludvig, R. Kearney, H. Mecheri, J.-M. Caron, and R. Preuss, "Identification of intrinsic and reflexive contributions to low-back stiffness: medium-term reliability and construct validity," *Journal of Biomechanics*, vol. 48, no. 2, pp. 254 – 261, 2015.

[205] T. Starret Visser, "Evaluation and application of an algorithm for the time-varying identification of ankle stiffness," Master's thesis, McGill University, 2009.

[206] E. S. Tehrani, K. Jalaleddini, and R. E. Kearney, "Identification of ankle joint stiffness during passive movements - a subspace linear parameter varying approach," in *Proceedings of IEEE Engineering in Medicine and Biology Society*, 2014, pp. 1603–1606.

[207] P. Morasso, "Spatial control of arm movements," *Experimental Brain Research*, vol. 42, no. 2, pp. 223–227, 1981.

[208] R. Kearney and R. Kirsch, "System identification and neuromuscular modeling," in *Biomechanics and Neural Control of Posture and Movement*, J. Winters and P. Crago, Eds. Springer New York, 2000, pp. 134–147.

[209] F. J. Valero-Cuevas, “An integrative approach to the biomechanical function and neuromuscular control of the fingers,” *Journal of Biomechanics*, vol. 38, no. 4, pp. 673 – 684, 2005.

[210] R. Shadmehr, F. Mussa-Ivaldi, and E. Bizzi, “Postural force fields of the human arm and their role in generating multijoint movements,” *The Journal of Neuroscience*, vol. 13, no. 1, pp. 45–62, 1993.

[211] J. Dolan, M. Friedman, and M. Nagurka, “Dynamic and loaded impedance components in the maintenance of human arm posture,” *Systems, Man and Cybernetics, IEEE Transactions on*, vol. 23, no. 3, pp. 698–709, May 1993.

[212] T. Tsuji, P. Morasso, K. Goto, and K. Ito, “Human hand impedance characteristics during maintained posture,” *Biological Cybernetics*, vol. 72, no. 6, pp. 475–485, 1995.

[213] H. Gomi and M. Kawato, “Human arm stiffness and equilibrium-point trajectory during multi-joint movement,” *Biological Cybernetics*, vol. 76, no. 3, pp. 163–171, 1997.

[214] E. J. Perreault, R. F. Kirsch, and A. M. Acosta, “Multiple-input, multiple-output system identification for characterization of limb stiffness dynamics,” *Biological Cybernetics*, vol. 80, no. 5, pp. 327–337, 1999.

[215] H. Lee, P. Ho, M. Rastgaar, H. Krebs, and N. Hogan, “Multivariable static ankle mechanical impedance with active muscles,” *Neural Systems and Rehabilitation Engineering, IEEE Transactions on*, vol. 22, no. 1, pp. 44–52, 2014.

[216] H. Lee, H. Krebs, and N. Hogan, “Multivariable dynamic ankle mechanical impedance with active muscles,” *Neural Systems and Rehabilitation Engineering, IEEE Transactions on*, vol. 22, no. 5, pp. 971–981, Sept 2014.

[217] L.-Q. Zhang, G. Nuber, J. Butler, M. Bowen, and W. Z. Rymer, “In vivo human knee joint dynamic properties as functions of muscle contraction and joint position,” *Journal of Biomechanics*, vol. 31, no. 1, pp. 71 – 76, 1997.

[218] M. Lakie, E. G. Walsh, and G. W. Wright, “Resonance at the wrist demonstrated by the use of a torque motor: an instrumental analysis of muscle tone in man.” *The Journal of Physiology*, vol. 353, no. 1, pp. 265–285, 1984.

[219] H. S. Cooker, C. R. Larson, and E. S. Luschei, "Evidence that the human jaw stretch reflex increases the resistance of the mandible to small displacements." *The Journal of Physiology*, vol. 308, no. 1, pp. 61–78, 1980.

[220] D. A. Kistemaker, A. K. J. Van Soest, and M. F. Bobbert, "Equilibrium point control cannot be refuted by experimental reconstruction of equilibrium point trajectories," *Journal of Neurophysiology*, vol. 98, no. 3, pp. 1075–1082, 2007.

[221] L. Zhang and W. Rymer, "Simultaneous and nonlinear identification of mechanical and reflex properties of human elbow joint muscles," *IEEE Transactions on Biomedical Engineering*, vol. 44, no. 12, pp. 1192–1209, 1997.

[222] P. J. Lee, K. P. Granata, and K. M. Moorhouse, "Active trunk stiffness during voluntary isometric flexion and extension exertions," *Human Factors: The Journal of the Human Factors and Ergonomics Society*, vol. 49, no. 1, pp. 100–109, 2007.

[223] K. M. Moorhouse, "Role of intrinsic and reflexive dynamics in the control of spinal stability," Ph.D. dissertation, Virginia Polytechnic Institute and State University, 2005.

[224] S. M. Tare, "Estimation of stretch reflex contributions of wrist using system identification and quantification of tremor in parkinson's disease patients," Master's thesis, University of Pittsburgh, 2009.

[225] B. Ikharia and D. Westwick, "A bootstrap term selection method for the identification of time-varying nonlinear systems," in *Engineering in Medicine and Biology Society, 2006. EMBS '06. 28th Annual International Conference of the IEEE*, 2006, pp. 3712–3715.

[226] W. Harwin, A. Murgia, and E. Stokes, "Assessing the effectiveness of robot facilitated neurorehabilitation for relearning motor skills following a stroke," *Medical & Biological Engineering & Computing*, vol. 49, no. 10, pp. 1093–1102, 2011.

[227] A. Swain, D. Westwick, and E. Perreault, "Frequency domain identification of a parallel-cascade joint stiffness model," in *American Control Conference (ACC), 2010*, 2010, pp. 4367–4372.

[228] M. Mirbagheri, L. Ness, C. Patel, K. Quiney, and W. Rymer, "The effects of robotic-assisted locomotor training on spasticity and volitional control," in *Rehabilitation Robotics (ICORR), 2011 IEEE International Conference on*, June 2011, pp. 1–4.

[229] R. B. Stein and R. E. Kearney, "Nonlinear behavior of muscle reflexes at the human ankle joint," *Journal of Neurophysiology*, vol. 73, no. 1, pp. 65–72, 1995.

[230] D. J. Bennett, J. M. Hollerbach, Y. Xu, and I. W. Hunter, "Time-varying stiffness of human elbow joint during cyclic voluntary movement," *Experimental Brain Research*, vol. 88, no. 2, pp. 433–442, 1992.

[231] X. Hu, W. M. Murray, and E. J. Perreault, "Muscle short-range stiffness can be used to estimate the endpoint stiffness of the human arm," *Journal of Neurophysiology*, vol. 105, no. 4, pp. 1633–1641, 2011.

[232] J. MacNeil, R. Kearney, and I. Hunter, "Identification of time-varying biological systems from ensemble data (joint dynamics application)," *IEEE Transactions on Biomedical Engineering*, vol. 39, no. 12, pp. 1213–1225, Dec 1992.

[233] I. Cathers, N. ODwyer, and P. Neilson, "Variation of magnitude and timing of wrist flexor stretch reflex across the full range of voluntary activation," *Experimental Brain Research*, vol. 157, no. 3, pp. 324–335, 2004.

[234] R. E. Kearney, M. Lortie, and R. B. Stein, "Modulation of stretch reflexes during imposed walking movements of the human ankle," *Journal of Neurophysiology*, vol. 81, no. 6, pp. 2893–2902, 1999.

[235] R. Kearney and I. Hunter, "Dynamics of human ankle stiffness: Variation with displacement amplitude," *Journal of Biomechanics*, vol. 15, no. 10, pp. 753 – 756, 1982.

[236] E. Toft, G. T. Espersen, S. Klund, T. Sinkjr, and B. C. Hornemann, "Passive tension of the ankle before and after stretching," *The American Journal of Sports Medicine*, vol. 17, no. 4, pp. 489–494, 1989.

[237] W. A. Qita, "Triceps surae fatigue, and its effects on intrinsic and reflex contributions of human ankle dynamics," Master's thesis, McGill University, 2000.

[238] S. Kuitunen, P. V. Komi, and H. Kyröläinen, "Knee and ankle joint stiffness in sprint running." *Medicine & Science in Sports & Exercise*, no. 34, pp. 166–73, 2002.

[239] M. J. Grey, C. W. Pierce, T. E. Milner, and T. Sinkjær, “Soleus stretch reflex during cycling.” *Motor control*, vol. 5, no. 1, pp. 36–49, 2001.

[240] A. H. Hansen, D. S. Childress, S. C. Miff, S. A. Gard, and K. P. Mesplay, “The human ankle during walking: implications for design of biomimetic ankle prostheses,” *Journal of Biomechanics*, vol. 37, no. 10, pp. 1467 – 1474, 2004.

[241] J. Rothwell, M. Traub, and C. Marsden, “Influence of voluntary intent on the human long-latency stretch reflex,” 1980.

[242] F. Doemges and P. M. Rack, “Task-dependent changes in the response of human wrist joints to mechanical disturbance.” *The Journal of Physiology*, vol. 447, no. 1, pp. 575–585, 1992.

[243] W. Greblicki and M. Pawlak, “Nonparametric identification of hammerstein systems,” *Information Theory, IEEE Transactions on*, vol. 35, no. 2, pp. 409–418, Mar 1989.

[244] W. Greblicki, “Continuous time Hammerstein system identification,” *IEEE Transactions on Automatic Control*, vol. 45, pp. 1232–1236, 2000.

[245] S. A. Billings and S. Y. Fakhouri, “Identification of a class of nonlinear systems using correlation analysis,” in *Proceedings of IEEE*, 1978, pp. 691–697.

[246] W. Greblicki, “Stochastic approximation in nonparametric identification of hammerstein systems,” *Automatic Control, IEEE Transactions on*, vol. 47, no. 11, pp. 1800–1810, 2002.

[247] M. Ranjbaran, K. Jalaleddini, D. G. Lopez, R. E. Kearney, and H. L. Galiana, “Analysis and modeling of noise in biomedical systems,” in *Proceedings of IEEE Engineering in Medicine and Biology Society*, 2013, pp. 997–1000.

[248] R. Kearney and I. Hunter, “Nonlinear identification of stretch reflex dynamics,” *Annals of Biomedical Engineering*, vol. 16, no. 1, pp. 79–94, 1988.

[249] D. Westwick and R. Kearney, “Separable least squares identification of nonlinear Hammerstein models: Application to stretch reflex dynamics,” *Annals of Biomedical Engineering*, vol. 29, pp. 707–718, 2001.

[250] E. J. Dempsey and D. T. Westwick, “Identification of Hammerstein models with cubic spline nonlinearities,” *IEEE Transactions on Biomedical Engineering*, vol. 51, no. 2, pp. 237–245, 2004.

[251] F. Le, I. Markovsky, C. T. Freeman, and E. Rogers, “Identification of electrically stimulated muscle models of stroke patients,” *Control Engineering Practice*, vol. 18, no. 4, pp. 396 – 407, 2010.

[252] E. Bai and D. Li, “Convergence of the iterative Hammerstein system identification algorithm,” *IEEE Transactions on Automatic Control*, vol. 49, no. 11, pp. 1929–1940, 2004.

[253] K. S. Narendra and P. Gallman, “An iterative method for the identification of nonlinear systems using a Hammerstein model,” *IEEE Transactions on Automatic Control*, vol. 11, pp. 546–550, 1966.

[254] P. Stoica, “On the convergence of an iterative algorithm used for Hammerstein system identification,” *IEEE Transactions on Automatic Control*, vol. 26, pp. 967–969, 1981.

[255] E. Bai, “An optimal two-stage identification algorithm for Hammerstein-Wiener nonlinear systems,” *Automatica*, vol. 34, no. 3, pp. 333–338, 1998.

[256] Y. Liu and E. W. Bai, “Iterative identification of Hammerstein systems,” *Automatica*, vol. 43, 2007.

[257] G. Q. Li and C. Wen, “Convergence of normalized iterative identification of hammerstein systems,” *Systems & Control Letters*, vol. 60, no. 11, pp. 929–935, 2011.

[258] K. Jalaleddini and R. E. Kearney, “An iterative algorithm for the subspace identification of SISO Hammerstein systems,” in *Proceedings of IFAC*, 2011, pp. 11 779–11 784.

[259] S. Kukreja, H. Galiana, and R. Kearney, “Narmax representation and identification of ankle dynamics,” *Biomedical Engineering, IEEE Transactions on*, vol. 50, no. 1, pp. 70–81, Jan 2003.

[260] D. L. Guarin, K. Jalaleddini, and R. E. Kearney, “Identification of a parametric, discrete-time model of ankle stiffness,” in *Proceedings of IEEE Engineering in Medicine and Biology Society*, 2013, pp. 5065–5070.

[261] D. L. G. Lopez, “Identification of multiple-input-single-output discrete transfer function models. application to ankle stiffness,” Master’s thesis, McGill University, 2013.

[262] G. Li, W. X. Z. C. Wen, and G. Zhao, “Iterative method in the identification of block-oriented systems based on biconvex optimization,” in *Proceedings of 16th IFAC Symposium on System Identification*, 2012, pp. 31–36.

[263] I. Goethals, K. Pelckmans, J. A. K. Suykens, and B. D. Moor, “Subspace identification of Hammerstein systems using least squares support vector machines,” *IEEE Transactions on Automatic Control*, vol. 50, no. 10, pp. 1509–1519, 2005.

[264] B. El-Sakkary, “Modulation of stretch reflex excitability with postural sway in the frontal plane,” Master’s thesis, McGill University, 2007.

[265] S. L. Kukreja, R. E. Kearney, and H. L. Galiana, “A least-squares parameter estimation algorithm for switched hammerstein systems with applications to the VOR,” *IEEE Transactions on Biomedical Engineering*, vol. 52, no. 3, pp. 431–444, 2005.

[266] K. Ogata, *Modern Control Engineering*. Prentice Hall, 2002.

[267] Y. Zhao and R. E. Kearney, “System identification of biomedical systems from short transients using space methods,” in *Proceedings of 30th Annual International IEEE EMBS Conference*, 2008, pp. 295–298.

[268] P. J. Bock, R. E. Kearney, S. M. Forster, and R. Wagner, “Modulation of stretch reflex excitability during quiet human standing,” in *Proceedings of the* 26^{th} *Annual International Conference of the IEEE EMBS*, 2004, pp. 4684–4687.

[269] J. C. Houk, “Regulation of stiffness by skeletomotor reflexes,” *Annual Review of Physiology*, vol. 41, no. 1, pp. 99–114, 1979.

[270] E. J. Perreault, P. E. Crago, and R. F. Kirsch, “Estimation of intrinsic and reflex contributions to muscle dynamics: A modeling study,” *IEEE Transactions on Biomedical Engineering*, vol. 47, no. 11, pp. 1413–1421, 2001.

[271] K. Jalaleddini and R. E. Kearney, “Subspace identification of SISO Hammerstein systems: Application to stretch reflex identification,” *IEEE Transactions on Biomedical Engineering*, vol. 60, no. 10, pp. 2725–2734, 2013.

[272] D. Ludvig and R. Kearney, “Estimation of joint stiffness with a compliant load,” in *Proceedings of International Conference of the IEEE Engineering in Medicine and Biology Society*, 2009, pp. 2967–2970.

[273] M. Schoukens, E. W. Bai, and Y. Rolain, "Identification of Hammerstein-Wiener systems," in *Proceedings of the 16th IFAC Symposium on System Identification*, 2012, pp. 274–279.

[274] K. Jalaleddini and R. Kearney, "Subspace method decomposition and identification of the parallel-cascade model of ankle joint stiffness: Theory and simulation," in *Engineering in Medicine and Biology Society (EMBC), 35th Annual International Conference of the IEEE*, 2013, pp. 5071–5074.

[275] G. Strang, *Linear Algebra and Its Applications.* Brooks Cole, February 1988.

[276] V. Laurain, R. Tth, M. Gilson, and H. Garnier, *Linear Parameter-Varying System Identification: New Developments and Trends.* World Scientific Publishing, 2011, ch. Identification of Input-Output LPV Models, pp. 95–131.

[277] V. Marmarelis, D. Shin, M. Orme, and R. Zhang, "Time-varying modeling of cerebral hemodynamics," *IEEE Transactions on Biomedical Engineering*, vol. 61, no. 3, pp. 694–704, March 2014.

[278] K. Jalaleddini, E. Sobhani Tehrani, and R. E. Kearney, "A subspace approach to the structural decomposition and identification of ankle joint dynamic stiffness," *IEEE Transactions on Biomedical Engineering*, pp. 1–11, 2014.

[279] A. Ghoreyshi and H. Galiana, "Simultaneous identification of oculomotor subsystems using a hybrid system approach: Introducing hybrid extended least squares," *IEEE Transactions on Biomedical Engineering*, vol. 57, no. 5, pp. 1089–1098, May 2010.

[280] M. Ranjbaran and H. Galiana, "Identification of the vestibulo-ocular reflex dynamics," in *2014 36th Annual International Conference of the IEEE Engineering in Medicine and Biology Society (EMBC)*, Aug 2014, pp. 1485–1488.

[281] M. Blackburn, P. van Vliet, and S. P. Mockett, "Reliability of measurements obtained with the modified ashworth scale in the lower extremities of people with stroke," *Physical therapy*, vol. 82, no. 1, pp. 25–34, 2002.

[282] M. M. Mirbagheri, K. Settle, R. Harvey, and W. Z. Rymer, "Neuromuscular abnormalities associated with spasticity of upper extremity muscles in hemiparetic stroke," *Journal of Neurophysiology*, vol. 98, no. 2, pp. 629–637, 2007.

[283] A. G. Feldman and M. F. Levin, "The equilibrium-point hypothesis - past, present and future," in *Progress in Motor Control*, ser. Advances in Experimental Medicine and Biology, D. Sternad, Ed. Springer US, 2009, vol. 629, pp. 699–726.

[284] G. E. Loeb, "The control and responses of mammalian muscle spindles during normally executed motor tasks." *Exercise and sport sciences reviews*, vol. 12, no. 1, pp. 157–204, 1984.

[285] S. L. Kukreja, H. L. Galiana, and R. E. Kearney, "A bootstrap method for structure detection of narmax models," *International Journal of Control*, vol. 77, no. 2, pp. 132–143, 2004.

[286] J. W. McDonald and C. Sadowsky, "Spinal-cord injury," *The Lancet*, vol. 359, no. 9304, pp. 417 – 425, 2002.

[287] Spinal cord injury canada. [Online]. Available: http://sci-can.ca/resources/sci-facts

[288] L. J. W., *Symposium synopsis*. Year Book Medical Publishers, 1980, pp. 485–495.

[289] K. Perell, A. Scremin, O. Scremin, and C. Kunkel, "Quantifying muscle tone in spinal cord injury patients using isokinetic dynamometric techniques," *Spinal Cord*, vol. 34, no. 1, pp. 46–53, 1996.

[290] B. Ashworth, "Preliminary trial of carisoprodol in multiple sclerosis." *The practitioner*, vol. 192, p. 540, 1964.

[291] R. W. Bohannon and M. B. Smith, "Interrater reliability of a modified ashworth scale of muscle spasticity," *Physical Therapy*, vol. 67, no. 2, pp. 206–207, 1987.

[292] J. F. Fleuren, G. E. Voerman, C. V. Erren-Wolters, G. J. Snoek, J. S. Rietman, H. J. Hermens, and A. V. Nene, "Stop using the ashworth scale for the assessment of spasticity," *Journal of Neurology, Neurosurgery & Psychiatry*, vol. 81, no. 1, pp. 46–52, 2010.

[293] M. Mirbagheri, M. Kindig, X. Niu, D. Varoqui, and P. Conaway, "Robotic-locomotor training as a tool to reduce neuromuscular abnormality in spinal cord injury: The application of system identification and advanced longitudinal modeling," in *Rehabilitation Robotics (ICORR), 2013 IEEE International Conference on*, June 2013.

[294] M. Mirbagheri and R. Kearney, "Mechanisms underlying a third-order parametric model of dynamic reflex stiffness," in *Engineering in Medicine and Biology Society, 2000. Proceedings of the 22nd Annual International Conference of the IEEE*, vol. 2, 2000, pp. 924–927.

[295] W. A. Lee, A. Boughton, and W. Z. Rymer, "Absence of stretch reflex gain enhancement in voluntarily activated spastic muscle," *Experimental neurology*, vol. 98, no. 2, pp. 317–335, 1987.

[296] R. Powers, J. Marder-Meyer, and W. Rymer, "Quantitative relations between hypertonia and stretch reflex threshold in spastic hemiparesis," *Annals of neurology*, vol. 23, no. 2, pp. 115–124, 1988.

[297] A. Thilmann, S. Fellows, and E. Garms, "The mechanism of spastic muscle hypertonus," *Brain*, vol. 114, no. 1, pp. 233–244, 1991.

[298] V. Dietz, M. Trippel, and W. Berger, "Reflex activity and muscle tone during elbow movements in patients with spastic paresis," *Annals of neurology*, vol. 30, no. 6, pp. 767–779, 1991.

[299] M. A. Golkar and R. E. Kearney, "Closed-loop identification of the dynamic relation between surface emg and torque at the human ankle," in *Proceedings of 17th IFAC Symposium on System Identification*, 2015.

[300] Y. Zhao, D. Ludvig, and R. Kearney, "Closed-loop system identification of ankle dynamics using a subspace method with reference input as instrumental variable," in *Proceedings of IEEE American Control Conference*, 2008, pp. 619–624.

[301] E. Sobhani Tehrani, K. Jalaleddini, and R. Kearney, "A novel algorithm for linear parameter varying identification of hammerstein systems with time-varying nonlinearities," in *Engineering in Medicine and Biology Society (EMBC), 2013 35th Annual International Conference of the IEEE*, 2013, pp. 4928–4932.

[302] E. S. Tehrani, M. A. Golkar, D. L. Guarin, K. Jalaleddini, and R. E. Kearney, "Methods for the identification of time-varying hammerstein systems with applications to the study of dynamic joint stiffness," in *Proceedings of 17th IFAC Symposium on System Identification*, 2015.

[303] V. Verdult and M. Verhaegen, "Identification of multivariable lpv state space systems by local gradient search," in *Proceedings of the European Control Conference 2001*, 2001.

[304] J.-W. van Wingerden and M. Verhaegen, "Subspace identification of bilinear and LPV systems for open- and closed-loop data," *Automatica*, vol. 45, no. 2, pp. 372 – 381, 2009.

[305] V. Verdult and M. Verhaegen, "Kernel methods for subspace identification of multivariable LPV and bilinear systems," *Automatica*, vol. 41, no. 9, pp. 1557 – 1565, 2005.

[306] K. Jalaleddini and R. E. Kearney, "Estimation of the gain and threshold of the stretch reflex with a novel subspace identification algorithm," in *Proceedings of IEEE Engineering in Medicine and Biology Society*, 2011, pp. 4431–4434.

[307] H. Schwetlick and T. Schütze, "Least squares approximation by splines with free knots," *BIT*, vol. 35, no. 3, pp. 361–384, 1995.

[308] W. V. Loock, G. Pipeleers, J. D. Schutter, and J. Swevers, "A convex optimization approach to curve fitting with B-splines," in *Proceedings of IFAC*, 2011, pp. 2290–2295.

[309] I. J. LeonTaritis and S. A. Billings, "Experimental design and identifiability for non-linear systems," *International Journal of System Science*, vol. 18, no. 1, pp. 189–202, 1987.